
Unravelling the nature of explosion of thermonuclear supernovae

A Thesis
Submitted for the Degree of
Doctor of Philosophy

in

The Department of Physics,
Pondicherry University,
Puducherry - 605 014, India



by

Anirban Dutta
Indian Institute of Astrophysics,
Bengaluru - 560 034, India



May 2023

Unravelling the nature of explosion of thermonuclear supernovae

Anirban Dutta

Indian Institute of Astrophysics



Indian Institute of Astrophysics
Bengaluru - 560 034, India

Title of the thesis : **Unravelling the nature of explosion of thermonuclear supernovae**

Name of the author : **Anirban Dutta**

Address : Indian Institute of Astrophysics
II Block, Koramangala
Bengaluru - 560 034, India

Email : anirban.dutta@iiap.res.in

Name of the supervisor : **Prof. G. C. Anupama**

Address : Indian Institute of Astrophysics
II Block, Koramangala
Bengaluru - 560 034, India

Email : gca@iiap.res.in

Declaration of Authorship

I hereby declare that the research contained in this thesis is the result of the investigations carried out by me at the Indian Institute of Astrophysics, Bengaluru, under the supervision of **Prof. G. C. Anupama**. This work has not been submitted for awarding a degree or any other qualification either in this university or any other institution.

Anirban Dutta

Anirban Dutta

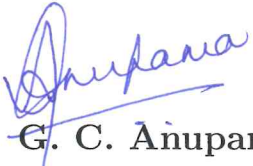
Ph.D Student, IIA,

Bengaluru-560034, India

Date : May, 2023

Certificate

This is to certify that the thesis titled “**Unravelling the nature of explosion of thermonuclear supernovae**” submitted to the Pondicherry University by Mr. Anirban Dutta for the award of the degree of Doctor of Philosophy, is based on the results of the investigations carried out by him under my supervision and guidance, at the Indian Institute of Astrophysics. This thesis has not been submitted to any other university or institute for the award of any degree, diploma, fellowship, etc.



G. C. Anupama

Thesis Supervisor,
Indian Institute of Astrophysics,
Bengaluru-560034, India

Date : May, 2023

List of Publications

1. ****SN 2017hpa: a carbon-rich Type Ia supernova;** **Anirban Dutta**, Avinash Singh, G. C. Anupama, D. K. Sahu & Brajesh Kumar *Monthly Notices of the Royal Astronomical Society, Volume 503, Issue 1, May 2021, Pages 896–910*
2. ****SN 2020sck: deflagration in a carbon-oxygen white dwarf;** **Anirban Dutta**, D. K. Sahu, G. C. Anupama, Simran Joharle, Brajesh Kumar, Nayana A J, Avinash Singh, Harsh Kumar, Varun Bhalerao & Sudhanshu Barway *The Astrophysical Journal, Volume 925, Number 2*
3. ****Can the Violent Merger of White Dwarfs Explain the Slowest Declining Type Ia supernova SN 2011aa?;** **Anirban Dutta**, G. C. Anupama, N. K. Chakradhari & D. K. Sahu *The Astrophysical Journal Letters, Volume 938, Number 2*
4. **Optical studies of a bright Type Iax supernova SN 2020rea;** Mridweeka Singh et al. [including **Anirban Dutta**] *Monthly Notices of the Royal Astronomical Society, Volume 517, Issue 4, December 2022, Pages 5617–5626*
5. **GROWTH on S190426c II: GROWTH-India Telescope search for an optical counterpart with a custom image reduction and candidate vetting pipeline;** Harsh Kumar et al. [including **Anirban Dutta**] *Monthly Notices of the Royal Astronomical Society, Volume 516, Issue 3, November 2022, Pages 4517–4528*
6. **India's First Robotic Eye for Time-domain Astrophysics: The GROWTH-India Telescope;** Harsh Kumar et al. [including **Anirban Dutta**] *The Astronomical Journal, Volume 164, Number 3*
7. **The long-active afterglow of GRB 210204A: detection of the most delayed flares in a gamma-ray burst;** Harsh Kumar et al. [including **Anirban Dutta**] *Monthly Notices of the Royal Astronomical Society, Volume 513, Issue 2, June 2022, Pages 2777–2793*

8. **Intermediate luminosity type Iax supernova 2019muj with narrow absorption lines: Long-lasting radiation associated with a possible bound remnant predicted by the weak deflagration model**; Miho Kawabata et al. [including **Anirban Dutta**] *Publications of the Astronomical Society of Japan*, Volume 73, Issue 5, October 2021, Pages 1295–1314
9. **SN 2020ank: a bright and fast-evolving H-deficient superluminous supernova**; Amit Kumar et al. [including **Anirban Dutta**] *Monthly Notices of the Royal Astronomical Society*, Volume 502, Issue 2, April 2021, Pages 1678–1693
10. **Kilonova Luminosity Function Constraints Based on Zwicky Transient Facility Searches for 13 Neutron Star Merger Triggers during O3**; Mansi M. Kasliwal et al. [including **Anirban Dutta**] *The Astrophysical Journal*, Volume 905, Number 2
11. **GROWTH on S190425z: Searching Thousands of Square Degrees to Identify an Optical or Infrared Counterpart to a Binary Neutron Star Merger with the Zwicky Transient Facility and Palomar Gattini-IR**; Michael W. Coughlin et al. [including **Anirban Dutta**] *The Astrophysical Journal Letters*, Volume 885, Number 1
12. **SN 2018hna: 1987A-like Supernova with a Signature of Shock Breakout**; Avinash Singh et al. [including **Anirban Dutta**] *The Astrophysical Journal Letters*, Volume 882, Number 2

** *Included in this thesis*

Presentations

1. Presented a talk on “[Probing the homogeneity/diversity in Type Ia supernova explosions](#)”, REcent Trends in the study of Compact Objects (RETCOV) : Theory and Observations, Kodaikanal Solar Observatory from 03 - 05 April, 2023.
2. Presented a 1 min flash talk on “[Can the violent merger of white dwarfs explain the slowest declining Type Ia supernova SN 2011aa?](#)”, SuperVirtual, held online from 07 - 11 November 2022.
3. Presented an online poster online on “[Can the violent merger of white dwarfs explain the slowest declining Type Ia supernova SN 2011aa?](#)”, Time Domain and Multi-messenger astrophysics NASA workshop, Annapolis, Maryland, USA from 22 - 24 August 2022.
4. Presented an online talk on “[Can the violent merger of white dwarfs explain the slowest declining Type Ia supernova SN 2011aa?](#)”, Boom! A Workshop on explosive transients with LSST, University of Illinois at Urbana-Champaign, USA, 25 - 29 July 2022.
5. Presented a poster on “[Understanding type Ia supernova explosion through time-dependent Monte Carlo radiative transfer simulations](#)”, 40th Meeting of the Astronomical Society of India, Jointly by IIT Roorkee and ARIES Nainital, 25 - 29 March 2022.
6. Presented a poster on “[Observational Study of nearby Type Ia Supernova 2019np for over 400 days](#)”, 9th Meeting of the Astronomical Society of India, held online from 18 - 23 February 2021.

7. Presented a talk on “Observation of Carbon-rich Supernova SN 2017hpa”, 38th Meeting of the Astronomical Society of India, IISER Tirupati, 13 - 17 February 2020.
8. Presented a 3 min flash talk on “SN 2017hpa: A Carbon-rich High Velocity Gradient Supernova ”, 20 Years of Himalayan Chandra Telescope, held at IIA from 29 - 30 September 2020.
9. Presented a poster on “Photometric and spectroscopic studies of Type Ia Supernova”, Applications of Data Science in Astrophysics and Gravitational Wave Research, IIT Allahabad, from 01 - 03 November 2019.

Schools and workshops

1. Participant in “Zwicky Transient Facility Summer School”, held online from 6 - 20 August 2021.
2. Tutor at “GROWTH Astronomy Online School”, held online from 17 - 21 August 2020.

Acknowledgements

From my school days, I used to get fascinated when I could discuss other planets or life on other planets with my family and friends. My mother took me to Birla Planetarium and Science City in Kolkata, where we enjoyed special shows on the Universe on weekends. This fostered my interest in Astronomy. I used to go for studies to one of my teachers, whom I called Samiran Sir, who discussed with me black holes, exploding stars and life on other planets. I took Science stream after class 10 only to study basic sciences. I want to thank all my teachers/professors in school, college and University for putting in the effort so that I can now write my PhD thesis.

I would express my heartfelt gratitude to my supervisor Prof. G. C. Anupama, who has always encouraged me to try new things for my research. As I am in the field of supernovae/transients, which can happen at any time in the Universe, she has taught me to be active and alert. I feel this is also important for other areas of life.

I want to thank my group members Prof. Devendra Sahu, Prof. Sudhanshu Barway, Dr Avinash Singh, Dr Brajesh Kumar, Dr Pavana M, Dr Mridweeka Singh, Dr Nayana A J, Dr. N. K. Chakradhari, and Rishabh S. Teja for providing valuable inputs to my work during group meetings. I have always enjoyed going to CREST to take observations and discuss supernovae, observations, and telescopes with Prof. Devendra Sahu. I want to thank my collaborators from IIT Bombay for many helpful scientific discussions and observations with the GIT. I want to thank my doctoral committee members, Prof. U. S. Kamath, and Prof. R. Sivakumar, for providing valuable comments and suggestions that helped improve the thesis content.

I want to thank Prof. P. Sreekumar, Prof. Jayant Murthy, Prof. Annapurni Subramaniam, Prof. G. C. Anupama, and Prof. B. E. Reddy for providing a great environment for learning, research, and career-building at IIA. I would also like to thank all the members of the Board of Graduate Studies and the administrative department of IIA for helping me with various academic and office-related works. I want to thank the library staff of IIA, and Pondicherry University for all the help they provided me. I would take this opportunity to thank the HOD, COE, and administrative staff of Pondicherry University for helping me with various office-related works. They have allowed me to focus only on my research without thinking much about the paper works. I would like to thank the Bhaskara staff for all the hospitality and care they have taken especially during the pandemic time. I thank Pramod, Sujith, Kiran, Rakesh, Mulchand, Anaswar, Yogita and all the members of CREST, and IAO, Hanle for helping me with the observations.

I think my PhD journey would not have been smooth without my friends. Thanking friends is not enough, but still, I would like to give a big shout out to my batchmates Indrani, Sonith, Sioree, Deepthi, Fazlu, Swastik, Satabdwa, Sharmila, Athira, Bharat, and Vikrant. These people were always there for me. I would also like to thank, Partha, Debjit, Anohita, Shubham, Judhajeet, Rishabh, Sushant, Suman, Manika for all the enjoying moments which I will never forget. I would apologise for missing some names, but I thank all my current friends, and seniors at Bhaskara, and IIA for making my stay such a memorable one.

I thank Prof. Wolfgang Kerzendorf for offering me a post-doctoral researcher position at Michigan State University.

I thank my sisters for constantly motivating me in every stage of life. Lastly, I would thank my inspiration, idol, and superstar - my mother for everything I have.

Data and Software usage

In this thesis, I have presented observational data from the 2.0 m Himalayan Chandra Telescope (HCT). This work made use of data from the 0.7 m GROWTH-India Telescope (GIT) set up by the Indian Institute of Astrophysics (IIA) and the Indian Institute of Technology Bombay (IITB) with funding from DST-SERB and IUSSTF. We acknowledge funding by the IITB alumni batch of 1994, which partially supports the operations of the telescope. Both the HCT, and the GIT are located at IAO, Hanle. I thank the staff of IAO, Hanle and CREST, Hosakote that made the observations possible. The facilities at IAO and CREST are operated by the Indian Institute of Astrophysics, Bengaluru, an autonomous Institute under the Department of Science and Technology, Government of India. I thank the observers of HCT who shared their valuable time for Target of Opportunity (ToO) observations during the initial follow-up of supernovae. This work is also based on observations from the 3.6 m Devasthal Optical Telescope (DOT), a National Facility run and managed by Aryabhata Research Institute of Observational Sciences (ARIES), an autonomous Institute under the Department of Science and Technology, Government of India. This research has made use of the High-Performance Computing (HPC) resources (<https://www.iiap.res.in/?q=facilities/computing/nova>) made available by the Computer Center of the Indian Institute of Astrophysics, Bangalore. NOVA is a 26 node high-performance computing cluster with 720 cores, 3.5 TB memory and 36 TB of storage capacity in total.

The research has made use of the archival data obtained from the High Energy

Astrophysics Science Archive Research Center (HEASARC) *, a facility of the Astrophysics Science Division at NASA/GSFC and of the Smithsonian Astrophysical Observatory's High Energy Astrophysics Division.

This work has made use of the NASA Astrophysics Data System[†] (ADS), the NASA/IPAC extragalactic database[‡] (NED) and NASA/IPAC Infrared Science Archive (IRSA)[§] which is operated by the Jet Propulsion Laboratory, California Institute of Technology. I acknowledge, Weizmann Interactive Supernova Data REPOSITORY[¶](WISeREP, Yaron & Gal-Yam 2012), Heidelberg Supernova Model Archive (HESMA, Kromer et al. 2017)^{||}, the Spanish Virtual Observatory** (Rodrigo & Solano 2020), HyperLeda database ^{††} (Makarov et al. 2014).

This research made use of TARDIS, a community-developed software package for spectral synthesis in supernovae (Kerzendorf & Sim 2014; Kerzendorf et al. 2019). The development of TARDIS received support from the Google Summer of Code initiative and from ESA's Summer of Code in Space program. TARDIS makes extensive use of Astropy and PyNE. The analysis has made use of the following software and packages - (i) *Image Reduction and Analysis Facility* (IRAF), Tody (1993). (ii) PyRAF, Science Software Branch at STScI (2012). (iii) NumPy, Van Der Walt et al. (2011), (iv) Matplotlib, Hunter (2007), (v) Scipy, Virtanen et al. (2020), (vi) pandas, pandas development team (2020), (vii) Astropy, Astropy Collaboration et al. (2013), (viii) emcee, Foreman-Mackey et al. (2013b), (ix) Corner, Foreman-Mackey (2016) (x) syn++, Thomas et al. (2011), (xi) TARDIS, Kerzendorf & Sim (2014), (xii) SEDONA, Kasen (2006).

*<https://heasarc.gsfc.nasa.gov/>

†<https://ui.adsabs.harvard.edu/>

‡<https://ned.ipac.caltech.edu/>

§<https://irsa.ipac.caltech.edu/applications/DUST/>

¶<https://wiserep.weizmann.ac.il/>

||<https://hesma.h-its.org>

**<https://svo.cab.inta-csic.es>

††<http://leda.univ-lyon1.fr>

Abstract

Type Ia supernovae (SNe Ia) result from thermonuclear explosions in binary systems consisting of at least one carbon-oxygen white dwarf. They are crucial for the understanding of galactic chemical composition as they are the principal producers of Iron (Fe)-group elements in the Universe, sites for cosmic ray production, probes of low mass star formation rates at high redshifts, understanding the binary star evolution, constraining the dark energy equation of state and also as standardizable candles to measure astronomical distances.

The rate of decline in normal Type Ia SNe ($0.85 < \Delta m_{15}(B) < 1.70$ mag) is correlated with the absolute magnitude in B -band. The radioactive decay of ^{56}Ni to ^{56}Co and finally to ^{56}Fe supplies the energy during the maximum of the light curve and its subsequent evolution. The luminosity increases with more ^{56}Ni produced in the explosion. While most SNe Ia follow the luminosity decline rate relation, it is important to note that a good fraction of supernova events of thermonuclear origin do not follow this relation. The over-luminous super-Chandrasekhar SNe Ia lie at the brighter end of the $\Delta m_{15}(B) - M_B$ relation. They are slowly declining objects. The SNe Iax (SN 2002cx-like) are a peculiar class of thermonuclear explosions with low luminosity and low kinetic energy and fast declining compared to other SNe Ia classes. There are other classes of thermonuclear explosions, such as the bright Ia's that show features due to circumstellar interaction in their spectra; the fast declining and faint Ia (also called .Ia); the Ca-rich events; and the SN 2002es-like slowly declining but sub-luminous objects.

To understand the nature of the explosion of these events, and to understand the diversity, various progenitor scenarios are proposed for SNe Ia - the exploding white dwarf (WD) can have a non-degenerate star (single degenerate, SD) or another white

dwarf (double degenerate, DD) as its binary companion. In the SD scenario, the white dwarf can accrete matter from a red-giant, sub-giant/main- sequence or a He star.

A range of explosion models is proposed to explain the observed diversity in SNe Ia. The three-dimensional subsonic pure deflagration in a M_{ch} mass white dwarf (WD) produces explosions that explain SNe Ia. The subsonic deflagration turns to a supersonic detonation due to turbulence called deflagration-to-detonation transition (DDT). The DDT models are capable of explaining normal SNe Ia. Double detonation in a sub- M_{ch} WD has been proposed to explain subluminal SNe like the Ca-rich Ia, faint Ia, and SN 2002es-like events. Detonation due to the merger of WDs can explain normal Ia, sub-luminous events, and bright events having super- M_{ch} ejected mass.

This thesis aims to understand the observed diversity/homogeneity of thermonuclear supernovae in terms of the various explosion mechanisms and progenitors. We have performed long-term monitoring of different kinds of thermonuclear explosions using the 2.0 m Himalayan Chandra Telescope (HCT), 3.6 m Devasthal Optical Telescope (DOT), 0.7 m GROWTH-India Telescope (GIT) in optical wavelengths. We have also used archival UV-optical data from the SWIFT observatory and public data in optical from the Zwicky Transient Facility (ZTF). Analytical modelling of light curves of individual supernovae have been used to estimate the explosion parameters like ^{56}Ni mass, kinetic energy (E_k), ejecta mass (M_{ej}). Numerical models have been generated with publicly available radiative transfer codes like TARDIS, and SEDONA to understand the density profile of the ejecta, abundances of elements in the ejecta of the supernovae. This has been compared with various explosion mechanisms and progenitor scenarios.

Contents

Abstract	i
List of Figures	vii
List of Tables	xv
Abbreviations	xvii
1 Introduction	1
1.1 The width-luminosity relation of SN Ia	3
1.2 ^{56}Ni as the power source	5
1.3 Diversity in thermonuclear SNe	6
1.4 Spectral Classification of SNe Ia	12
1.5 Progenitors	13
1.6 Explosion mechanisms	16
1.7 Outline of the thesis	19
2 Observational Facilities and Data Reduction	21
2.1 Introduction	21
2.2 Observing Facilities	22
2.2.1 Himalayan Chandra Telescope (HCT)	22
2.2.2 GROWTH India Telescope	24
2.2.3 Swift Observatory	25
2.3 Data Reduction Techniques	27
2.3.1 Pre-processing	28
2.3.2 Photometry	30
2.3.3 Spectroscopy	37
3 Analytical and Numerical Modelling	39
3.1 Light Curve Modelling	40
3.1.1 Analytical relation	40

3.1.2	Fitting analytical relation with Markov Chain Monte Carlo (MCMC) technique	43
3.1.3	Interpolating light curves with Gaussian process regression	46
3.2	Spectral Modelling	49
3.2.1	syn++	49
3.2.2	TARDIS	52
3.2.3	SEDONA	55
4	Probing the homogeneity/diversity in Type Ia supernova explosions	59
4.1	SN 2017hpa: A carbon-rich Type Ia Supernova	61
4.1.1	Introduction	61
4.1.2	Extinction and Distance Modulus	64
4.1.3	Light Curve Analysis	68
4.1.4	Estimation of Nickel Mass	72
4.1.5	Spectral Analysis	74
4.1.6	Spectral Fitting in the pre-maximum phase	83
4.1.7	Summary	86
4.2	SN 2011aa: the slowest declining Type Ia supernova	88
4.2.1	Introduction	88
4.2.2	Light Curve Analysis	89
4.2.3	Nickel mass and ejecta mass	93
4.2.4	Spectral evolution	94
4.2.5	Explosion Models	97
4.2.6	Modelling of the spectra and light curves	101
4.2.7	Discussions	107
4.3	Probing the similarity/diversity in Type Ia supernovae	108
4.3.1	Models	109
4.3.2	Model comparison with observations	114
4.3.3	Discussions	125
5	Understanding the explosion mechanism of Type Iax supernovae	131
5.1	SN 2020sck: deflagration in a carbon-oxygen white dwarf	134
5.1.1	Introduction	134
5.1.2	Observations	134
5.1.3	Extinction and distance modulus	140
5.1.4	Light curve	141
5.1.5	Spectral Analysis	150
5.1.6	Spectral Modelling	153
5.1.7	Host Galaxy	160
5.2	Diversity in the Iax class: 2022eyw and 2022xlp	161
5.2.1	Introduction	161
5.2.2	Light Curve Analysis	162

5.2.3	Spectral Analysis	166
5.2.4	Estimation of Ni mass	173
5.3	Explosion Models	175
5.4	Summary	181
6	Conclusions and Future Work	185
6.1	Future with thermonuclear explosions	186
	Bibliography	191

List of Figures

1.1	[A] An illustration of Δm_{15} , the difference in magnitude between maximum and 15 days from maximum using the B -band light curve of SN 2005cf (Wang et al. 2009a) [B] The Phillips relation scaled to $H_0 = 72$ km/s/Mpc. Also shown is the $1\text{-}\sigma$ scatter about the relation.	4
1.2	Absolute magnitudes in $UBVRI$ of SNe 1991T, 1999by (1991bg-like), 2005cf (normal SN Ia), 2005hk (Type Iax), 2009dc (super-Chandra 2003fg-like), 2008J (Ia-CSM), PTF10ops (peculiar) are shown. SNe 1999by, 2009dc, 2005hk does not show prominent secondary I -band peak.	6
1.3	Spectrum of SNe 1991T, 1999by (1991bg-like), 2005cf (normal SNe Ia), 2005hk (Type Iax), 2009dc (super-Chandra SN 2003fg-like), 2008J (Ia-CSM), 2010X (.Ia/SN 2002bj-like), iPTF10iuv (Ca-rich), PTF10ops (peculiar) at pre-max [A], near-max [B], and nebular/post-max phase [C]. All the spectra are redshift-corrected. The spectra have been obtained from WISeREP database.	7
1.4	The diversity in thermonuclear explosions. This figure is adapted from Taubenberger (2017).	9
1.5	Branch classification scheme. The data presented is taken from (Blondin et al. 2012).	14
1.6	Wang classification scheme (Wang et al. 2009b). The data is taken from Blondin et al. (2012).	14
1.7	Spectral classification of SNe Ia according to Benetti et al. (2005). The data presented in this figure is from Benetti et al. (2005).	15
2.1	A schematic diagram of the HFOSC instrument on the 2.0 m HCT. A few important components like the camera, grism wheel, filter wheel, collimator, and aperture wheel are marked.	23
2.2	The filter transmission functions for <i>Swift</i> -UVOT, Bessell $UBVRI$, and SDSS $u'g'r'i'z'$	26
3.1	The effect of varying ^{56}Ni ([A]), t_{1c} ([B]), and t_γ ([C]) on the luminosity of the supernova as given by EQUATION 3.5.	41

3.2	[A] Simulated dataset with the linear model (slope $m=3.0$, and intercept $b=25.0$) overplotted. [B] Positions of the chain in the parameter space of m , and b . We start the chain at $m=2.8$, and $b=-70$. Also shown is the true value ($m=3.0$, and $b=25.0$). [C] The posterior space, data, models drawn from the posterior distribution, and the 1D chains of m , b , and $\ln\pi$	45
3.3	Interpolation of the B -band light curve of SN 2014J (Srivastav et al. 2016) with Gaussian process regression using the <code>scikit-learn</code> package in <code>python</code> . At each interpolated point, we get the interpolated value along with the covariance. The light curve maximum is shown with a star mark.	48
3.4	Simulation of a single P-Cygni profile at a rest wavelength of 5000 Å under Sobolev approximation. The effect of varying the photospheric velocity [A], photospheric temperature [B], the optical depth at the photosphere [C], power law index for the optical depth [D] are shown.	50
4.1	2017hpa in the host galaxy UGC 3122. This is a $\sim 7 \times 7$ arcmin ² image in V -band (50 sec exposure) taken with HCT on 2017 October 31. The supernova is marked with crosshairs. Secondary standards are also marked.	63
4.2	$UBVRI$, and <i>Swift</i> -UVOT light curves of 2017hpa. The phase is wrt B -max. The light curves in individual bands have been shifted for representation purpose.	63
4.3	$UBVRI$ light curve fit with MLCS2k2.	69
4.4	$UBVRI$ light curve fit with SALT2.	69
4.5	$UBVRI$ light curves of 2017hpa compared with other normal Ia. The light curves are shifted so that their peak magnitudes matches. The phase is with respect to B -max.	70
4.6	$ww1 - uvv$, $U - B$, $B - V$, $V - R$, and $R - I$ colours of 2017hpa plotted along with some well studied SNe Ia. Plotted as black dotted line with $(B - V)$ colour is the Lira relation which has been used to find the host $E(B - V)$	72
4.7	The bolometric luminosity of 2017hpa plotted with 1D Radiation Diffusion model.	74
4.8	Top panel: Spectral evolution of 2017hpa at pre-maximum phases. Bottom panel: The -8.9 d spectrum of 2017hpa compared with 2011fe, 2009dc, 2005cf, and 2003du around similar phases.	78
4.9	Top panel: Spectral evolution of 2017hpa around maximum – early post-max. Bottom panel: The $+0.9$ d spectrum of 2017hpa compared with 2011fe, 2009dc, 2005cf, and 2003du around maximum.	78
4.10	Top panel: Post maximum spectral evolution of 2017hpa. Bottom panel: The $+39.0$ d spectrum of 2017hpa compared with the spectra of 2014J, 2009dc, 2005cf, 2003du around similar phase.	80

4.11	Top panel: Spectral evolution of 2017hpa in the early nebular phase. Bottom panel: The +86.8 d spectrum of 2017hpa compared with the spectra of 2014J, 2005cf and 2003du around similar phase. . . .	80
4.12	Velocity evolution of C II λ 6580, Si II λ 6355 and Ca II λ 3951 for 2017hpa (left panel). Comparison of the velocity evolution of Si II λ 6355 for 2017hpa with other Ia (right panel).	81
4.13	2017hpa plotted along with core-normal, cool, shallow-silicon, and faint classes.	82
4.14	2017hpa plotted along with HVG, LVG, and Faint. 2017hpa is plotted with a black star.	82
4.15	Dereddened and redshift corrected spectra of 2017hpa at -13.8 d and -8.9 d. The synthetic spectra generated using <code>syn++</code> are plotted (black solid line). The contributions from each element are shown.	84
4.16	Velocity evolution of C II λ 6580. The velocity is calculated with respect to rest wavelength of C II λ 6580. The dotted solid lines indicate TARDIS fit to the observed spectra with different mass fraction for Carbon.	84
4.17	Identification plot for 2011aa. The local calibration stars are marked with numbers 1-8. East to the right and South is up. The field of view is $10' \times 10'$	88
4.18	Optical <i>UBVRI</i> and <i>Swift</i> -UVOT LCs of 2011aa. The horizontal axis represent rest frame time since <i>B</i> -max $(t - t_{\text{max}})/(1 + z)$. The magnitudes are in <i>Vega</i> system. The light curves are vertically shifted for better presentation. We also plot the <i>JHK_s</i> light curves from Friedman et al. (2015)	90
4.19	Spectral evolution of 2011aa from -10.16 to $+68.6$ day in the rest frame since <i>B</i> -max. C II λ 6580 region is shaded between $+3.5$ to $+17.3$ d. The spectra are redshift and extinction corrected. The important lines for the pre-maximum spectra are marked.	95
4.20	The comparison of 2011aa with luminous SN 1991T, peculiar SN 2001ay and SN 2013cv, normal SN 2005cf and super-Chandra SN 2006gz and SN 2009dc at pre-maximum [A], near-maximum [B] and post-maximum [C] phase.	98
4.21	Spectral evolution of 2011aa from -10.16 to $+10.36$ d since rest frame time in <i>B</i> -max. We show the model spectra calculated using <code>SEDONA</code> . Also shown are the angle averaged spectra of accreting white dwarf model (AWD1) from Fink et al. (2018) and violent merger model from P12. These are taken from the HESMA database. The important lines in the early phase are marked in [A]. The observed spectra are de-reddened and redshift corrected.	103

4.22	[A] The <i>UBVRI</i> band light curves of 2011aa along with synthetic light curves generated using <i>SEDONA</i> . From the model spectral energy distribution we calculate the light curves in <i>AB</i> system and convert to <i>Vega</i> system using values given in Blanton & Roweis (2007) . The horizontal axis is time since explosion (JD 245 5591.62). [B] The $B - V$ colour of 2011aa plotted with the <i>SEDONA</i> models. [C] The optical, UV-optical and <i>UVOIR</i> bolometric light curves are shown along with the models.	106
4.23	Si II $\lambda 6355$ velocity evolution of 2011aa plotted along with other SNe Ia.	107
4.24	The velocity evolution of Si II $\lambda 6355$, C II $\lambda 6580$, and C II $\lambda 7234$ for 2011aa.	107
4.25	Analytical density profiles with masses 1.0, 1.2, 1.4, 1.6, 1.8, and 2.0 M_{\odot} , and kinetic energies 0.7, 1.0, 1.3, 1.5, 1.7, and 1.8×10^{51} erg. Highlighted solid lines represent the models with mass 1.4 M_{\odot} and different kinetic energy. The dashed lines are the one-dimensional angle averaged density profiles for the violent merger model P12 and delayed detonation model S13 taken from HESMA database (Kromer et al. 2017).	110
4.26	Abundance structure of the elements formed in the ejecta for the two explosion models considered. Dashed lines are for the violent merger model, whereas solid lines represent the abundance of the delayed detonation scenario. Panel [A] consists of C, O and the Fe group elements, while IMEs are shown in panel [B]. The abundances for both the explosion scenarios are taken from HESMA database (Kromer et al. 2017).	111
4.27	^{56}Ni mass vs $\Delta m_{15}(B)$ for the models. Left shows the model parameters from VM models, and right panel shows the same from DDT models. Time to B -max is shown in colourbar.	113
4.28	The light curves of 2006bt in <i>UBVRI</i> . The best-fit synthetic light curves are overplotted.	115
4.29	The spectra of SN 2006bt at different phases plotted with the DDT, and VM models.	116
4.30	The light curves of 2011aa in <i>UBVRI</i> . The best-fit synthetic light curves for the DDT-N40, and VM models are overplotted.	117
4.31	The spectra of 2011aa at different phases plotted with the DDT, and VM models.	118
4.32	The light curves of 2012dn in <i>UBVRI</i> . The best-fit synthetic light curves for the DDT-N40, and VM models are also shown.	119
4.33	The spectra of 2012dn at different phases plotted with the DDT, and VM models.	120

4.34	The light curves of 2017hpa in <i>UBVRI</i> . The best-fit synthetic light curves for the DDT, and VM models are shown. To reproduce the secondary maximum, we have used an $\epsilon=0.0$ for Ca and $\epsilon=1.0$ for the other elements in the DDT models. This is shown with yellow in the plots.	121
4.35	The spectra of 2017hpa at different phases plotted with the DDT, and VM models.	122
4.36	The light curves of 2018oh in <i>UBVRI</i> . The best-fit synthetic light curves for the DDT, and VM models are shown.	123
4.37	The spectra of 2018oh at different phases plotted with the DDT, and VM models.	124
4.38	SEDONA models based on varying C abundances.	126
4.39	The NUV-blue and NUV-red group from Milne et al. (2013). For the NUV-blue sample, we have taken SNe 2008hv, 2008Q, 2011by, 2011fe, 2012cg, and 2017cbv. The NUV-red sample consists of SNe 2005cf, 2007sr, 2007af, 2008ec, 2009an, 2009ig, PTF10icb, and 2017erp. The NUV-blue SNe 2011aa, 2012dn, 2017hpa, and 2018oh are also shown. The colours are corrected only for Galactic extinction.	127
4.40	Peak absolute magnitude in <i>B</i> vs $\Delta m_{15}(B)$ for the models. Also shown, the observed M_B and $\Delta m_{15}(B)$ for the five objects considered in this work. The blue stars are parameters from the VM models, while the orange solid circles are from the DDT models. . .	128
5.1	The field of SN 2020sck. This is a $\sim 7 \times 7$ arcmin ² image in <i>B</i> -band (300 sec exposure) taken with HCT on 2020 September 11. The stars circled in blue are the secondary standards used for photometric calibration. The SN is marked with crosshair.	136
5.2	<i>UBVRI</i> , <i>ZTF-g</i> , <i>ZTF-r</i> , <i>GIT-r'</i> band light curves of SN 2020sck. Also plotted are the <i>g</i> , <i>r</i> and <i>i</i> -band magnitudes obtained from DOT. <i>UBVRI</i> magnitudes are in <i>Vega</i> system, and <i>ZTF-g</i> , <i>ZTF-r</i> , <i>GIT-r'</i> , <i>DOT-g</i> , <i>DOT-r</i> and <i>DOT-i</i> magnitudes are in <i>AB</i> system. .	136
5.3	<i>UBVRI</i> LCs of 2020sck plotted with other Iax. The phase is measured with respect to <i>B</i> -max. The light curves are shifted to their peak magnitudes. The $\Delta m_{15}(B)$ of each SN are quoted in parentheses.	142
5.4	<i>ZTF-g</i> and <i>ZTF-r</i> light curves of 2020sck plotted with other Iax in similar filters. The phase is measured with respect to <i>g</i> -maximum. The light curves are normalised with respect to their respective peak magnitudes. The $\Delta m_{15}(g)$ of each SN are quoted in parentheses. The light curve data for SN 2020sck has been obtained from https://alerce.online/object/ZTF20abwrcmq	144
5.5	Colour evolution of 2020sck plotted with other Iax.	145
5.6	$(g - r)$ colour evolution of 2020sck plotted along with other Iax. . .	145
5.7	$F \sim t^n$ fit to the pre-max <i>ZTF-g</i> light curve. Flux errors are shown in blue.	147

- 5.8 The quasi-bolometric LC of 2020sck fitted with 1D radiation diffusion model. Also plotted are the angle-averaged bolometric LC from the three dimensional pure deflagration models of M_{ch} WD from F14. The models have been obtained from the HESMA database. 149
- 5.9 One and two dimensional projections of the posterior probability distribution of the fit parameters to the quasi-bolometric LC of 2020sck. The vertical dashed lines show the 16th, 50th and 84th percentiles of the samples in the distribution. See FIGURE. 5.8 for the fit. 149
- 5.10 Spectral evolution of 2020sck from -5.5 to $+27.5$ day since the B -max. The spectra are dereddened and redshift corrected. The telluric features are removed. The spectra are smoothed for visual clarity. 151
- 5.11 Comparison of the spectra of 2020sck with other Iax around similar phase. The dashed vertical lines show the position of the absorption minima of the ions for 2020sck. All spectra have been smoothed for visual clarity. 153
- 5.12 Dereddened and redshift corrected spectra of SN 2020sck at $+1.4$ d since B -max (shown in red). Overplotted in blue is the synthetic spectra calculated using `syn++`. The contributions from each ion are shown by dashed vertical lines. The observed spectrum has been smoothed for visual clarity. 157
- 5.13 Comparison of the uniform abundance of elements used for SN 2020sck with the stratified abundance for SN 2005hk (Barna et al. 2018). The solid lines show the mass fractions of the elements in the ejecta of SN 2020sck while the dotted lines in the same colour shows the mass fraction in the ejecta of SN 2005hk. 158
- 5.14 Density against velocity plot (in red) used in TARDIS for generating the synthetic spectrum. The density is similar to N5-def density profile below 7200 km s^{-1} and N5-def $\rho \times 0.1$ for velocity above 7200 km s^{-1} . Also plotted for comparison - N5-def profile (F14), W7 profile (Nomoto et al. 1984), density profile for 2005hk from Sahu et al. (2008) and Barna et al. (2018), density profile used for the study of PS1-12bwh (Magee et al. 2017). 158
- 5.15 Panel (a) Spectrum of SN 2020sck at -5.5 d plotted along with synthetic spectrum generated using TARDIS with N5-def density profile (darkorange) and a modified N5-def density profile (black). Panel (b) The $+1.4$ d spectrum of 2020sck plotted with TARDIS spectrum generated using the modified N5-def density profile. Panel (c) Post-maximum $+10.4$ d spectrum of 2020sck compared with TARDIS spectrum generated using the N5-def modified density profile without (black) and, with Ti and Cr (gold). The angle-averaged density profile has been obtained from HESMA database. The observed spectra of 2020sck have been smoothed. 159

5.16	$12 + \log(\text{O}/\text{H})$ plotted against r -band peak magnitude for a sample SNe Iax. The luminous objects have higher metallicity.	161
5.17	$u'g'r'i'z'$ light curves of 2022eyw.	163
5.18	$u'g'r'i'z'$ light curves of 2022xlp.	163
5.19	The early phase spectral evolution of 2022eyw. The phases are with respect to the g' -max.	169
5.20	The early phase spectral evolution of 2022xlp. The phases are with respect to the g' -max.	171
5.21	Comparison of SNe 2022eyw, and 2022xlp with other Type Iax SNe at pre-max phases. The comparison spectra are corrected for redshift.	172
5.22	Comparison of SNe 2022eyw, and 2022xlp with other Type Iax SNe at post-max phases. The comparison spectra are corrected for redshift.	172
5.23	1D radiation diffusion model fit to 2022eyw, and 2022xlp. Quasi-bolometric LCs are constructed by considering the flux from 3800 Å to 10000 Å . See Table 5.15 for the fit parameters.	174
5.24	1D radiation diffusion model fit to a sample of SNe Iax. A quasi-bolometric LC has been constructed by considering the flux from 3000 Å to 9500 Å for all objects. See Table 5.15 for the fit parameters.	177
5.25	Comparison of 2022eyw, and 2022xlp spectra with models from Lach et al. (2022).	179

List of Tables

2.1	Information on the filters used in this work	27
3.1	Comparison between TARDIS, and SEDONA.	57
4.1	Parameters of 2017hpa and its host galaxy.	62
4.2	<i>UBVRI</i> magnitudes of secondary standards used for calibrating the photometry of 2017hpa.	63
4.3	Optical photometry of 2017hpa from HCT.	64
4.4	<i>Swift</i> UV-Optical photometry of 2017hpa.	65
4.5	Best-fit parameters of the light curve for 2017hpa.	68
4.6	Photometric parameters of 2017hpa.	71
4.7	Spectroscopic observations log of 2017hpa from HCT.	75
4.8	<i>syn++</i> fit to the pre-maximum spectra of 2017hpa.	85
4.9	TARDIS fit to the pre-maximum spectra of 2017hpa.	85
4.10	Magnitudes of the secondary standards for the calibration of 2011aa. The ID is as shown in FIGURE 4.17	89
4.11	<i>UBVRI</i> magnitudes of 2011aa from HCT.	90
4.12	<i>Swift</i> -UVOT magnitudes of 2011aa	92
4.13	Spectroscopic observations log of 2011aa from HCT.	96
4.14	SEDONA model features	104
4.15	Details of the objects used in the study	112
4.16	Comparing models with observations of SNe	126
5.1	Parameters of 2020sck and its host.	135
5.2	Magnitudes of the secondary calibration stars in the field of 2020sck.	137
5.3	Spectroscopic observations log of 2020sck from HCT.	138
5.4	<i>UBVRI</i> magnitudes of 2020sck from HCT.	138
5.5	Photometry of 2020sck in r' -band with GIT.	139
5.6	<i>gri</i> magnitudes of 2020sck from DOT.	140
5.7	Photometric parameters of 2020sck.	142
5.8	Properties of the comparison sample.	143
5.9	<i>syn++</i> fit to the near maximum spectrum of 2020sck.	154
5.10	Fit parameters of TARDIS model and comparison of ejecta compo- sition with N5-def model (Fink et al. 2014).	155
5.11	$u'g'r'i'z'$ magnitudes of 2022eyw from GIT.	164

5.12	$u'g'r'i'z'$ magnitudes of 2022xlp from GIT.	167
5.13	Spectroscopic observations log of 2022eyw from HCT.	170
5.14	Spectroscopic observations log of 2022xlp from HCT.	172
5.15	Fit parameters of 1D radiation diffusion model (CHAPTER 3, EQUATION 3.5) to SNe Iax.	174
5.16	Comparing the explosion properties of SN 2020sck with single degenerate M_{ch} white dwarf explosion models.	181

Abbreviations

c	speed of light
c_s	speed of sound
m_e	electron mass
μ	Distance Modulus
\AA	Angstrom
M_\odot	solar mass
M_{ch}	Chandrasekhar mass
${}^{56}\text{Ni}$	Nickel Mass
M_{ej}	Ejecta Mass
AGB	A symptotic G iant B ranch
ASAS-SN	A ll S ky A utomated S urvey for S uper N ovae
ATLAS	A steroid T errestrial-impact L ast A lert S ystem
CD	C ore D egenerate
CO	C arbon O xygen
CONe	C arbon O xygen N eon
CREST	C entre For R esearch and E ducation in S cience and T echnology
CSI	C ircum S tellar I nteraction
CSM	C ircum S tellar M edium
DD	D ouble D egenerate
ELT	E xtrremely L arge T elescope
FOV	F ield O f V iew
FWHM	F ull W idth at H alf M aximum

GIT	G rowth I ndia T elescope
HCT	H imalayan C handra T elescope
HFOSC	H imalayan F aint O bject S pectrograph C amera
IAO	I ndian A stronomical O bservatory
IME	I ntermediate M ass E lement
IGE	I ron G roup E lement
IRAF	I mage R eduction and A nalysis F acility
JWST	J ames W ebb S pace T elescope
LC	L ight C urve
LSST	L egacy S urvey of S pace and T ime
LTE	L ocal T hermodynamic E quilibrium
MC	M onte C arlo
MCMC	M arkov C hain M onte C arlo
MW	M ilky W ay
NS	N eutron S tar
NASA	N ational A eronautics and S pace A dministration
NIR	N ear I nfra R ed
NLTE	N on- L ocal T hermodynamic E quilibrium
RG	R ed G iant
SD	S ingle D egenerate
SDSS	S loan D igital S ky S urvey
SED	S pectral E nergy D istribution
S/N	S ignal-to- N oise ratio
SFR	S tar F ormation R ate
SNe	S upernovae
TMT	T hirty M eter T elescope
TN	T hermo N uclear
UV	U ltra V iolet
UVOT	U ltra V iolet O ptical T elescope
WD	W hite D warf

WLR	Width Luminosity Relation
wrt	With Respect To
y-m-d	Year-Month-Date
ZAMS	Zero Age Main Sequence
ZTF	Zwicky Transient Facility
1D	One Dimension
2D	Two Dimension
3D	Three Dimension

Chapter 1

Introduction

Some of the stars in the Universe end their life as a Supernova explosion. The explosion releases about 10^{51} ergs of kinetic energy. To get a feeling for this energy budget, the bolometric luminosity of the Sun, L_{\odot} is 3.8×10^{33} erg s^{-1} . In a year, the Sun releases about 1.2×10^{41} erg. So, the Sun would take 8.3 billion years to emit as much energy as a supernova explosion. In the explosion, the ejected matter attains a high velocity of around $10\,000$ km s^{-1} (3% of speed of light). Shock waves are generated when the ejecta proceeds through the pre-explosion matter from the star and the interstellar medium. The shock waves accelerate particles like muons, electrons, and protons to ultra-relativistic energies (cosmic rays). The shock from the ejecta compresses the molecular clouds triggering star formation. SNe are the factories for forming heavy elements ($Z > 2$) that enrich the interstellar medium. They are used to study single and binary star evolution. Because of the high intrinsic luminosity of an SN ($\sim 10^{43}$ erg s^{-1}) they are used as standardizable candles. SNe explosions can be broadly classified into two categories - (i) Core-collapse (CC, [Smartt 2009](#)), and (ii) Thermonuclear (TN, [Jha et al. 2019](#)).

Core-collapse SNe

Stars produce heavy elements up to Fe by nuclear reactions. Formation of elements heavier than Fe requires energy. The star is formed of a degenerate core surrounded by a “layered structure” of elements. The electron degeneracy in the core provides support against gravitational collapse. The core is composed of ONeMg, for $8 - 10 M_{\odot}$ stars. The core collapses as the electron degeneracy pressure is decreased due to increased electron capture. This leads to an electron capture supernova (ECSN). Fe core is formed for stars with ZAMS mass $\geq 10 M_{\odot}$. The temperature and the density increases. Since Fe has a tightly bound nucleus among the elements, the high-energy photons get absorbed in the endothermic reaction reducing the radiation pressure support. Also, the electron capture reactions increase due to the large density in the core, further reducing electron degeneracy pressure support. The two processes reduce the thermal pressure support, and the core collapses on free-fall timescales. This collapsing core increases the temperature and pressure further, producing more neutrons and a core composed of degenerate neutrons. The fall of the stellar matter surrounding the core onto the neutron star’s surface sets shock waves that propagate through the star and unbinds the material in what is known as core-collapse supernovae (CCSNe). SNe coming from CC are Type Ib, Ibn, Ic, Icn, Ic-BL, IIL, IIP, I Ib, and IIn.

Thermonuclear SNe

Stars with masses less than $8 M_{\odot}$ form white dwarfs (He, CO, ONeMg) at the end of their evolution, where the temperature is insufficient for further nuclear burning. In a WD, the density is such that the separation distance between the electrons is less than the de-Broglie wavelength, and the electrons reach degeneracy. For the WD to remain in hydrostatic equilibrium, the electron degeneracy pressure must provide support against gravitational collapse. However, above $1.4 M_{\odot}$, a WD cannot remain in hydrostatic equilibrium (Chandrasekhar mass limit, M_{ch}). A WD

in isolation will be devoid of nuclear reactions and almost inert. But the situation becomes interesting when the WD is in a binary. The WD can reach M_{ch} through accretion from a companion. As the WD mass nears M_{ch} , any slight increase in the mass results in an increased density at the centre, this increases the temperature and accelerates *thermonuclear reactions*. This acts as positive feedback, where the reaction increases the temperature further, causing a runaway. This is slowed down to some extent by neutrino cooling, convection, and conduction. But, the energy release rate due to thermonuclear runaway overwhelms the rate at which energy flows out from the system. A change in pressure in a degenerate system does not regulate the increase in temperature. So, the thermonuclear reactions are not slowed down, and the temperature increases. At some point, the temperature becomes so high that the thermal pressure becomes comparable to electron degeneracy pressure, and the materials expand. When the sum total of kinetic and thermal energies of the materials overcome the energy of self-gravitation, the WD becomes unbound and expands (Gamezo et al. 2003). Thermonuclear runaway in a degenerate matter is widely accepted as the main reason for *Type Ia supernovae* (*SNe Ia*). Though all Type Ia come from a thermonuclear origin, the reverse is not valid. Burning a CO WD produces intermediate mass elements (IMEs) like Si, S, Ca, Ti, Fe-group elements (IGEs) like Fe, Ni, Co, and unburned elements like Ne, O, C.

1.1 The width-luminosity relation of SN Ia

After the explosion, the light curves rises to maximum (~ 20 days), and then declines. The decline rate is the difference in the magnitudes at maximum and 15 days from maximum, and is denoted as Δm_{15} (mag) (FIGURE 1.1[A]). A reasonably tight correlation exists between the absolute magnitude at maximum (M_B) and decline rate (Δm_{15}), with brighter objects having broader light curves and

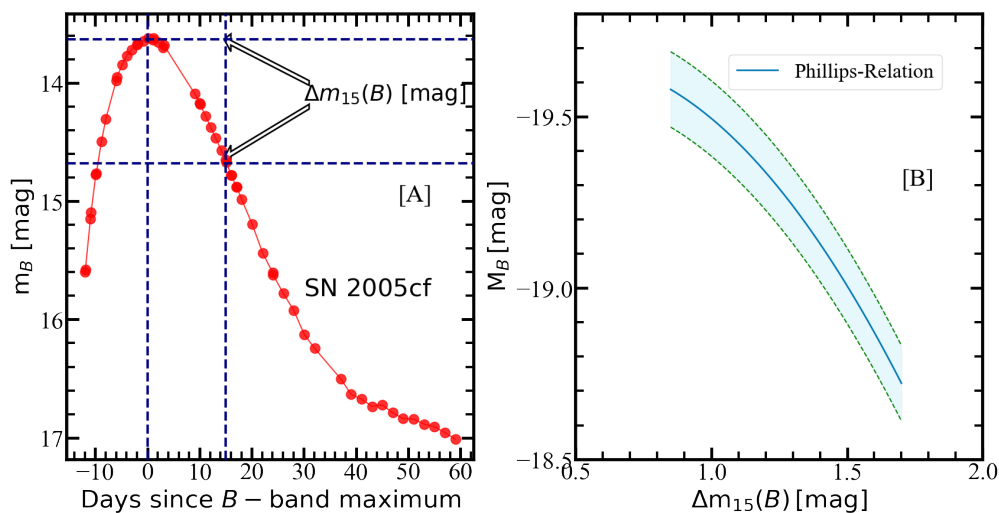


FIGURE 1.1: [A] An illustration of Δm_{15} , the difference in magnitude between maximum and 15 days from maximum using the B -band light curve of SN 2005cf (Wang et al. 2009a) [B] The Phillips relation scaled to $H_0 = 72$ km/s/Mpc. Also shown is the $1\text{-}\sigma$ scatter about the relation.

vice-versa. Using 9 SNe, Phillips (1993) derived a linear relation as given in Equation 1.1.

$$M_B(0.36) = -21.726(0.498) + 2.698(0.359)\Delta m_{15}(B) \quad (1.1)$$

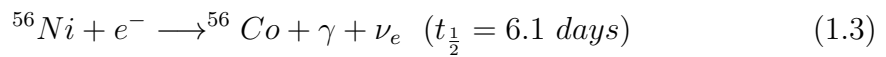
With an increased sample, the $M_B - \Delta m_{15}(B)$ relation was revised as given in Equation 1.2 (FIGURE 1.1[B]).

$$\Delta M_{max}(0.11) = 0.786(0.398)[\Delta m_{15}(B) - 1.1] + 0.633(0.742)[\Delta m_{15}(B) - 1.1]^2 \quad (1.2)$$

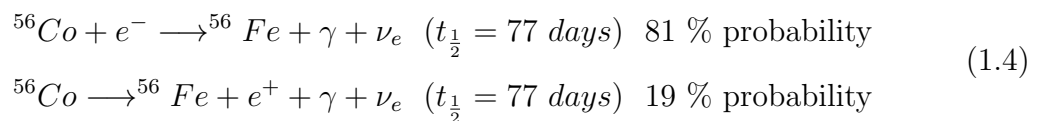
where, $\Delta M_{max} = M_{max} - M_{max}[\Delta m_{15}(B) = 1.1]$. Due to this correlation, SNe Ia can be standardized, and better precision in distance measurements can be achieved. This has allowed for the discovery of the Universe's accelerated expansion (Riess et al. 1995, 1996, 1998a,b).

1.2 ^{56}Ni as the power source

The energy from thermonuclear reactions is converted to kinetic energy (which causes the ejecta's expansion), and thermal energy (which can radiate away). For compact systems, most of this energy is used up in the star's expansion. When the star has expanded enough that photons can radiate away, the ejecta cools down (due to the ejecta's expansion and loss of photons). So, the light curve becomes dim. SNe Ia would be difficult to observe if no other energy source powers the light curves. Fortunately, the radioactive decay of a few isotopes comes to the rescue. The thermonuclear reactions in a CO WD lead to the burning of ^{12}C and ^{16}O to nuclear-statistical-equilibrium (NSE), producing mostly ^{56}Ni (most tightly bound nucleus with $Z=N$). The decay of ^{56}Ni to ^{56}Co (see Equation 1.3) and then to ^{56}Fe (see Equation 1.4) powers the light curves (Pankey 1962; Colgate & McKee 1969; Branch & Wheeler 2017).



^{56}Co then decays by electron capture or positron decay-



These positrons and γ -rays produced as a result of ^{56}Ni decay deposit their energy due to Compton scattering and photoelectric absorption and thermalized in the ejecta to ultraviolet, optical and infrared emission (Ambwani & Sutherland 1988; Kasen et al. 2006). The ν 's mostly escape from the ejecta without depositing their energy.

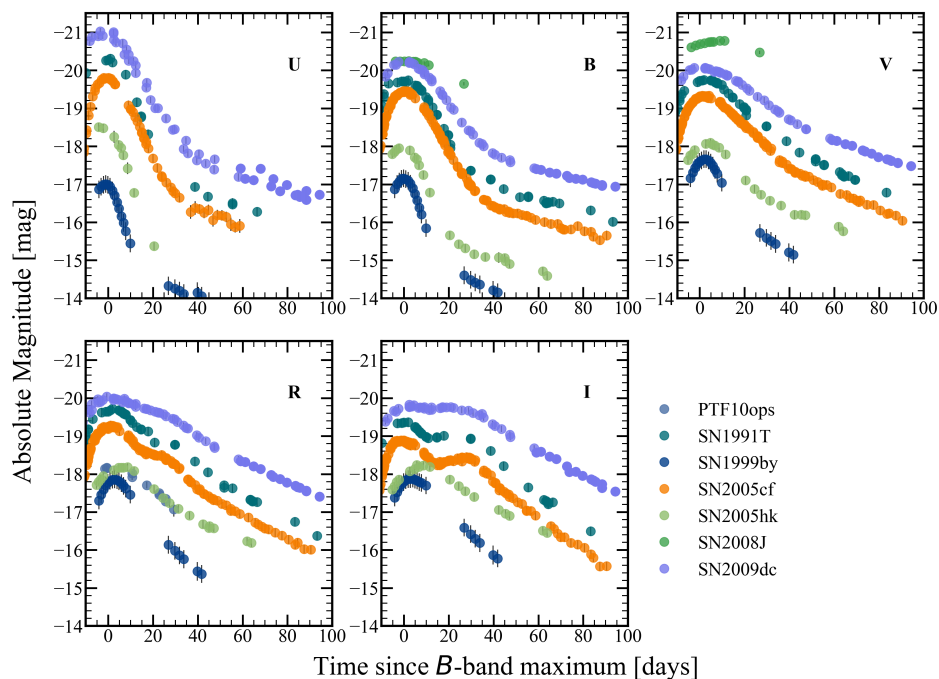


FIGURE 1.2: Absolute magnitudes in $UBVRI$ of SNe 1991T, 1999by (1991bg-like), 2005cf (normal SN Ia), 2005hk (Type Iax), 2009dc (super-Chandra 2003fg-like), 2008J (Ia-CSM), PTF10ops (peculiar) are shown. SNe 1999by, 2009dc, 2005hk does not show prominent secondary I -band peak.

1.3 Diversity in thermonuclear SNe

Most of the SNe Ia show similarities in their spectroscopic and light curves properties (normal SNe Ia), based on which the scatter in their peak luminosities can be standardized. However, observations over the last few decades have revealed that there are few thermonuclear explosions which are either different from normal Type Ia in their spectroscopic or light curve features or they do not obey the Phillips relation (Equation 1.2). It is quite clear now that SNe Ia cannot be understood considering a single explosion mechanism and progenitor channel (Maeda & Terada 2016; Taubenberger 2017). Nonetheless, based on the knowledge of nucleosynthesis from spectral modelling of individual SNe, it is clear that all “varieties” arise from thermonuclear explosions of WDs (FIGURE 1.4). Below we discuss the observed diversity in thermonuclear explosions.

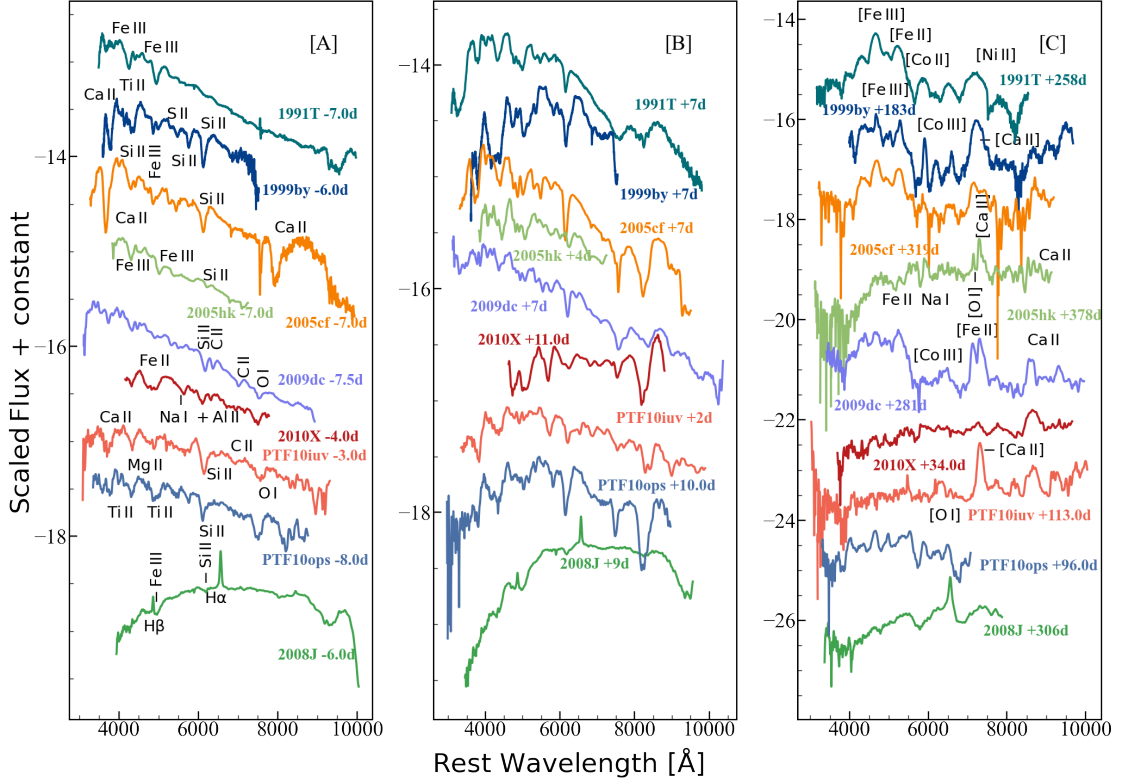


FIGURE 1.3: Spectrum of SNe 1991T, 1999by (1991bg-like), 2005cf (normal SNe Ia), 2005hk (Type Iax), 2009dc (super-Chandra SN 2003fg-like), 2008J (Ia-CSM), 2010X (.Ia/SN 2002bj-like), iPTF10iuv (Ca-rich), PTF10ops (peculiar) at pre-max [A], near-max [B], and nebular/post-max phase [C]. All the spectra are redshift-corrected. The spectra have been obtained from WISeREP database.

1. **Normal Ia** - SNe Ia whose photometric evolution follows the Phillips relation are classified as normal Ia. The decline rate lies between 0.85–1.70 mag and the average peak magnitude (M_B) is -19.2 mag ($\sigma = 0.3$ mag). There is a secondary maximum seen in the I -band (FIGURE 1.2). The extinction corrected $B - V$ colour at peak lies between -0.2 to 0.1 mag. The spectral evolution shows features due to IMEs like Mg II, Si II $\lambda 6355$, Si III, Si II, Ca II and IGEs like Fe III at the early phases. Near and post maximum, Si II $\lambda 5972$, Fe II develops indicating the lowering of the temperature (FIGURE 1.3). The nebular phase spectral evolution shows forbidden lines due to [Fe III], [Co III], [Fe II], [Ni II]. Few normal Ia with detailed studies are - SNe 2005cf (FIGURE 1.2, Wang et al. 2009a), 2014J (Srivastav et al.

2016), 2011fe (Zhang et al. 2016), 2018oh (Li et al. 2019a).

2. **1991T-like** SNe have luminosities higher compared to normal Ia. SN 1991T has been studied in details by Lira et al. 1998; Filippenko et al. 1992a. In the pre-maximum phases, the $(U - B)$ colour evolution is bluer than normal Ia. They are characterized by Fe III $\lambda 4404$ and $\lambda 5129$ in the pre-maximum spectra. The pseudo-continuum is bluer, and the IME features like Si II and Ca II are absent before maximum and appear near maximum (Phillips et al. 1992). Close to the maximum, the spectra of 1991T-like objects become similar to normal Ia, but the strength of Si II $\lambda 6355$ is not as strong. In the nebular phase, forbidden emission features due to [Fe II] and [Fe III] are seen but they are broader than normal Ia (Mazzali et al. 1998). These SNe are found in late-type galaxies (Li et al. 2011a). In FIGURE 1.2, the light curves, and in FIGURE 1.3, the spectral evolution of 1991T are shown.

3. **2003fg-like super-Chandrasekhar** objects have high luminosities, and broad light curves (Howell et al. 2006). Broad light curves ($\Delta m_{15}(B) = 0.7 - 0.9$ mag) point towards higher ejecta/Ni masses, and some of the explosions cannot be explained in terms of a $1.4 M_{\odot}$ WD. Hence they are called “super-Chandra” objects. The NUV-optical colours are bluer compared to normal Ia. The I -band light curve decreases monotonically without any secondary maximum (Ashall et al. 2020). The pre-maximum spectra show features due to Si II at lower velocities than normal Ia, and Ca II, Fe III, prominent presence of unburned C II. The nebular spectra show emission features due to [Fe II], [Fe III], [Co II], but the ratio of [Fe III] 4700 \AA to [Fe II] 5200 \AA is lower than normal Ia, indicating towards lower ionization and higher densities in the inner regions (Taubenberger et al. 2013b). Super-Chandra objects have been found in low-mass galaxies and metal-poor environments (Taubenberger et al. 2011). In FIGURE 1.2, and FIGURE 1.3, we show the light curves, and spectral evolution of SN 2009dc (Taubenberger et al. 2011) which is a well studied member of this class.

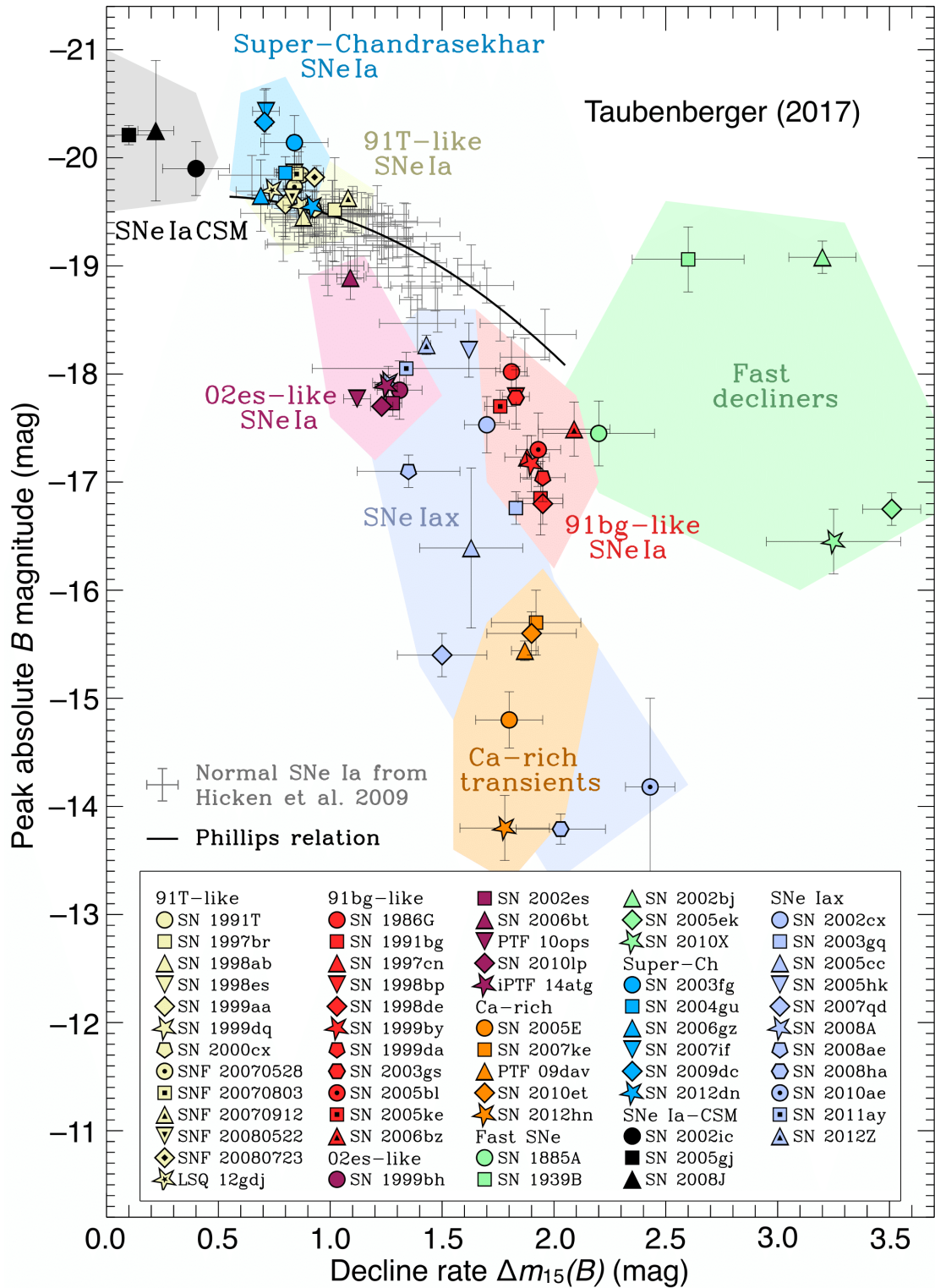


FIGURE 1.4: The diversity in thermonuclear explosions. This figure is adapted from Taubenberger (2017).

4. **Ia-CSM** objects are bright objects with peak magnitudes between -21.3 to -19.0 mag (Silverman et al. 2013). They are characterized by H α emission feature in their spectra which forms when the SN ejecta collides with the CSM shells (see FIGURE 1.3). He I lines are generally absent in the spectra. Ia-CSM are predominantly found in late-type spiral galaxies indicating a young stellar environment. Sharma et al. (2023) have carried out a recent study on Ia-CSM from the ZTF, and found the rate of Ia-CSM to be < 0.2 % of the Ia rate. SN 2002ic was the first of this kind and in FIGURE 1.2, and FIGURE 1.3, we plot the light curves, and spectra of SN 2008J (Taddia et al. 2012).
5. **1991bg-like** objects have lower luminosities and faster decline rate (1.8 - 2.1 mag) than normal Ia (Filippenko et al. 1992b). The $B - V$ colour is redder near maximum. The secondary maximum in I -band merges with the primary, and the light curve declines monotonically (see the I -band panel in FIGURE 1.2). The pre-maximum spectra are dominated by IMEs like Si II, S II, Ca II. Si II λ 5972 absorption feature is very strong (FIGURE 1.3). This is a proxy for lower temperatures (cool spectra) and lower ionization states. Ti II (\sim 4000 Å), and O I λ 7774 are quite strong in the spectra. The nebular phase spectra show broad features of [Ca II] $\lambda\lambda$ 7291, 7324, and [Fe II] (Mazzali & Hachinger 2012). They are predominantly found in massive elliptical galaxies (Howell 2001). The spectra, and light curves of a 1991bg-like object - SN 1999by (Garnavich et al. 2004) are shown in FIGURE 1.2, and FIGURE 1.3.
6. **Type Iax** - These have much lower luminosities (-18.2 to -13.0 mag) compared to SNe Ia and faster decline (Foley et al. 2013). The rise time is also faster than normal Ia. The decline rate in R -band is slower than normal Ia. The I -band secondary maximum is not seen in SNe Iax. The spectra of Type Iax show the presence of Fe III, Si III, indicating higher temperatures. The velocities of Si II (3000 - 8000 km s⁻¹), Fe III, C II are lower than normal

Ia. SNe Ia show the most interesting feature in their late-time spectra. The late phase spectra show permitted lines due to Fe II which means higher density near the central regions along with [Ni III], [Fe II], [Ca II] (Jha et al. 2006). The occurrence of these objects is predominant in late-type galaxies. SN 2005hk (Sahu et al. 2008) is shown as an example in FIGURE 1.2, and FIGURE 1.3.

7. ***Ca-rich gap*** transients are sub-luminous (-16.5 to -14.0 mag), faster rising and have redder colours. There is no *I*-band secondary peak. The spectra at the early phase shows features due to Mg II, Si II, Ti II, Sc II, Fe II. The most important distinguishing factor is the presence of [Ca II] $\lambda\lambda 7291, 7324$ in the nebular phase and the lack of features due to [Fe] (See the spectra of PTF10iuv (Kasliwal et al. 2012) in FIGURE 1.3). [O I] $\lambda\lambda 6300, 6364$ is also detected. These are more similar to stripped-envelope SNe. Still, the derived ejected mass and their preferred location in early-type galaxies is an argument against their core-collapse origin.
8. ***Peculiar*** - Few SNe like 2010X (Kasliwal et al. 2010), 2002bj, 2002es, 2005ek are quite peculiar in their observed properties, and thermonuclear explosion involving a WD is one of the possible explanations for these events. 2010X, 2005ek, 2002bj (Poznanski et al. 2010) rise and decline rapidly ($\Delta m_{15}(B) = 3.2$ mag for SN 2002bj). SN 2002bj showed the presence of C, O, Si, He and the ejecta velocity is ~ 4000 km s $^{-1}$. For 2005ek (Drout et al. 2013), the spectra showed presence of Si II, Fe II, O I, C II, Mg II, Fe II. Modeling of the nebular spectra for SN 2005ek showed presence of [Ca II] $\lambda\lambda 7291, 7324$, [O I] $\lambda\lambda 6300, 6364$, [O I] $\lambda 5577$. The velocities for the case of SN 2005ek and SN 2010X (FIGURE 1.3) are around 8000 - 10000 km s $^{-1}$.

SN 2002es-like objects (Ganeshalingam et al. 2012) have sub-luminous nature, no secondary *I*-band peak, redder colours, presence of Si II $\lambda 5972$, O I, Ti II in their spectra. But the light curves decline slowly compared to sub-luminous Ia. Other objects with similar sub-luminous and slowly declining

nature are SNe 2006bt (Foley et al. 2010c), 2010lp (Taubenberger et al. 2013a), PTF10ops (Maguire et al. 2011). The velocity evolution is quite diverse in this class. The light curve in R -band, and spectral evolution of PTF10ops are shown in FIGURE 1.2, and FIGURE 1.3.

1.4 Spectral Classification of SNe Ia

SNe Ia can be classified based on their spectroscopic properties. The peak absolute magnitude in the B -band has been shown to correlate with $R(\text{Si II})$ - the ratio of the fractional depths of the absorption minimum of Si II $\lambda 5972$ to $\lambda 6355$. This ratio is more for the less luminous objects and vice-versa. This can be used as an independent measure of the luminosity of the SN without the knowledge of redshift (Nugent et al. 1995). Another way of classifying the spectra is using the ratio of pseudo-equivalent widths (pEW's) of Si II $\lambda 5972$ to $\lambda 6355$. Based on this, SNe Ia are classified into - core-normal (CN), broadline (BL), cool (CL), and shallow-silicon (SS). The CN Ia forms a homogeneous class, the BL have broader and deeper Si II $\lambda 6355$ than CN. The CL objects have stronger Si II $\lambda 5972$ feature while the SS have smaller values of pEW for both the Si II lines. This classification arises due to different abundance structure of the ejecta, differences in temperature, and optical depths. For example, the CN objects have spectral similarities among each other and forms a homogeneous group, SS objects have higher temperature than CN and lower optical depths. Cool objects have lower temperature (Branch et al. 2006). The classification is shown in FIGURE 1.5.

Based on the expansion velocity (v_{exp}) during B -band maximum, obtained from the absorption minimum of the Si II $\lambda 6355$ feature, SNe Ia are broadly classified into Normal Velocity (NV) with an average v_{exp} of $10600 \pm 400 \text{ km s}^{-1}$ and High Velocity (HV) with $v_{\text{exp}} \geq 11800 \text{ km s}^{-1}$ (Wang et al. 2009b). Such a classification

mainly can be understood by considering different explosion mechanisms. It has also been found that HV SNe are redder either due to dust in their environments, or the opacity is such that they are redder intrinsically. Wang et al. (2009b) found that the two groups are associated with different extinction law. The scatter in the peak luminosity can be reduced if such corrections due to reddening are applied. FIGURE 1.6 shows the Si II velocity plotted against its pEW near maximum.

Another classification of SNe Ia is based on the time evolution of Si II $\lambda 6355$ absorption. The average rate of decline is denoted by $\dot{v} = -\Delta v/\Delta t$, and measured between maximum and either the time the Si II feature can be clearly identified and its velocity can be measured or the last spectrum available (Benetti et al. 2005). According to this scheme, SNe Ia are clustered into Low-Velocity Gradient (LVG) - with $\dot{v} < 70 \text{ km s}^{-1} \text{ d}^{-1}$, High-Velocity Gradient (HVG) - with $\dot{v} \geq 70 \text{ km s}^{-1} \text{ d}^{-1}$, and FAINT with $\langle M_B \rangle = -17.2$ and have HVG. This classification can be understood considering different amounts of mixing within the ejecta, or differences in the opacity. Different explosion mechanisms/progenitor scenarios can give rise to HVG/LVG objects (Dessart et al. 2014). We show this classification in FIGURE 1.7.

1.5 Progenitors

Various progenitor scenarios are put forward to understand the observed diversity of SNe Ia. The leading progenitor channels are the double degenerate (DD, Webbink 1984) and the single degenerate (SD, Nomoto 1982a,b). In the SD channel, a CO WD accretes H/He-rich matter from its non-degenerate companion. It could be a He star, main-sequence (MS)/sub-giant, or red-giant (RG). The WD can grow in mass to M_{ch} limit if the mass transfer rate is such that the system

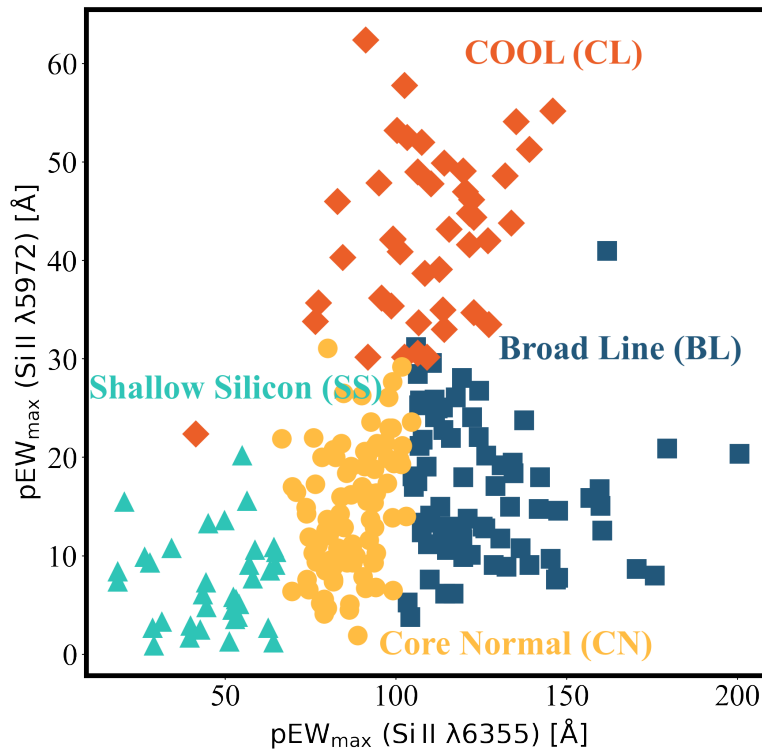


FIGURE 1.5: Branch classification scheme. The data presented is taken from (Blondin et al. 2012).

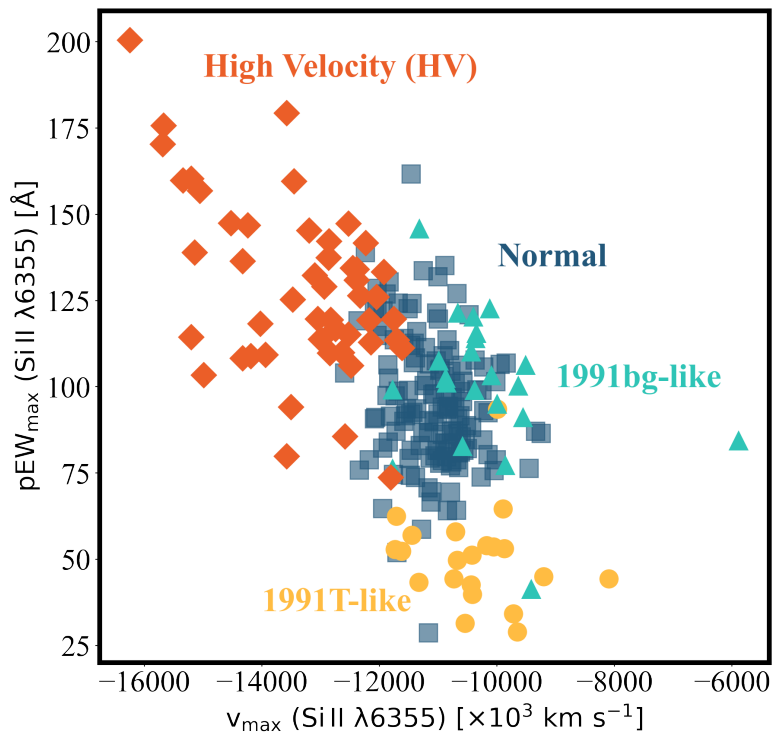


FIGURE 1.6: Wang classification scheme (Wang et al. 2009b). The data is taken from Blondin et al. (2012).

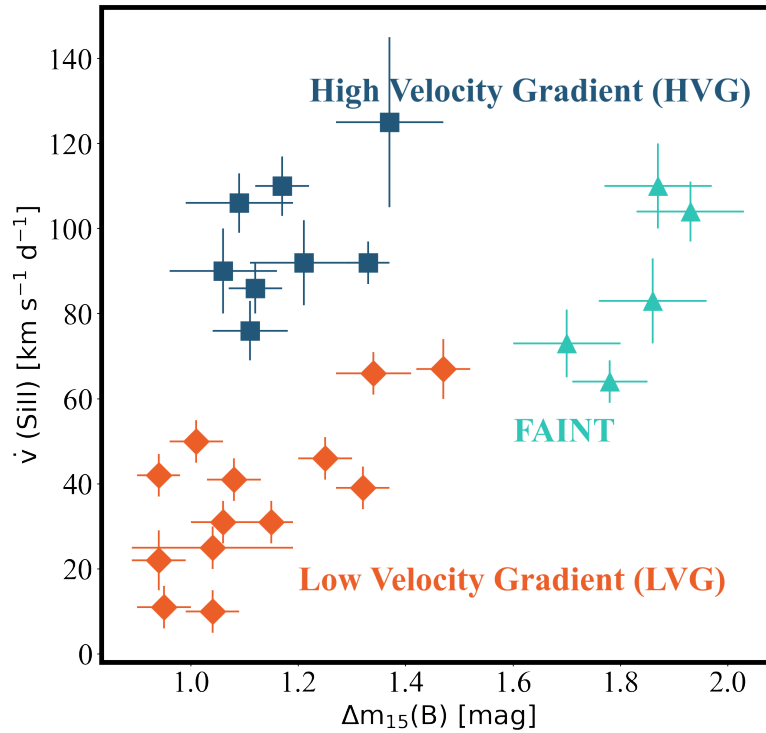


FIGURE 1.7: Spectral classification of SNe Ia according to Benetti et al. (2005). The data presented in this figure is from Benetti et al. (2005).

neither enters into a common-envelope phase (for high accretion rates) nor unstable nuclear burning leads to novae-like explosions for low accretion rates (Nomoto 1982b; Starrfield et al. 1972).

In one of the SD scenarios involving two main-sequence stars having initial masses ($M_1 = 4.0 - 7.0 M_\odot$, $M_2 = 1.0 - 2.0 M_\odot$), and period ($P = 5 - 30$ days), the primary massive star while in the Hertzsprung Gap (HG) or First Giant Branch (FGB) stage, fills its Roche Lobe (RL). Due to large mass ratio between the stars, a convective envelope (CE) is formed. The CE is ejected, and the primary evolves to a He star and finally to a red-giant (RG). The He-RG now has a CO core which fills its RL and transfers mass rich in He from the envelope to the main-sequence companion, forming a CO + MS system. In the CO + MS channel, H-rich matter is accreted by the WD, which is burned to He followed by C and O burning. This CO WD increases its mass to M_{ch} limit exploding as SN Ia (Wang & Han 2012; Paczynski 1976).

In the DD channel, the companion of the primary WD is another WD (He, CO, ONeMg). In case of two CO WD binary, the orbital separation decreases by gravitational wave emission, and they merge. During the merger, high temperatures are produced to start C burning, and the system explodes as SN Ia (Pakmor et al. 2012). In this case, the system's total mass exceeds the M_{ch} limit. In another case, two WDs are in a binary system with another star in an highly inclined orbit. The presence of this star increases the ellipticity of the inner orbit of the two WDs, and they collide (Thompson 2011). The temperature and pressure at the point of collision increases to an extent to start C burning. Collision of WDs can also occur in systems having high concentration of stars such as central regions of globular clusters (Rosswog et al. 2009).

Another progenitor scenario proposed for explaining the super-Chandrasekhar SNe as well as Ia-CSM objects is the core-degenerate (CD). For such case, an AGB star transfers mass on a WD companion when it fills its Roche-lobe. For unstable mass transfer, a common envelope is formed. The WD and the AGB star's core (another WD) merges within this common envelope. The presence of H α in SNe Ia-CSM has been explained by the merger ejecta interacting with the H-rich common envelope (Sparks & Stecher 1974; Livio & Riess 2003).

1.6 Explosion mechanisms

Different explosion mechanisms have been proposed to explain the diversity of SNe Ia (Hillebrandt & Niemeyer 2000). A successful explosion model should predict an ejecta composition, and velocity distribution that matches the observed spectra and light curves. There should be enough ^{56}Ni produced by the explosion models to explain the luminosity. The compressional heating and neutrino losses compete near the core for a WD approaching M_{ch} limit through accretion. Near

a density of around $\sim 2 \times 10^9 \text{ g cm}^{-3}$, the energy generation rate due to nuclear reactions increases compared to neutrino losses. This marks the beginning of the thermonuclear runaway. There are two timescales of interest in the core - the convective timescale (τ_{conv}) and the nuclear burning timescale (τ_{burn}). As the core temperature increases due to thermonuclear reactions the burning timescale τ_{burn} decreases (nuclear reaction rates are strongly dependent on temperature). At a temperature of $\sim 1.5 \times 10^9 \text{ K}$, τ_{burn} becomes less than τ_{conv} , and a flame originates (Woosley & Weaver 1986; Hillebrandt & Niemeyer 2000).

Prompt detonation - If the flame propagates at speed equal to or greater than the speed of sound (c_s), the white dwarf does not get enough time to expand. This detonation wave converts the C and O into Fe-peak elements, leaving nearly no IMEs. This is in strict contradiction to observations of SNe Ia (Khokhlov 1991a; Landau & Lifshitz 1987).

Pure deflagration - If the flame speed propagates subsonically at a fraction of sound speed ($0.3 c_s$, fast deflagration), instabilities sets in due to turbulence. The expansion of the star finally quenches this. The production of ^{56}Ni is low such that it can explain the sub-luminous SNe Iax, but not the normal Ia (Fink et al. 2014). A pure deflagration is unable to fully unbind the WD, so a bound remnant is expected for SNe Iax, and searches for a bound remnant is ongoing. A popular deflagration model in 1D is the W7 which is a time-dependent propagation of the burning front based on mixing-length approach. It predicts no IMEs above 15000 km s^{-1} (Nomoto et al. 1984).

Delayed detonation (DDT) - The turbulent deflagration flame propagating subsonically ($0.1 c_s$) gives the WD enough time to expand. At a density (ρ_{DDT}) $\sim 10^7 \text{ g cm}^{-3}$, turbulent velocity fluctuations cause this flame to transition into a supersonic detonation. Unburned elements, and IMEs are produced at high velocities which matches the observations of normal SNe Ia (Khokhlov 1991a).

Pulsational delayed detonation (PDD) - The turbulent deflagrations are not strong enough to unbind the star. This causes the WD to collapse again (pulse), producing a detonation during the pulses. The transition density can be parametrized to obtain various ^{56}Ni . However, the models are lesser luminous and produce more unburned elements (C and O) in the outer layers than delayed detonation. SN 1991bg-like objects can be understood in terms of this scenario (Hoeflich et al. 1995).

Sub- M_{ch} explosion - In this scenario, CO WD having mass less than the M_{ch} limit goes into explosion. When a CO WD develops a He-rich outer layer, detonations can happen in that He layer due to instabilities resulting in shock waves, which propagate inwards, causing a secondary detonation in the CO core. The explosion mechanism is also known as a double detonation scenario (Woosley & Weaver 1994). This scenario can occur if the companion to the CO WD is a He-rich donor or H-donor where H is converted to a He shell. In these kind of explosions, burning of He produces ^{56}Ni in the outer layers. This explosion mechanism can explain the sub-luminous faster declining SNe Ia like SN 2002bj, SN 2010X, Ca-rich transients etc.

Violent mergers - Normal, sub-luminous Ia are produced from the merger of two WDs (Pakmor et al. 2010, 2012). The nature of the explosion may vary with the masses of the WDs. In this scenario, the WDs merge as they lose angular momentum. The secondary, less massive WD is disrupted, forming an envelope around the massive primary. As the secondary violently merges with the primary, a detonation is created at a temperature $\sim 10^9$ K and at a density of around 10^6 K, which is sufficient to cause CO ignition in CO WDs.

Gravitationally confined detonation (GCD) - In this scenario, the flame starts as an off-center deflagration in a near M_{ch} WD. This deflagration flame rises to the surface due to buoyancy and confined by gravity, where it expands on

reaching the outer, low pressure layers. A lateral component of this flame develops at the surface, which converges at the opposite side. Due to compression at this convergence point, the pressure and temperature becomes such to start a detonation which consumes the WD. The deflagration flame rises slowly if the ignition start close to the centre and may not produce a detonation (Seitenzahl et al. 2016). The presence of Fe absorption features in the early spectra of SN 1991T can be explained by the high velocity burning of CO at the outer layers.

1.7 Outline of the thesis

This thesis aims to understand the diversity in the explosion mechanisms/progenitor systems of thermonuclear SNe in the Universe. We have performed observations of thermonuclear explosions (focusing on SNe Ia, Iax) and radiative transfer modelling with publicly available radiative transfer codes like TARDIS, and SEDONA to understand the diversity in their respective classes.

1. Chapter 2 describes the facilities used to perform the observations used in this work. The data reduction steps that have been followed to reduce raw data to science ready data have been discussed in detail.
2. Chapter 3 provides details of the modelling approach that have been used in this thesis to simulate light curves and spectra of various SNe Ia.
3. Chapter 4 gives detailed analysis using analytical and numerical modelling of various normal SNe Ia. In this chapter, we have studied the explosion mechanism and progenitor properties of SN 2006bt, SN 2011aa, SN 2012dn, SN 2017hpa and SN 2018oh.

4. Chapter 5 discusses the peculiar SNe Iax and the understanding of this class based on different explosion models. The Type Iax SNe 2020sck, 2022eyw and 2022xlp have been studied in detail.
5. Chapter 6 summarises the work and provides some future prospects in this field.

Chapter 2

Observational Facilities and Data Reduction

2.1 Introduction

To understand any transient astrophysical phenomenon, studying its luminosity variation over time is essential. For this, collecting the light from the source over a broad range of wavelengths is crucial. This technique is known as *photometry*. To study the change of temperature over the evolution of the transient, it is important to collect light in different wavelength regions using filters. Filters are also used because some transients are intrinsically redder while some are bluer. Similarly, it is important to understand how the photons interact with matter to study the composition of the ejecta. The technique of breaking white light into its constituent colours and studying the absorptions and emissions superimposed on a continuum is called *spectroscopy*.

This work has brought together new photometric and spectroscopic data for five

thermonuclear supernovae - SN 2017hpa, SN 2011aa, SN 2020sck, SN 2022xlp, and SN 2022eyw in the optical wavelengths using Indian observing facilities, namely the 2.01 m HCT (Prabhu & Anupama 2010) and 0.7 m GIT (Kumar et al. 2022). In addition, archival ultraviolet-optical data from the *Swift* observatory (Gehrels et al. 2004) has been obtained for SNe 2011aa and 2017hpa. For SN 2020sck, public data from ZTF (Bellm et al. 2019) has been used. We have followed standard data reduction techniques to reduce the raw data from the telescopes to science-ready products. This Chapter describes the facilities and instruments used to perform the observations and the techniques used for data reduction.

2.2 Observing Facilities

2.2.1 Himalayan Chandra Telescope (HCT)

HCT is an optical-infrared telescope, with a 2.01 m aperture diameter. It is located at IAO Hanle, at an altitude of 4500 m above mean sea level (Cowsik et al. 2002; Prabhu & Anupama 2010). The site is well suited for optical-infrared observations due to high altitude, low temperatures and humidity, low seismic activities, around 1'' median seeing, less than 10 cm of average annual rainfall, and with a median wind speed of 8 km/hr at night. Using a dedicated satellite link, HCT is remotely operated from the CREST campus at Hosakote. The telescope saw its first light in September 2000 and was released for regular science operations in May 2003.

The primary mirror of HCT is made with ultra-low expansion (ULE) coefficient glass. HCT has a modified Ritchey-Chrétien design, and alt-az mount. There are three instruments available with HCT at its Cassegrain focus with an f/9 F-ratio and an image scale of 11.5''/mm. There is an autoguider available with the telescope which can guide a ~ 17 mag star with 0.1'' accuracy.

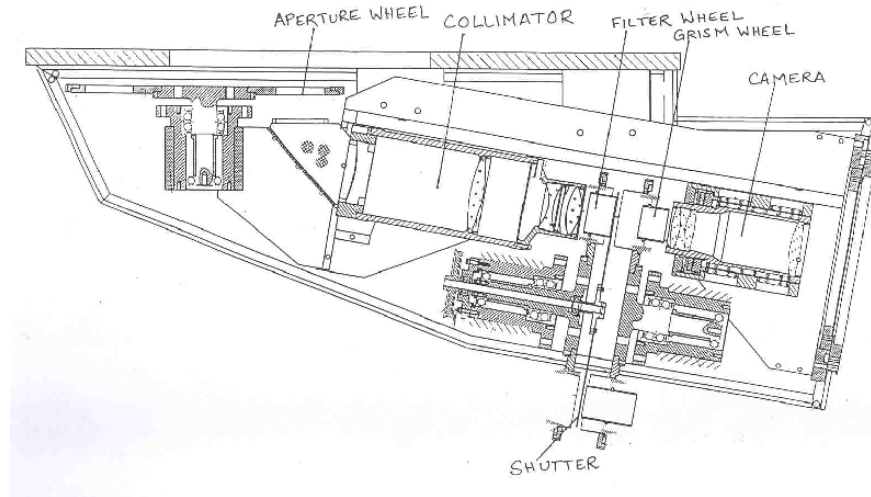


FIGURE 2.1: A schematic diagram of the HFOSC instrument on the 2.0 m HCT. A few important components like the camera, grism wheel, filter wheel, collimator, and aperture wheel are marked.

The three instruments available with HCT are

1. Himalayan Faint Object Spectrograph Camera (HFOSC) - it has a low-medium resolution spectrograph and an optical imager.
2. TIFR near InfraRed SPECTrometer and imager (TIRSPEC) - NIR imager and medium resolution spectrograph covering a wavelength range of 1 - 2.5 μm .
3. Hanle Echelle SPectrograph (HESP) - high resolution ($R = 30000$ and 60000) optical (3000 - 10000 \AA) spectrograph.

This work has extensively used the HFOSC instrument on HCT. The objects were observed based on time allocation through observation proposals.

2.2.1.1 HFOSC

The HFOSC consists of an optical bench with the camera and collimator mounted. An aperture/slit wheel is placed in front of the collimator, followed by a filter wheel or grism wheel and then the camera (FIGURE 2.1). It has a wavelength range of operation between 3500 - 9000 Å. The detector used with HFOSC is a SITE ST-002 CCD with a size of 2048 × 4096 pixels for imaging. The size of each pixel is 15 μm. The central region of 2048 × 2048 pixels is used for imaging and a part of the whole detector is used for spectroscopy. The readout of the central 2K × 2K pixels takes about ~ 90 secs. The gain and read-noise of HFOSC are 1.22 e⁻/ADU, and 4.8 e⁻, respectively. There are two separate software controllers for the instrument and the CCD. The objects/SNe are observed with *UBVRI* filters in imaging mode (FIGURE 2.2). The spectroscopy of SNe are performed with slit 167 μm, width 1.92", and length 11'. The standard stars are observed with slit 1340 μm, width 15.41", and the same length as 167. The grisms used for the observations of both standards and SNe are Gr7 with a wavelength of 3500-7800 Å and resolution of 1330, and Gr8 with a wavelength of 5200-9100 Å and resolution of 2190. The spectral lamps used for wavelength calibration in this work are FeAr and FeNe which are housed in the Filter and Spectral lamp unit (FASU). The lamp spectra are observed with a narrow slit 67 μm, to obtain a higher resolution *.

2.2.2 GROWTH India Telescope

GROWTH, which stands for Global Relay of Observatories Watching Transients Happen, is an international, multi-institutional collaboration to observe various cosmic explosions in a way so that as the Sun rises in some part of the world, the other part can continue observing the night sky. With this motivation, many

*https://www.iiap.res.in/?q=iao_2m_hfosc

telescopes around the world are employed. GROWTH India Telescope (GIT) is a wide-field 0.7 m facility at IAO, Hanle designed for automatic observations with/without human intervention, for a rapid follow-up of transients. The telescope has an alt-az mount with an f-ratio of 6.5. The telescope and camera system provides a field of view of 0.7° (Kumar et al. 2022).

2.2.2.1 Andor camera

The primary instrument of GIT is the Andor XL 230 camera. The camera has 4096×4108 pixels of size $15 \mu\text{m}$. The pixel scale is $0.676''$. The gain and read-noise of the CCD are $1.04 e^-/\text{ADU}$, and $12 e^-$ respectively. The observations of the SNe are mostly carried out with SDSS $u'g'r'i'z'$ filters (FIGURE 2.2). GIT reaches a depth of around 20.5 mag in SDSS r' -band for a 300 seconds exposure.

2.2.3 Swift Observatory

Swift is a space-based facility to perform multi-wavelength observations of supernovae, gamma-ray bursts etc (Gehrels et al. 2004). It was placed in low earth orbit in November 2004. It has three science instruments - (i) UltraViolet Optical Telescope (UVOT), (ii) Burst Alert Telescope (BAT), and (iii) X-Ray Telescope (XRT). These three instruments are coaligned, and once the BAT detects a burst, the spacecraft “swiftly” repoints itself so that the XRT and UVOT can observe the transient.

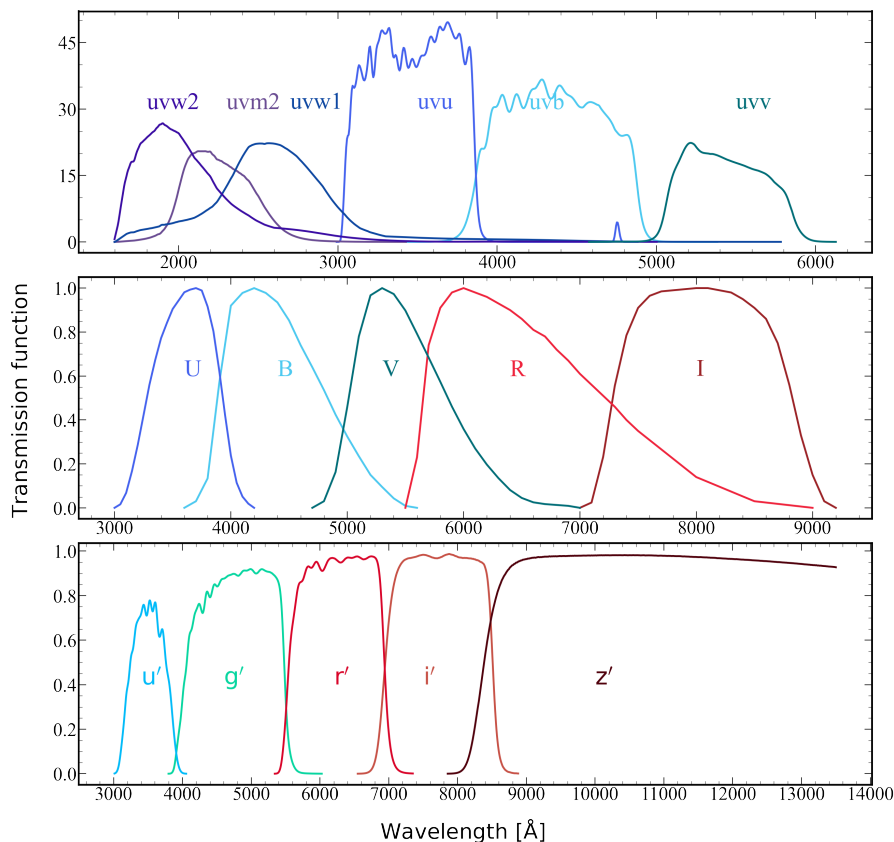


FIGURE 2.2: The filter transmission functions for *Swift*-UVOT, Bessell *UBVR*, and SDSS *u'g'r'i'z'*.

2.2.3.1 UVOT

UVOT has an aperture diameter of 0.3 m with a Ritchey-Chretien design and an f-ratio of 12.7. The detector operates in photon counting mode. The detector size is 385×288 pixels with a field-of-view of $17' \times 17'$ at a pixel scale of $4''/\text{pixel}$. The SNe are observed with six different filters namely *u*, *b*, *v*, *uvw2*, *uvm2*, and *uvw1* (FIGURE 2.2) covering a wavelength range of 1700 - 6500 Å (Romig et al. 2005).

The central wavelengths, and the flux zeropoints for the *Swift*-UVOT, Bessell *UBVR*, and SDSS *u'g'r'i'z'* are provided in TABLE 2.1.

TABLE 2.1: Information on the filters used in this work

Filter	Central Wavelength (\AA)	Flux zeropoints ($\text{erg cm}^{-2} \text{s}^{-1} \text{\AA}^{-1}$)
<i>uvw2</i>	2140.26	5.36e-9
<i>uvm2</i>	2272.71	4.68e-9
<i>uvw1</i>	2688.46	4.15e-9
<i>uvw</i>	3492.67	3.63e-9
<i>uwb</i>	4377.97	6.48e-9
<i>uvv</i>	5439.64	3.73e-9
<i>U</i>	3605.07	3.97e-9
<i>B</i>	4413.08	6.13e-9
<i>V</i>	5512.10	3.63e-9
<i>R</i>	6585.92	2.17e-9
<i>I</i>	8059.88	1.13e-9
<i>u'</i>	3517.43	3.56e-9
<i>g'</i>	4820.09	5.28e-9
<i>r'</i>	6287.06	2.42e-9
<i>i'</i>	7759.38	1.26e-9
<i>z'</i>	11128.81	4.88e-10

*Data from The SVO Filter Profile Service (Rodrigo et al. 2012).

2.3 Data Reduction Techniques

The images obtained with a CCD on a typical observing night are called raw images. These raw images need correction to remove various instrumental effects before they can be used for scientific measurements. This work has used various tasks available with the software IRAF (Tody 1993) as well as several other software packages like SEXtractor (Bertin & Arnouts 1996), Astrometry.net (Lang et al. 2010), SWARP (Bertin et al. 2002), SCAMP (Bertin 2006), PSFEX (Bertin 2011) and several packages written in python like Astrocrappy (McCully et al. 2018; van Dokkum 2001), Astropy (Astropy Collaboration et al. 2022).

2.3.1 Pre-processing

The following pre-processing steps are followed on the images obtained with both GIT and HCT -

1. Bias subtraction - In a CCD, the analogue voltage signal is converted to a digital signal using an Analog-to-Digital Converter (ADC). An unexposed pixel after readout and A/D conversion show a mean of zero counts with a standard deviation. So, the counts can go negative, which is not represented by an ADC. A positive offset value is applied to avoid negative numbers, known as “bias”. This bias value may vary over the entire CCD array, in which case pixel-by-pixel removal is required. Several bias frames are taken with zero exposure time throughout the observing night and coadded using the `ZEROCOMBINE` task. This removes any variations over the image and increases the S/N of the master bias frame. The `IMARITH` task is used to subtract the master bias from object and flat frames.
2. Flat Removal - In a CCD, the quantum efficiency varies over pixels which causes variation in the response of the pixels to incoming radiation. Variations can also be caused by dust in the CCD, filters, and the fact that the light is non-uniformly transmitted across the telescope’s field-of-view. Flat images are obtained along with the observations to correct the values of the science images for the varying pixel response. Flat images are obtained by uniformly illuminating the detector, either by pointing the telescope to the twilight sky (sky flats) or by a part of the dome/using a screen located inside the dome (dome flats). Since the properties of the dust or the quantum efficiency of the CCD depends on wavelength, the flats are taken in the same filter as the objects are observed. Multiple flats with adequate exposure time are obtained on the same night in different filters. The flats are bias subtracted, normalized and combined using the `FLATCOMBINE` task to increase

the SNR and to remove any variations. Finally, the science image is divided by this master flat frame to flatten the response over the entire array.

3. Cosmic Ray rejection - High-energy particles like muons, protons or gamma rays from space or telescope dome walls may hit some pixels of the CCD during an exposure causing ionisation and liberation of electrons. This will cause an increase in the count of pixels. They usually have a sharply peaked profile and can occupy single/multiple pixels. Combining multiple frames can remove the cosmic rays. But sometimes, multiple images in the same filter are not available to combine. So, we remove the cosmic rays from individual images. The `CRMEDIAN` task in `IRAF` works by detecting cosmic rays from pixels which deviate by a statistical amount from a box constructed centring that pixel. Sometimes long exposures for late-phase observations of SNe contain many cosmic rays spread over many pixels. We use the `ASTROCRAPPY` package (McCully et al. 2018; van Dokkum 2001) in python, which can identify cosmic rays of various sizes and shapes based on their edge sharpness.
4. Astrometry and image stacking - SNe are transient sources that vary in brightness. During the late phase of SN evolution, it becomes faint and multiple exposures are obtained. These exposures need to be co-aligned and added to increase the S/N. Before performing co-addition, it is important to know the relative positions of the stars in the images. We perform astrometry to map the CCD coordinates of the stars in the images to sky coordinates. The software `Astrometry.net` (Lang et al. 2010) is used to perform astrometry. To give an astrometric solution of an image, the code detects stars and produces subsets of geometric patterns describing their relative positions. These patterns called “quads” are then matched to index files generated with various catalogues like 2MASS, USNO-B etc. After matching the quads in the input image with that in the index - the plate scale, pointing, and orientation of the image is hypothesized. A Bayesian

decision process is used to verify the hypothesis against other hypothesized matches. The solved images having astrometric information are then passed to **SCAMP** to improve the astrometric precision and finally to **SWARP** to perform resampling of the images to a common grid. The co-aligned images have astrometric differences within $0.1\text{--}1''$ ($1 - 3$ pixels), with most differences appearing in the U -band images due to lesser number of stars registered. All the images of the supernova field are aligned, and multiple images on the same night and in the same filter are co-added.

2.3.2 Photometry

The information about the supernova's flux ($\text{erg cm}^{-2} \text{s}^{-1} \text{\AA}^{-1}$ received on earth is obtained from its apparent magnitude. However, CCDs measure photons in terms of counts. The counts can be converted to apparent magnitudes (m_λ) for each bandpass by using the relation -

$$m_\lambda = -2.5 \log_{10} \frac{C_\lambda}{C_\lambda^0} \quad (2.1)$$

where C_λ , and C_λ^0 are the counts per unit time in exposure of the target object and the standard star (Vega), respectively. The flux from the star convolved with the filter transmission function $T_b(\lambda)$ gives the photon counts -

$$C_\lambda = \int \frac{f_\lambda(\lambda)}{hc/\lambda} T_b(\lambda) d\lambda \quad (2.2)$$

$$C_\lambda^0 = \int \frac{f_\lambda^0(\lambda)}{hc/\lambda} T_b(\lambda) d\lambda \quad (2.3)$$

Here, f_λ and f_λ^0 are the fluxes of the target and the standard star, respectively (Hogg 2022).

The apparent magnitude of a star for a particular observing site and telescope-detector system is called instrumental magnitude. The instrumental magnitudes are converted to a standard magnitude system using Equation 2.1. To extract the counts from the CCD images of the stars and convert them to instrumental magnitudes, we use two techniques - (i) Aperture photometry and (ii) Point Spread Function (PSF) photometry. We describe the two techniques in details below -

Aperture photometry

The technique of aperture photometry involves finding an optimal aperture to sum the counts of an object in a CCD image. This depends on finding a proper centroid and an aperture radius. The optimal choice of an aperture radius is crucial to obtain the counts. It should not be small so as to underestimate the source counts and also not very large to include background noise or other stars. The “curve-of-growth” method is used to determine an optimal aperture, in which it is found that an aperture of 3-4 times the FWHM of several stars in the field gives a good estimate of the source counts. The sky background is subtracted and the counts in this optimal aperture is summed by using the formula -

$$counts = sum - (a \times m_{sky}) \quad (2.4)$$

Here, m_{sky} is the sky value per pixel, a is the area of the circular aperture with an optimal radius obtained from the COG. The magnitude is calculated from the counts for an exposure time t using the formula -

$$mag = -2.5 \log_{10}(counts/t) \quad (2.5)$$

Aperture photometry works well when the sources are well separated and the background does not vary within the image. The DAOPHOT task in IRAF is used to perform aperture photometry.

Point Spread Function photometry

Aperture photometry becomes inaccurate for crowded fields, non-linearly varying backgrounds near the aperture, and low S/N of the object of interest compared to nearby stars. For this, we use the technique of PSF photometry, which fits the stellar profile with various analytical functions like Gaussian, Lorentzian, Moffat or a combination of these functions to extract the counts from the objects of interest. The steps of PSF photometry are as follows -

1. The task DAOFIND is used to select isolated, bright and unsaturated stars.
2. The candidate PSF stars' radial profile is used to determine the *psfrad*, which is usually taken to be the median FWHM of the stellar profile.
3. The task PSTSELECT is used to select good PSF stars from the DAOFIND list.
4. The PSF task is used to build a PSF image from the catalog of stars generated by PSTSELECT.
5. The PSF model is fit to the group of stars and is subtracted from the original image to extract the instrumental PSF magnitudes using the ALLSTAR task.
6. Since the secondary stars are bright and isolated, aperture photometry is performed at a radius 3-4 times the FWHM, and the flux from the tail of the radial distribution is accounted for by the aperture correction.

Instrumental magnitude to standard magnitude

The instrumental magnitudes obtained through PSF/aperture photometry are corrected for the atmospheric extinction and detector response to obtain calibrated magnitudes. The light from the astronomical source has to traverse the earth's

atmosphere before falling on the CCD. The atmosphere at the observing site and the elevation of the source decide how much light is extinguished. Dust and aerosols, water vapour, and O₂ in the atmosphere absorb/scatter the light, and this effect is wavelength dependent. The instrumental magnitudes are thus corrected for extinction using the relation -

$$m_{\lambda}^0 = m_{\lambda} - k_{\lambda}X(z) \quad (2.6)$$

where, k_{λ} is the extinction coefficient, and $X(z)$ is the airmass for the target with zenith angle z . In this work, the extinction coefficients for IAQ, Hanle in *UBVRI* bands are taken from [Stalin et al. \(2008\)](#). The instrumental magnitudes are transformed to a standard magnitude using the relations -

$$(U - B) = \alpha_{u-b}(u - b) + \beta_{u-b} \quad (2.7)$$

$$(B - V) = \alpha_{b-v}(b - v) + \beta_{b-v} \quad (2.8)$$

$$(V - R) = \alpha_{v-r}(v - r) + \beta_{v-r} \quad (2.9)$$

$$(V - I) = \alpha_{v-i}(v - i) + \beta_{v-i} \quad (2.10)$$

$$(V - v) = \alpha_v(b - v) + \beta_v \quad (2.11)$$

Here, *UBVRI* are the calibrated apparent magnitudes, and *ubvri* are the instrumental magnitudes corrected for extinction. α 's, β 's are the colour coefficients and zero points, respectively. The average colour coefficients for the HFOSC instrument are taken from [Stalin et al. \(2008\)](#). Standard stars from [Landolt \(1992\)](#) are observed on photometric nights to calculate the nightly zero points.

Correction for Host galaxy flux

For some SNe, which explode close to the galaxy nucleus, in the bright H II regions, or spiral arms, PSF photometry becomes inaccurate. The problem increases

during the late phase evolution when the signal from the SN is fainter than its environment. The *image subtraction* technique is helpful to remove the contamination of the SN flux by the counts from the host galaxy. It is performed by subtracting the SN field from an image taken before the explosion or after the SN fades beyond detection. For the SNe observed with HCT, we have taken multiple exposures of the SN field under good seeing conditions after the SN has faded (template images). The steps for image subtraction are as follows -

1. For each filter, multiple exposures of the template have been aligned and coadded to increase the S/N.
2. The master template image is then aligned with respect to the SN image.
3. The median sky background from the master template and the SN images are estimated and subtracted to produce background-subtracted images.
4. We then use `SEXtractor` to make catalogues of bright, unsaturated and isolated stars in the template and SN images.
5. The mean FWHM of the template and science frames are calculated from the `SEXtractor` catalogues, and the frame with the lower FWHM (typically the template) is convolved by a 2D kernel using the task `PSFMATCH` in `IRAF`. This process is performed to match the PSF of the science and the template images.
6. `SEXtractor` is run again on the PSF-matched template and science frames to obtain the flux ratio of the stars. The scaling factor is useful for bringing the template and science frames to the same flux level.
7. The science frame is subtracted by the scaled template frame.

2.3.2.1 Supernova Photometry with HCT

The supernova fields are observed with the HFOSC on 2.0 m HCT in *UBVRI* bands. On photometric nights, multiple Landolt fields are also observed along with the supernova field. The steps to obtain SN magnitudes are as follows -

1. The images are pre-processed as outlined in Section 2.3.1.
2. An optimal radius is calculated from the stars in the Landolt field to perform aperture photometry. PSF photometry is performed at the median FWHM of the 1D profile of the stars. Aperture correction is determined and the instrumental magnitudes for the Landolt stars are obtained. These are extinction corrected using the values mentioned in [Stalin et al. \(2008\)](#). Average colour coefficients are used to estimate the nightly zero points.
3. Since, every night we do not observe Landolt stars, multiple secondary standard stars in the SN field are chosen. PSF photometry is performed on these secondary stars and their extinction-corrected magnitudes are determined. The nightly zero points are used to find the apparent magnitudes of the stars in the SN field.
4. The supernova apparent magnitudes are obtained either using PSF photometry or aperture photometry after template subtraction. The nightly zero points are obtained from the list of secondary standards for the nights when we do not have Landolts observed.

2.3.2.2 Supernova Photometry with GIT

GIT can be used in both targeted and tiled modes of operation. For the SN observations, we use the targeted mode of operation. Images are obtained in

SDSS $u'g'r'i'z'$ bands. Either SDSS images in $ugriz$ or PanSTARRS images in $griz$ -filters are used for host galaxy subtraction. The photometric zero points are calculated using the SDSS or PanSTARRS catalogue. We used PYZOGY based on the ZOGY algorithm, to perform the host galaxy subtraction if needed. The PSF model generated by PSFex for the pre-processed GIT image is used for the photometry of the SN.

2.3.2.3 Supernova Photometry with UVOT

The pre-processing of the *Swift*-UVOT data is performed using various tools available with the HEASOFT package along with the latest calibration database (CALDB) (Brown et al. 2009; Poole et al. 2008). A bad pixel map is created for each image using the UVOTBADPIX tool. As mentioned earlier, the CCD has a dimension of 385×288 pixels. Using a centroiding algorithm, a large format image of 2048×2048 pixels is made by sub-sampling each pixel into an 8×8 virtual pixel with $0.5''$ /pixel resolution. At the cost of increasing the resolution, this process introduces an artificial 8×8 pixels fixed pattern. The UVOTMODMAP tool removes this “mod-8” noise. The UVOTFLATFIELD tool performs flat fielding of the images. Astrometry is performed on the images using the SWIFTXFORM tool. Finally, UVOTEXPMAP is used to create an exposure map. The supernova magnitudes are obtained using aperture photometry using the UVOTSOURCE task. The supernova magnitudes are extracted with a $5''$ aperture. A similar aperture size is chosen to get the background counts. Source/background regions are selected using the DS9 software. The background-subtracted counts are summed and divided by the exposure time to obtain the count rate. The aperture correction and photometric calibration specified in “zerofile” in CALDB is used to obtain the apparent magnitudes of the supernova.

2.3.3 Spectroscopy

The spectra of SNe carries information on the velocity, and temperature of the photosphere. It can be used to know the composition, and ionisation state of the ejecta. Since in a SN explosion, the ejecta velocity is of the order of 1000 km s^{-1} , the observations are usually carried out at a lower resolution of $\lambda/\Delta\lambda = 300\text{-}700$. This optimizes the S/N of the spectra and also provides sufficient information to understand the explosion physics and progenitor properties. The CCD images of the spectra obtained are of dimension 250×3500 pixels. The spatial axis is along the horizontal direction, while the dispersion axis is in the vertical direction. The 2D spectrum is bias subtracted, corrected for cosmic-rays (see Section 2.3.1), and clipped along the vertical axis using the `IMCOPY` task in `IRAF`. The clipping removes the effects of bad CCD response at the edges. The 2D images are converted to 1D spectra (flux vs wavelength) using the following steps -

1. Optimal extraction - This process is performed interactively using the `APALL` task in `IRAF`. The dispersion axis is spread over several columns. Similar to photometry, to extract the counts along the dispersion axis, we need to define an optimal aperture, and background region. But the dispersion axis is not exactly perpendicular to the spatial axis. After defining the aperture, we trace the centre of the spatial profile along the dispersion axis by fitting a third order spline. The spectrum is then obtained by summing the values in the aperture based on the trace at each point along the dispersion axis. To increase S/N of the extracted spectrum, summing is performed after weighing with respect to the variance of the spectrum (Horne 1986). Lamp spectra are extracted similarly, using the object spectrum as a reference.
2. Wavelength calibration - The extracted spectrum gives information in counts as a function of pixels. But the desired output should be counts as a function of wavelength. After extracting the lamp spectrum, the lines are identified

interactively with the IDENTIFY task in IRAF to know their wavelengths. A cubic spline is fit to pixels as a function of wavelengths. The HEDIT task is used to modify the object's header with the wavelength solution. Finally, the wavelength solution is applied to the SN spectrum using the DISPCOR task. Night sky emission lines $\lambda 5577$, $\lambda 5890$, $\lambda 6300$ are used to verify the wavelength calibration. Small linear shifts of $3 - 4 \text{ \AA}$ are applied wherever necessary.

3. Flux calibration - To find physical quantities like the temperature of the photosphere, flux ratios etc., it is needed to convert the spectrum to flux units. This is done by observing spectrophotometric standard stars. The standard star is extracted and wavelength calibrated using the same technique as described for the object. The standard star flux is obtained using the STANDARD task. The sensitivity function of the instrument is obtained using the observed spectrum and a calibrated spectrum. The extinction information of the observing site is also used to estimate the sensitivity correctly. This is performed using the SENSFUNC task. The SN spectrum is corrected for detector sensitivity, and flux calibrated using the CALIBRATE task in IRAF. The spectrum thus obtained is on a relative scale.
4. Combined spectrum - A common overlapping region near a flat continuum is used to get a scale factor for combining the spectra from the two grisms. The flux-calibrated spectrum in individual grisms are combined using the task SCOMBINE in IRAF.
5. Scaling - After combining, the SN spectrum is scaled to broadband photometric magnitudes to correct for any slit losses, as well as varying sky conditions.

Chapter 3

Analytical and Numerical Modelling

This chapter discusses various analytical relations which are used to extract the explosion parameters. We have used techniques like Markov Chain Monte Carlo (MCMC) to fit the relations to the observed data and constrain the errors on the parameters. We have also used Gaussian process regression to interpolate the light curves. For the spectral modelling of various observables, we used various numerical codes available in the literature like `syn++`, TARDIS and SEDONA.

3.1 Light Curve Modelling

3.1.1 Analytical relation

A simple analytical relation exists for the emergent luminosity of SNe Ia (Arnett 1982). The relation is used to understand the origin of luminosity and the factors governing it.

The luminosity of the supernova can be obtained starting from the first law of thermodynamics,

$$\frac{dE_{int}(t)}{dt} = -p \frac{dV}{dt} + \dot{Q}(t) - L(t) \quad (3.1)$$

where E_{int} is the total internal energy of the ejecta of mass M and volume V , the $p \frac{dV}{dt}$ term is the rate of work done by the pressure (p) of the ejecta, $\dot{Q}(t)$ is input energy deposition due to radioactivity, and L is the luminosity coming out of the ejecta. We can calculate $L(t)$ from EQUATION 3.1 by using few assumptions which are as follows -

1. The ejecta expands homologously in which $R_{ej}(t) = vt + R_0$, where R_{ej} is the ejecta radius at time (t), v expansion velocity, R_0 initial radius.
2. The energy from radiation dominates over the gas energy. The pressure and internal energy density are given as

$$p = \frac{aT^4}{3}, \quad u = aT^4 \quad (3.2)$$

Here, $u = \frac{E_{int}}{V}$ is the specific energy density in a one-zone model, and T is the temperature.

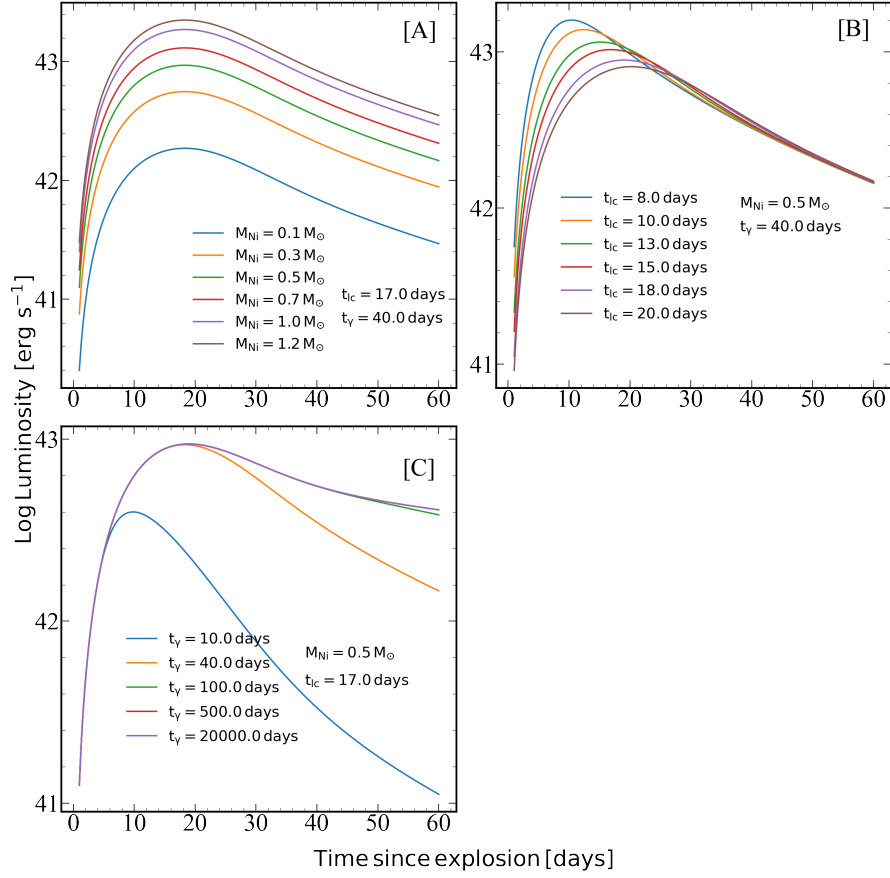


FIGURE 3.1: The effect of varying ^{56}Ni ([A]), t_{1c} ([B]), and t_γ ([C]) on the luminosity of the supernova as given by EQUATION 3.5.

3. The luminosity is expressed by the spherical diffusion equation

$$L(r) = -4\pi r^2 \frac{c}{3\kappa\rho} \frac{\partial u}{\partial r} \quad (3.3)$$

Here, κ is the opacity.

4. The ejecta has a constant opacity throughout its evolution.
5. The energy density profile has a fixed spatial dependence independent of time.
6. The above assumption leads to a final assumption that the spatial distribution of heating is proportional to the energy density.

Let us consider the supernova ejecta of mass M_{ej} and kinetic energy E_k expanding with time. The photon escape is modified by the increase of the radius of the ejecta and the density/opacity(κ) decreasing with time. The timescale (t_{lc}) at which the photons can escape is set by equating the diffusion time to the expansion time of the ejecta. This t_{lc} (days) depends on the ejected mass, opacity, and kinetic energy in the following manner.

$$t_{lc} \propto M_{ej}^{\frac{3}{4}} \kappa^{\frac{1}{2}} E_k^{-\frac{1}{4}} \quad (3.4)$$

This relation is used as a scaling relation between t_{lc} , M_{ej} , and E_k . The main source which powers the supernova light is the decay of ^{56}Ni and ^{56}Co . Using an analytical relation for the heating rate due to ^{56}Ni decay, positron and gamma-ray heating in EQUATION 3.1, we can calculate the output luminosity. The output luminosity is given as -

$$L(t) = M_{\text{Ni}} e^{-x^2} [(\epsilon_{\text{Ni}} - \epsilon_{\text{Co}}) \int_0^x 2ze^{z^2-2zy} dz + \epsilon_{\text{Co}} \int_0^x 2ze^{z^2-2yz+2zs} dz] (1 - e^{-(\frac{t_\gamma}{t})^2}) \quad (3.5)$$

where $x \equiv t/t_{lc}$, t is the time since explosion (days). $y \equiv t_{lc}/(2t_{\text{Ni}})$ with $t_{\text{Ni}} = 8.8$ d, $s \equiv [t_{lc}(t_{\text{Co}} - t_{\text{Ni}})/(2t_{\text{Co}}t_{\text{Ni}})]$ with $t_{\text{Co}} = 111.3$ d. t_γ is the γ -ray time scale (days), and M_{Ni} is the initial Ni mass. $\epsilon_{\text{Co}} = 6.8 \times 10^9$, and $\epsilon_{\text{Ni}} = 3.9 \times 10^{10}$ erg s $^{-1}$ g $^{-1}$ are the energy generation rates due to decay of Co, and Ni respectively.

The luminosity of the SN increases as more ^{56}Ni is synthesized. In panel[A] of FIGURE 3.1, we have varied the ^{56}Ni mass keeping the parameters t_{lc} , and t_γ as constants. The effect of large t_{lc} with the same ^{56}Ni and t_γ is to broaden the light curves (panel[B] of FIGURE 3.1). The factor t_γ comes in EQUATION 3.5 as a factor affecting the light curve decline (Chatzopoulos et al. 2012). This quantifies gamma rays and positron trapping in the ejecta. For smaller t_γ , the luminosity declines rapidly, while for more efficient trapping (larger t_γ , panel[C] of FIGURE 3.1) the luminosity increases.

The fit parameters of the model are t_{lc} - the light curve time scale, t_{exp} - the epoch of explosion, M_{Ni} - the initial ^{56}Ni mass produced, and t_γ - the gamma-ray leaking time scale. We can obtain the ejecta mass (M_{ej}) and kinetic energy (E_k) using the relations -

$$M_{ej} = 0.5 \frac{\beta c}{\kappa} v_{exp} t_{lc}^2 \quad (3.6)$$

$$E_k = 0.3 M_{ej} v_{exp}^2 \quad (3.7)$$

Here, v_{exp} is the expansion velocity of the ejecta, $\beta = 13.8$ is a constant of integration.

3.1.2 Fitting analytical relation with Markov Chain Monte Carlo (MCMC) technique

Bayes' theorem states that the probability of event A, given that of an event B is the conditional probability -

$$P(A) = \frac{P(A \cap B)}{P(B)} \quad (3.8)$$

where, $P(A \cap B)$ is the probability of both occurring, and $P(B) \neq 0$. The Bayesian framework can be used to infer model parameters given some observations. For inferencing, Bayes' rule can be written as -

$$P(\theta | x) = \frac{P(x | \theta) P(\theta)}{P(x)} \quad (3.9)$$

$P(x | \theta)$ is the likelihood \mathcal{L} , which is conditional probability of the data for some parameters, $P(\theta)$ is the prior, which is the probability of the model parameters, $P(x)$ is the probability of the data, and $P(\theta | x)$ is the posterior π , which is the conditional probability of the model parameters given the data. We need to know $P(x)$ to calculate the posterior in Equation 3.9. To calculate $P(x)$, we need to

integrate over all possible values of θ .

$$P(x) = \int_{\Theta} P(x | \theta) d\theta \quad (3.10)$$

This integration becomes highly challenging to solve analytically when the number of parameters increases. Hence, MCMC techniques calculate the posterior distribution by performing random moves and jumping from one move to another. The model parameters are estimated by sampling the posterior distribution. One such famous sampling technique is the Metropolis-Hastings (MH) algorithm. The steps for the MH algorithm are as follows -

1. The algorithm is started by choosing some initial position (θ_i) in the parameter space and calculating the posterior $P(\theta_i | x)$.
2. Propose a jump from the current position θ_i to a new position θ_{i+1} and calculate the posterior at θ_{i+1} , $P(\theta_{i+1} | x)$.
3. Draw a random number $Z \in \mathcal{U}(0, 1)$.
4. If the ratio $P(\theta_{i+1} | x)/P(\theta_i | x) > Z$, then the move is accepted, and the chain advances to θ_{i+1} .
5. Else, the move is rejected and $\theta = \theta_i$.
6. The chain is repeated and the accepted positions of the parameter set are collected.

Since we are dividing the proposed posterior with the current posterior, we eliminate $P(x)$

$$\frac{P(\theta_{i+1} | x)}{P(\theta_i | x)} = \frac{\frac{P(x|\theta_{i+1})P(\theta_{i+1})}{P(x)}}{\frac{P(x|\theta_i)P(\theta_i)}{P(x)}} \quad (3.11)$$

Thus, the posterior $\pi \propto \mathcal{L}P(\theta)$. The product of likelihood and prior can be maximized to maximize the posterior. Assuming Gaussian distributed scatter in

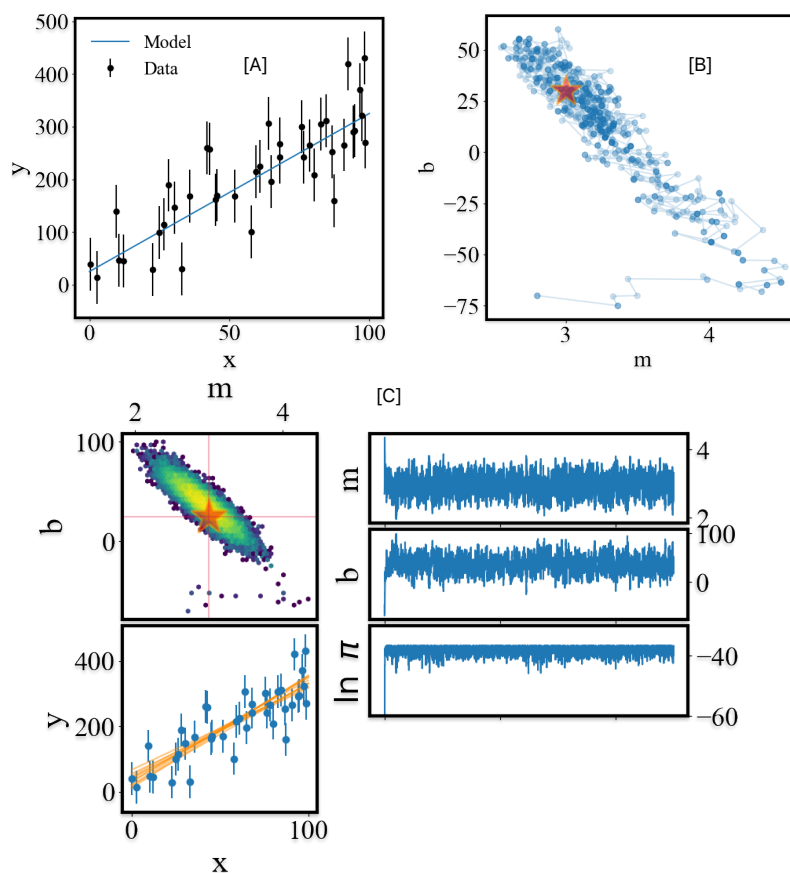


FIGURE 3.2: [A] Simulated dataset with the linear model (slope $m=3.0$, and intercept $b=25.0$) overplotted. [B] Positions of the chain in the parameter space of m , and b . We start the chain at $m=2.8$, and $b=-70$. Also shown is the true value ($m=3.0$, and $b=25.0$). [C] The posterior space, data, models drawn from the posterior distribution, and the 1D chains of m , b , and $\ln \pi$.

the observations, we can describe the probability of any individual observation in terms of the model parameters

$$p(x | \theta) = \frac{1}{\sqrt{2\pi\sigma_x^2}} \exp -\frac{(x - x_{model})^2}{2\sigma_x^2} \quad (3.12)$$

where, σ_x is the error on x . Assuming the observations are independent, the probability of all the observations is the product of the individual observations

$$\mathcal{L} = \prod_i p(x | \theta) \quad (3.13)$$

To avoid numerical instabilities while dealing with small numbers, the likelihood is often written in log as

$$\log \mathcal{L} = -K \sum_i \frac{(x - x_{model})^2}{2\sigma_x^2} \quad (3.14)$$

To understand the working of MCMC, we simulated observations between 0 and 100 from a linear model with slope $m = 3.0$, and intercept $b = 25.0$. Each observation has random gaussian noise with mean $\mu = 0.0$, and sigma $\sigma = 50.0$ (panel [A] in FIGURE 3.2). We have build our own Metropolis-Hastings sampler to estimate the posterior. We start the chain at $m = 2.8$, and $b = -70$ with covariance of 0.25, and 5 respectively. The posterior is sampled by running the chain for 1000 steps (panel [B] in FIGURE 3.2). The covariance of the parameters determines how the chain will explore the posterior. If they are too small the chain will take large time to find the maximum of the posterior. If they are too large, the full posterior is not explored. In panel [C] in FIGURE 3.2, the posterior space, data, 10 models drawn from the posterior, and the 1D-chains of the parameters, $\ln \pi$ are shown.

To model the bolometric light curves with EQUATION 3.5, we used the `emcee` package (Foreman-Mackey et al. 2013a) to perform the parameter estimation (M_{Ni} , t_{IC} , t_γ , and t_{exp}). From the posterior distribution we also constrain the errors on the parameters.

3.1.3 Interpolating light curves with Gaussian process regression

Let us consider a variable x from a Gaussian distribution with mean μ , and variance σ^2 . The probability distribution for which is -

$$p(x) = \frac{1}{\sqrt{2\pi}\sigma} \exp \left[-\frac{(x - \mu)^2}{2\sigma^2} \right] \quad (3.15)$$

This is denoted by $x \sim \mathcal{N}(\mu, \sigma^2)$. For a pair of variables x_1 and x_2 , drawn from a bivariate Gaussian distribution. The joint probability density for x_1 and x_2 is

$$\begin{bmatrix} x_1 \\ x_2 \end{bmatrix} \sim \mathcal{N} \left(\begin{bmatrix} \mu_1 \\ \mu_2 \end{bmatrix}, \begin{bmatrix} \sigma_1^2 & C \\ C & \sigma_2^2 \end{bmatrix} \right), \quad (3.16)$$

where $C = \text{cov}(x_1, x_2)$ is the covariance between x_1 and x_2 . The second term on the right-hand side is the covariance matrix, K . Now consider N variables $\mathbf{x} = (x_1, x_2, \dots, x_N)^T$ drawn from a multivariate Gaussian distribution

$$\mathbf{x} \sim \mathcal{N}(\boldsymbol{\mu}, K) \quad (3.17)$$

where, $\boldsymbol{\mu} = (\mu_1, \mu_2, \dots, \mu_N)^T$ is the mean vector, and K is an $N \times N$ positive semi-definite covariance matrix, with elements $K_{ij} = \text{cov}(x_i, x_j)$.

Gaussian process (GP) is an extension of this concept to N -dimensions ($N \rightarrow \infty$). GP is a Bayesian regression approach in a non-parametric way. It is not limited by any functional form to interpolate. GP calculates the probability distribution over all possible functions that can represent the data. It uses only a prior defined by a mean and covariance function.

$$y(x) = \mathcal{GP}(\mu(x), k(x, x')). \quad (3.18)$$

Using the observed data as training points, it can predict the value of the function and its covariance at a specified point. Choosing a mean function and a suitable covariance function/kernel is important. The mean function is usually the mean of the observed data and Matern 3/2 is chosen as the covariance kernel

$$k_{3/2}(x, x') = A \left(1 + \frac{\sqrt{3}r}{l} \right) \exp \left(-\frac{\sqrt{3}r}{l} \right), \quad (3.19)$$

where $r = |x - x'|$, l is the length scale over which the function varies, and A is the variance.

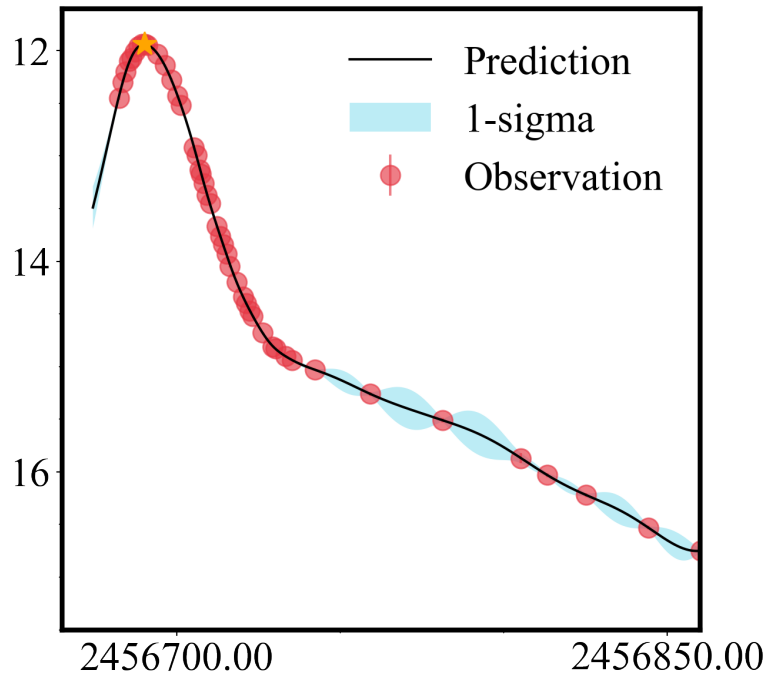


FIGURE 3.3: Interpolation of the B -band light curve of SN 2014J (Srivastav et al. 2016) with Gaussian process regression using the `scikit-learn` package in `python`. At each interpolated point, we get the interpolated value along with the covariance. The light curve maximum is shown with a star mark.

We used `scikit-learn` in `python` to interpolate the multi-band light curves of the SNe presented in this thesis. In FIGURE 3.3, the B -band light curve of SN 2014J (Srivastav et al. 2016) is interpolated with GP regression. The light curve maximum is at $\text{JD } 2456690.12 \pm 0.18$, $\Delta m_{15}(B) = 0.96 \pm 0.01$ mag, and magnitude at maximum is 11.94 ± 0.01 mag. Srivastav et al. (2016) calculated the maximum at $\text{JD } 2456690.14 \pm 0.5$, maximum magnitude of 11.94 ± 0.02 , and $\Delta m_{15}(B) = 0.96 \pm 0.03$ mag.

3.2 Spectral Modelling

3.2.1 syn++

A fast parametrized model called the “elementary supernova model” is used to understand a supernova spectrum qualitatively (Jeffery & Branch 1990; Thomas et al. 2011). The code `syn++` is also written using a similar approach. The assumptions of the code are

1. A sharp blackbody photosphere represents the continuum at a temperature T_{ph} . The temperature can be estimated using Stefan’s law,

$$L = 4\pi R_{ph}^2 \sigma_{sb} T_{ph}^4 \quad (3.20)$$

where, σ_{sb} is the Stefan-Boltzmann constant, L is the luminosity and R_{ph} is the photospheric radius. The intensity $I_{ph} = B_\lambda(T_{ph})$ is constant in every directions.

2. The expansion of the ejecta is homologous.
3. The continuum opacity in the line formation region above the photosphere is zero.
4. The atomic and ionic level populations are calculated assuming LTE.
5. The opacity comes from line resonance assuming Sobolev formalism. The photon will feel the opacity due to a line transition if its co-moving frame wavelength gets redshifted into resonance with the line. The line has some intrinsic width so that the redshifted photon will feel the opacity over a spatial extent, also called the resonance region. The thermal velocity (~ 5 km s⁻¹) is lesser than the ejecta velocities (~ 1000 km s⁻¹), so the resonance

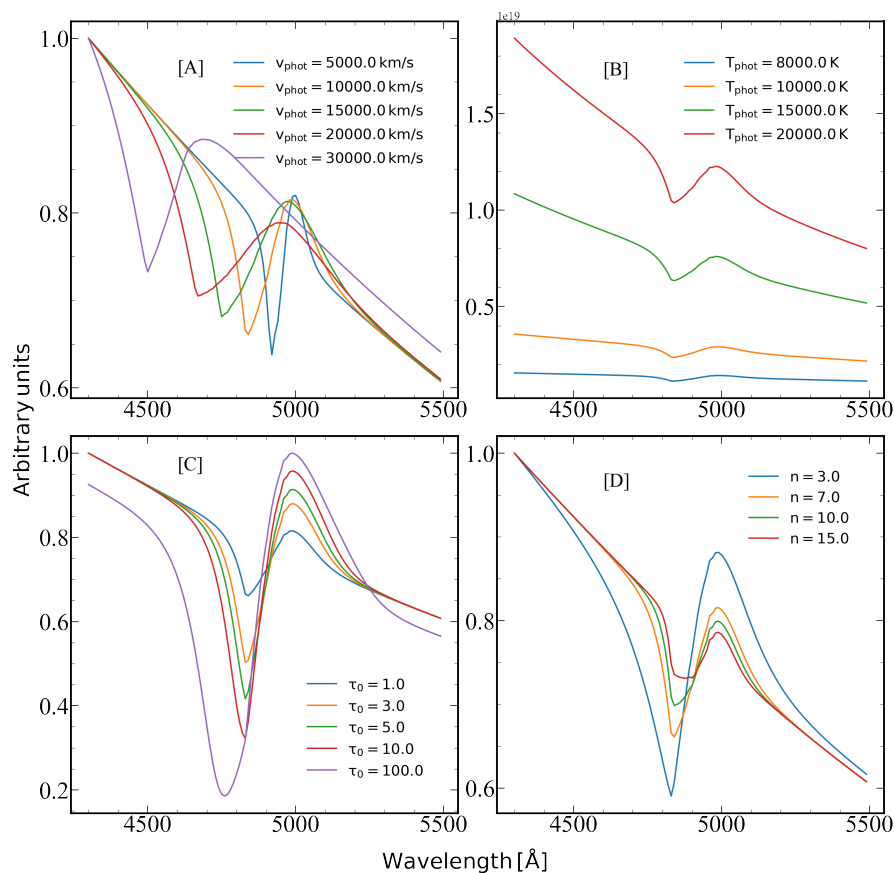


FIGURE 3.4: Simulation of a single P-Cygni profile at a rest wavelength of 5000 Å under Sobolev approximation. The effect of varying the photospheric velocity [A], photospheric temperature [B], the optical depth at the photosphere [C], power law index for the optical depth [D] are shown.

region is essentially a point. This is called Sobolev approximation, and it makes the photon interaction a local event.

6. The spectrum is calculated time-independently using the “snapshot” technique. Since the continuum opacity above the photosphere is zero, the travel time for a photon to escape the ejecta is much less compared to the expansion timescale.
7. It does not solve rate equations or ratios of ionization.

The `syn++` code is used in an empirical spirit to calculate a synthetic spectrum, which can be compared with the observed spectrum. This is used to perform line

identifications, find the velocity of the photosphere, the velocity range over which a line is formed, and the temperature of the photosphere. Several ions are given as input along with their photospheric (v_{phot}), minimum (v_{min}), and maximum (v_{max}) velocities. The optical depth of a reference line is kept as a free parameter, and using Boltzmann excitation, the optical depths of the lines of an ion are calculated. A velocity law is assumed for the optical depth in which a scale parameter v_e varies. In this fitting technique, an ion used as input is detached if the v_{min} exceeds v_{phot} .

In FIGURE 3.4, we show a simple P-Cygni line at a rest wavelength of 5000 Å constructed assuming Sobolev approximation. The effect of increasing the photospheric velocity (v_{phot}) is a more blue-shifted absorption component (Panel [A]). Increasing the photospheric temperature (T_{phot}) (panel [B]) makes the continuum bluer, which reflects a hot photosphere. The primary effect of increasing the optical depth at the photosphere (panel [C]) is to strengthen the absorption and emission components of the P-Cygni profile. As the optical depth increases further, the line becomes saturated. Also, the minimum moves to the blue region with increasing optical depth. We use a simple power law to represent the optical depth - the index (n) is varied in panel [D]. As n is decreased, the optical depth profile extends out to higher velocities (less steep), making the absorptions and emissions wider. The emission peak also gets stronger (for example, $n=3.0$), because there is more material at higher velocities to scatter photons into the light of sight. The absorption minimum does not change position much. This simple approach is very useful for understanding SN spectra. However, there will be other effects like line bending, electron scattering etc. which should be considered for a more realistic picture of the SN ejecta. The codes `TARDIS` and `SEDONA` are useful to get a more physics-involved picture of the SN atmosphere.

3.2.2 TARDIS

Temperature And Radiation Diffusion In Supernovae (TARDIS) is a radiative transfer code for modelling a supernova spectrum in one-dimension using Monte Carlo approach (Kerzendorf & Sim 2014; Vogl et al. 2019; Kerzendorf et al. 2023). TARDIS calculates synthetic spectrum in a time-independent (“snapshot”) manner. The input parameters to TARDIS are the supernova’s luminosity at a particular epoch, the time since the explosion, density profile (density as a function of velocity), and an abundance structure. The main assumptions of the code are –

1. The ejecta is spherically symmetric.
2. The radiation is emitted as Monte Carlo photons (MC-photons) which are not destroyed by radiation-matter interactions. Each interaction can only change the direction and frequency of the photon.
3. The photosphere is defined by an inner boundary from which the MC-photons start travelling the ejecta.
4. The entire ejecta above the inner boundary is divided into spherically symmetrical cells.
5. The ejecta is in homologous expansion.

3.2.2.1 Monte Carlo scheme

At the beginning of the Monte Carlo simulation, a bunch of MC-photons having frequency ν , and comoving frame energy E are generated from the inner boundary at a particular velocity. The MC-photons have a blackbody distribution of

temperature T_i , and the luminosity is matched to the value given as input

$$L_i = 4\pi r_i^2 \sigma T_i^4 \quad (3.21)$$

where, r_i is the radius of the inner boundary. In a simulation of N -packets, each packet has an energy of -

$$E = \frac{L_i}{N} \Delta t \quad (3.22)$$

The Δt is an arbitrary time interval within the simulation. The packets are given initial directions $\mu = \sqrt{z}$ using a random number $z \in (0, 1]$. The main opacity sources in supernova ejecta are bound-bound transitions/line opacity and Thomson scattering due to free electrons. The bound-bound opacity is treated in the Sobolev approximation with optical depth (τ_{sob}) given by

$$\tau_{sob} = \frac{\pi e^2}{m_e c} f \lambda_{lu} t_{exp} n_l \left(1 - \frac{g_l n_u}{g_u n_l}\right) \quad (3.23)$$

Here, m_e is the mass of the electron, f is the oscillator strength for the transition, n_l and n_u are the number densities in the lower and upper states, g_l , and g_u are the statistical weights of the two states, λ_{lu} is the wavelength of the transition from $l \rightarrow u$, t_{exp} is the time since the explosion. During the travelling of the photons through the ejecta, they can undergo three types of line interactions - (i) resonance scattering (scatter mode), (ii) generating a macro atom to the upper level and simulating the re-emission of the absorbed energy (macro atom mode) through all internal transitions before returning as a radiation packet, and (iii) Macro atoms deactivate directly to the state from which it was initially activated with no internal transitions (downbranch mode).

The propagation of the MC-photons through the ejecta is performed using the Monte Carlo approach. The photon packet can end its journey by three different ways - it reaches any of the boundaries of the computation zone, electron

scattering, or bound-bound absorption. Monte Carlo formalism is used to determine which event has occurred. There are three competing distances, the shortest determining which interaction has occurred. If the distance (d_l) to the nearest resonance line the photon can Doppler shift into is shorter than the distance due to electron scattering (d_e) and the nearest zone boundary (d_s), then a bound-bound absorption will take place. Similarly, if d_e is shorter than d_l , and d_s - an electron scattering occurs, and if d_s is shorter than the other two, then the photon crosses the boundary. If the boundary is within the velocity domain used to model the spectra, the above procedures are repeated for the new cell. The photon contributes to the synthetic spectrum if it crosses the outer boundary.

3.2.2.2 Radiation field

Input parameters like density and elemental abundances are used to calculate the number densities of the states of the various atomic/ionic species. TARDIS calculates the ionization number densities using Saha's ionization equation and excited level populations using the Boltzmann equation. Modified versions for ionization and excitation calculations are the nebular, and dilute-Ite mode in which a dilution factor is introduced in the Saha ionization equation and Boltzmann equation (Mazzali & Lucy 1993). Several estimators are used to calculate the dilution factor W , and radiation temperature T_R in an iterative manner after each MC calculation. The total energy coming out of the defined outer boundary of the model ejecta is compared to the luminosity given as an input (a free parameter). T_R , W are changed iteratively until the solution converges. Typically, the solution converges within 20 - 30 iterations.

3.2.2.3 Synthetic spectrum

The synthetic spectrum can be calculated by binning the photons from the defined outer boundary in frequency space. But this spectrum usually has Monte Carlo noise. To reduce the noise, TARDIS uses the concept of virtual packets. Virtual packets (N_v) with identical properties are generated in one last MC simulation from radiation packets. These virtual packets do not suffer from scattering and contribute to luminosity. This decreases the MC noise and increases the S/N.

3.2.2.4 TARDIS settings

The abundances of elements in the TARDIS simulations are kept fixed at every cell (spatial) in the ejecta (uniform composition). The inner and outer velocity are provided as input. If we have taken a 1D density profile from hydrodynamical modelling (HESMA, [Kromer et al. 2017](#)), then the number of zones are set by the density profile (typically ~ 100). For the Monte Carlo, we use 1×10^5 particles, with another 5×10^4 particles used in the last step to increase the S/N. We have used the dilute-lte mode for excitation, nebular mode for ionization, and macroatom scheme for line interaction. The spectra are calculated from 3000 – 9500 Å with 5000 wavelength bins. The line list is taken from Kurucz CD23 with additional inputs from CHIANTI ([Kerzendorf & Sim 2014](#)).

3.2.3 SEDONA

SEDONA is a multi-dimensional MC radiative transfer code ([Kasen 2006](#)). The MC step is similar to TARDIS. It can calculate the radiation signatures within a SN ejecta in a time-dependent manner. It takes the ejecta’s density, temperature, and

abundance structure as input and calculates the light curves, spectral evolution and polarization. The main assumptions of the code are

1. The ejecta is in homologous expansion.
2. Line treatment is performed assuming Sobolev approximation.
3. The ionization and excitation calculations are performed assuming local thermodynamic equilibrium.

SEDONA considers the radioactive energy deposition due to ^{56}Ni decay. For each time step, a spatial grid is constructed, and the energy deposition rate in every grid cell is followed by a gamma-ray transfer routine. The important opacity sources for gamma-ray transfer are Compton scattering and photoelectric absorption. **SEDONA** treats the line source function in the two-level atom formulation, the source function for which is given as -

$$S_\lambda = (1 - \epsilon)J_\lambda + \epsilon B_\lambda(T) \quad (3.24)$$

here, ϵ is the probability of absorption, $B_\lambda(T)$ is the Planck function, $J_\lambda(T)$ is the angle-averaged intensity. A high-energy UV photon originating in the inner, hotter ejecta has long diffusion times. This photon performs line interaction with an atom, exciting it, which de-excites by a redder transition. The lines can absorb or scatter depending on a probability parameter ϵ in the two-level atom approximation. In general, the value of ϵ should be different for different lines, but in this work a common value of ϵ is chosen as suggested by [Kasen \(2006\)](#). The important features of **TARDIS**, and **SEDONA** are compared in TABLE 3.1

TABLE 3.1: Comparison between TARDIS, and SEDONA.

Properties	TARDIS	SEDONA
Radiation Transfer	Monte Carlo	Monte Carlo
Homologous expansion	✓	✓
Time-Dependence	✗	✓
γ -ray transfer	✗	✓
Ionization and excitation	LTE	LTE

3.2.3.1 SEDONA settings

In our work, we have initialized the simulation with 10^6 particles, and additional 10^6 particles are added per time step due to radioactivity. The simulations start at 1.0 day and run up to 100.0 days since the explosion with a maximum time step of 1.0 day. The ejecta has been divided into 100 zones in our calculations. The spectrum is calculated between 2×10^{16} Hz (150 Å) to 1×10^{14} Hz (30 000 Å) with 1500 frequency bins spaced in a logarithmic way. The opacity grid is calculated within the same wavelength region but with a finer grid. For opacity calculations, we have used electron scattering, free-free, bound-free, bound-bound, and line expansion opacity. The line list for bound-bound opacity is taken from “kurucz_cd23” (Kurucz & Bell 1995).

3.2.3.2 Light Curves from SEDONA

The output spectrum from SEDONA simulation is obtained by collecting the photons that crosses the outer boundary of the model ejecta, in discrete frequency and time bins. The output spectrum is calculated at each time stamp from 1.0 day to 100.0 days. The light curves are obtained by convolving the spectrum with the transmission functions of the filters given in TABLE 2.1 using the Vega spectrum. For the light curve extraction we use `wsynphot` in `Starkit`*

*<https://github.com/starkit>

Chapter 4

Probing the homogeneity/diversity in Type Ia supernova explosions

SNe Ia are explosions due to thermonuclear runaway in a WD, most likely carbon-oxygen with a mass close to M_{ch} . However, specific progenitor systems and mechanisms driving the explosions have not been clearly identified. Two of the most favoured models for the progenitors are the single degenerate, (SD, [Nomoto 1982a,b](#)), and double-degenerate systems (DD, [Iben & Tutukov 1984](#)). The best-studied models so far are the delayed detonation in M_{ch} WDs ([Mazzali et al. 2007](#)), but studies of sub- M_{ch} mass models ([Sim et al. 2010](#); [Goldstein & Kasen 2018](#)) have been successful in reproducing the peak brightness and light curve widths of the normal and fast-declining SNe Ia.

Spectroscopy of SNe at different stages can unravel the nature of the explosion and the progenitor scenarios. In some cases, absorption features from C, and O are present in the very early spectra, which result from incomplete burning ([Parrent](#)

et al. 2011). The expansion velocity inferred using these features could provide an essential hint to the velocity structure of the outer expanding ejecta. It is not certain whether the unburned material is present only in the outer layers or is mixed within the ejecta, and if so, the extent of mixing. The objects with detection of unburned materials are of great significance as they can constrain the amount of material still unburned and hence the explosion channel. The pure deflagration model (W7, Nomoto et al. 1984), and the pulsating delayed detonation models (Hoefflich et al. 1995; Dessart et al. 2014) leave unburned carbon in the ejecta, while the delayed detonation model burn most of the carbon (Khokhlov 1991b; Kasen et al. 2009).

Speaking in terms of observations, pre-explosion HST images (Li et al. 2011b) have ruled out He stars or luminous red giants as the companion of a well studied normal Ia, SN 2011fe. But main-sequence (Nugent et al. 2011) or another WD as a companion cannot be ruled out. Observations of early UV emission in a thermonuclear supernova iPTF14atg (Cao et al. 2015) hinted towards collision of ejecta material with its companion, supporting a single degenerate scenario. The excess flux can also be explained by ^{56}Ni in the outer layers (Magee & Maguire 2020). Some circumstellar mass can be formed from ejection of mass in tidal tails before the merger of two WDs. The interaction of the SN ejecta with the tidal tail ejecta produces signatures in X-ray/UV/optical (Raskin & Kasen 2013). The presence of $\text{H}\alpha$, $\text{H}\beta$ in the spectra of PTF11kx can be understood in terms of ejecta interacting with circumstellar mass indicating a non-degenerate companion (Dilday et al. 2012). The detection of $[\text{O I}] \lambda\lambda 6300, 6364$ in the nebular spectra of 2010lp indicates that oxygen is present close to the center which is predicted by violent merger model (Kromer et al. 2016). So, the very question of single/double degenerate progenitor still persists. The observed diversity in the explosions along with different models proposed to explain the diversity makes it important to study these systems.

In this chapter, we present new observations of two normal Ia, SN 2017hpa and SN 2011aa. We also present ejecta models by varying total mass, and kinetic energy. The synthetic light curves and spectra calculated with SEDONA are compared with observational data of these two events and three other SN Ia, SN 2006bt, SN 2012dn and SN 2018oh.

4.1 SN 2017hpa: A carbon-rich Type Ia Supernova

4.1.1 Introduction

We present a detailed spectroscopic and photometric study of 2017hpa that showed the presence of unburned carbon in its early spectrum. FIGURE 4.1 shows the field of 2017hpa along with the secondary standards. The observed properties of 2017hpa are compared with normal Ia, and its explosion parameters are estimated. 2017hpa* was discovered by Gagliano et al. (2017) on 2017 October 25, 08:18:16 UT (JD=2458051.84) in the galaxy UGC 3122[†]. A spectrum obtained on 2017 October 25 at 23:55:02 UT with the Asiago 1.82 m Copernico Telescope equipped with AFOSC was consistent with the very early spectrum of a SN Ia, particularly, SN 1990N \sim 14 days before the maximum light (Floers et al. 2017). The important parameters of 2017hpa, and its host UGC 3122 are presented in TABLE 4.1.

Bessell *UBVRI* photometric observations of 2017hpa were taken with HCT+HFOSC. Landolt photometric standard field PG0231+051 was observed on 2017 November 22 and 2018 January 5, while the field PG0918+029 was observed on 2017 December 29. The photometry of the secondary standards in the field of 2017hpa is

*<https://wis-tns.weizmann.ac.il/object/2017hpa>

[†]<http://leda.univ-lyon1.fr/>

TABLE 4.1: Parameters of 2017hpa and its host galaxy.

Parameters	Value	Ref.
<i>SN2017hpa:</i>		
RA (J2000)	$\alpha = 04^{\text{h}}39^{\text{m}}50^{\text{s}}73$	2
DEC (J2000)	$\delta = +07^{\circ}03'55''22$	2
Galactocentric Location	11.2'' W, 35.6'' N	2
Discovery Date	$t_{\text{d}} = 2017 \text{ October } 25 \text{ 08:18 (UTC)}$ (JD 2458051.84)	2
Date of <i>B</i> -band Maxima	$t_0 = 2017 \text{ November } 08 \text{ 17:45 (UTC)}$ (JD 2458066.29 \pm 0.11)	1
$\Delta m_{15}(B)$	0.98 \pm 0.16 mag	1
$E(B - V)_{\text{MW}}$	0.1518 \pm 0.0069 mag	3
$E(B - V)_{\text{Host}}$	0.08 \pm 0.06 mag	1
$(B - V)_0$	-0.26 \pm 0.03	1
M_B	-19.45 \pm 0.15 mag	1
μ	34.08 \pm 0.09 mag	1
Peak Luminosity	$L_{\text{peak}}^{\text{bol}} = 1.43 \times 10^{43} \text{ erg s}^{-1}$	1
^{56}Ni mass	0.61 \pm 0.02 M_{\odot}	
M_{ej}	1.10 \pm 0.22 M_{\odot}	
\dot{v}	128 \pm 6 km s $^{-1}$ d $^{-1}$	1
R(Si II) $_{\text{max}}$	0.13 \pm 0.02	1
v_{max}	9643 \pm 110 km s $^{-1}$	1
v_{10}	8320 \pm 120 km s $^{-1}$	1
E_k	0.80 \pm 0.23 $\times 10^{51} \text{ erg s}^{-1}$	1
<i>UGC 3122:</i>		
Alternate name	MCG+01-12-013, PGC15760, MCG1-12-013, CGCG419-21	4
Type	SBc	4
RA (J2000)	$\alpha = 04^{\text{h}}39^{\text{m}}51^{\text{s}}50$	4
DEC (J2000)	$\delta = +07^{\circ}03'19''0$	4
Red-shift	$z = 0.015647 \pm 0.000027$	4

- (1) This paper; (2) [Gagliano et al. \(2017\)](#) (3) [Schlafly & Finkbeiner \(2011\)](#) (4) [Skrutskie et al. \(2006\)](#)

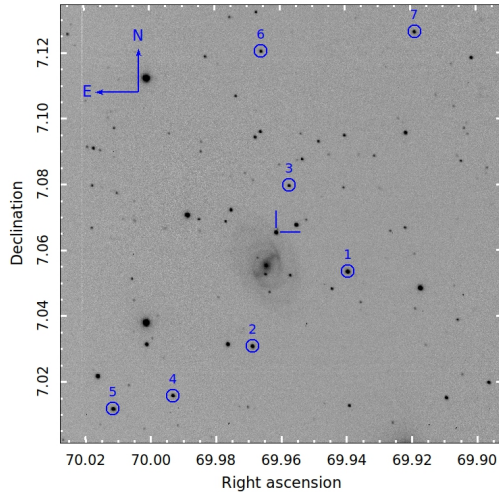


FIGURE 4.1: 2017hpa in the host galaxy UGC 3122. This is a $\sim 7 \times 7$ arcmin² image in *V*-band (50 sec exposure) taken with HCT on 2017 October 31. The supernova is marked with crosshairs. Secondary standards are also marked.

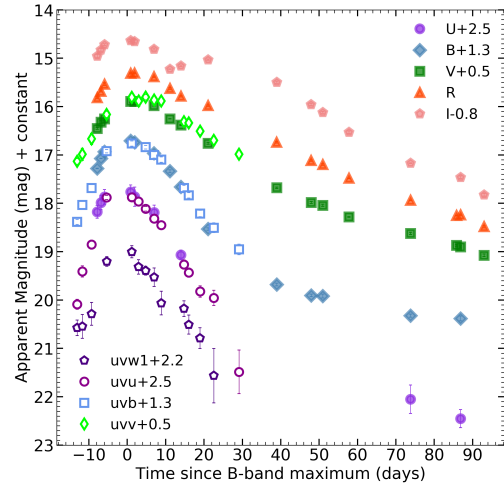


FIGURE 4.2: *UBVRI*, and *Swift*-UVOT light curves of 2017hpa. The phase is wrt *B*-max. The light curves in individual bands have been shifted for representation purpose.

TABLE 4.2: *UBVRI* magnitudes of secondary standards used for calibrating the photometry of 2017hpa.

ID	<i>U</i>	<i>B</i>	<i>V</i>	<i>R</i>	<i>I</i>
1	18.45 ± 0.03	16.99 ± 0.01	15.66 ± 0.02	14.85 ± 0.01	14.16 ± 0.03
2	17.49 ± 0.03	17.13 ± 0.02	16.26 ± 0.02	15.75 ± 0.01	15.27 ± 0.02
3	18.13 ± 0.04	18.24 ± 0.02	17.63 ± 0.01	17.20 ± 0.02	16.79 ± 0.02
4	18.02 ± 0.03	17.52 ± 0.02	16.61 ± 0.01	16.07 ± 0.02	15.54 ± 0.02
5	16.89 ± 0.03	16.81 ± 0.02	16.04 ± 0.01	15.56 ± 0.01	15.06 ± 0.02
6	18.79 ± 0.02	18.25 ± 0.03	17.38 ± 0.01	16.86 ± 0.01	16.38 ± 0.02
7	18.62 ± 0.04	17.76 ± 0.02	16.72 ± 0.01	16.08 ± 0.02	15.52 ± 0.02

presented in TABLE 4.2. The photometric observations log of 2017hpa is given in TABLE 4.3.

The spectroscopic monitoring of 2017hpa with HCT started on 2017 October 30 (JD 2458057.4) and continued till 2018 February 25 (JD 2458175.1). The data are reduced following the procedures described in **Section 2.3.3**. We remove the telluric features from the spectra by using the TELLURIC package in IRAF.

TABLE 4.3: Optical photometry of 2017hpa from HCT.

Date (y-m-d)	JD (2458000+)	Phase* (d)	U	B	V	R	I
2017-10-31	58.45	-7.8	15.68 ± 0.13	15.98 ± 0.03	15.95 ± 0.02	15.82 ± 0.02	15.75 ± 0.03
2017-11-01	59.43	-6.8	15.49 ± 0.15	15.77 ± 0.03	15.82 ± 0.02	15.69 ± 0.02	15.63 ± 0.02
2017-11-02	60.37	-5.9	15.37 ± 0.15	15.63 ± 0.06	15.75 ± 0.03	15.54 ± 0.03	15.52 ± 0.02
2017-11-09	67.19	0.9	15.26 ± 0.14	15.41 ± 0.02	15.39 ± 0.01	15.31 ± 0.02	15.43 ± 0.02
2017-11-10	68.21	2.0	15.36 ± 0.19	15.44 ± 0.03	15.40 ± 0.01	15.30 ± 0.01	15.45 ± 0.01
2017-11-15	73.27	7.0	15.69 ± 0.15	15.68 ± 0.03	15.39 ± 0.01	15.39 ± 0.01	15.61 ± 0.01
2017-11-19	77.43	11.1	—	16.04 ± 0.04	15.48 ± 0.01	15.63 ± 0.02	16.02 ± 0.04
2017-11-22	80.28	13.9	16.57 ± 0.09	16.36 ± 0.02	15.75 ± 0.01	15.79 ± 0.01	15.96 ± 0.02
2017-11-29	87.36	21.1	—	17.23 ± 0.02	16.26 ± 0.02	15.98 ± 0.01	15.83 ± 0.02
2017-12-17	105.24	38.9	—	18.38 ± 0.02	17.18 ± 0.02	16.74 ± 0.01	16.30 ± 0.02
2017-12-26	114.21	47.9	—	18.60 ± 0.03	17.48 ± 0.02	17.12 ± 0.01	16.76 ± 0.02
2017-12-29	117.24	50.9	—	18.62 ± 0.04	17.54 ± 0.02	17.20 ± 0.02	16.92 ± 0.02
2018-01-05	124.09	57.8	—	—	17.78 ± 0.02	17.48 ± 0.01	17.33 ± 0.03
2018-01-21	140.12	73.8	19.55 ± 0.25	19.02 ± 0.03	18.12 ± 0.03	17.94 ± 0.02	17.97 ± 0.03
2018-02-02	152.11	85.8	—	—	18.37 ± 0.02	18.25 ± 0.02	—
2018-02-03	153.14	86.9	19.95 ± 0.19	19.08 ± 0.07	18.40 ± 0.02	18.24 ± 0.03	18.26 ± 0.04
2018-02-09	159.27	93.0	—	—	18.58 ± 0.03	18.48 ± 0.02	18.63 ± 0.04

*Time since B -maximum (JD 2458066.3).

2017hpa was also observed with *Swift*-UVOT. The UVOT observations were made with broadband filters $uvw2$, $uvm2$, $uvw1$, and ubv starting from 2017 October 26 (JD 2458053.2) and continued till 2017 December 07 (JD 2458095.4). The SN was not detected in $uvw2$, and $uvm2$ with considerable signal-to-noise. The archived data for this object are downloaded from the *Swift* archive. The photometric observations log from *Swift*-UVOT is presented in TABLE 4.4.

4.1.2 Extinction and Distance Modulus

The dust map of [Schlafly & Finkbeiner \(2011\)](#) gives an $E(B-V) = 0.1518 \pm 0.0069$ along the direction of 2017hpa in the Milky Way (MW). The host galaxy reddening

TABLE 4.4: *Swift* UV-Optical photometry of 2017hpa.

Date (y-m-d)	JD (2458000+)	Phase* (d)	<i>uvw1</i>	<i>u</i>	<i>b</i>	<i>v</i>
2017-10-26	53.25	-13.05	18.37±0.16	17.59±0.10	17.09±0.05	16.63±0.06
2017-10-28	54.58	-11.72	18.35±0.24	16.91±0.12	16.74±0.07	16.49±0.12
2017-10-30	56.98	-9.32	18.09±0.23	16.35±0.09	16.38±0.07	16.17±0.11
2017-11-03	60.89	-5.41	17.00±0.10	15.38±0.04	15.62±0.04	15.66±0.06
2017-11-09	67.48	1.18	16.80±0.13	15.37±0.07	15.46±0.05	15.31±0.08
2017-11-11	69.26	2.97	17.11±0.15	15.46±0.05	—	15.38±0.09
2017-11-13	71.11	4.82	17.19±0.09	15.61±0.09	15.54±0.04	15.31±0.05
2017-11-15	73.32	7.02	17.33±0.19	15.82±0.08	15.70±0.06	15.36±0.09
2017-11-17	75.18	8.88	17.86±0.25	15.95±0.08	15.80±0.06	15.39±0.05
2017-11-23	81.08	14.78	17.97±0.16	16.77±0.09	16.39±0.05	15.81±0.08
2017-11-24	82.35	16.05	18.31±0.19	16.93±0.09	16.53±0.06	15.84±0.07
2017-11-27	85.27	18.97	18.59±0.21	17.32±0.12	16.91±0.07	16.01±0.07
2017-12-01	88.86	22.56	19.36±0.56	17.46±0.16	17.21±0.10	16.20±0.10
2017-12-07	95.43	29.13	—	18.99±0.45	17.65±0.11	16.48±0.10

*Time since *B*-maximum (JD 2458066.3).

can be estimated using various empirical relations.

Turatto et al. (2003) have shown that the reddening within the host is correlated with the equivalent width of Na I D. We do not detect Na I D absorption feature in our low-resolution spectra near maximum light at the redshift of the host galaxy. This indicates minimal reddening within the host. The Phillips-Lira relation uses the $(B - V)$ colour from 30 to 90 days since the *V*-max, and is used to estimate host reddening. After correcting the $(B - V)$ colour of 2017hpa for reddening in the Milky-Way it matches well with the colour predicted by Lira relation if shifted by a value of 0.08 ± 0.06 mag. After including the intrinsic dispersion of the Lira relation of ~ 0.05 mag in quadrature, the reddening estimated from the tail of the $(B - V)$ colour evolution $E(B - V)_{tail}$ is 0.08 ± 0.08 mag. Note the large scatter in the value due to the difference in the observed $(B - V)$ slope with Lira relation. Phillips et al. (1999) also used $B_{max} - V_{max}$ colour index to estimate $E(B - V)_{host}$. We estimate $E(B - V)_{max}$ to be 0.06 ± 0.05 mag. We take an

average of $E(B - V)_{\text{tail}}$ and $E(B - V)_{\text{max}}$ to get an estimate of $E(B - V)_{\text{host}}$ to be 0.07 ± 0.09 mag using the $(B - V)$ colours, a value not significantly different from zero.

We have used MLCS2k2[‡] to estimate the host reddening and distance modulus, and SALT2 to confirm it. We used the updated version of MLCS2k2 (Jha et al. 2007) in which the calibration was improved by using 133 SNe Ia for training and extending the model by incorporating U -band data. The observed LC in each passband X is expressed as follows,

$$m_{\vec{X}}(t - t_0) = \vec{M}_X^0 + \mu_0 + \vec{\zeta}_X(\alpha_X + \frac{\beta_X}{R_V})A_V^0 + \vec{P}_X\Delta + \vec{Q}_X\Delta^2, \quad (4.1)$$

where t_0 is the epoch of B -max, \vec{M}_X^0 is the absolute magnitude of a standard SN, μ_0 is the true distance modulus, A_V^0 , R_V are the host extinction parameters, \vec{P}_X , \vec{Q}_X are vector functions describing the light curve shape, and Δ is the light curve shape parameter. The arrow-marked quantities are given in the SN rest frame phase.

We fit our observed $UBVRI$ data with MLCS2k2 and kept the ratio of total-to-selective extinction R_V to be fixed at the Galactic value of 3.1. With this value of R_V we get an extinction A_V^0 of 0.25 ± 0.09 and μ of 33.99 ± 0.06 . Hicken et al. (2009) in a study of 185 SNe Ia in the CfA3 sample, indicate that the Galactic R_V leads to an overestimate of the host extinction, while R_V of 1.7 based on their MLCS2k2 fits provides a more realistic extinction estimate. Recent studies have also indicated a non-Milky Way extinction law for the hosts of SNe Ia. For example, an R_V of 1.7 was estimated for SN 2017cfd (Han et al. 2020), and an R_V of 2.0 was used for the host of SNe 2017cbv and 2013aa (Burns et al. 2020). Hence, we proceeded with the fit again, keeping R_V as a fit parameter, which resulted in a lower value of $R_V = 1.9$ for the host galaxy and the lowest χ^2 for the fit. The change in R_V has

[‡]<https://www.physics.rutgers.edu/~saurabh/mlcs2k2/>

a negligible effect on the distance when the extinction is low because, for such low reddening, it is not possible to disentangle the effect of R_V on the colour of the SN from the intrinsic colour differences between the observed SN and the template. FIGURE 4.3 shows the best-fit MLCS2k2 templates to the observed data. With this fit, we estimate a μ of 34.07 ± 0.06 mag and using [Fitzpatrick \(1999\)](#), the absolute magnitude in B is -19.45 ± 0.15 mag. The $E(B - V) = 0.08$ matches the value estimated based on the observed $(B - V)$ colours at maximum. We further fit the light curve with Spectral Adaptive Light Curve template (SALT2[§]), which models the spectral energy distribution as:

$$F_{\text{SN}}(p, \lambda) = x_0(M_0(p, \lambda) + x_1 M_1(p, \lambda)) \exp(c C_L(\lambda)), \quad (4.2)$$

The phase-dependent flux density in the rest-frame of the SN is F_{SN} , $p = t - t_0$ is the phase of the SN, x_0 , x_1 , and c are the normalisation, shape, and colour parameters respectively. M_0 , M_1 and C_L are the mean spectral sequence, first-order deviation around the mean sequence and time-independent colour law. These are the trained vectors of SALT2. We applied the SALT2 model ([Betoule et al. 2014](#)) with the Landolt-Bessell filter set and used the Vega magnitude system. We used only the observed $UBVRI$ data in the fit. The best-fit templates to the observed data are shown in FIGURE 4.4. SALT2 does not fit the distance as a parameter. We calculated the distance modulus using the following relation:

$$\mu_0 = m_B^* - M_B + \alpha x_1 - \beta c, \quad (4.3)$$

where, m_B^* , x_1 and c are the fit parameters from SALT2 and M_B , α and β are parameters for the distance estimate. We used the values of M_B , α and β from [Betoule et al. \(2014\)](#). The M_B parameter used in the calibration is valid for SNe, which exploded in galaxies having total stellar mass $M_{\text{stellar}} \leq 10^{10} M_{\odot}$. For a more massive host galaxy, a correction of -0.061 has to be added to M_B . As the value of H_0 adopted in MLCS2k2 and SALT2 is 65, and 68 km s⁻¹Mpc⁻¹, respectively

[§]<http://supernovae.in2p3.fr/salt/doku.php>

TABLE 4.5: Best-fit parameters of the light curve for 2017hpa.

Parameter	Value	Error	Parameter	Value	Error
MLCS2k2	<i>UBVRI</i>		SALT2.4	<i>UBVRI</i>	
R_V	1.9		T_{\max} (MJD)	58066.89	0.06
T_{\max} (MJD)	58066.29	0.11	c	-0.07	0.03
A_V^{host} (mag)	0.16	0.06	x_0	0.02	0.00
Δ (mag)	-0.17	0.03	x_1	0.19	0.07
μ_0 ($H_0=73$) (mag)	34.07	0.05	m_B^* (mag)	14.84	0.03
χ^2/dof	0.78		μ_0 ($H_0=73$) (mag)	34.09	0.08
			χ^2/dof	2.67	

we have converted them to $H_0 = 73 \text{ km s}^{-1} \text{Mpc}^{-1}$ using -

$$\mu_0(H_0) = \mu_0(\text{Model}) - 5 \log_{10}(H_0/H_0^{\text{Model}}) \text{ mag}, \quad (4.4)$$

where ‘‘Model’’ refers to MLCS2k2/SALT2. From SALT2 fit we get a μ of 34.09 ± 0.08 mag. The μ is 34.15 ± 0.08 for a host galaxy of stellar mass $\geq 10^{10} M_{\odot}$. The main parameters of both the model fits are listed in TABLE 4.5. Throughout the analysis, we used an $R_V = 3.1$ for the Milky Way and an $R_V = 1.9$ for the host galaxy obtained from MLCS2k2 fit. The $E(B - V)$ used for the host is 0.08 ± 0.06 mag. The μ of 34.08 ± 0.09 mag of the SN is obtained by averaging the values from SALT2 and MLCS2k2 fits, assuming the host galaxy stellar mass is $\leq 10^{10} M_{\odot}$.

4.1.3 Light Curve Analysis

The *UBVRI*, *uvw1*, *uvu*, *uvb*, and *uvv* light curves of 2017hpa are plotted in FIGURE 4.2. The light curve in *UBVRI* bands are fit with MLCS2k2 (Jha et al. 2007). The light curve parameters such as $\Delta m_{15}(B)$, time of maximum, and magnitude at maximum have been calculated from the model fit. The *B*-band peak magnitude is 15.48 ± 0.11 mag, and $\Delta m_{15}(B) = 0.98 \pm 0.15$ mag. The associated errors are observed error propagated with model error. The *I*-band LC shows a

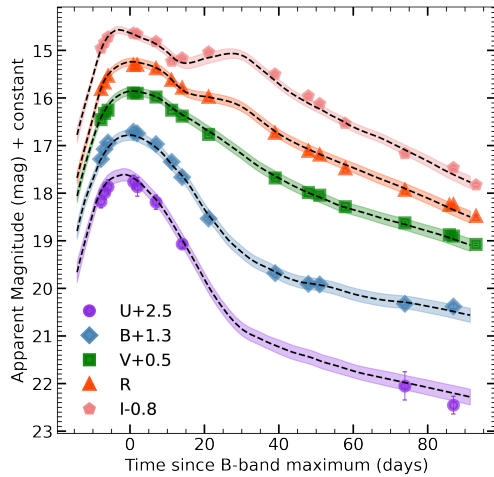


FIGURE 4.3: *UBVRI* light curve fit with MLCS2k2.

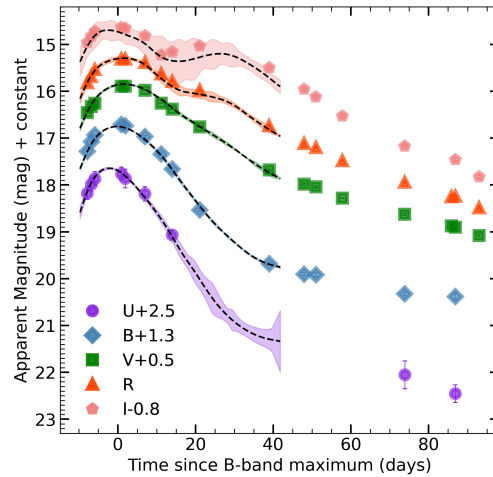


FIGURE 4.4: *UBVRI* light curve fit with SALT2.

distinct secondary peak characteristic of normal Ia. An increase is also seen in the *R*-band light curve around the same epoch. The maximum in the *U*, and *I* bands occurs at 2.03 d and 3.04 d before *B*-max, respectively, and that of *V* and *R* band occurs around ~ 1.02 day after *B*-band. The early occurrence of *I*-band maximum is consistent with some other SNe Ia (Phillips et al. 1999; Anupama et al. 2005). The appearance of *U*-band maximum before, and *V*, and *R* band maxima after the *B*-max is consistent with an expanding cooling atmosphere model (Contardo et al. 2000). However, the appearance of *I*-band maximum before *B* band is in sharp contrast to the simple thermal model.

The *I*-band secondary maximum occurred at +30.46 d after the *B*-max, with a magnitude 0.44 mag fainter than peak. The double-peaked nature is related to the ionisation evolution of Fe-group elements in the SN ejecta, (Kasen 2006). As the ejecta expands, it cools down, and at a temperature close to 7000 K, the NIR emission of Fe/Co increases, which marks the transition from doubly to singly ionised state. About 30 – 35 days since the explosion, the ejecta starts redistributing the high energy photons to longer wavelengths and the NIR emissivity increases. After the secondary peak, the ionization front from doubly to singly ionised Fe species recedes further into the ejecta, the emissivity decreases and the light curve

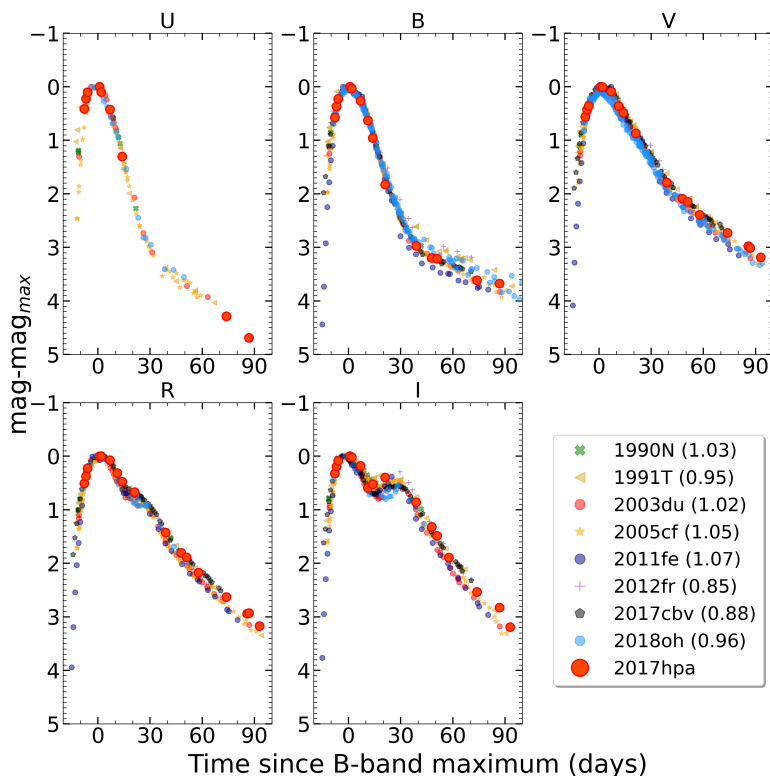


FIGURE 4.5: *UBVRI* light curves of 2017hpa compared with other normal Ia. The light curves are shifted so that their peak magnitudes matches. The phase is with respect to *B*-max.

declines monotonically.

In FIGURE 4.5, the *UBVRI* light curves of 2017hpa have been compared with other SNe Ia, like 1990N, 1991T (Lira et al. 1998), 2003du (Anupama et al. 2005; Stanishev et al. 2007), 2005cf, 2011fe (Vinkó et al. 2012), 2012fr (Zhang et al. 2014), 2017cbv (Wee et al. 2018), and 2018oh. It is evident from FIGURE 4.5, that the light curves of 2017hpa are similar to normal Ia. The decline rate around 30–80 days after *B*-max, has been calculated by a least-square fit, and it is given in units of $\text{mag} (100 \text{ d})^{-1}$. The decline rate in *B* and *I* are estimated as 2.03 ± 0.01 and 4.48 ± 0.01 , respectively.

The reddening corrected colours of 2017hpa are displayed in FIGURE 4.6 and compared with well-studied events. All the SNe have been corrected for the

TABLE 4.6: Photometric parameters of 2017hpa.

Filter	JD (Max)	m_{λ}^{\max}	M_{λ}^{\max}	$\Delta m_{15}(\lambda)$	Decline rate* (30–80 d)	Colours at B max
U	2458064.26	15.11 ± 0.13	-19.97 ± 0.18	1.26 ± 0.18	2.332 ± 0.005	–
B	2458066.29	15.48 ± 0.11	-19.45 ± 0.15	0.98 ± 0.16	2.026 ± 0.007	–
V	2458067.31	15.35 ± 0.09	-19.34 ± 0.13	0.59 ± 0.13	3.155 ± 0.005	$(B - V)_0 = -0.26 \pm 0.03$
R	2458067.31	15.24 ± 0.08	-19.31 ± 0.13	0.67 ± 0.12	3.605 ± 0.004	$(V - R)_0 = -0.02 \pm 0.01$
I	2458063.25	15.36 ± 0.07	-19.05 ± 0.13	0.62 ± 0.12	4.483 ± 0.005	$(R - I)_0 = -0.24 \pm 0.01$

*in unit of $\text{mag} (100 \text{ d})^{-1}$ and epoch is relative to B -max.

MW and host reddening, as mentioned in the respective studies. The reddening correction for SN 2017hpa is discussed in SECTION 4.1.2. The $(B - V)_{Bmax}$ is -0.26 ± 0.03 mag, which is bluer than the comparison SNe. The $(uvw1 - uvv)$ colour of 2017hpa is bluer, similar to other NUV-blue Ia (see FIGURE 4.6) and hence can be included in the NUV-blue category as defined by Milne et al. (2013). However, the $(uvw2 - uvv)$ colour evolution could not be verified. Studies of carbon-positive SNe in the past decade indicate bluer near UV colours (Milne et al. 2013) due to unburned carbon present during the pre-maximum phases. The presence of lower opacity elements in the outer layers (such as C) causes the photosphere to recede quickly in the ^{56}Ni -rich layers - thus the blue photons can come out without suffering much energy redistribution. The $(U - B)$ colour at maximum is slightly redder owing to the absorption by Ca H & K at shorter wavelengths. This trend has been observed in 2018oh (Li et al. 2019a). The $(V - R)$ colour at maximum is -0.02 ± 0.01 mag. The $(V - R)$ colour is redder than the comparison SNe around 10 to 20 d past the maximum, and it follows the same trend as other SNe in the late phase. The $(R - I)$ colour at maximum is -0.24 ± 0.01 mag. The important photometric parameters of 2017hpa are tabulated in TABLE 4.6.

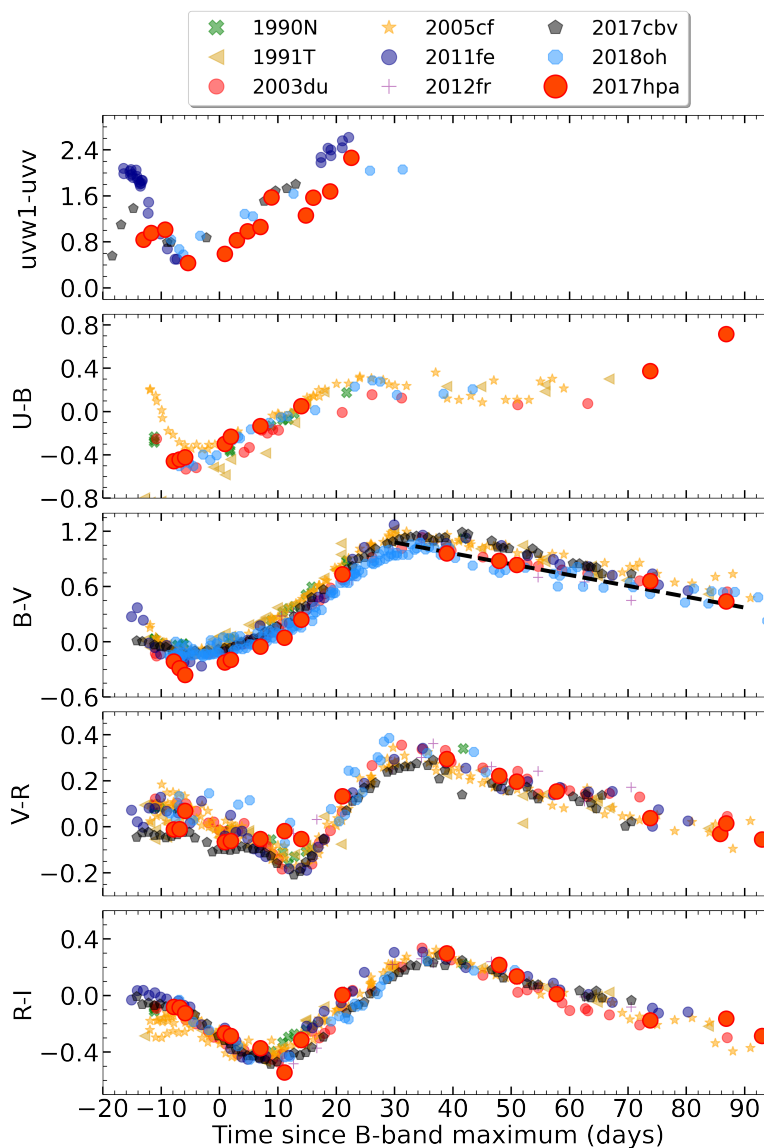


FIGURE 4.6: $uvw1 - uvv$, $U - B$, $B - V$, $V - R$, and $R - I$ colours of 2017hpa plotted along with some well studied SNe Ia. Plotted as black dotted line with $(B - V)$ colour is the Lira relation which has been used to find the host $E(B - V)$.

4.1.4 Estimation of Nickel Mass

The bolometric light curve (LC), constructed using the $UBVRI$ and $uvw1$ magnitudes, is shown in FIGURE 4.7. The apparent magnitudes are corrected for $E(B - V)_{MW}$ of 0.1518 ± 0.0069 with $R_V = 3.1$, and a host galaxy $E(B - V)$ of 0.08 ± 0.06 with $R_V = 1.9$. The reddening corrected magnitudes are transformed to flux using zero-points from TABLE 2.1. Magnitudes in $UBVRI$ have

been interpolated from the MLCS2k2 model light curve, and the *Swift*-UVOT bands are interpolated with a cubic spline. Then, the SED is constructed using the fluxes in *UBVRI*, and UVOT. A spline curve is fit to the SED, and the area under the curve is calculated by trapezoidal rule, integrating from 2500–9500 Å. The NIR (9500–24000 Å) flux contribution is estimated from Wang et al. (2009a) and added to the uv-optical flux. The total flux thus obtained is converted to luminosity, adopting a μ of 34.08 mag. The maximum of the bolometric LC for 2017hpa is $L_{\text{peak}}^{\text{bol}} = 1.43 \times 10^{43}$ erg s $^{-1}$. To estimate ^{56}Ni mass, M_{ej} and other parameters of the explosion, we applied EQUATION 3.5. To fit the model, we used the MCMC method described in SECTION 3.1.2. From the fit to the bolometric LC, we get rise time to maximum $t_{\text{exp}} = 16.93 \pm 0.23$ days, $t_{\text{lc}} = 13.38 \pm 0.47$ days, $t_{\gamma} = 41.4 \pm 0.8$ days, and $M_{\text{Ni}} = 0.61 \pm 0.02 M_{\odot}$. The M_{ej} and v_{exp} are related to the two timescale parameters t_{lc} and t_{γ} of the radiation model by

$$t_{\text{lc}}^2 = \frac{2\kappa M_{\text{ej}}}{\beta c v_{\text{exp}}} \quad \text{and} \quad t_{\gamma}^2 = \frac{3\kappa_{\gamma} M_{\text{ej}}}{4\pi v_{\text{exp}}^2}. \quad (4.5)$$

Here, κ is the effective optical opacity, $\kappa_{\gamma} = 0.03$ cm 2 g $^{-1}$ is the opacity for γ -rays (Clocchiatti & Wheeler 1997; Wheeler et al. 2015), and $\beta = 13.8$ is a constant of integration. These two equations can be used to constrain three parameters of the explosion, M_{ej} , v_{exp} and κ . Following Li et al. (2019a) and Könyves-Tóth et al. (2020), we can get a lower bound on κ assuming $M_{\text{ej}} \leq M_{\text{Ch}}$, while the upper limit on κ is obtained assuming v_{exp} has a lower limit of 9500 km s $^{-1}$, estimated from Si II $\lambda 6355$ near maximum light. The limits of $\kappa - \kappa_{\text{lower}} = 0.12 \pm 0.01$, and $\kappa_{\text{upper}} = 0.16 \pm 0.01$ cm 2 g $^{-1}$ are estimated to get an effective optical opacity of $\kappa = 0.14 \pm 0.01$. Finally, by using the equations

$$M_{\text{ej}} = \frac{3\kappa_{\gamma} t_{\text{lc}}^4 \beta^2 c^2}{16\pi t_{\gamma}^2 \kappa^2}; \quad v_{\text{exp}} = \frac{3\kappa_{\gamma} t_{\text{lc}}^2 \beta c}{8\pi \kappa t_{\gamma}^2} \quad \text{and} \quad E_{\text{kinetic}} = 0.3 M_{\text{ej}} v_{\text{exp}}^2, \quad (4.6)$$

we estimate $M_{\text{ej}} = 1.10 \pm 0.22 M_{\odot}$, $v_{\text{exp}} = 11\,060 \pm 1200$ km s $^{-1}$ and kinetic energy $E_{\text{kinetic}} = 0.80 \pm 0.23 \times 10^{51}$ erg.

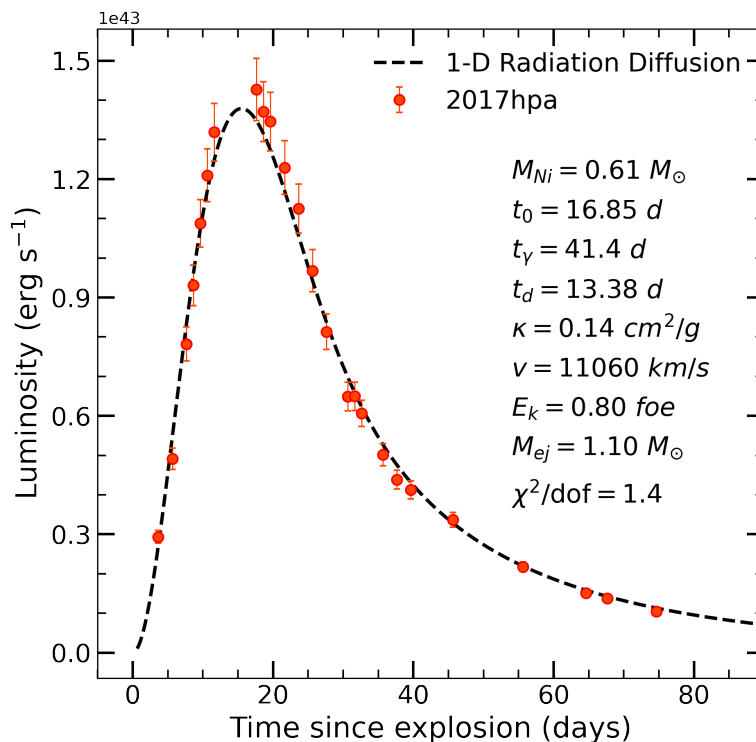


FIGURE 4.7: The bolometric luminosity of 2017hpa plotted with 1D Radiation Diffusion model.

4.1.5 Spectral Analysis

The spectra of 2017hpa were obtained from days -8.9 to $+108$ since the B -max. In our analysis, we have also used the earliest spectrum available for 2017hpa in WISEREP (Yaron & Gal-Yam 2012), taken at -13.8 d with the Asiago Faint Object Spectrograph and Camera (AFOSC). All spectra are corrected for a redshift of 0.015. The spectra are dereddened with $E(B - V)_{MW} = 0.15$ mag, and $E(B - V)_{host} = 0.08$ mag. The spectroscopic features have been identified by comparing with other SNe Ia around similar phases. The spectroscopic observations log is provided in TABLE 4.7

The pre-maximum spectra during -13.8 to -5.9 d are plotted in FIGURE 4.8. The spectra show blue continuum with prominent absorption of Ca II H & K $\lambda\lambda 3934, 3968$, Fe III, Mg II, Si III, Si II $\lambda 6355$. The absorption feature of Ca II NIR triplet

TABLE 4.7: Spectroscopic observations log of 2017hpa from HCT.

Date (y-m-d)	JD (2458000+)	Phase* (d)	Range (Å)
2017-10-30	57.43	-8.9	3500-7800; 5200-9100
2017-10-31	58.46	-7.8	3500-7800; 5200-9100
2017-11-01	59.47	-6.7	3500-7800
2017-11-02	60.39	-5.9	3500-7800; 5200-9100
2017-11-09	67.22	0.9	3500-7800; 5200-9100
2017-11-10	68.23	1.9	3500-7800; 5200-9100
2017-11-19	77.36	11.1	3500-7800; 5200-9100
2017-11-22	80.30	14.1	3500-7800; 5200-9100
2017-11-29	87.23	20.9	3500-7800; 5200-9100
2017-12-01	89.31	23.1	3500-7800; 5200-9100
2017-12-05	93.19	26.9	3500-7800; 5200-9100
2017-12-17	105.26	39.0	3500-7800; 5200-9100
2017-12-26	114.24	47.9	3500-7800; 5200-9100
2017-12-29	117.25	51.0	3500-7800; 5200-9100
2018-01-05	124.13	57.9	3500-7800; 5200-9100
2018-01-21	140.22	73.9	3500-7800; 5200-9100
2018-01-30	149.17	82.9	3500-7800; 5100-9100
2018-02-03	153.07	86.8	3500-7800
2018-02-09	159.14	92.8	3500-7800; 5200-9100
2018-02-13	163.13	96.8	3500-7800
2018-02-20	170.07	103.8	3500-7800
2018-02-25	175.06	108.8	3500-7800

*Time since *B*-maximum (JD 2458066.3).

slowly starts developing. As the SN evolves, the above lines become stronger, and the lines due to the Fe-group start appearing in the spectra. In the pre-max phase, Si II $\lambda 6355$ absorption profile is broad and asymmetric with respect to line minimum. This is due to a high-velocity (HV) component in the spectra. The HV feature is usually seen in the Ca II NIR triplet in a significant fraction of SNe Ia observed during the pre-maximum phase (Maguire et al. 2014; Mulligan & Wheeler 2017). In the emission part of Si II $\lambda 6355$ at ~ 6300 Å a prominent absorption feature is seen which is due to blueshifted C II $\lambda 6580$ absorption. This is due to the presence of unburned C in the ejecta.

The spectrum at -13.8 d shows weak blended features of Fe II $\lambda 4924$, 5018 , Fe III $\lambda 4421$, 5075 , 5158 , Co II $\lambda 4161$, Mg II $\lambda 4481$, 7890 , S II $\lambda 4716$, 5032 , 5321 , 5429 , 5454 , 5510 , Si II $\lambda 4128$, 5972 , 6355 , Si III $\lambda 4568$, which become prominent around the maximum. Also, Si II $\lambda 5972$ starts appearing at -6 d. Weak Si II $\lambda 5972$, and strong Si II $\lambda 6355$ indicate that the photosphere is hot.

The pre-maximum spectrum (-8.9 d) of 2017hpa is compared with those of SNe 2003du (Blondin et al. 2012), 2005cf (Garavini et al. 2007), 2009dc (Taubenberger et al. 2011), 2011fe (Zhang et al. 2016). Among these events, 2003du, 2005cf and 2011fe are normal SNe Ia, whereas 2009dc belongs to the super- M_{ch} category. All the compared spectra (bottom panel of FIGURE 4.8) exhibit C II $\lambda 6580$ absorption feature during this phase. However, the C II $\lambda 6580$ feature is prominent than normal Ia, and similar to 2009dc. By fitting a Gaussian to the absorption feature of C II $\lambda 6580$, we estimate that the pEW of C II evolves from 13.56 ± 1.49 Å at -13.8 d to 4.49 ± 0.43 Å at -5.9 d. The Si II $\lambda 5972$ line is weaker than other objects at this phase. The IME signatures are weak in 2017hpa while these are prominent in other objects (see bottom panel of FIGURE 4.8). The relatively weak IME features suggest ongoing burning (Taubenberger et al. 2011). The line formation depends on the composition as well as on the ionisation state of the ejecta. The weakness of the singly ionised IME features can also be explained by higher temperature and, in turn, higher ionisation.

The flat-bottom, broad profile of Si II $\lambda 6355$ (at -13.8 d, -8.9 d and -7.8 d) and the asymmetric profile (at -6.8 d and -5.9 d) is most likely due to a high-velocity (HV) component detached from the photosphere. An HV component in Si II has been observed in other well-studied SNe Ia like 1990N (Mazzali 2001), 2003du (Anupama et al. 2005), 2005cf (Wang et al. 2009a), 2009ig (Foley et al. 2012; Marion et al. 2013), 2012fr (Childress et al. 2013), 2019ein (Kawabata et al. 2020; Pellegrino et al. 2020). The HV components in the absorption features can arise due to multiple reasons. There could be an increase in density/abundance

in the outer layers (Mazzali et al. 2005), interaction of the outer ejecta with the CSM (Gerardy et al. 2004), or an asymmetric explosion (Maeda et al. 2010).

By fitting a Gaussian to the absorption profile of Si II $\lambda 6355$ and $\lambda 5972$ at -5.9 d we estimate the pEW of Si II $\lambda 5972$ to be 13.75 ± 1.70 Å and that of Si II $\lambda 6355$ to be 67.22 ± 4.88 Å, implying a ratio $R(\text{Si II})$ of 0.20 ± 0.03 . At $+0.9$ d the pEW of Si II $\lambda 5972$ is 9.22 ± 1.02 Å, that of $\lambda 6355$ is 75.16 ± 1.96 Å, and $R(\text{Si II})$ is 0.13 ± 0.02 . From the value of $R(\text{Si II})$, 2017hpa can be placed among the Core-Normal (CN) SNe. Refer to SECTION 1.4, and FIGURE 4.13.

4.1.5.1 Maximum to early post-maximum phase

The spectral evolution during maximum and early post-maximum epochs are presented in FIGURE 4.9. The C II $\lambda 6580$ line observed pre-maximum is not present in the spectrum close to the maximum. Around this phase, the IME features have become prominent. The ‘W’ feature due to S II $\lambda 5468, 5654$ line is prominent in the maximum spectrum, and it becomes weak in the spectrum taken at $+11$ d. The high-velocity (HV) feature in the Si II $\lambda 6355$ absorption seen in the pre-max phase disappears near maximum, and the photospheric component is dominant. Because of the HV feature in the Ca II NIR, the absorption feature shows two minima till $+2$ d and is not seen in the next spectrum at $+11$ d. The Si III $\lambda 4568$ line was seen in the spectrum till $+2$ d but was not present in the later spectra. The spectrum of 2017hpa near maximum is compared with the spectra of a few well-studied SNe Ia (see bottom panel of FIGURE 4.9) and is found to be similar.

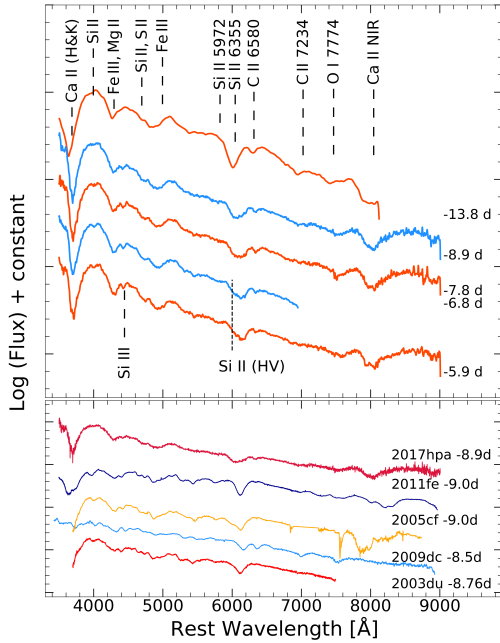


FIGURE 4.8: Top panel: Spectral evolution of 2017hpa at pre-maximum phases. Bottom panel: The -8.9 d spectrum of 2017hpa compared with 2011fe, 2009dc, 2005cf, and 2003du around similar phases.

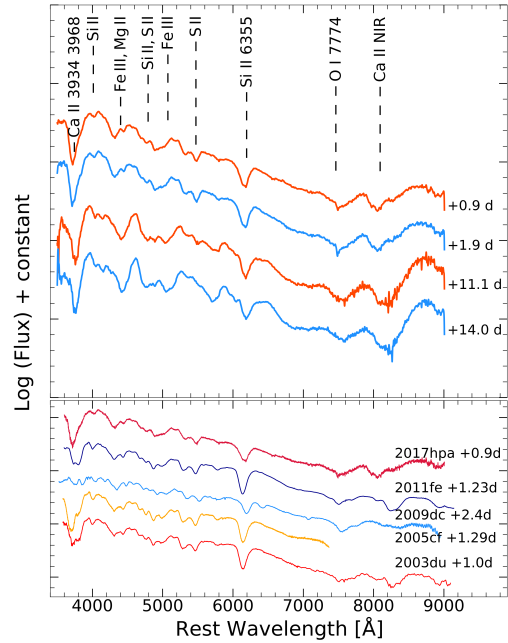


FIGURE 4.9: Top panel: Spectral evolution of 2017hpa around maximum – early post-max. Bottom panel: The $+0.9$ d spectrum of 2017hpa compared with 2011fe, 2009dc, 2005cf, and 2003du around maximum.

4.1.5.2 Post-maximum to early nebular phase

The spectral evolution of 2017hpa from post-max to early nebular phases are presented in FIGURE 4.10, and FIGURE 4.11. The Si II line is weakening, and Fe II $\lambda 6238$, 6248 lines are getting stronger (FIGURE 4.10). The pEW of Si II $\lambda 6355$ evolves from 75.16 ± 1.96 at $+0.9$ d to 57.04 ± 1.38 at $+14.0$ d. This weakening of the Si II indicates that the ejecta is diluting and the SN enters into an Fe II dominated phase. Further, the Ca II H & K feature begins to weaken around $+23$ day. In contrast, the Ca II NIR remains as a broad, absorption profile with an emission component until $+57$ day.

During the late post-maximum phase to the early nebular phase, the ejecta begins to get transparent, and the inner regions of the explosion can be probed. The

Fe II absorption feature at $\lambda 4555$ remains prominent, and the Fe II lines at $\lambda 4924$ and $\lambda 5018$ are clearly seen till +58.0 d. The Fe II line at $\lambda 5169$ shows a deep absorption feature at 5100 \AA , and to the redward wing, the Fe II $\lambda 5536$ is seen as a prominent notch. Around 6000 \AA there are blended lines of Fe II $\lambda 6238$, $\lambda 6248$ and $\lambda 6451$, $\lambda 6456$. Fe II lines at $\lambda 7462$ and $\lambda 7308$ are weak. In the bottom panel of FIGURE 4.10, the +39.0 day spectra of 2017hpa has been plotted with SNe 2014J (Srivastav et al. 2016), 2009dc, 2005cf, 2003du, and 2002bo around similar phases.

The ejecta expands and the temperature decreases as the SN ages. Forbidden emission lines are seen due to low density in the ejecta, marking the SN evolution into nebular phase. The spectrum at +74 d shows strong forbidden emission due to Fe and Co. Early nebular phase spectra show features of [Fe III], [Fe II], [Ni II], [Co III]. The emission near 4700 \AA is the strongest feature in the nebular spectra. This is a blend of [Fe III] with [Fe II]. The emission line around 5100 \AA in our early nebular spectra has contributions from [Fe II] and [Fe III] lines. In the very early nebular spectra, the [Co III] emission line at around 5900 \AA is quite strong, but with SN evolution, the [Co III] lines gets weaker from ^{56}Co decaying to ^{56}Fe . In the bottom panel of FIGURE 4.11, the +86.8 d spectrum of 2017hpa has been compared with SNe 2014J, 2005cf and 2003du. The [Fe II] emission feature around 4700 \AA at +86.8 d is stronger in the spectrum of 2017hpa than the comparison SNe.

4.1.5.3 Velocity Evolution

The line velocities are measured by fitting a single Gaussian function to the absorption features. The velocities of Ca II (H & K) $\lambda 3951$, Si II $\lambda 6355$, C II $\lambda 6580$ lines estimated based on the absorption minimum are plotted in FIGURE 4.12 (left panel). The unblended, prominent feature of Si II $\lambda 6355$ in optical, traces the evolution of the expansion velocity of the ejecta for over 3–4 weeks since the

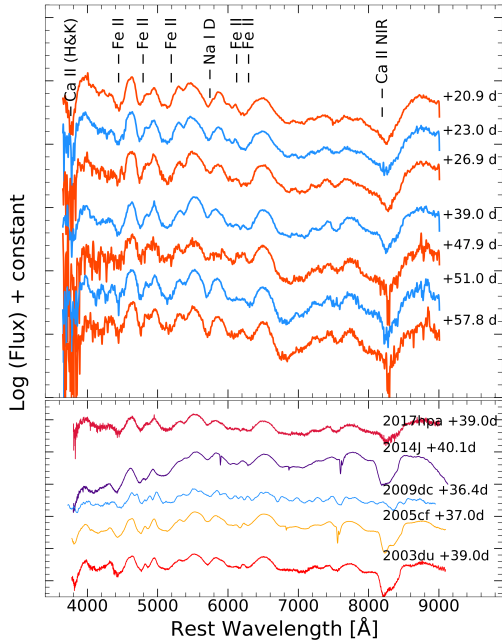


FIGURE 4.10: Top panel: Post maximum spectral evolution of 2017hpa. Bottom panel: The +39.0 d spectrum of 2017hpa compared with the spectra of 2014J, 2009dc, 2005cf, 2003du around similar phase.

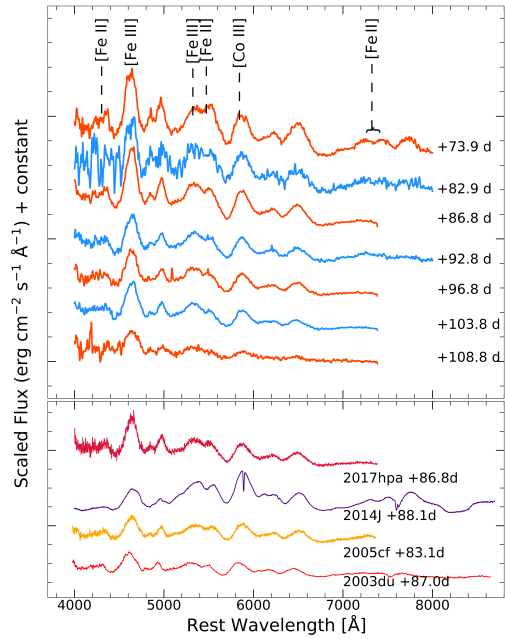


FIGURE 4.11: Top panel: Spectral evolution of 2017hpa in the early nebular phase. Bottom panel: The +86.8 d spectrum of 2017hpa compared with the spectra of 2014J, 2005cf and 2003du around similar phase.

explosion. The Si II line has a velocity of $16\,150 \pm 160 \text{ km s}^{-1}$ around -13 d , which is quite normal for type Ia SNe around this phase. The Si II velocity drops rapidly to $9400 \pm 140 \text{ km s}^{-1}$ close to maximum. The subsequent decline is slow, reaching a velocity of $\sim 8000 \text{ km s}^{-1}$ at $+15 \text{ d}$.

The C II $\lambda 6580$ absorption feature evolves from $12\,720 \pm 220$ to $10\,670 \pm 180 \text{ km s}^{-1}$ (left of FIGURE 4.12). The measured C II $\lambda 6580$ velocity is significantly lower than Si II $\lambda 6355$, with the $v_{\text{C II}}/v_{\text{Si II}}$ ratio varying from ~ 0.78 on day -13.8 to ~ 0.91 on day -5.9 . This variation in the velocity ratio is dissimilar with the results of Parrent et al. (2011), who have shown the ratio to be constant over time, in a sample of 19 SNe Ia. Their sample also indicates the ratio to be ~ 1 within 10%. The discrepancy between the carbon and the photospheric (Si II $\lambda 6355$) velocity is explained by Foley et al. (2010b), Parrent et al. (2011) as being due to a clumpy

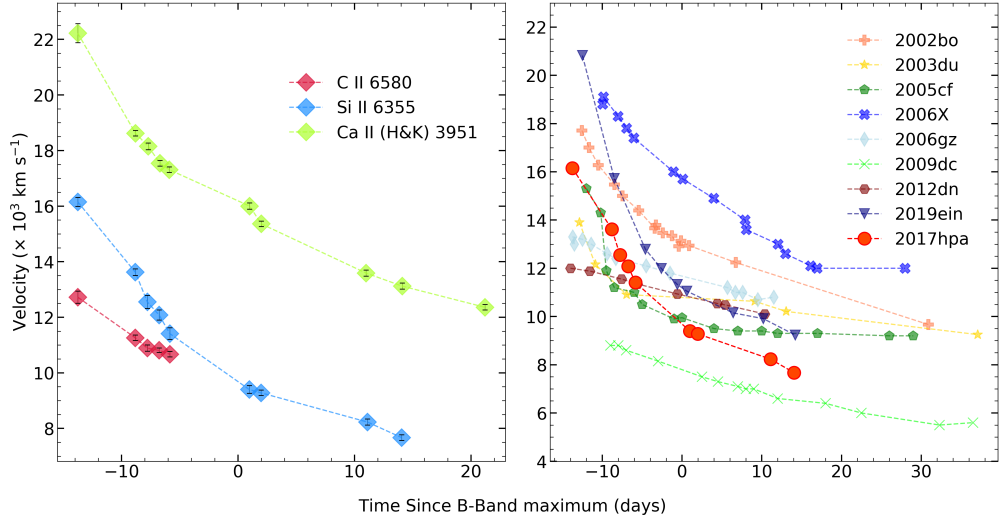


FIGURE 4.12: Velocity evolution of C II $\lambda 6580$, Si II $\lambda 6355$ and Ca II $\lambda 3951$ for 2017hpa (left panel). Comparison of the velocity evolution of Si II $\lambda 6355$ for 2017hpa with other Ia (right panel).

carbon layer that is offset by an angle θ from the line of sight. The angle can be estimated if $v_{\text{C II}} < v_{\text{Si II}}$. The observed velocity ratios indicate θ to be $\sim 40^\circ$ on day -13.8 and $\sim 25^\circ$ on day -5.9 . It is suggested that the change in the ratio (and angle from the line of sight) is indicative of an initial asymmetry that became more symmetric as the SN evolved to the maximum, or a clumpiness that became more homogeneous as the SN ejecta evolved. Another possible explanation for the lower velocity ratio is mixing within the ejecta. Various explosion mechanisms in 3D suggest mixing of unburned elements (Pakmor et al. 2012). The Ca II (H & K) $\lambda 3951$ feature has velocity of $\sim 22000 \text{ km s}^{-1}$ at -13.8 d and always remains higher than Si II $\lambda 6355$.

Benetti et al. (2005) made a cluster analysis based on both photometric ($\Delta m_{15}(B)$, M_B) and spectroscopic ($R(\text{Si II})_{\text{max}}$, \dot{v} , $v_{10}(\text{Si II})$) parameters. Refer to SECTION 1.4 for the classification. The velocity of Si II, 10 days past maximum, is denoted as v_{10} .

From the velocity evolution of 2017hpa, values of \dot{v} , v_{10} and velocity at maximum are estimated as $127.9 \pm 6.1 \text{ km s}^{-1} \text{ d}^{-1}$, ~ 8320 , and $\sim 9640 \text{ km s}^{-1}$, respectively.

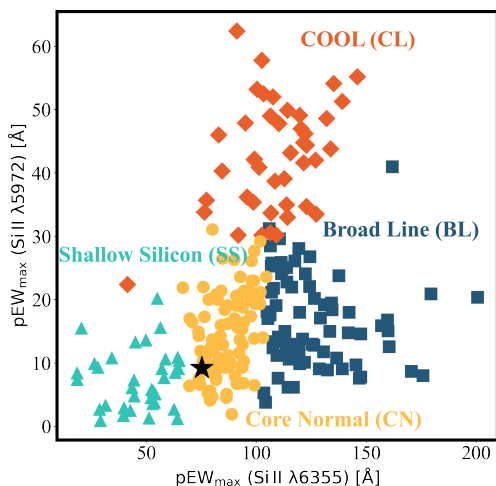


FIGURE 4.13: 2017hpa plotted along with core-normal, cool, shallow-silicon, and faint classes.

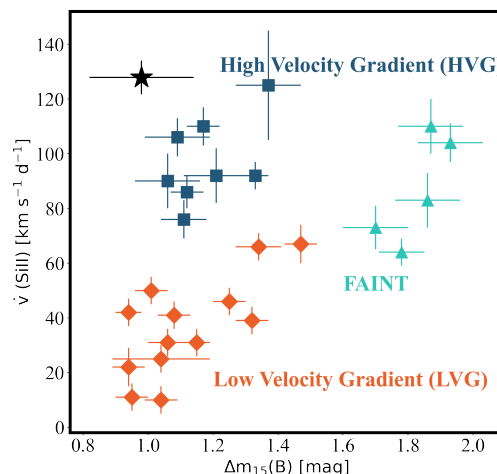


FIGURE 4.14: 2017hpa plotted along with HVG, LVG, and Faint. 2017hpa is plotted with a black star.

With the measured value of \dot{v} , 2017hpa can be placed under the HVG group of [Benetti et al. \(2005\)](#) scheme FIGURE 4.14. It is worth mentioning that the average value of v_{10} for the HVG group is $12\,200 \pm 1100 \text{ km s}^{-1}$ which is significantly higher than v_{10} estimated for 2017hpa ($\sim 8320 \text{ km s}^{-1}$). Based on the photometric and spectroscopic properties, 2017hpa can be placed under normal Ia with HVG.

The Si II $\lambda 6355$ line velocity evolution is plotted along with high-velocity gradient and normal SNe (FIGURE 4.12, right panel). The post-maximum velocity evolution for SN 2003du, and SN 2005cf is flat. From the velocity evolution, sometimes the channel of explosion can be inferred.

[Foley et al. \(2011\)](#) used a linear fit between $-6 \leq t \leq 10 \text{ d}$. The slope gives the velocity gradient, and the offset (v^0) is the velocity at B -max. Using this relation, the velocity gradient is $306.9 \pm 25.1 \text{ km s}^{-1}\text{d}^{-1}$ and $v^0 \sim 9870 \text{ km s}^{-1}$. Using the expansion velocity of Si II $\lambda 6355$ at maximum, 2017hpa falls in the normal velocity group ([Wang et al. 2009b](#)). Thus, 2017hpa has normal velocity with a high-velocity gradient.

4.1.6 Spectral Fitting in the pre-maximum phase

The spectral features in the pre-maximum phases at -13.8 day and -8.9 day are identified using synthetic spectra generated with `syn++` code. The spectrum at -13.8 day is fit with a blackbody temperature (T_{BB}) of 10 000 K, and photospheric velocity (v_{phot}) of $\sim 15\,000$ km s $^{-1}$. The temperature is consistent with that obtained by a blackbody fit to the photometric SED. The spectrum is fit with ions of IMEs like C II, Mg II, Si II (PV & HV), Ca II (PV & HV) and IGEs like Fe II and Fe III. An excitation temperature of 10 000 K and maximum velocity of 30 000 km s $^{-1}$ have been used for all the ions. To fit the Si II $\lambda 6355$ line profile in the observed spectrum, a high velocity component at 22 000 km s $^{-1}$ has been introduced. From the fit to the spectrum, it is found that both C II $\lambda 6580$, and Si II $\lambda 6355$ features can be reproduced with a photospheric velocity of 15 000 km s $^{-1}$. This indicates that the line forming region of Si II and C II are moving at the same velocity. Two components are required also for Ca II (H & K) - one at 17 000 km s $^{-1}$, and another high-velocity component at 25 000 km s $^{-1}$.

The spectrum at -8.9 d is fit with a $v_{\text{phot}} = 13\,800$ km s $^{-1}$ and $T_{\text{BB}} = 11\,000$ K. In this phase also, the observed Si II $\lambda 6355$ feature can be reproduced by a combination of the photospheric and high velocity component at 18 000 km s $^{-1}$. The C II feature is fit with a velocity of 13 800 km s $^{-1}$, similar to Si II photospheric component. Si III ($\lambda 4553, 4568, 4575$) features are well reproduced with the v_{phot} of 13 800 km s $^{-1}$. The spectral fits are shown in FIGURE 4.15.

Most prominent features in the pre-max spectra of 2017hpa are reproduced in the `syn++` synthetic spectra. We note that certain components will require careful fitting in an iterative way. TABLE 4.8 gives the details of the fit.

To study the explosion mechanism and to put a constraint on the mass of unburned C present in the ejecta, we applied TARDIS (Kerzendorf & Sim 2014) to

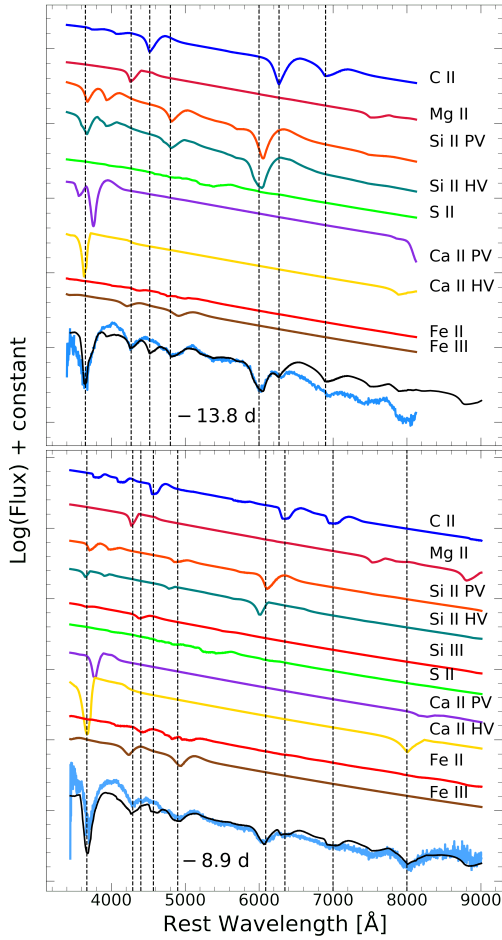


FIGURE 4.15: Dereddened and redshift corrected spectra of 2017hpa at -13.8 d and -8.9 d. The synthetic spectra generated using `syn++` are plotted (black solid line). The contributions from each element are shown.

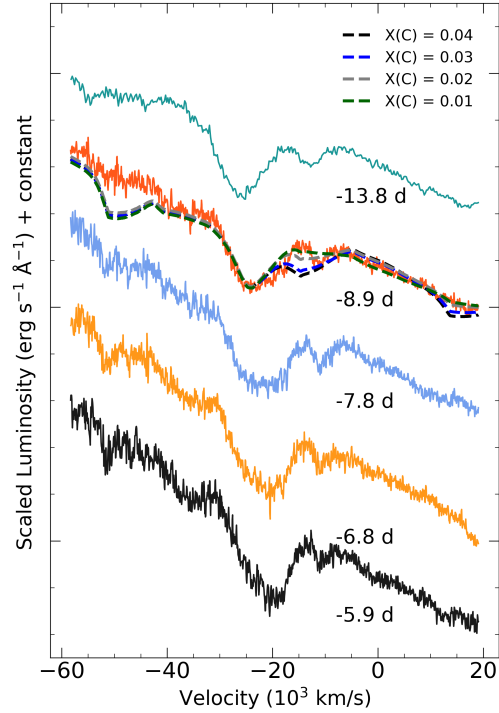


FIGURE 4.16: Velocity evolution of C II $\lambda 6580$. The velocity is calculated with respect to rest wavelength of C II $\lambda 6580$. The dotted solid lines indicate TARDIS fit to the observed spectra with different mass fraction for Carbon.

our spectrum at -8.9 d (See also CHAPTER 3, SECTION 3.2.2). The fit parameters of TARDIS are listed in TABLE 4.9. The spectrum is modelled using a uniform abundance of elements, and a density profile similar to W7 ($\rho \sim v^{-7}$, Branch et al. 1985). The observed spectrum does not have prominent lines due to IGEs; hence we consider only C, O, Mg, Si and Ca for generating the model spectrum.

By using a uniform composition in all the cells, a satisfactory fit to the observed spectrum was not possible in the entire wavelength range. Since we observe strong

TABLE 4.8: **syn++** fit to the pre-maximum spectra of 2017hpa.

Phase: -13.8 d v_{phot} : 15 000 km s $^{-1}$ v_{max} : 30 000 km s $^{-1}$ T_{BB} : 10 000 K									
Parameters	C II	Mg II	Si II _{PV}	Si II _{HV}	S II	Ca II _{PV}	Ca II _{HV}	Fe II	Fe III
log (tau)	-0.5	0.5	0.9	1.5	0.2	1.0	2.3	1.0	-0.8
v_{min} ($\times 10^3$) km s $^{-1}$	15.0	16.0	15.0	22.0	15.0	17.0	25.0	17.0	15.0
aux ($\times 10^3$) km s $^{-1}$	2.1	1.8	2.6	2.45	1.0	2.0	2.7	0.8	3.2
T_{exc} ($\times 10^3$) K	10	10	10	10	10	10	10	10	10

Phase: -8.9 d v_{phot} : 13 800 v_{max} : 30 000 T_{BB} : 11 000										
Parameters	C II	Mg II	Si II _{PV}	Si II _{HV}	Si III	S II	Ca II _{PV}	Ca II _{HV}	Fe II	Fe III
log (tau)	0.2	0.2	0.03	0.5	-0.6	-0.8	0.5	1.5	-0.5	-0.5
v_{min}	13.8	15.0	13.8	18.0	13.8	13.8	14.0	20.0	13.8	13.8
aux	0.4	1.7	3.5	2.5	2.5	0.8	2.0	4.0	1.0	3.0
T_{exc}	10	10	10	10	10	10	10	10	10	10

TABLE 4.9: **TARDIS** fit to the pre-maximum spectra of 2017hpa.

Phase*: -8.9 d t_{exp}^* : 8.0 day v_{inner}^* : 14 000 km s $^{-1}$ v_{outer} : 30 000 km s $^{-1}$ Luminosity ($\log L_{\odot}$): 9.45					
Elements	C	O	Mg	Si	Ca
Abundances	0.03	0.29	0.10	0.50	0.08

*Time since B-maximum (JD 2458066.3).

*Time since explosion (JD 2458049.41).

*velocity at the inner boundary of the photosphere.

C feature in the pre-maximum spectra around $\lambda 6580$, we tried to constrain the mass of unburned C. The region around Si II, and C II was fit by varying the mass fraction of C $[X(\text{C})]$ from 0.01 to 0.04, the mass fraction of O from 0.31 to 0.28, and keeping the mass fraction of other elements same (FIGURE 4.16). It is found that for $X(\text{C})$ more than 0.03, the C II line blends with Si II, hence we put an upper limit to $X(\text{C})$ as 0.03. By integrating the contribution from all cells, we find $\sim 0.019 M_{\odot}$ of C in the ejecta above 14 000 km s $^{-1}$. The estimated carbon mass is lower than the deflagration model W7 ($0.049 M_{\odot}$). This could be due to mixing of C in the ejecta or an asymmetric explosion.

4.1.7 Summary

The properties of 2017hpa make it an interesting object. From the photometric and spectroscopic properties, it can be classified as a normal Ia with $\Delta m_{15}(B) = 0.98 \pm 0.16$ and $M_B^{\max} = -19.45 \pm 0.15$ with a distinct secondary maximum in I -band. With standard light curve fitting methods like SALT2, and MLCS2k2 the μ is estimated to be 34.08 ± 0.09 with a host reddening of $E(B - V) = 0.08$ and an R_V of 1.9. The $(B - V)$ colour is bluer than the comparison SNe, and from the $(uvw1 - uvv)$ colour evolution, 2017hpa can be placed under NUV-blue group. Fitting the bolometric LC with Arnett's model, we derive M_{Ni} of $0.61 M_{\odot}$ and ejecta mass of $1.10 M_{\odot}$.

The pre-maximum spectral sequence of 2017hpa shows a relatively featureless continuum. The spectral evolution shows strong C II $\lambda 6580$ line, which can be seen until 5.9 days before the maximum. The observed C II velocity is lower than Si II $\lambda 6355$. However, `syn++` fit to the observed spectra shows that both the C II and Si II line-forming regions have the same photospheric velocity. The Si II $\lambda 6355$ shows rapid evolution in velocity, and the velocity gradient measured is $127.9 \pm 6.1 \text{ km s}^{-1} \text{ d}^{-1}$ which places 2017hpa along with the HVG objects according to the Benetti scheme. The velocity measured at the maximum is $\sim 9643 \text{ km s}^{-1}$, within the range for normal velocity SNe Ia. Typically, C II is associated with the LVG group. This is because for HVG, the Si II feature may blend with C II. [Maeda et al. \(2010\)](#) gave an explanation for LVG objects with presence of C as due to an explosion where we see the deflagration side of an off-center detonation. At maximum, the $(B - V)$ colour is redder for the HVG subtype ([Wang et al. 2009b](#)). The observed properties of 2017hpa are strikingly opposite to this. `Tardis` model fit to our spectrum requires unburned C mass to be $\sim 0.019 M_{\odot}$, lower than that expected by deflagration alone, indicating either C mixing in the ejecta or an asymmetric explosion. Detailed 3D modelling may confirm the exact nature of the explosion mechanism for 2017hpa.

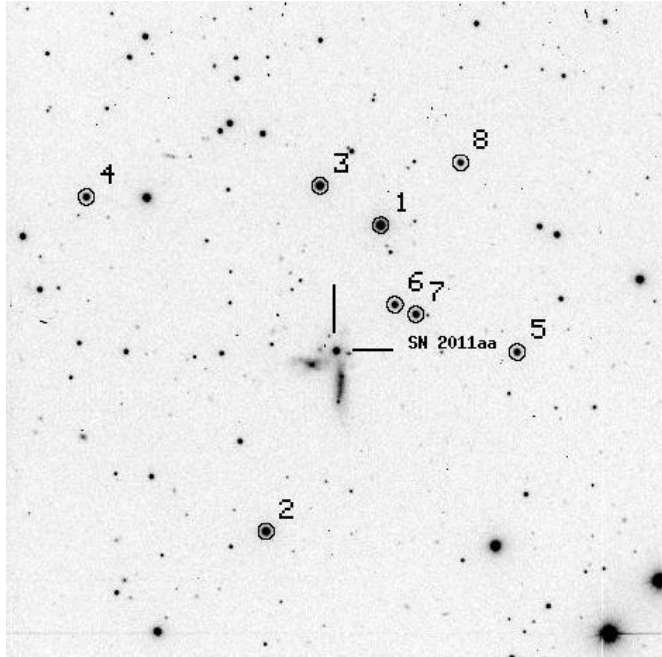


FIGURE 4.17: Identification plot for 2011aa. The local calibration stars are marked with numbers 1-8. East to the right and South is up. The field of view is $10' \times 10'$.

4.2 SN 2011aa: the slowest declining Type Ia supernova

4.2.1 Introduction

We present optical observations, radiative transfer modelling of the spectra, and light curves of a peculiar Type Ia SN 2011aa. 2011aa was discovered on 2011, February 6.3 in the galaxy UGC 3906 (PGC 021381) at α (J2000) = $07^h36^m42^s.63$ and δ (J2000) = $+74^\circ26'34''.80$ (Puckett et al. 2011). There is another nearby galaxy PGC 021386, with a similar radial velocity as PGC 021381, making it a galaxy pair, with the SN located in between the two galaxies (FIGURE 4.17). Gurugubelli et al. (2011) classified it as Type Ia. The *Swift*-UV observations of 2011aa are presented in Brown et al. (2014). The JHK_s photometry of 2011aa are catalogued in Friedman et al. (2015).

TABLE 4.10: Magnitudes of the secondary standards for the calibration of 2011aa. The ID is as shown in FIGURE 4.17

ID	U	B	V	R	I
1	14.595±0.003	14.441±0.013	13.828±0.011	13.462±0.007	13.088±0.017
2	14.493±0.018	14.568±0.024	14.127±0.001	13.820±0.001	13.503±0.006
3	16.143±0.014	15.350±0.008	14.449±0.006	13.951±0.008	13.466±0.019
4	15.579±0.007	15.565±0.017	14.973±0.006	14.600±0.014	14.185±0.009
5	15.902±0.021	15.758±0.021	15.142±0.006	14.747±0.004	14.388±0.005
6	15.820±0.007	15.808±0.012	15.230±0.010	14.866±0.009	14.493±0.010
7	16.161±0.013	15.781±0.004	15.056±0.014	14.621±0.007	14.211±0.017
8	15.703±0.003	15.814±0.024	15.366±0.007	15.064±0.002	14.739±0.017

SN 2011aa was observed in imaging and spectroscopic mode with the HCT. Photometric monitoring of 2011aa began on 2011 February 08 (JD 2455601.33) and continued till 2011 June 27 (JD 2455740.13). Spectroscopic observations of 2011aa were carried out from 2011 February 08 (JD 2455601.36) to 2011 April 29 (JD 2455681.18). The photometric log of the secondary stars is provided in TABLE 4.10. The photometric log of 2011aa with HCT is presented in TABLE 4.11. The images were obtained in Bessell $UBVRI$ filters, and the spectra using Gr7, and Gr8 with HFOSC. Magnitudes are estimated using PSF photometry. The UVOT on *Swift* observed 2011aa in three broadband optical filters u , b and v and three UV filters $uvw2$, $uvm2$ and $uvw1$, from ~ -8 d to $\sim +45$ d with respect to B -max. The UVOT photometric log is given in TABLE 4.12.

4.2.2 Light Curve Analysis

The light curves of 2011aa in Bessell $UBVRI$, *Swift*-UVOT $uvw2$, $uvm2$, $uvw1$, u , b , v bands and J , H , K bands are plotted in FIGURE 4.18. The date of maximum, maximum magnitude, and decline rate are estimated by performing Gaussian process regression (Rasmussen & Williams 2006) with Matern kernel on the light curves. The errors are the standard deviation of 1000 such iterations. The

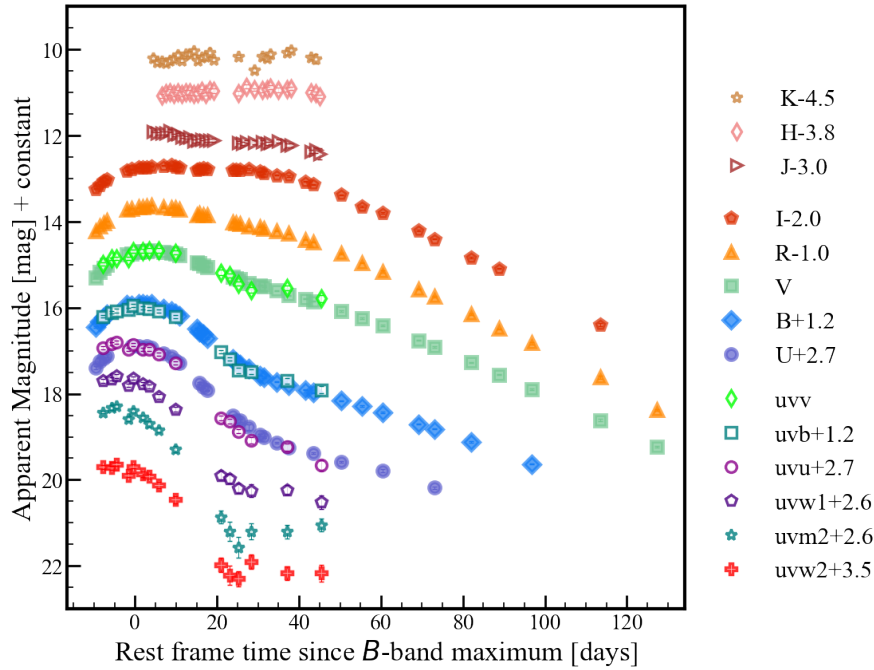


FIGURE 4.18: Optical *UBVRI* and *Swift*-UVOT LCs of 2011aa. The horizontal axis represent rest frame time since *B*-max $(t - t_{\max})/(1 + z)$. The magnitudes are in *Vega* system. The light curves are vertically shifted for better presentation. We also plot the *JHK_s* light curves from Friedman et al. (2015).

TABLE 4.11: *UBVRI* magnitudes of 2011aa from HCT.

JD	Phase*	<i>U</i> (error)	<i>B</i>	<i>V</i>	<i>R</i>	<i>I</i>
2455601.3	-10.3	14.70 0.03	15.25 0.01	15.30 0.02	15.23 0.01	15.24 0.01
2455602.4	-9.2	14.55 0.07	15.12 0.01	15.16 0.02	15.12 0.01	15.15 0.02
2455603.4	-8.3	14.48 0.02	15.03 0.01	15.08 0.01	15.04 0.01	15.06 0.01
2455604.2	-7.4	14.42 0.03	14.96 0.01	15.01 0.02	14.99 0.01	15.02 0.01
2455609.2	-2.5	– 0.00	14.72 0.04	14.76 0.01	14.73 0.01	14.82 0.02
2455610.2	-1.5	14.20 0.07	14.76 0.06	14.74 0.02	14.70 0.02	14.79 0.01
2455612.1	0.5	14.20 0.04	14.72 0.01	14.71 0.01	14.68 0.01	14.75 0.01
2455613.1	1.5	14.23 0.04	14.72 0.01	14.69 0.01	14.66 0.01	14.74 0.01
2455614.1	2.4	14.20 0.04	14.73 0.01	14.69 0.00	14.66 0.01	14.73 0.01
2455615.2	3.5	14.24 0.03	14.72 0.01	14.67 0.02	14.62 0.01	14.72 0.02
2455618.2	6.5	14.36 0.01	14.83 0.02	14.70 0.02	14.66 0.01	14.70 0.02
2455620.1	8.5	14.43 0.01	14.88 0.01	14.73 0.00	14.68 0.00	14.69 0.01

SN 2011aa *UBVRI* - Continued on next page

Table 4.11 – continued from previous page

JD	Phase*	U (error)	B	V	R	I
2455621.1	9.4	14.53 0.05	14.93 0.02	14.74 0.02	14.70 0.02	14.73 0.03
2455622.1	10.4	14.59 0.02	14.99 0.01	14.79 0.02	14.73 0.02	14.73 0.02
2455626.4	14.8	–	15.29 0.02	14.94 0.03	14.85 0.03	14.79 0.02
2455627.1	15.4	15.05 0.02	15.36 0.02	14.97 0.03	14.82 0.02	14.77 0.03
2455628.1	16.4	15.14 0.04	15.42 0.02	15.02 0.01	14.85 0.01	14.76 0.01
2455629.1	17.4	15.22 0.01	15.50 0.02	15.05 0.01	14.86 0.02	14.78 0.02
2455635.2	23.6	15.82 0.02	15.99 0.02	15.28 0.01	15.01 0.02	14.80 0.01
2455636.2	24.5	15.93 0.04	16.06 0.01	15.32 0.02	15.03 0.02	14.80 0.02
2455637.1	25.5	15.92 0.04	16.12 0.02	15.34 0.02	15.05 0.02	14.80 0.04
2455639.2	27.6	16.08 0.07	16.21 0.04	15.43 0.02	15.11 0.02	14.78 0.02
2455642.1	30.4	16.26 0.03	16.38 0.01	15.48 0.01	15.13 0.01	14.84 0.01
2455643.1	31.4	16.31 0.02	16.42 0.02	15.51 0.02	15.16 0.02	14.87 0.02
2455646.2	34.5	16.43 0.02	16.53 0.01	15.60 0.01	15.22 0.01	14.92 0.01
2455649.2	37.5	16.54 0.05	16.61 0.01	15.71 0.01	15.29 0.01	14.94 0.02
2455653.2	41.5	–	16.71 0.01	15.80 0.01	15.42 0.01	15.07 0.01
2455655.3	43.6	16.67 0.02	16.78 0.01	15.85 0.01	15.48 0.01	15.14 0.01
2455662.1	50.4	16.88 0.02	16.96 0.01	16.08 0.02	15.74 0.02	15.38 0.01
2455667.2	55.6	–	17.09 0.02	16.24 0.02	15.96 0.01	15.66 0.02
2455672.3	60.6	17.09 0.04	17.23 0.02	16.41 0.02	16.17 0.02	15.79 0.02
2455681.2	69.6	–	17.50 0.01	16.76 0.01	16.58 0.01	16.20 0.02
2455685.2	73.5	17.49 0.02	17.62 0.01	16.92 0.02	16.75 0.02	16.40 0.02
2455694.1	82.5	–	17.92 0.01	17.27 0.01	17.16 0.02	16.83 0.02
2455701.1	89.4	–	–	17.56 0.01	17.50 0.01	17.09 0.01
2455709.2	97.5	–	18.43 0.01	17.89 0.02	17.83 0.02	–
2455726.1	114.5	–	–	18.62 0.03	18.62 0.03	18.40 0.03
2455740.1	128.5	–	–	19.23 0.02	19.37 0.02	–

*Rest frame time since B -max (JD 2455611.65).

TABLE 4.12: *Swift*-UVOT magnitudes of 2011aa

JD	Phase*	uvw2 (err)	uvm2 (err)	uvw1 (err)	u (err)	b (err)	v (err)
2455605.9	-5.7	16.22 0.05	15.72 0.05	15.05 0.04	14.14 0.04	14.91 0.03	14.86 0.03
2455603.7	-8.0	16.20 0.05	15.83 0.03	15.10 0.04	14.23 0.04	15.00 0.02	14.99 0.04
2455607.1	-4.6	16.13 0.05	15.69 0.05	14.99 0.04	14.10 0.03	14.87 0.04	14.85 0.04
2455610.0	-1.7	16.39 0.05	15.98 0.05	15.20 0.04	14.27 0.04	14.85 0.04	14.85 0.04
2455611.2	-0.4	16.19 0.05	15.79 0.05	15.04 0.04	14.16 0.04	14.75 0.04	14.69 0.04
2455613.6	2.0	16.37 0.06	15.95 0.05	15.17 0.04	14.27 0.04	14.81 0.04	14.68 0.04
2455615.1	3.4	16.42 0.06	16.10 0.06	15.23 0.05	14.26 0.04	14.82 0.04	14.67 0.05
2455617.5	5.9	16.62 0.07	16.24 0.06	15.46 0.06	14.38 0.04	14.88 0.04	14.67 0.05
2455621.6	9.9	16.96 0.08	16.69 0.07	15.76 0.05	14.59 0.04	15.01 0.04	14.72 0.05
2455632.9	21.2	18.47 0.17	18.27 0.15	17.29 0.11	15.86 0.06	15.82 0.04	15.18 0.06
2455635.1	23.4	18.72 0.22	18.60 0.22	17.38 0.11	15.94 0.06	15.99 0.04	15.25 0.05
2455637.3	25.6	18.80 0.18	18.97 0.24	17.59 0.11	16.17 0.04	16.26 0.06	15.44 0.05
2455640.2	28.6	18.40 0.17	18.60 0.19	17.65 0.15	16.38 0.08	16.29 0.06	15.59 0.07
2455649.1	37.5	18.67 0.16	18.60 0.16	17.63 0.11	16.54 0.08	16.50 0.06	15.54 0.06
2455657.7	46.1	18.67 0.19	18.45 0.15	17.92 0.15	16.96 0.12	16.71 0.08	15.79 0.08

*Rest frame time since *B*-maximum (JD 2455611.65).

peak in *B*-band occurred at JD 2455611.65±1.05 with a magnitude of 14.72±0.01 mag. The $\Delta m_{15}(B)$ is estimated to be 0.59±0.07, making it the slowest declining SN Ia. The peak in *U* occurred at JD 2455611.35±0.53 (−0.3 d) and that in *VRI*-bands occurred at JD 2455615.52±0.44 (+3.8 d), 2455616.10±0.44 (+4.5 d) and 2455618.72±0.46 (+7.1 d). The *I*-band LC does not show the characteristic secondary peak.

SN 2011aa exploded 20".4 east and 10".2 south of the center of UGC 3906 (Puckett et al. 2011). The radial velocity of UGC 3906 corrected for Local Group infall onto Virgo is 3995 ± 20 km s^{−1} (Makarov et al. 2014). The calculated luminosity distance is 56.3 ± 0.3 Mpc and μ is 33.75 ± 0.27 mag, assuming $H_0 = 70$ km s^{−1} Mpc^{−1}, $\Omega_M = 0.27$ and $\Omega_\Lambda = 0.73$. The reddening is $E(B - V) =$

0.0237 ± 0.0006 due to the Milky Way. However, in the near maximum spectrum of 2011aa we observe Na I D ($\lambda 5890$) absorption with a pseudo-equivalent width (pEW) of $0.41 \pm 0.02 \text{ \AA}$ due to ISM in the MW. Using the empirical relation $E(B - V) = 0.16 \times \text{pEW (Na I D)}$ (Turatto et al. 2003), we get $E(B - V) = 0.065 \pm 0.003 \text{ mag}$. We do not detect any Na I D at the host galaxy redshift, consistent with the location of the supernova. The extinction in each band is estimated using Cardelli et al. (1989) with $R_V = 3.1$. The peak M_B is $-19.30 \pm 0.27 \text{ mag}$, similar to normal Ia.

4.2.3 Nickel mass and ejecta mass

We obtain the *UVOIR* bolometric LC using the *Swift*-UVOT, *UBVRI* and *JHK_s* band magnitudes. The UV-contribution is 20% at -8.7 d and decreases to 3% at $+27 \text{ d}$ since *B*-max. For the first two epochs before -8.7 d we do not have UV-magnitudes, so we add a 20% contribution to the optical. The NIR data coverage is from JD 2455616.17 to JD 2455657.19. The NIR contribution to the UV-optical luminosity is 10% at JD 2455616 ($+4.4 \text{ d}$) and increases to 25% at JD 2455640 ($+28.6 \text{ d}$). We assume a constant contribution of 10% from NIR before $+4.4 \text{ d}$. The *UVOIR* spectral energy distribution has been integrated from 1600 \AA to 24800 \AA .

We fit the light curve with EQUATION 3.5 (SECTION 3.1.1) upto 70 days since *B*-max to obtain the parameters t_{exp} - epoch of explosion, M_{Ni} - ^{56}Ni mass produced, t_{lc} - light curve time scale, and t_{γ} - γ -ray leaking time scale. It is assumed that the initial radius of the progenitor is negligible compared to the ejecta's expansion. A more realistic picture of the ejecta includes non-constant opacity, varying spatial distribution of the energy density (^{56}Ni mixing) (Khatami & Kasen 2019; Kushnir & Katz 2019). We used the `emcee` package in `python` to find the posterior distribution and hence the upper and lower error limits.

The fit to the *UVOIR* bolometric LC gives $t_{\text{exp}} = 2455591.62^{+1.01}_{-1.41}$, $M_{\text{Ni}} = 0.87^{+0.06}_{-0.06} M_{\odot}$, $t_{\text{lc}} = 16.82^{+1.68}_{-1.79}$ days and $t_{\gamma} = 55.42^{+3.00}_{-3.02}$ days. The rise time in *B*-band from t_{exp} is $20.03^{+1.58}_{-1.48}$ days. Using constant optical opacity $\kappa_{\text{opt}} = 0.1 \text{ cm}^2\text{g}^{-1}$ and $v_{\text{exp}} = 12000 \text{ km s}^{-1}$ derived from the near-maximum spectrum, we get $M_{\text{ej}} = 2.64^{+0.53}_{-0.56} M_{\odot}$ and a kinetic energy of explosion $E_{\text{k}} = 2.26^{+0.45}_{-0.48} \times 10^{51} \text{ erg}$. For a constant optical opacity of $0.15 \text{ cm}^2\text{g}^{-1}$, we get $M_{\text{ej}} = 1.76^{+0.35}_{-0.37} M_{\odot}$ and a kinetic energy of explosion $E_{\text{k}} = 1.51^{+0.30}_{-0.32} \times 10^{51} \text{ erg}$. The ^{56}Ni mass is within the range for normal Ia, $0.09 - 0.87 M_{\odot}$ with $\Delta m_{15}(B)$ between $0.8 - 1.9 \text{ mag}$ (Stritzinger et al. 2006). The estimated M_{ej} is higher than expected for a normal Ia from a M_{ch} WD explosion. To understand the explosion mechanism and progenitor, we explore models that can produce the ejecta and ^{56}Ni mass as estimated by the analytical 1D model (See SECTION 4.2.5).

4.2.4 Spectral evolution

The spectral sequence of 2011aa is shown in FIGURE 4.19 and the log is provided in TABLE 4.13. The spectra at -10.2 d shows features due to C, O, Si, S, Ca, Fe. We observe features due to Fe III, Si III indicating hot photosphere. 2011aa falls under the core-normal class of the Branch classification. C II $\lambda 6580$, and $\lambda 7234$ are seen in the spectra till $+17 \text{ d}$ (FIGURE 4.19).

A Gaussian function is fit to the Si II $\lambda 6355$ absorption to estimate the photospheric velocity. The velocity is $\sim 14000 \text{ km s}^{-1}$ at -10.2 d and decreases by 200 km s^{-1} each day to reach 12200 km s^{-1} around maximum. After maximum, the velocity evolves more slowly reaching about 12000 km s^{-1} at 3.5 day post maximum. The spectroscopic evolution is slow and forms a velocity plateau. This places 2011aa in the low velocity gradient group of the Benetti scheme. The velocity of C II $\lambda 6580$ is 8980 ± 200 at -10.2 d and decreases to 3600 km s^{-1} at $+10.4 \text{ d}$. The velocity of C II $\lambda 7234$ is 6650 ± 690 at -1.4 d and decreases to $3670 \pm 180 \text{ km s}^{-1}$ at $+10.4 \text{ d}$.

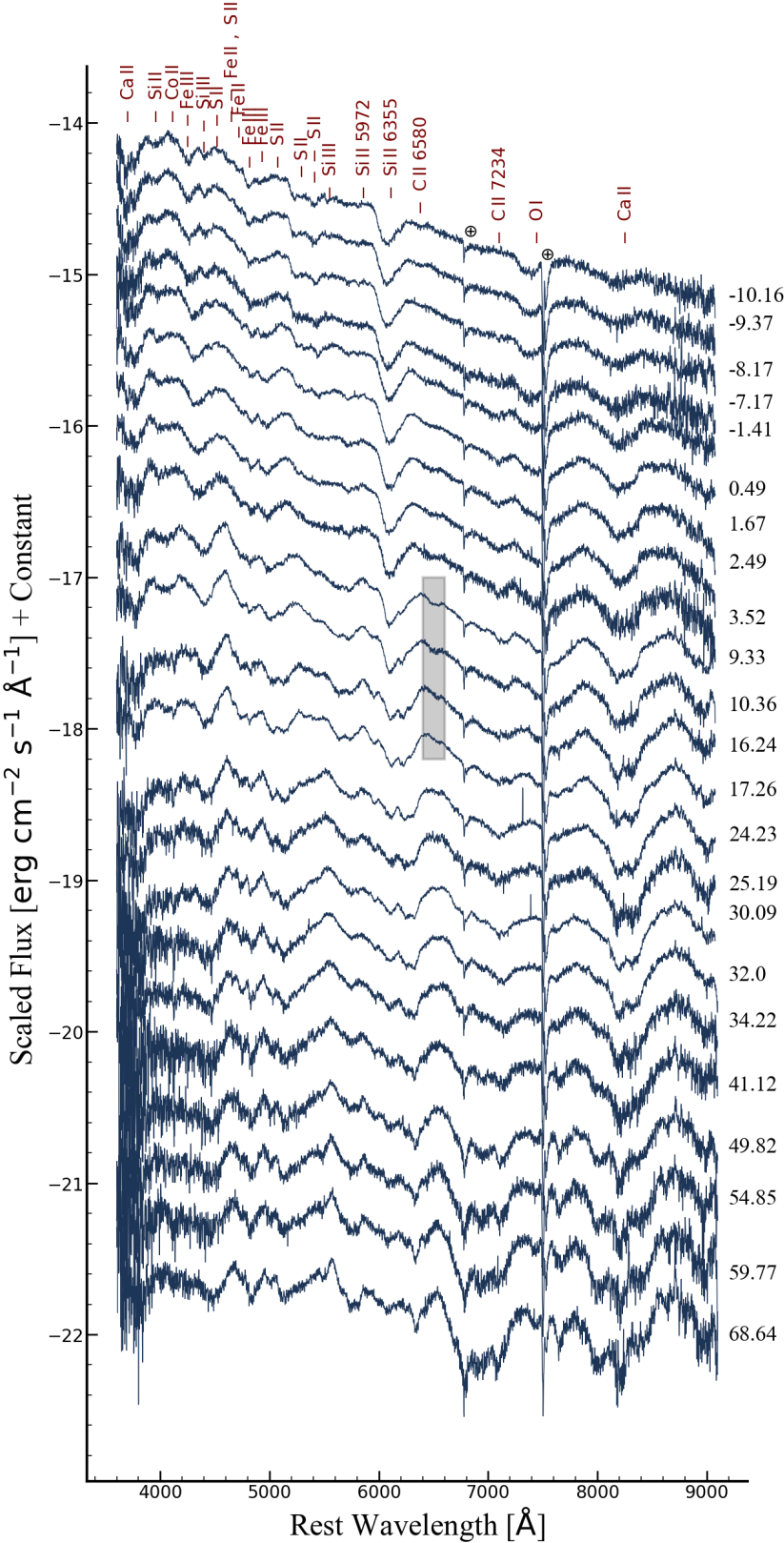


FIGURE 4.19: Spectral evolution of 2011aa from -10.16 to +68.6 day in the rest frame since *B*-max. $\text{C II } \lambda 6580$ region is shaded between +3.5 to +17.3 d . The spectra are redshift and extinction corrected. The important lines for the pre-mamimum spectra are marked.

TABLE 4.13: Spectroscopic observations log of 2011aa from HCT.

Date	JD	Phase*	Range
		(d)	(Å)
2011/02/08	2455601.36	-10.16	3500-7800; 5200-9100
2011/02/09	2455602.16	-9.37	3500-7800; 5200-9100
2011/02/10	2455603.37	-8.17	3500-7800; 5200-9100
2011/02/11	2455604.39	-7.17	3500-7800; 5200-9100
2011/02/17	2455610.22	-1.41	3500-7800; 5200-9100
2011/02/19	2455612.15	0.49	3500-7800; 5200-9100
2011/02/20	2455613.34	1.67	3500-7800; 5200-9100
2011/02/21	2455614.17	2.49	3500-7800; 5200-9100
2011/02/22	2455615.22	3.52	3500-7800; 5200-9100
2011/02/28	2455621.10	9.33	3500-7800; 5200-9100
2011/03/01	2455622.14	10.36	3500-7800; 5200-9100
2011/03/07	2455628.10	16.24	3500-7800; 5200-9100
2011/03/08	2455629.13	17.26	3500-7800; 5200-9100
2011/03/15	2455636.20	24.23	3500-7800; 5200-9100
2011/03/16	2455637.17	25.19	3500-7800; 5200-9100
2011/03/21	2455642.13	30.09	3500-7800; 5200-9100
2011/03/23	2455644.07	32.0	3500-7800; 5200-9100
2011/03/25	2455646.31	34.22	3500-7800; 5200-9100
2011/04/01	2455653.30	41.12	3500-7800; 5200-9100
2011/04/10	2455662.12	49.82	3500-7800; 5200-9100
2011/04/15	2455667.21	54.85	3500-7800; 5200-9100
2011/04/20	2455672.20	59.77	3500-7800; 5200-9100
2011/04/29	2455681.18	68.64	3500-7800; 5200-9100

*Rest frame time since B -max (JD 2455611.65).

The detonation wave proceeds faster at higher densities and the unburned material like C should be present at a higher velocity, lower density layer as compared to Si. The presence of C at velocities lower than Si indicate that the photosphere at that epoch moves with the velocity of C, while Si layer is moving faster or ejecta asymmetries/clumping (Parrent et al. 2011).

In FIGURE 4.20([A], B] and [C]) we compare the spectra of 2011aa with 1991T, 2001ay (Krisciunas et al. 2011), 2005cf, 2006gz (Hicken et al. 2007), 2009dc, and 2013cv (Cao et al. 2016) at various epochs of evolution. The spectroscopic evolution of 2011aa shows most differences with the comparison SNe in the early phase.

It is quite different from bright SN 1991T-like objects that shows weak/no features due to IMEs in the pre-maximum spectra. Super-Chandra object like SN 2009dc ($M_B = -20.22$ mag with a $\Delta m_{15}(B) = 0.71$ mag) produces $1.8 M_\odot$ of ^{56}Ni mass and $2.8 M_\odot$ of ejecta (Taubenberger et al. 2011). It shows strong absorption feature of C II 6580 Å in its spectra and is part of the shallow silicon (SS) group. Another super-Chandra object SN 2006gz has velocity of $\sim 12\,000$ km s $^{-1}$ near maximum and falls in SS group. The velocity of C is more than Si in SN 2006gz. SN 2011aa does not show strong features due to Ca II as seen in normal SN 2005cf. SN 2013cv shows transitional nature between super-Chandra and normal SNe. It lack IGEs in the early phase spectra and persistent presence of C after maximum.

Now we discuss two objects which show some similarity with SN 2011aa in their light curve evolution. The peculiar SN 2001ay (Krisciunas et al. 2011) exhibits slow decline ($\Delta m_{15}(B) = 0.68$ mag) with $M_B = -19.19$ mag. The Si II $\lambda 6355$ line is broad and its velocity evolution after maximum is quite rapid (~ 200 km s $^{-1}$ d $^{-1}$) which makes it to fall under high velocity gradient group. This has been explained in terms of pulsational delayed detonation in a M_{ch} WD (Baron et al. 2012). For the peculiar ASASSN-15hy (Lu et al. 2021) with a $\Delta m_{15}(B) = 0.72$ mag and $M_B = -19.14$ mag, the slow decline has been explained in terms of a degenerate core exploding inside a non-degenerate shell. A massive core is required in this case for understanding the broad light curves. The proposed progenitor in this case is the merger of a WD with the core of an AGB star. The observed spectral properties of ASASSN-15hy is more similar to 2009dc with low velocity near maximum (8000 km s $^{-1}$) and falls in the SS group. 2011aa is quite different in terms of spectroscopic evolution from both these objects.

4.2.5 Explosion Models

Here we discuss various possible explosion models for SN 2011aa.

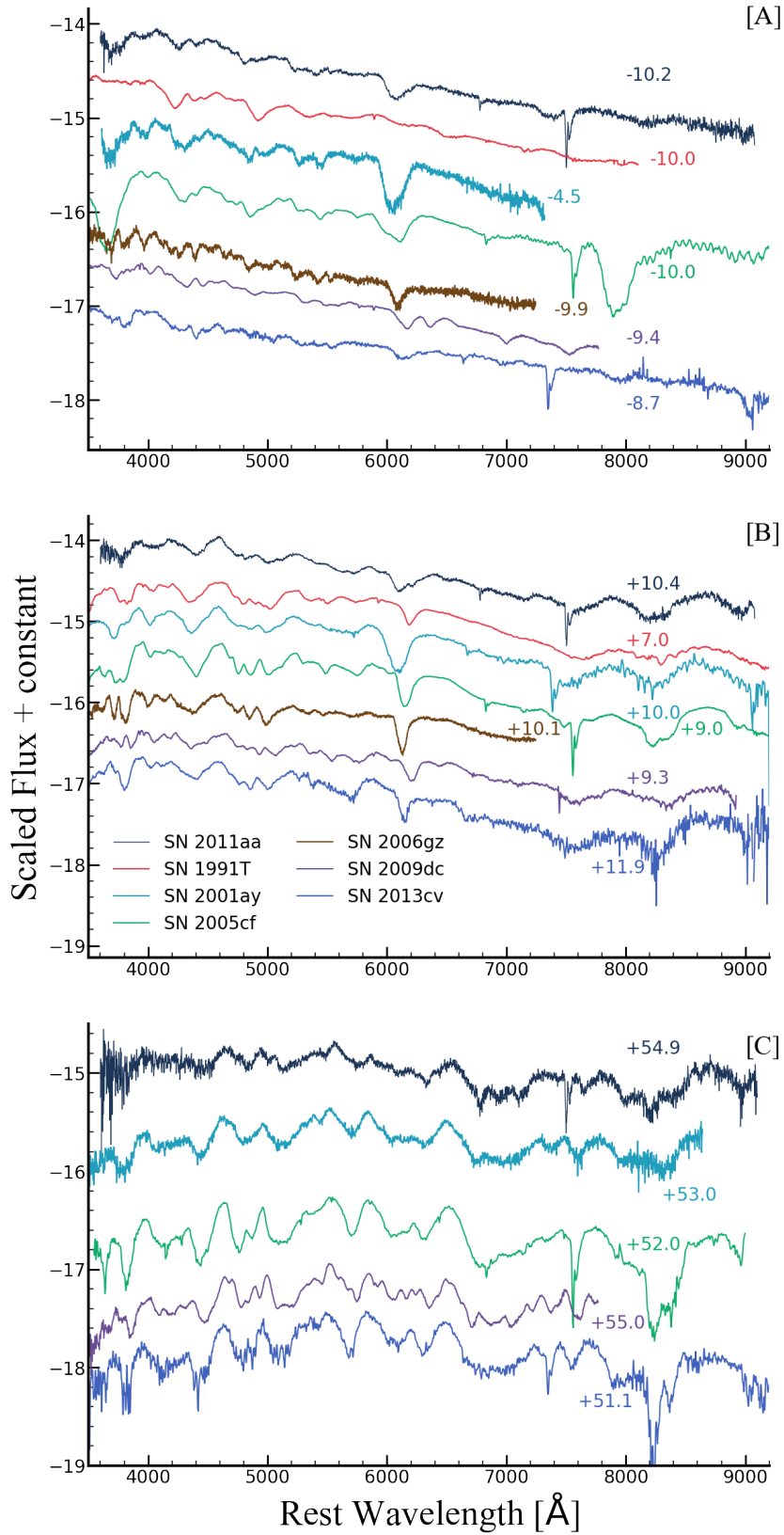


FIGURE 4.20: The comparison of 2011aa with luminous SN 1991T, peculiar SN 2001ay and SN 2013cv, normal SN 2005cf and super-Chandra SN 2006gz and SN 2009dc at pre-maximum [A], near-maximum [B] and post-maximum [C] phase.

4.2.5.1 Collision of white dwarfs

Collision between two WDs can occur in dense stellar environments like the core of globular clusters. [Raskin et al. \(2009\)](#) calculated about 10-100 WD collisions per year at redshift ≤ 1 . They calculated the explosion parameters for the collision of two equal mass white dwarfs ($0.6 M_{\odot}$) for different impact parameters. The ^{56}Ni mass is maximum ($\sim 0.4 M_{\odot}$) for a head on collision and decreases with increasing impact parameter. This ^{56}Ni mass is not consistent with SN 2011aa. Collision of higher mass white dwarfs ($\sim 0.9 M_{\odot}$) with low impact parameter can produce brighter events that broadly follow the Phillips relation (See Fig. 3 of [Rosswog et al. 2009](#)) with some dependence on viewing angle. Using similar and dissimilar masses of the colliding WDs [Kushnir et al. \(2013\)](#) showed that SN Ia explosions are produced with ^{56}Ni mass in the range of $0.1 - 1.0 M_{\odot}$. Both works of [Rosswog et al. \(2009\)](#) and [Kushnir et al. \(2013\)](#) showed that the ejecta structure is stratified with C and O in the outer layers, intermediate mass elements (IMEs) in the inner, and IGEs in the innermost layers caused as a result of detonation.

4.2.5.2 Rotating white dwarfs

The maximum mass of an inert, non-rotating WD is $\sim 1.4 M_{\odot}$ (M_{ch}). CO WDs having differential rotation can support mass exceeding the M_{ch} limit ([Yoon & Langer 2005](#)). For a rotating WD having a non-degenerate companion, the accreting WD can reach a maximum possible mass of $2 M_{\odot}$ ([Langer et al. 2000](#)). We discuss explosion models based on rapidly rotating CO WDs under hydrostatic equilibrium.

[Fink et al. \(2018\)](#) constructed white dwarfs within mass range of $1.6 - 2.0 M_{\odot}$ and angular momentum between $0.9 - 2.2 \times 10^{50} \text{ g cm}^2 \text{ s}^{-1}$. Different explosion models like prompt detonation, DDT, and pure deflagration models are tested.

The prompt detonation model produces $1.44 M_{\odot}$ of ^{56}Ni . In this model, the IMEs produced are extremely low. In the delayed detonation models, an initial deflagration transitions to a detonation due to the Zel'dovich gradient mechanism (mixing hot ash with cold fuel under gravity). The mass of ^{56}Ni varies between $1.06 - 1.45 M_{\odot}$ based on the white dwarf mass. All the DDT models show asymmetric ejecta structure. The models are luminous with peak B -band absolute magnitude around ~ -20 mag. Of particular interest is the model AWD1, in which $1.06 M_{\odot}$ of ^{56}Ni is produced. This value is close to the ^{56}Ni mass estimate of 2011aa. But the model spectra is bluer with high blueshift of Si II line. The model produces huge amount of IGEs ($1.31 M_{\odot}$) inconsistent with the observed spectra of 2011aa. The ejecta structure is also highly stratified with very less unburned C/O in the outer layers due to detonation. We show the angle averaged spectra of AWD1 model (Fink et al. 2018) compared with 2011aa in FIGURE 4.21.

4.2.5.3 Violent Merger

3D simulations of violent merger of two CO WDs of dissimilar masses ($0.9+1.1 M_{\odot}$) can explain the normal SN Ia explosions (Pakmor et al. 2012)[P12]. The material from the secondary is violently accreted onto the primary. The material is then compressed, and heated up on the surface of the primary where carbon burning is ignited. At a density (ρ) $2 \times 10^6 \text{ g cm}^{-3}$, and at temperature greater than $2.5 \times 10^9 \text{ K}$ a detonation occurs. The detonation flame propagates through the final merged object and burns the material. The energy released unbinds the object. The total ejected mass of this model ($\sim 1.95 M_{\odot}$) is comparable to that of 2011aa estimated using Arnett's model. This model leads to an asymmetric explosion, hence the observables have a line of sight dependence. The peak in B -band varies between -19.5 to -18.7 mag and the angle averaged magnitude is -19.0 mag. Similarly, the $\Delta m_{15}(B)$ varies between 0.5 and 1.4 mag with a mean of 0.95 mag. The estimated values of the observables of 2011aa lie well within the

range predicted by the violent merger model. The primary white dwarf is burned and its ashes expand while the unburned and incompletely burned materials like C, O, Ne, Mg from the secondary WD resides near the center. Hence, the presence of CO at lower velocities may be crucial in determining the explosion scenario. We show the angle averaged spectra of violent merger model from P12 in FIGURE 4.21. The spectra shows some similarity in velocities and line strengths to 2011aa. This encourages us to use the violent merger model varying the abundances at different velocities to accurately model the line strengths and velocities and get estimates of mass of different elements synthesized. We used SEDONA with violent merger density profile to model the observed spectra and light curve.

4.2.6 Modelling of the spectra and light curves

We use SEDONA to simulate the spectral and light curve evolution of SN 2011aa. For all the models in this work, we use the spherical 1D ejecta structure and the 1D angle averaged density profile of the violent merger model (merger_2012_11+09, P12). In this work, we start the simulation at 2 days since explosion and evolve the models till 60 days. We do not consider any best-fitting technique in this work.

FIGURE 4.21 shows the spectral evolution of 2011aa along with synthetic spectrum generated with SEDONA. We consider C, O, Ne, Na, Mg, Si, S, Ca, ^{54}Fe , ^{56}Ni and ^{58}Ni in the models. We consider four models in this work based on the violent merger density profile. The integrated ejected mass is $1.95 M_{\odot}$ with a kinetic energy of 1.7×10^{51} erg for the models.

In the first model (Model 1), we use the abundance of the violent merger model from P12 which produces $0.62 M_{\odot}$ of ^{56}Ni . In the model, C and O are present in the very inner layers ($< 1000 \text{ km s}^{-1}$). This is due to the fact that the burning is not complete for the lesser dense secondary WD and unburned elements dominate

near the center after the ashes of the primary has expanded. ^{56}Ni is present upto 11 600 km s $^{-1}$ from the center. The layers between 10 000 - 15 000 km s $^{-1}$ are dominated by Si, S, Mg. The outer layers above 20 000 km s $^{-1}$ are mostly C and O.

The ^{56}Ni mass is lower than the mass estimated for SN 2011aa using Arnett model fit to the *UVOIR* light curve. In this model, total mass of unburned elements (C, O and Ne) is $0.82 M_{\odot}$, intermediate mass elements (Mg, Si, S, Ca) is $0.47 M_{\odot}$ and Fe-group elements (^{54}Fe , ^{56}Ni and ^{58}Ni) is $0.67 M_{\odot}$. The model spectrum at -10.16 d is quite red and does not reproduce the observed continuum (FIGURE 4.21[A]). The Fe III, S II and Mg II lines are very strong in the model (FIGURE 4.21[C] and [D]) indicating an over abundance of these elements. Near the maximum ($+0.49$ d) Si II $\lambda 6355$ and C II $\lambda 6580$ are reproduced well. In the spectrum taken $+10.4$ d after maximum, we see C II $\lambda 6580$ absorption feature (see inset of FIGURE 4.28[F]). In normal SNe Ia, C is seen in the spectra during pre-max to maximum phases. However, in super-Chandrasekhar objects like 2009dc (Taubenberger et al. 2011), C can be seen post-maximum also. The detection of C in this phase indicates that C is present in the inner layers. This supports our argument of a violent merger scenario. At $+10.4$ d, the region below 5000 Å gets redder. This is mostly because of line blocking by Fe group elements.

To account for the ^{56}Ni mass estimate from the analytical light curve model ($0.87 \pm 0.06 M_{\odot}$), we increased the mass fraction of ^{56}Ni at the expense of Mg and S between 10 000 - 16 000 km s $^{-1}$ in the second model (Model 2). Between 8000 - 10 000 km s $^{-1}$, we decreased S and increased ^{56}Ni . Between 8000 - 16 000 km s $^{-1}$, we reduced the ^{54}Fe . This allows to reproduce the line strengths of Fe III and S II in the models (FIGURE 4.21[C] and [D]). Near the maximum, the red wing of the Si II $\lambda 6355$ is stronger compared to the first model (see inset of FIGURE 4.21[D]). This is because of the higher ionization at lower velocities caused by an increased ^{56}Ni abundance. In this model, the ^{56}Ni mass is $0.68 M_{\odot}$. Further increasing

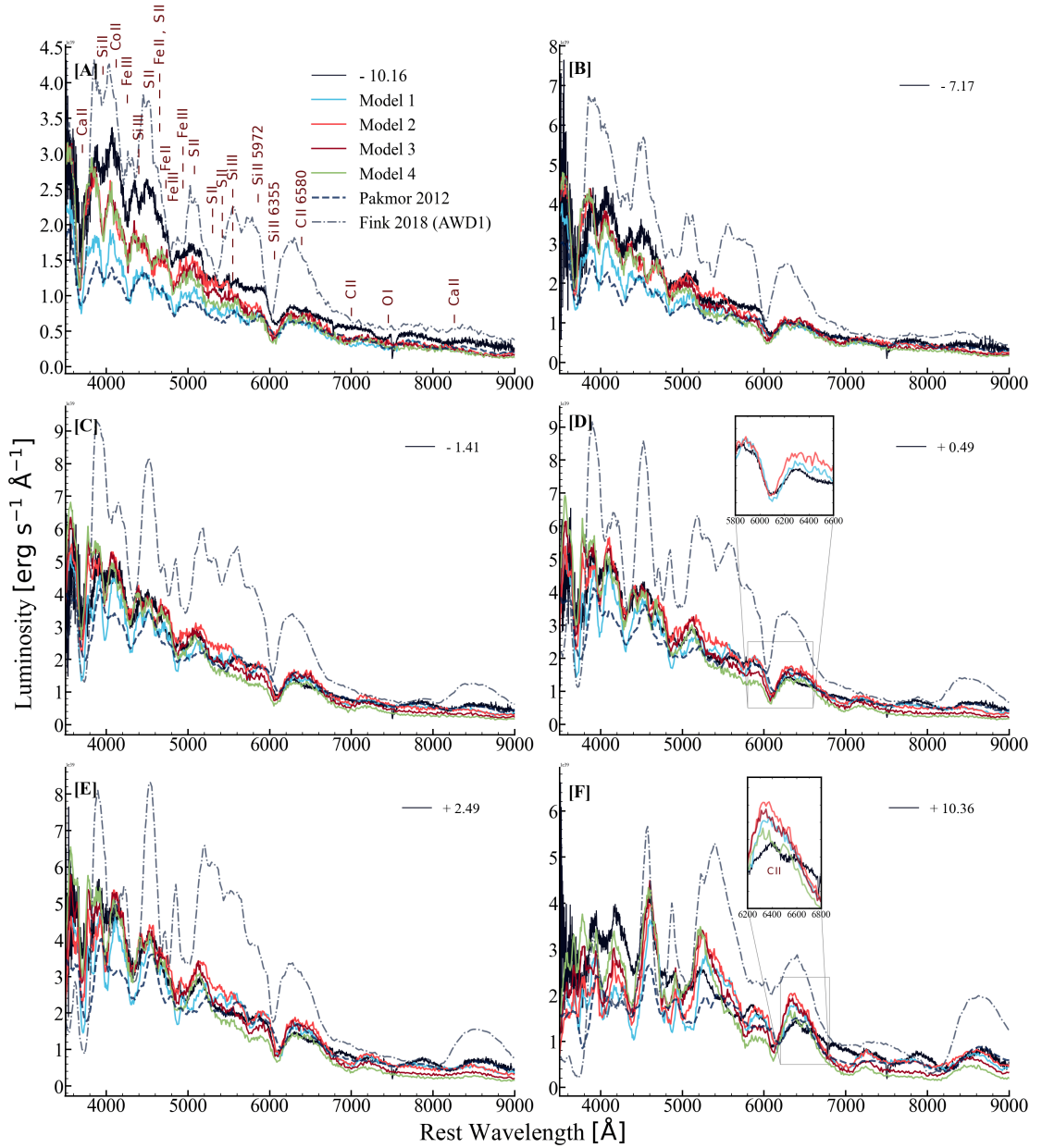


FIGURE 4.21: Spectral evolution of 2011aa from -10.16 to $+10.36$ d since rest frame time in B -max. We show the model spectra calculated using SEDONA. Also shown are the angle averaged spectra of accreting white dwarf model (AWD1) from Fink et al. (2018) and violent merger model from P12. These are taken from the HESMA database. The important lines in the early phase are marked in [A]. The observed spectra are de-reddened and redshift corrected.

TABLE 4.14: SEDONA model features

Model Name	Density*	Abundance	ϵ	$\Delta m_{15}(B)$ (mag)	M_B (mag)	^{56}Ni (M_\odot)
Model 1	violent merger	violent merger	1.0	0.96	-19.20	0.62
Model 2	violent merger	modified abundance + increased ^{56}Ni	1.0	0.96	-19.39	0.68
Model 3	violent merger	same as Model 2	0.5	0.77	-19.35	0.68
Model 4	violent merger	same as Model 2	0.3	0.59	-19.31	0.68

*One dimensional density of the violent merger model.

the ^{56}Ni mass makes the red wing of Si II $\lambda 6355$ even stronger. Hence we do not consider increasing ^{56}Ni further.

The region below 5000 Å is redder than observed in this model also. For both the models, the redistribution probability ϵ is 1.0 which means absorption-dominated treatment of the redistribution of radiation. Following a source function the absorption by a line is followed by a re-emission in another frequency. This acts as fluorescence. We construct two more models varying the ϵ parameter. In these two models the abundances are same as the second model. In the third model (Model 3), with $\epsilon=0.5$, meaning equal probability for scattering and absorption, we find slight improvement in reproducing the blueward flux at +10.4 d over the second model. In the fourth model (Model 4) $\epsilon=0.3$, there is severe flux depression in the region around 5200 - 6000 Å and an increase in flux in the bluer region. This means in this model, the blue photons are scattered out of the ejecta more rather than being absorbed.

The light curves in each bandpass is obtained from the synthetic spectral energy distribution by convolving it with the HFOSC filter response. In FIGURE 4.22[A], we plot the observed light curves of 2011aa in $UBVRI$ along with the model light curves from SEDONA simulation. Model 1 (solid curve in FIGURE 4.22[A]), under predicts the magnitude in all bands. This is due to lower ^{56}Ni mass in the model ejecta. In Model 2 (dashed), we increase the ^{56}Ni mass and find that the peak in B -band is close (-19.39 mag) to the observed value (-19.30 \pm 0.27 mag).

But the decline rate is 0.96 mag which is faster than the observed light curve (0.59 mag). The model with $\epsilon=0.5$ (dash-dot), the peak magnitude in B -band is -19.35 mag with $\Delta m_{15}(B)$ of 0.77 mag. In the fourth model $\epsilon=0.3$ (dotted), the peak magnitude is -19.31 mag with $\Delta m_{15}(B) = 0.59$ mag. But the flux in I -band is severely under predicted. The absence or equally bright secondary maximum is reproduced by our violent merger models (particularly Model 1 & Model 2). The extinction corrected $B - V$ colour is plotted and compared with the models in FIGURE 4.22[B]. Model 1 is redder and Model 4 is bluer than the observed values throughout. Increasing ^{56}Ni makes Model 2 bluer than Model 1 around 10-20 days since explosion, however this model becomes redder after 30 days. Model 3 predicts the colour evolution better around 30-50 days. The optical, UV-optical and $UVOIR$ bolometric luminosity are plotted in FIGURE 4.22[C] along with the SEDONA models. Due to less ^{56}Ni in Model 1, the luminosity in the early phase is dimmer than the other models. The early time flux increases, if ^{56}Ni is distributed to the outer layers ($\sim 16\,000\text{ km s}^{-1}$). This is because more high-energy blue photons are coming out of the ejecta. The effect of ϵ is not seen in the model bolometric light curves.

All the models generated considering the violent merger density profile can reproduce the observed light curves and spectra fairly reasonably. Using non-LTE calculations in one-dimension, Shen et al. (2021) showed that there is a reduction in Fe II line blanketing and Ca II emission after peak which increases the magnitude in U , B -bands and decreases in I while the V -band is mostly unaffected. A detailed 3D, non-LTE consideration of the radiation diffusion treating fluorescence for each line separately may give better match to the observables of SN 2011aa.

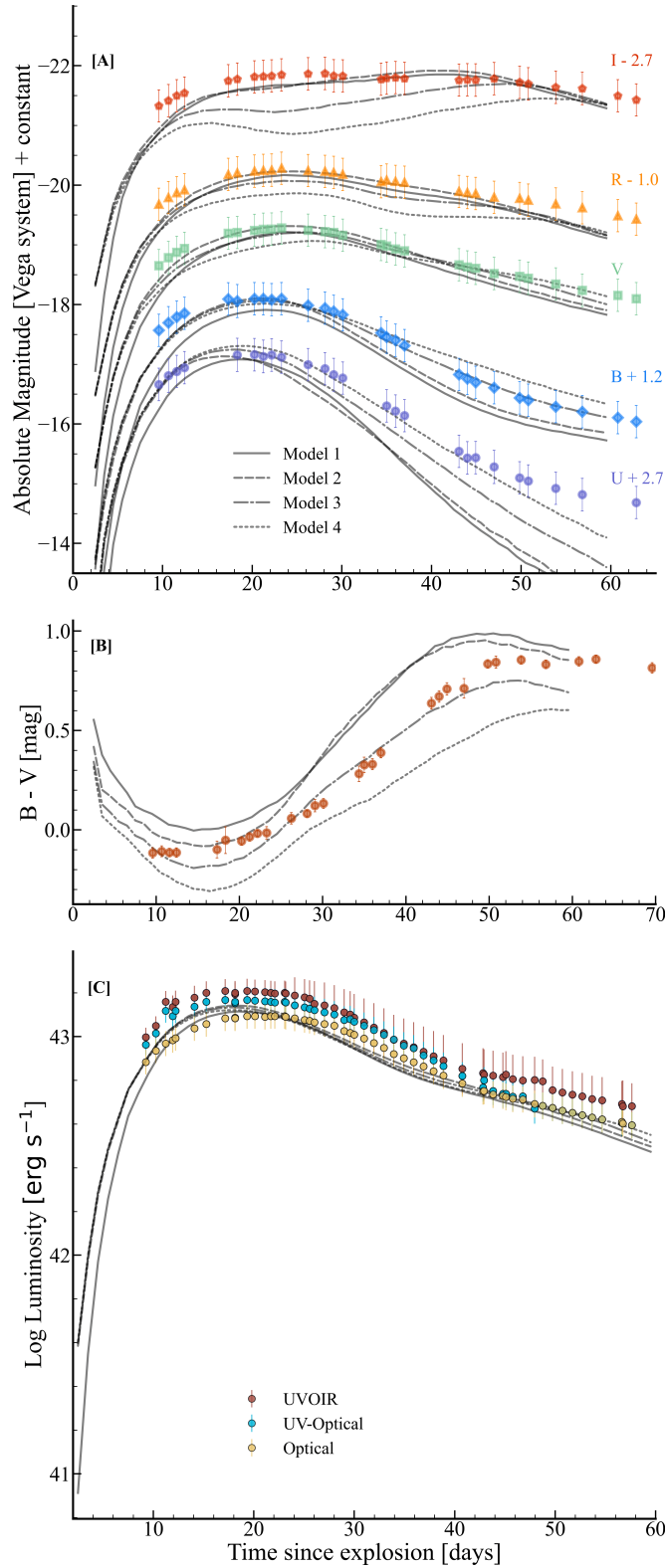


FIGURE 4.22: **[A]** The *UBVRI* band light curves of 2011aa along with synthetic light curves generated using SEDONA. From the model spectral energy distribution we calculate the light curves in *AB* system and convert to *Vega* system using values given in Blanton & Roweis (2007). The horizontal axis is time since explosion (JD 245 5591.62). **[B]** The $B - V$ colour of 2011aa plotted with the SEDONA models. **[C]** The optical, UV-optical and *UVOIR* bolometric light curves are shown along with the models.

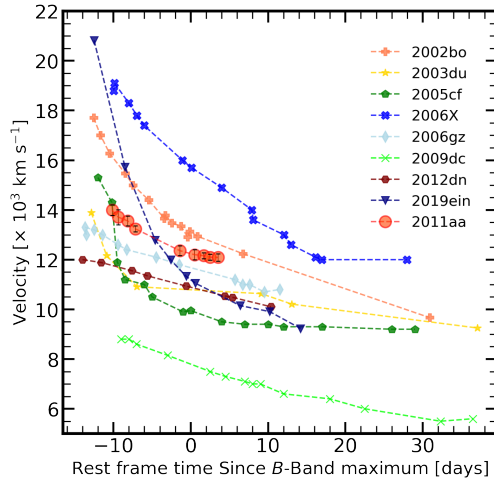


FIGURE 4.23: Si II $\lambda 6355$ velocity evolution of 2011aa plotted along with other SNe Ia.

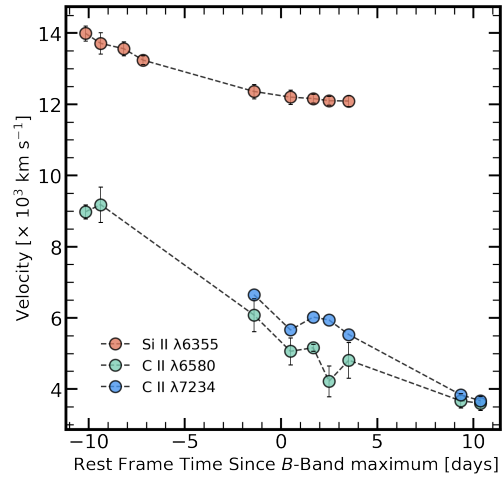


FIGURE 4.24: The velocity evolution of Si II $\lambda 6355$, C II $\lambda 6580$, and C II $\lambda 7234$ for 2011aa.

4.2.7 Discussions

For normal Ia, the average $\Delta m_{15}(B)$ is 1.2 mag with M_B of -19.3 ± 0.1 mag (Benetti et al. 2005). They show the presence of a secondary maximum in the *I*-band LC. The average expansion velocity near maximum is $10\,600 \pm 400$ km s $^{-1}$ (Wang et al. 2009b). The favoured explosion mechanisms for the normal Ia, is the delayed detonation (Mazzali et al. 2007) in a M_{ch} or detonation in a sub- M_{ch} WD (Sim et al. 2010).

SN 2011aa is the slowest declining SN Ia with $\Delta m_{15}(B) = 0.59 \pm 0.07$ mag, and $M_B = -19.30 \pm 0.27$ mag. Analytical models indicate ^{56}Ni mass is $0.87 M_{\odot}$ and ejected mass is between 1.76 - 2.64 M_{\odot} . The *I*-band LC declines monotonically without a secondary peak. This is explained as due to absence of Fe core/low Fe abundance (Kasen 2006). The abundance pattern of the violent merger model also supports the absence of secondary peak in *I*. The Si II velocity evolution shows a plateau after maximum (FIGURE 4.23). The velocity plateau can be explained in terms of a merger scenario where there is a CO WD inside an extended envelope (Khokhlov et al. 1993). This extended envelope is formed by the destruction of the

secondary white dwarf. A detonation shock wave propagating outwards will collide with this low density envelope, and an inward shock wave will cause deceleration of the outward-moving material. The duration of the plateau observed in the velocity will depend on the envelope's mass. The shock wave interacting with the envelope will create density and pressure gradients which will cause mixing of the materials in the ejecta. The velocity of C II $\lambda 6580$, and $\lambda 7234$ is less than Si II $\lambda 6355$ (FIGURE 4.24). This can be due to C II present in the inner layers or clumping/ line of sight effect. SN 2011aa shows a slow decline similar to that seen in super-Chandra objects. However, the spectral evolution is not similar to either normal or super-Chandra objects. The merger scenario produces similar ^{56}Ni mass as compared to normal SNe Ia and more ejecta mass ($\sim 1.95 M_{\odot}$). So, the peak luminosity is similar to normal Ia and with more ejecta the diffusion time for the photons is large making the decline rate slower. In this work, we have demonstrated that SN 2011aa with a slower decline rate but normal peak magnitude can be explained by the violent merger of WDs.

4.3 Probing the similarity/diversity in Type Ia supernovae

Most SNe Ia are understood to arise from a CO WD explosion. The propagation of the thermonuclear burning flame through the WD, causing explosive nucleosynthesis, mainly determines the elemental structure of the ejecta. At the lower density outer regions the temperature decreases. The peak temperature behind this front decides the burning of the materials. At higher temperatures, complete Si burning happens - the product of which is mostly ^{56}Ni , followed by incomplete Si burning, which are mostly Si, S, ^{56}Ni , Ar, Ca and Fe-peak elements. O burning happens at a comparatively lower temperature - the products are O, Si, Ar, Ca. However, Ca acts as a bottleneck with a magic number of protons. So, O burning does not go

beyond Ca. At a much lower temperature, C burning happens to produce O, Mg, Ne and some Si. So, the abundance structure is stratified with unburned elements like C/O, mostly in the outer regions at lower density and higher velocity.

Over the years, observations indicate there are a few SNe Ia for which unburned C (C II $\lambda 6578.05$; $2s^2 3s \ ^2S \rightarrow 2s^2 3p \ ^2P$) velocity is lower than Si (Si II $\lambda 6355$; $\lambda 6347.11$ $3s^2 4s \ ^2S \rightarrow 3s^2 4p \ ^2P$ J $1/2 \rightarrow 3/2$ and $\lambda 6371.37$ $3s^2 4s \ ^2S \rightarrow 3s^2 4p \ ^2P$ J $1/2 \rightarrow 1/2$). As Si has the most prominent feature till the maximum of the SN evolution, the velocity of Si is used as the photospheric velocity. The measured velocity of C lower than Si could either mean that the photosphere moves with the velocity of C or both C and Si are moving at the same photospheric velocity, and, instead of forming in a shell, C is formed in clumps at the photospheric velocity, offset by an angle θ to the line of sight (Foley et al. 2010b; Parrent et al. 2011), or the C layer is mixed to the inner regions.

This motivates us to look into these objects more deeply to understand their progenitor and explosion mechanism. We took five such objects - SNe 2006bt (Foley et al. 2010b), 2011aa (Dutta et al. 2022), 2012dn (Chakradhari et al. 2014), 2017hpa (Dutta et al. 2021) and 2018oh (Li et al. 2019a) for the study. The details of the objects are presented in TABLE 4.15.

4.3.1 Models

We use the Monte Carlo radiative transfer code `SEDONA` to generate light curves and spectral sequences. The inputs to the code are the density profiles and the elemental abundances of the model ejecta.

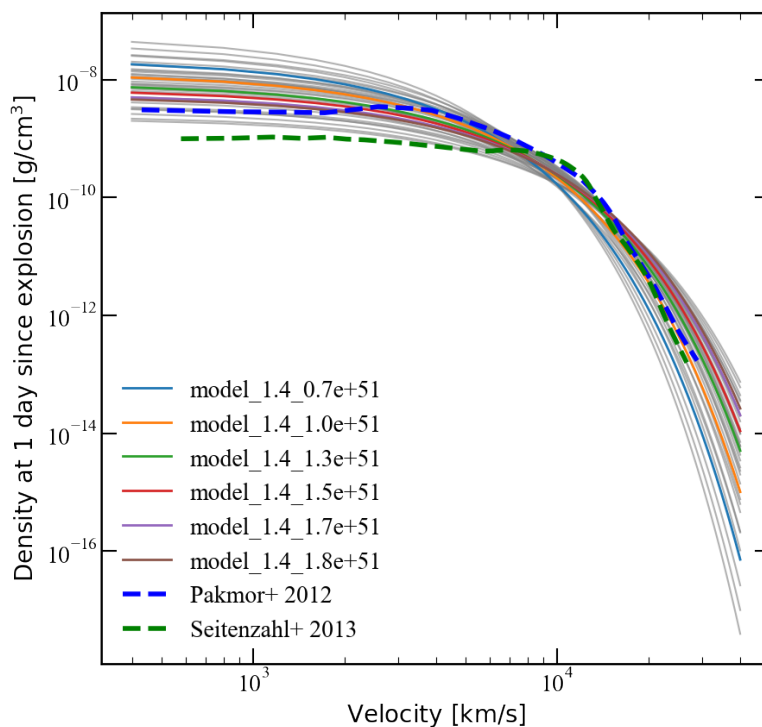


FIGURE 4.25: Analytical density profiles with masses 1.0, 1.2, 1.4, 1.6, 1.8, and $2.0 M_{\odot}$, and kinetic energies $0.7, 1.0, 1.3, 1.5, 1.7,$ and 1.8×10^{51} erg. Highlighted solid lines represent the models with mass $1.4 M_{\odot}$ and different kinetic energy. The dashed lines are the one-dimensional angle averaged density profiles for the violent merger model P12 and delayed detonation model S13 taken from HESMA database (Kromer et al. 2017).

4.3.1.1 Density Profiles

We construct 1D parametric density profiles (FIGURE 4.25) similar to the 1D angle-averaged density profile of the violent merger of two dissimilar mass WD (P12) and the delayed detonation in a M_{ch} WD (N40, Seitenzahl et al. 2013)[S13]. The analytical density profile $\rho(v, t)$ is given by -

$$\rho(v, t) = \rho_0 \left(\frac{t_0}{t}\right)^3 \exp\left(-\frac{v}{v_e}\right), \quad (4.7)$$

where, ρ_0 is the central density at a time t_0 . The total mass is expressed as -

$$M = 8\pi\rho_0(v_e t_0)^3 \quad (4.8)$$

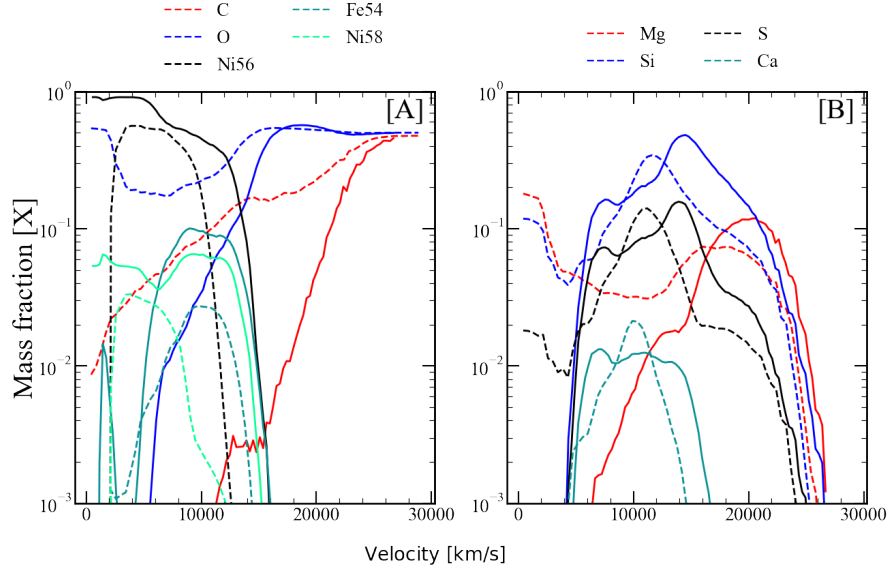


FIGURE 4.26: Abundance structure of the elements formed in the ejecta for the two explosion models considered. Dashed lines are for the violent merger model, whereas solid lines represent the abundance of the delayed detonation scenario. Panel [A] consists of C, O and the Fe group elements, while IMEs are shown in panel [B]. The abundances for both the explosion scenarios are taken from HESMA database (Kromer et al. 2017).

Here, v_e is the e-folding velocity expressed in terms of total mass and total kinetic energy E_K as -

$$E_K = 6Mv_e^2 \quad (4.9)$$

The density profiles are generated by varying the mass (M), and kinetic energy (E_k). Mass is varied between $1.0 M_\odot$ and $2.0 M_\odot$, E_k is varied between 0.7×10^{51} to 1.8×10^{51} erg. All the models are generated with 100 spatial zones with the outer velocity fixed at $40\,000 \text{ km s}^{-1}$. The density profiles are generated at one day since the explosion.

4.3.1.2 Abundances

We have used the one-dimensional stratified abundance structure of the violent merger of two CO WDs (P12), and delayed detonation in a M_{ch} WD (S13). In

TABLE 4.15: Details of the objects used in the study

Object	Redshift (z)	$E(B - V)_{Gal}$ (mag)	$E(B - V)_{Host}$ (mag)	B_{max} (mag)	$\Delta m_{15}(B)$ (mag)	μ^* (mag)	v_{CII} (near max)	v_{SiII} km s ⁻¹
SN 2006bt	0.033	0.0424 ± 0.0013	0.0	2453856.9	1.09 ± 0.06	35.72 ± 0.11	5200	12 500
SN 2011aa	0.013	0.065 ± 0.003	0.0 ± 0.0	2455611.65	0.59 ± 0.07	33.66 ± 0.27	5400	12 200
SN 2012dn	0.010	0.06 ± 0.0009	0.12 ± 0.01	2456132.89	0.92 ± 0.04	33.12 ± 0.36	7500	11 000
SN 2017hpa	0.016	0.1518 ± 0.0069	0.08 ± 0.06	2458066.29	0.98 ± 0.16	34.08 ± 0.09	10 700	11 300
SN 2018oh	0.011	0.0369 ± 0.0027	0.0	2458162.9	0.96 ± 0.02	33.61 ± 0.05	9250	10 100

* $H_0 = 73.0$ km s⁻¹ Mpc⁻¹.

the delayed detonation case, towards the inner layers of the ejecta, C is present up to 9000 km s⁻¹ and O is present up to 5000 km s⁻¹. In contrast, in the violent merger scenario (VM), C and O are present in the inner layers with a significant mass fraction. In the outer regions ($> 20\,000$ km s⁻¹) C is present more in the VM abundances compared to DDT. In the DDT-N40 model inner layers, Mg is present up to 5500 km s⁻¹, while Si and S are present up to 4000 km s⁻¹. In comparison, these IMEs are present in the innermost layers of the VM model (< 1000 km s⁻¹). Ca is present upto 16 000 km s⁻¹ in the DDT N40 model while it is present upto 14 000 km s⁻¹ in the VM abundances. A significant amount of ⁵⁴Fe ($X \sim 0.1$) and ⁵⁸Ni are present in the DDT-N40 abundances compared to the VM model. The innermost layers (< 1000 km s⁻¹) of the DDT-N40 abundances are mostly ⁵⁶Ni ($X \sim 0.9$), while the innermost layers in the VM abundances have O ($X \sim 0.5$), Si ($X \sim 0.1$), S ($X \sim 0.1$), Mg ($X \sim 0.2$), and C ($X \sim 0.1$). See FIGURE 4.26 for comparing the abundances in both models.

In this work, we have generated 72 models varying the density profiles, based on the abundances of the DDT-N40 (36) and VM (36) models. The value of $\epsilon = 1.0$ for all the models. We aim to fit the light curves of the five objects with these 72 models. The decline rates, and absolute magnitudes of the models are obtained with third-order spline fit to the light curves in the initial phase up to 30 days. The model which has the value of $\Delta m_{15}(B)$ and M_B close to the observed value is chosen as the “best model” and has been considered for further spectroscopic investigation. Since, we are considering the “best model” based on peak magnitude

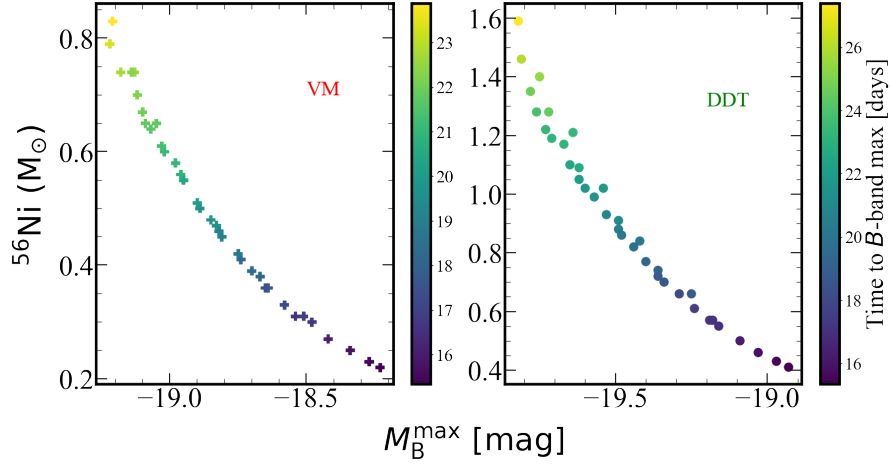


FIGURE 4.27: ^{56}Ni mass vs $\Delta m_{15}(B)$ for the models. Left shows the model parameters from VM models, and right panel shows the same from DDT models. Time to B -max is shown in colourbar.

which is dependent on extinction, and distance modulus, we should caution that changing $E(B - V)$, and μ will change peak magnitude value but not the decline rate and some other model may best explain the light curve.

The VM model peak magnitudes are within the range of -18.23 to -19.22 mag. The lowest ^{56}Ni mass is $0.22 M_{\odot}$ for the model with mass $1.0 M_{\odot}$ and kinetic energy 1.8×10^{51} erg. The maximum ^{56}Ni mass is $0.83 M_{\odot}$ for the model with mass $2.0 M_{\odot}$ and kinetic energy 0.7×10^{51} erg (FIGURE 4.27). The DDT models of the same mass range are brighter than the VM models due to more ^{56}Ni in the ejecta. The DDT models have ^{56}Ni mass within $0.41 M_{\odot}$ to $1.59 M_{\odot}$. The peak magnitude varies between -18.93 to -19.82 mag. We find that the models with the same mass but lower kinetic energy are brighter. This is because, the density profile is such that more mass is present in the inside than the outside layers (FIGURE 4.25). So, more ^{56}Ni is produced. In this work, we have only considered comparing the optical light curves and spectra with the models. The observed properties of the explosion show more diversity with viewing angle in UV-bands compared to optical (Kromer et al. 2016). Since, we have generated the models in 1D we have focused on the optical signatures.

The models are designated as *model_mass.kineticenergy_modelname* (for example - a model with $1.2 M_{\odot}$ of ejecta, 1.4×10^{51} erg of kinetic energy, and the abundances are that for the DDT-N40 model is denoted as *model_1.2_1.4e + 51_ddt*).

4.3.2 Model comparison with observations

4.3.2.1 SN 2006bt

SN 2006bt has been studied by [Foley et al. \(2010b\)](#). The SN has low luminosity, and slowly declining light curves ($\Delta m_{15}(B) = 1.09 \pm 0.06$). There is no prominent *i*-band secondary peak. Using a μ of 35.72 ± 0.11 , we get $M_B = -18.75 \pm 0.11$ mag. The spectral evolution is similar to low luminosity SNe Ia indicating a cool photosphere. The velocity of C II $\lambda 6580$ is less than Si II 6355. The SN exploded in a region with no signs of recent star formation. This object has no reported *Swift*-UV observations.

Among the models based on the DDT-N40 abundances, SN 2006bt is best described by a model with a mass of $1.2 M_{\odot}$, and kinetic energy 1.3×10^{51} erg. The DDT model has $\Delta m_{15}(B) = 1.08$ mag, and $M_B = -19.29$ mag. The model with a mass of $1.4 M_{\odot}$, kinetic energy 1.8×10^{51} erg and with violent merger abundances has $\Delta m_{15}(B) = 1.07$ mag, and $M_B = -18.74$ mag. The DDT model is brighter in every band with a prominent secondary peak in *i*-band. The violent merger model is brighter in the *U*-band but matches the observed light curves in the other bands. This model has no secondary peak in redder bands.

The spectra of SN 2006bt at pre-maximum (-1.93 day), near-maximum (-0.01 day), and post-maximum ($+6.69$ day) phases have been compared with models which best match the light curves. Near maximum, the VM model is bluer than

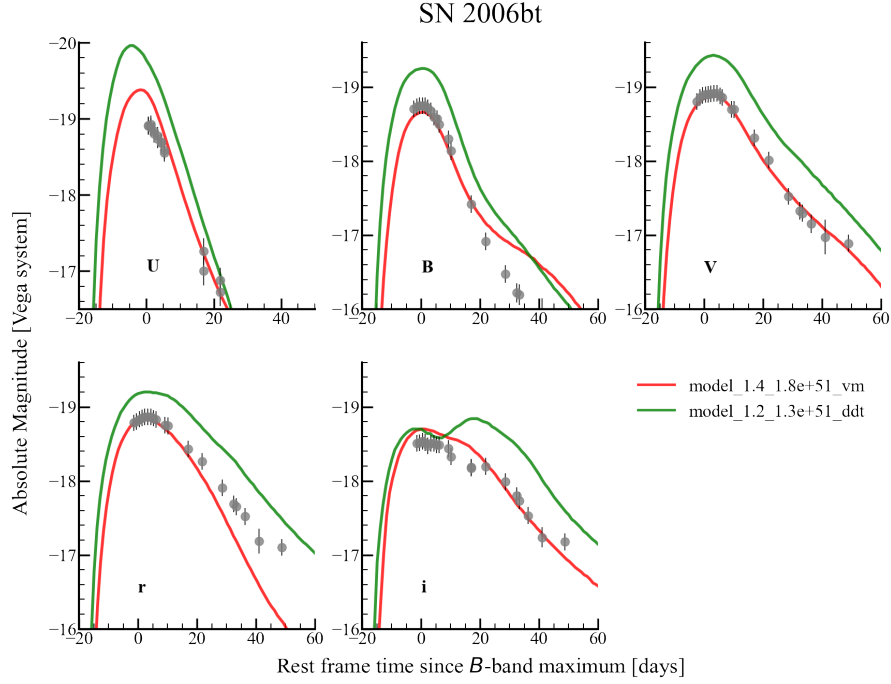


FIGURE 4.28: The light curves of 2006bt in $UBVRi$. The best-fit synthetic light curves are overplotted.

the observed spectrum, but matches the continuum well in the post-maximum phase. The Si II $\lambda 6580$ velocity also matches the observed one. Prominent features of C II $\lambda 6580$, C II $\lambda 7234$ are seen in the synthetic spectrum till maximum. The mass of C produced in the VM model is $0.15 M_{\odot}$. The DDT synthetic spectra are bluer, have high blue-shift of the Si line, and no presence of C II features.

4.3.2.2 SN 2011aa

A detailed study of SN 2011aa has already been presented in **Section 4.2**, and also in [Dutta et al. \(2022\)](#). Although the VM models described earlier explain this event, for the sake of completeness, we also present comparison with DDT models. The SN has the slowest declining B -band light curve ($\Delta m_{15}(B) = 0.59$ mag). The secondary maximum in I is either absent or equally bright. Using a μ of 33.66 ± 0.27 , we get $M_B = -19.21 \pm 0.27$ mag. 2011aa is NUV-blue according

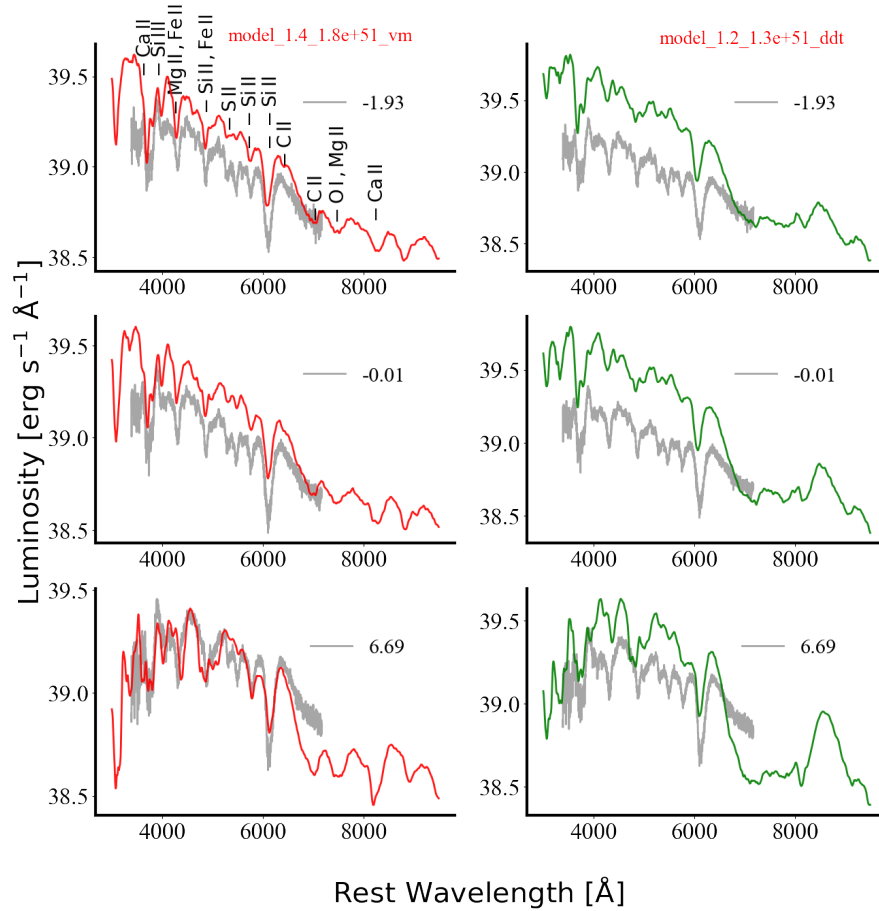


FIGURE 4.29: The spectra of SN 2006bt at different phases plotted with the DDT, and VM models.

to Milne classification. The velocity of C II $\lambda 6580$ is less than Si II $\lambda 6355$ and the C II feature is present post-maximum.

Among the DDT-N40 models, SN 2011aa is best described with a mass of $2.0 M_{\odot}$, and kinetic energy 1.3×10^{51} erg. The DDT model has $\Delta m_{15}(B) = 0.59$ mag, and $M_B = -19.78$ mag. The model with a mass of $1.8 M_{\odot}$, kinetic energy 1.0×10^{51} erg and violent merger abundances has $\Delta m_{15}(B) = 0.59$ mag, and $M_B = -19.12$ mag. The DDT model is brighter in every band, with a prominent secondary peak in *I*. The violent merger model matches the observed light curves in all the bands, but the synthetic light curve in *U*-band declines faster. This model has no secondary peak in the *I*-band. In Dutta et al. (2022), the 1D density profile (mass $1.95 M_{\odot}$, and kinetic energy 1.7×10^{51} erg) and the abundances from the VM

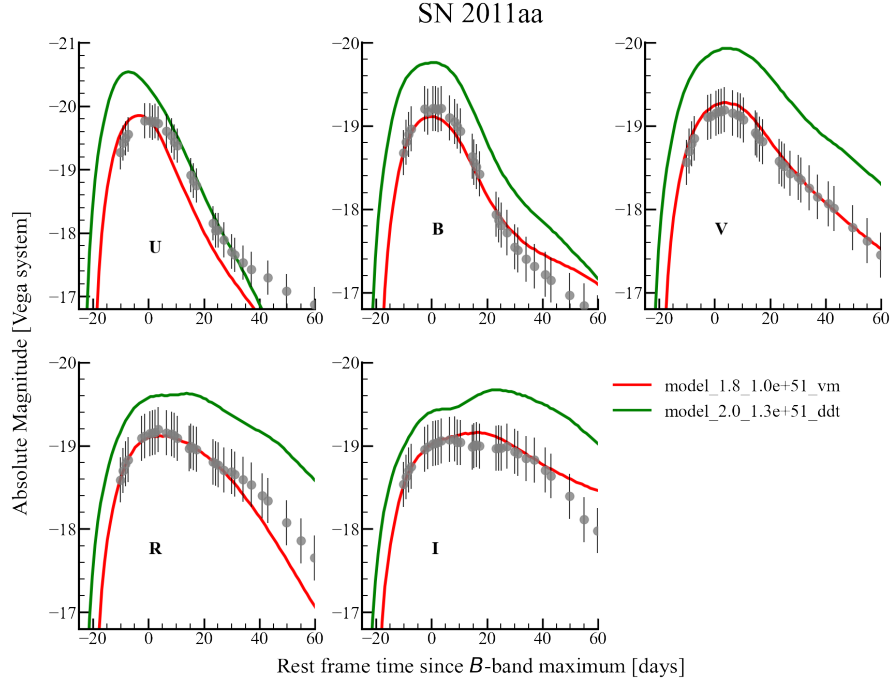


FIGURE 4.30: The light curves of 2011aa in *UBVRI*. The best-fit synthetic light curves for the DDT-N40, and VM models are overplotted.

merger model (P12) has been used to generate synthetic light curves and spectra. Also the redistribution probability ϵ has been changed to understand its effect on the observables. But, in this work we have generated a suite of models based on fixed masses and kinetic energy. So the difference in values of mass and kinetic energy may arise.

The spectral evolution at various phases (-10.2 , $+0.5$, and $+10.4$ days) are better matched with the synthetic spectra generated with the VM abundances. The continuum, Si II $\lambda 6355$ velocity, and C II absorption are better represented by the VM model than the DDT model. The mass of unburned C in the VM model is $0.11 M_{\odot}$. The O I/Mg II feature at around 7500 \AA , and Ca II NIR feature is better reproduced by the violent merger abundances in the spectrum at $+10.4$ day. This points to correct abundances which has been used to model the spectra. The DDT model does not reproduces the O I, and the Ca II profiles.

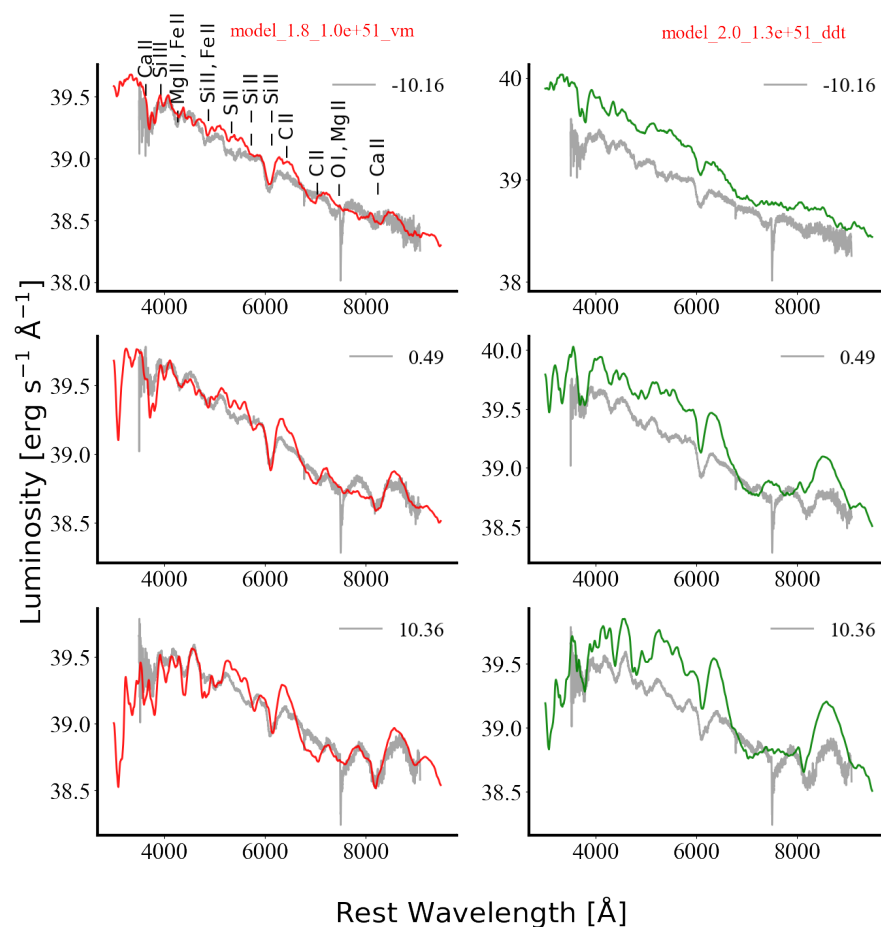


FIGURE 4.31: The spectra of 2011aa at different phases plotted with the DDT, and VM models.

4.3.2.3 SN 2012dn

The observed properties of 2012dn are similar to super-Chandrasekhar SNe, but it has lower luminosity (Chakradhari et al. 2014). The $\Delta m_{15}(B)$ is 0.92 ± 0.04 mag, and $M_B = -19.47 \pm 0.36$ mag. The I -band secondary peak is absent. The $uvw1 - uvv$ colour is bluer. The C II $\lambda 6580$ velocity is lower than Si II $\lambda 6355$. This feature is present in the post-maximum phases also. The nebular phase spectra show forbidden lines of Ca and O.

The DDT model best describing SN 2012dn is with a mass of $1.6 M_\odot$, and kinetic energy 1.8×10^{51} erg. The DDT model has $\Delta m_{15}(B) = 0.93$ mag, and $M_B =$

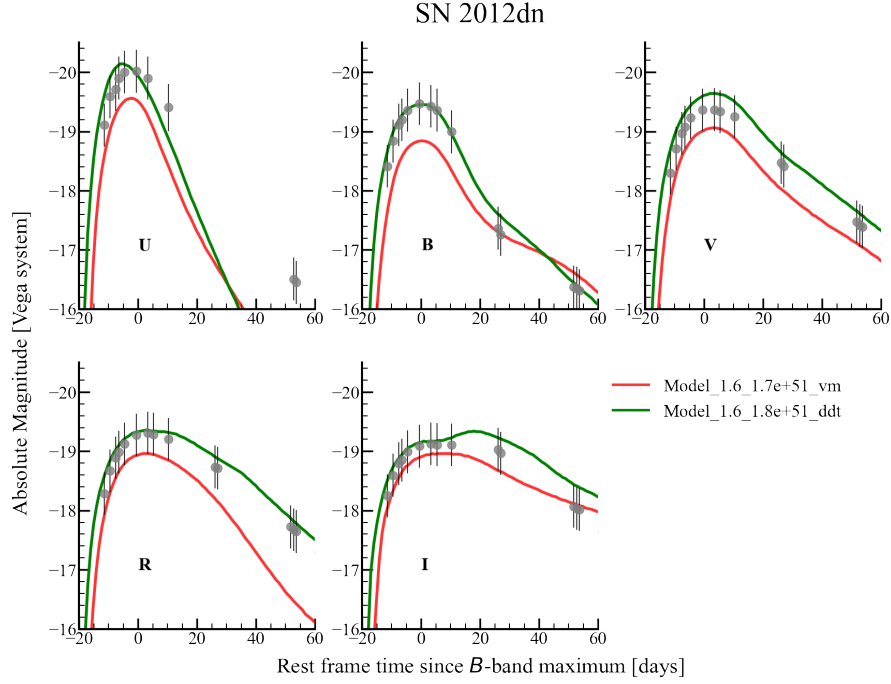


FIGURE 4.32: The light curves of 2012dn in *UBVRI*. The best-fit synthetic light curves for the DDT-N40, and VM models are also shown.

−19.48 mag. The model with VM abundances, mass $1.6 M_{\odot}$, and kinetic energy 1.7×10^{51} has $\Delta m_{15}(B) = 0.94$ mag, and $M_B = -18.85$ mag. The DDT model matches the light curves in all bands except *I*-band, where there is a secondary maximum. The observed light curve does not show prominent secondary maximum. The violent merger model is fainter in all bands.

We compare the spectral evolution of SN 2012dn with the VM, and the DDT models. The continuum and the absorption features in the blue regions are better represented by DDT model. However, the Si II line is blue-shifted more compared to the observations. The synthetic spectra generated with the VM model matches the Si II line better near, and post-maximum. In the observed pre-maximum spectra, the C II absorption feature is very strong, whose strength is not reproduced by either of the models. In the VM model, unburned C mass is $0.15 M_{\odot}$. This C II is also present in the post-maximum spectra, which is not reproduced in the models. Ca II absorption feature is better modelled with the VM abundances.

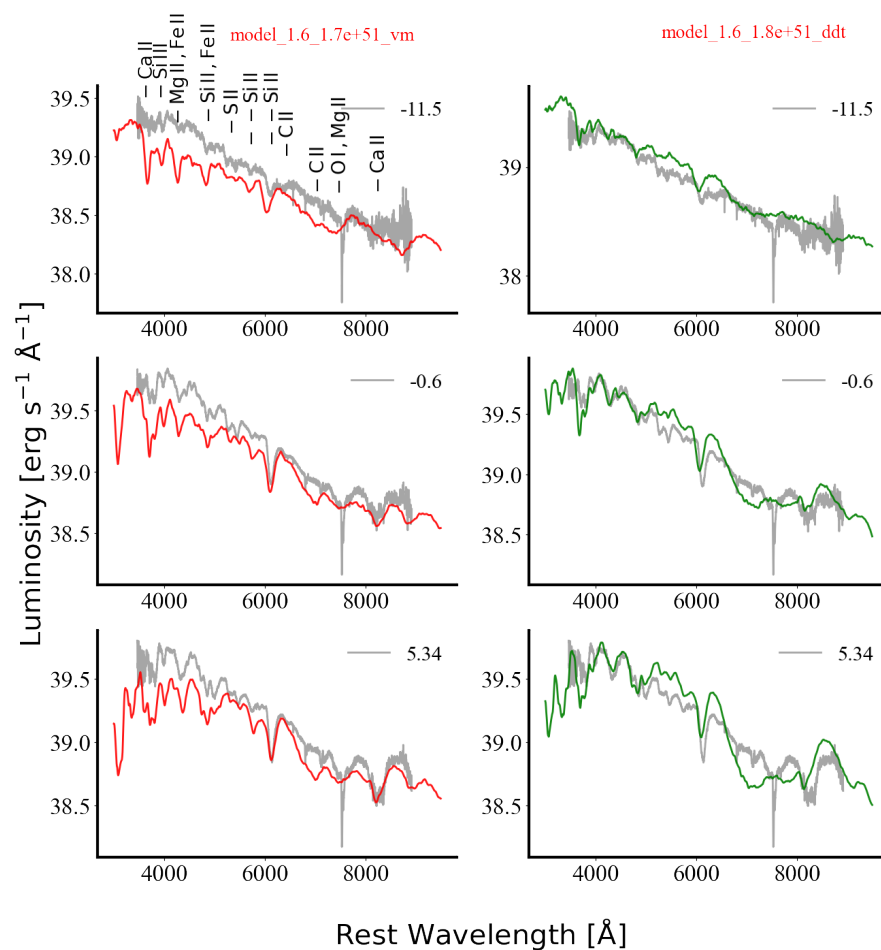


FIGURE 4.33: The spectra of 2012dn at different phases plotted with the DDT, and VM models.

4.3.2.4 SN 2017hpa

SN 2017hpa is a normal Ia with $\Delta m_{15}(B) = 0.98 \pm 0.16$ mag, and peak magnitude $M_B = -19.45 \pm 0.15$ mag (Dutta et al. 2021). There is a prominent secondary peak in the I -band. The SN falls in the NUV-blue group. The SN shows a prominent presence of C in the early phase, and the C II $\lambda 6580$ velocity is less than Si II 6355.

From the list of our DDT models, 2017hpa is best described with a mass of $1.4 M_{\odot}$, and kinetic energy 1.5×10^{51} erg. The model has $\Delta m_{15}(B) = 0.98$ mag with a peak absolute magnitude $M_B = -19.40$ mag. The I -band secondary peak is

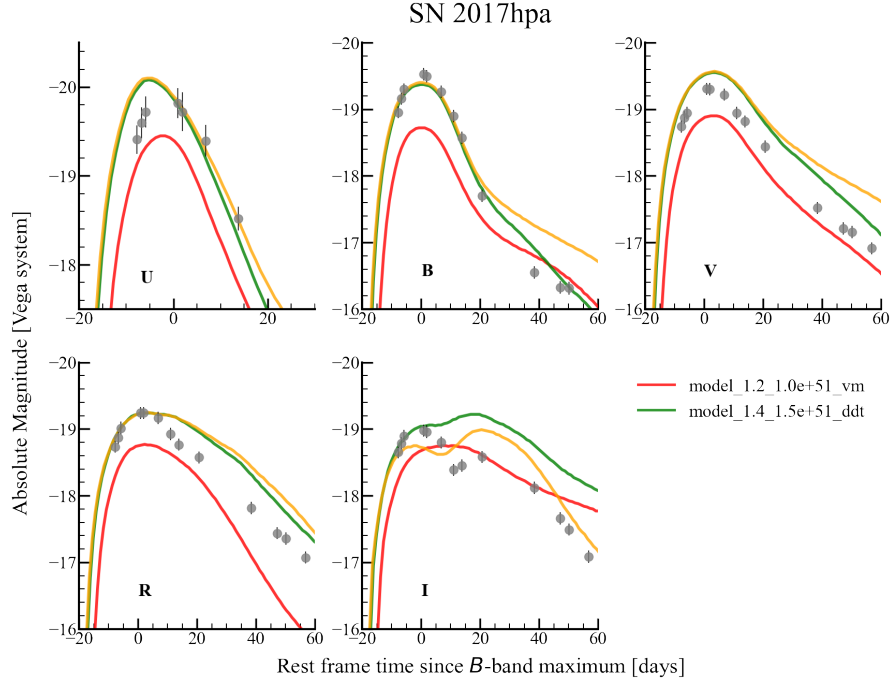


FIGURE 4.34: The light curves of 2017hpa in *UBVRI*. The best-fit synthetic light curves for the DDT, and VM models are shown. To reproduce the secondary maximum, we have used an $\epsilon=0.0$ for Ca and $\epsilon=1.0$ for the other elements in the DDT models. This is shown with yellow in the plots.

brighter than the primary in the model. We have considered another model based on the suggestions by Kasen (2006) to use a scattering-dominated line source function for Ca ($\epsilon=0.0$) and all other elements to be absorption dominated. This produces a prominent secondary peak, and the declining phase of the light curve is better represented. The violent merger model with mass $1.2 M_{\odot}$, and kinetic energy 1.0×10^{51} erg has $\Delta m_{15}(B) = 0.98$ mag, and $M_B = -18.74$ mag. The light curves are fainter in every band with no secondary maximum in *I*.

The spectra of 2017hpa at three phases are compared with VM, and DDT models that gives the $\Delta m_{15}(B)$, and M_B close to the observed values. The VM model matches the Si II line velocity, while the DDT model has a higher blue blueshift. The continuum in the blue is better represented by the DDT model. Presence of C II $\lambda 6580$ is reproduced by the VM model. The mass of C in the VM model is $0.1 M_{\odot}$, and that in DDT model is $0.02 M_{\odot}$. In SECTION 4.16, by modelling a

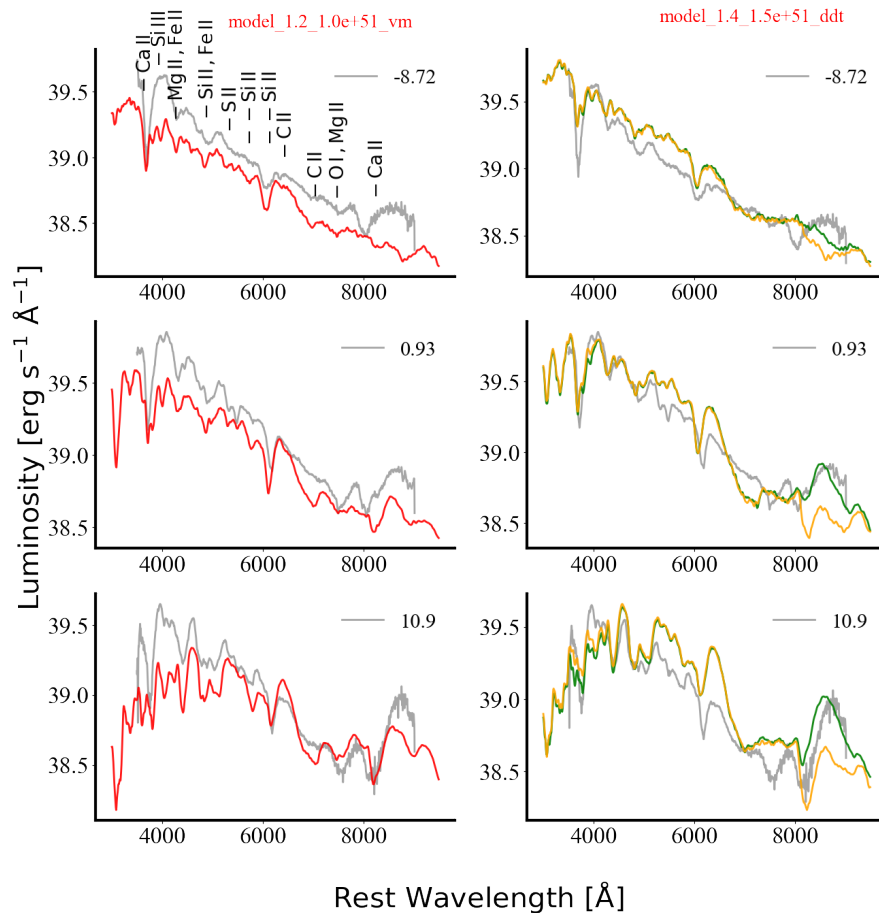


FIGURE 4.35: The spectra of 2017hpa at different phases plotted with the DDT, and VM models.

single spectrum at -8.9 day with TARDIS, we found $0.019 M_{\odot}$ of C. In that case, we had only considered the ejecta above 14000 km s^{-1} . The DDT model with $\epsilon = 0.0$ for Ca, produces a strong Ca absorption feature in the NIR.

4.3.2.5 SN 2018oh

SN 2018oh is a normal Ia with $\Delta m_{15}(B) = 0.96 \pm 0.02 \text{ mag}$, and $M_B = -19.41 \pm 0.05 \text{ mag}$ (Li et al. 2019a). The SN showed presence of I -band secondary peak, NUV-blue colours, and persistent C absorption feature. The velocity of C II $\lambda 6580$

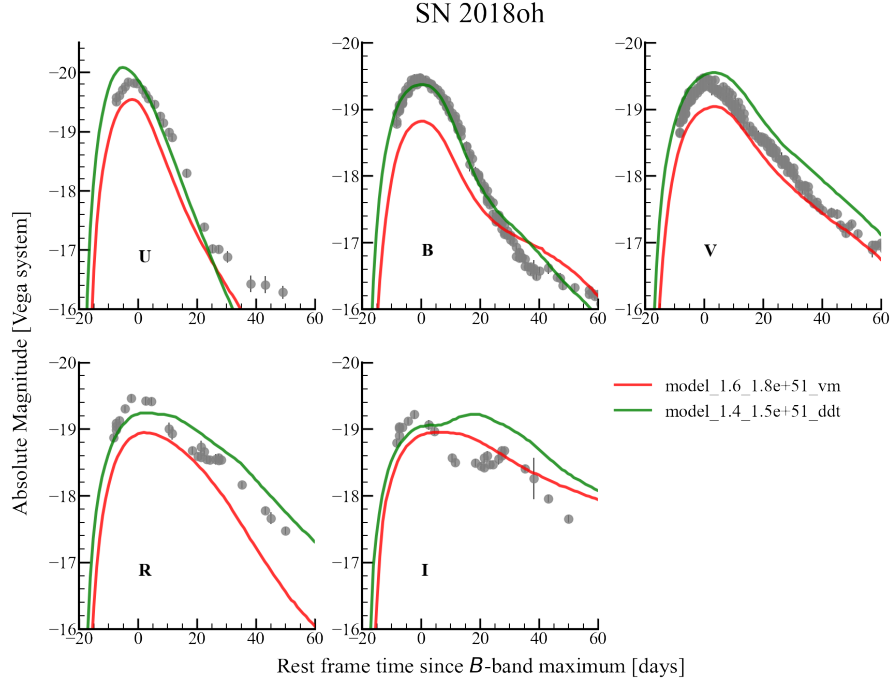


FIGURE 4.36: The light curves of 2018oh in *UBVRI*. The best-fit synthetic light curves for the DDT, and VM models are shown.

is initially higher than Si II 6355, but decreases near maximum and this trend is seen post-maximum.

The DDT model with mass $1.4 M_{\odot}$, and kinetic energy 1.5×10^{51} erg has $\Delta m_{15}(B) = 0.98$ mag, and $M_B = -19.40$ mag. The model reproduces the *B*-band light curve of SN 2018oh, but it does not reproduce the redder bands. There is a secondary peak in the *I*-band. The violent merger model with mass $1.6 M_{\odot}$, and kinetic energy 1.8×10^{51} erg is significantly fainter with a peak magnitude of -18.83 mag.

The synthetic spectra generated with the DDT, and VM models are compared with SN 2018oh. We find that the Si II line profile for the DDT model has a higher blueshift compared to the observations. At -8.7 d, the VM model has a higher blueshift of the Si II feature but matches well with the observed spectrum near and post-maximum. The DDT model better represents the continuum. The C II absorption feature is present in the VM model. The mass of C in the VM model

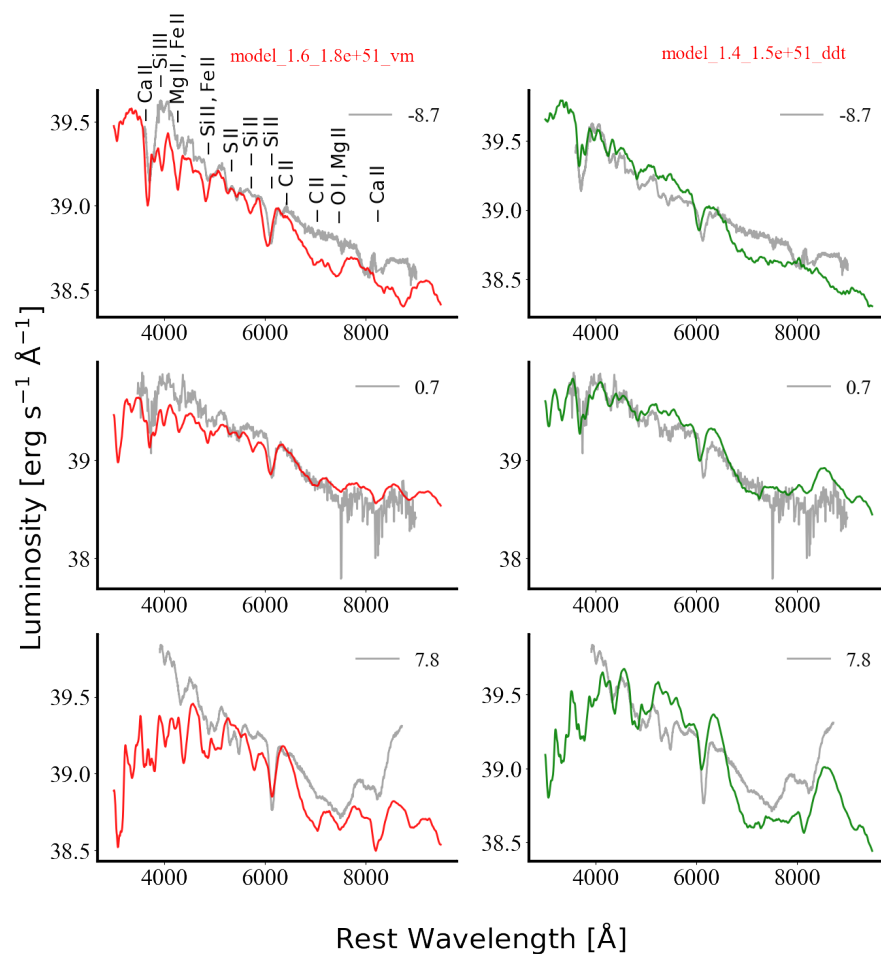


FIGURE 4.37: The spectra of 2018oh at different phases plotted with the DDT, and VM models.

is $0.16 M_{\odot}$. We find that Si II $\lambda 5972$ feature is strong in the violent merger model, compared to the DDT model. Ca II NIR feature is better reproduced by the VM abundances.

4.3.2.6 Effect of varying C abundances

We generated three more models by varying the C abundance in the model ejecta. We consider the model, *model_1.4_1.5e + 51_vm*, with VM abundances and varied the C abundance at various layers. In the first model, named *Model_VM_C1*, we increased C abundance by $X(C) = 0.1$ between 10 000 to 15 000 km s⁻¹, and by

$X(\text{C}) = 0.2$ between 15 000 to 20 000 km s^{-1} . In the second model *Model_VM_C2*, we kept the C abundance to be similar to *Model_VM_C1* and increased the C abundance by $X(\text{C}) = 0.1$ between 6 000 to 10 000 km s^{-1} . In the third model *Model_VM_C3*, we increased $X(\text{C})$ by 0.05 between 6 000 to 10 000 km s^{-1} . The models are shown in FIGURE 4.38. The mass of C in *model_1.4_1.5e + 51_vm* is $0.13 M_{\odot}$, and we increase to $0.26 M_{\odot}$ in *Model_VM_C3*. We find that the absorption feature gets stronger in *Model_VM_C3* around -8 d since *B*-max. Near maximum, most of the models show similar C absorption feature. Post-maximum, the model with no C enhancement does not show any C feature. But the C feature is seen in the other three models (see inset of FIGURE 4.38). It is to be noted that as the temperature drops with the expansion of the ejecta, the higher ionization states are less populated, and the opacity of C drops. So, the SNe with the unburned features of C seen post-maximum can be explained by either higher C abundance or higher photospheric temperature. It is also possible that due to off-center delayed detonation we see the side of the deflagration, and hence more unburned materials (Maeda et al. 2010).

4.3.3 Discussions

Supernova spectral modelling works generally consider the “abundance tomography” method, in which the spectral sequences are fit in a time-independent manner iteratively from the very early phase till the phase at which the assumptions of the code are valid (Stehle et al. 2005). This method relies on fitting a photospheric velocity, luminosity and varying the abundances till a good match is obtained (Mazzali et al. 2008). In this work, we have varied the density profiles (by varying the mass and kinetic energy), and kept the abundances fixed as given by the 3D hydrodynamical simulations. It is obvious that the abundance stratification should change with varying mass/kinetic energy. It is possible that different SNe

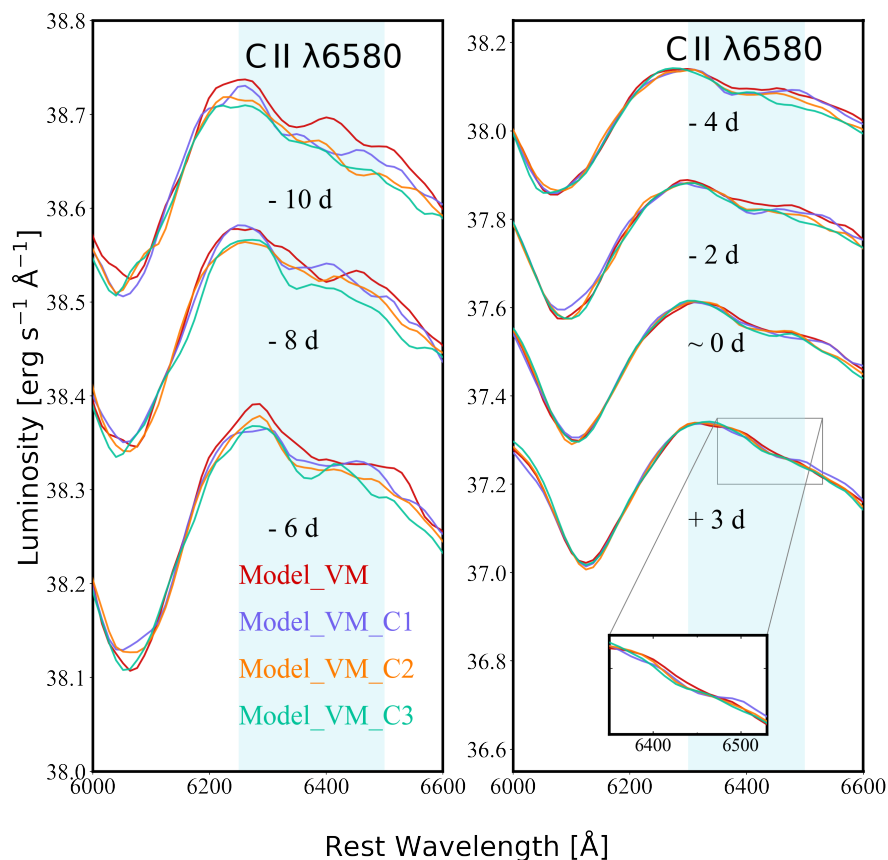


FIGURE 4.38: SEDONA models based on varying C abundances.

TABLE 4.16: Comparing models with observations of SNe

Supernova	$\Delta m_{15}(B)$ (mag)	M_B (mag)	Second I -band peak	Si II velocity	Presence of C II
SN 2006bt	VM	VM	VM	VM	VM
SN 2011aa	VM	VM	VM	VM	VM
SN 2012dn	DDT	DDT	VM	VM	VM
SN 2017hpa	DDT	DDT	DDT	VM	VM
SN 2018oh	DDT	DDT	DDT	VM	VM

Note: If the observable is best matched with DDT model, we write DDT, else VM.

have different abundances and exploring various abundances may give better results. But instead of fine-tuning the abundances with hand in our simulations for every object, we explore the effect of changing mass and kinetic energy. The ejecta's time evolution is considered without the assumption of sharp blackbody photosphere.

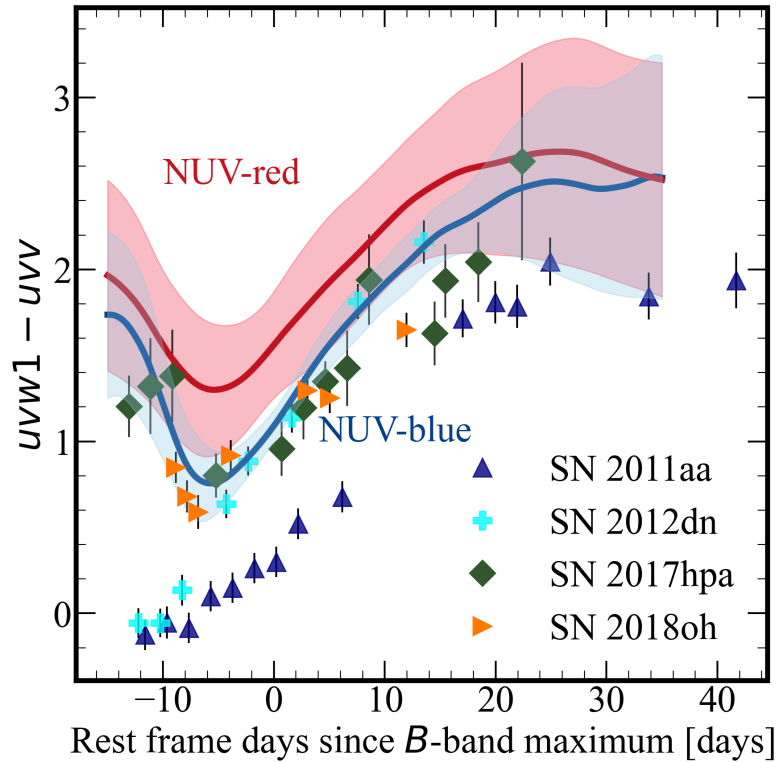


FIGURE 4.39: The NUV-blue and NUV-red group from Milne et al. (2013). For the NUV-blue sample, we have taken SNe 2008hv, 2008Q, 2011by, 2011fe, 2012cg, and 2017cbv. The NUV-red sample consists of SNe 2005cf, 2007sr, 2007af, 2008ec, 2009an, 2009ig, PTF10icb, and 2017erp. The NUV-blue SNe 2011aa, 2012dn, 2017hpa, and 2018oh are also shown. The colours are corrected only for Galactic extinction.

In this work, we study the optical light curves, and spectral evolution of five objects that showed similarities in their photometric/spectroscopic properties. For these five objects, the observed velocity of C II which is an unburned signature of the explosion is lower than Si II. Apart from SN 2006bt, all the other objects are also NUV-blue (FIGURE 4.39). We performed, 1D radiative transfer simulations with abundances generated by three-dimensional hydrodynamical simulations (P12, S13), and varied the density profiles. For SNe Ia, originating from violent mergers of two CO WDs with different masses, unburned elements like C, and O are present in the inner regions of the ejecta. This could possibly mean that we may find C at lower velocity layers and also at phases post-maximum. For SNe 2006bt, and 2011aa we find that these objects are better explained by the VM scenario. The $\Delta m_{15}(B)$, and M_B of these two objects falls within the

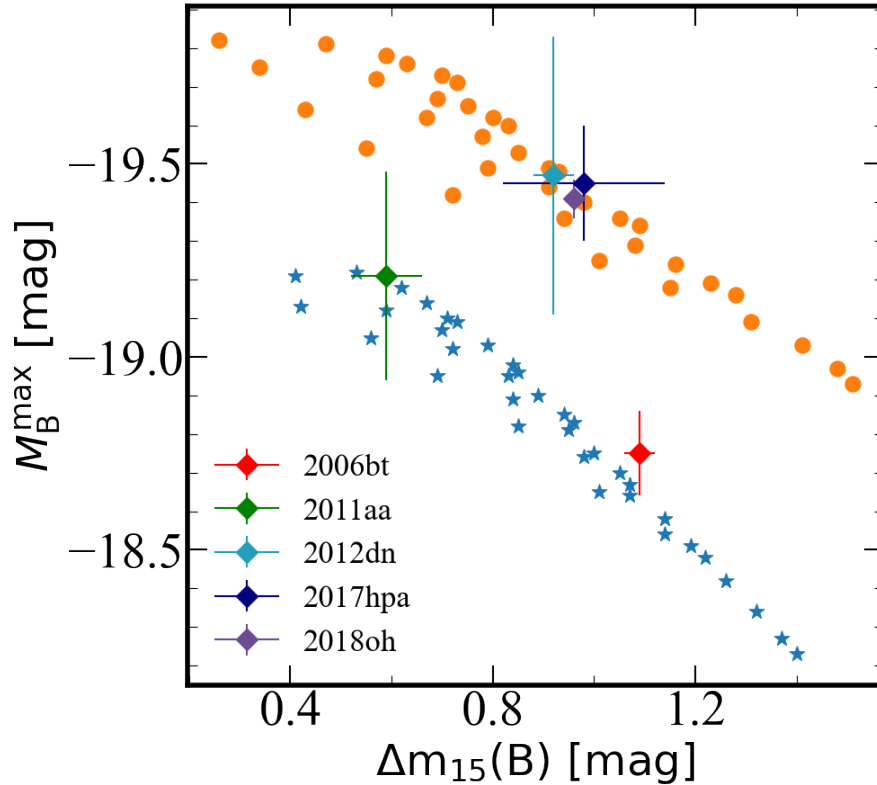


FIGURE 4.40: Peak absolute magnitude in B vs $\Delta m_{15}(B)$ for the models. Also shown, the observed M_B and $\Delta m_{15}(B)$ for the five objects considered in this work. The blue stars are parameters from the VM models, while the orange solid circles are from the DDT models.

VM models (FIGURE 4.40). For SNe 2012dn, 2017hpa, and 2018oh, the observed $\Delta m_{15}(B)$, and M_B falls among the DDT models. SNe 2006bt, 2011aa, and 2012dn do not show the secondary maximum in I . The VM models also do not exhibit the secondary maximum. SN 2012dn showed $[O\ I] \lambda\lambda 6300, 6364$ (Taubenberger et al. 2019) in its nebular spectra which can be understood by the presence of unburned materials in the inner regions. 2017hpa, and 2018oh exhibit prominent secondary I -band feature. See TABLE 4.16 for a comparison of the models with the observables. SNe 2011aa, 2012dn, and 2018oh showed presence of C post-maximum. But this is not reproduced in our models. In homologous expansion, the opacity drops with time as t^{-2} , and also the temperature decreases. Despite of having C in the inner layers, the spectral sequence does not show C post-maximum. This means that the temperature is not sufficient to populate the higher ionization levels. An

ionizing source such as the presence of ^{56}Ni layer with high abundance C layer may help in understanding the presence of this feature post-maximum. The NUV-blue nature of these objects can be understood by a range of processes - presence of ^{56}Ni in the outer layers, interaction with circumstellar materials/companion, and opacity effect. If the outer ejecta layers are composed of elements with lower opacity (such as C), the ^{56}Ni rich layers will be exposed quickly due to the receding of the photosphere and hence exhibit bluer colours (Stritzinger et al. 2018).

We find that even though there are some similarities in these five objects, such as lower velocity of C than Si and NUV-blue colours, they cannot be understood by a single progenitor scenario/explosion mechanism. The models based on the violent merger abundances can better explain SN 2006bt, and SN 2011aa. The models based on DDT-N40 abundances can explain the decline rate, peak magnitude, secondary *I*-band feature for SN 2012dn, SN 2017hpa, and SN 2018oh but not the presence of C, and velocity of Si. For a better modelling of the spectroscopic features, we need to consider varying the abundance stratification for every object. Asymmetrical explosions can also explain the presence of C in the post-maximum phases. The ejecta structure of the violent merger model is asymmetrical (P12) and hence showed high polarization levels which is not seen in normal Ia (Bulla et al. 2016). Their work was based on the ejecta structure of Pakmor et al. (2012). However, consistency with polarisation observations may be obtained if different ejecta structures, secondary to primary mass ratio, ignition location, and distance between the stars are considered.

Here, we have changed the total mass, and kinetic energy to construct various density profiles. This has given us various ^{56}Ni masses, with which we probed the luminosity and decline rate of five SNe Ia. We also want to change the abundance structure within the ejecta to model the spectra more accurately. Changing the metallicity (Fe, and ^{56}Ni abundances) in the outer layers may cause the SN to be bluer/redder (Barna et al. 2021). We will also model a few other SNe showing

prominent C features upto post-maximum phases like SN 2013cv (Cao et al. 2016), SN 2002fk (Cartier et al. 2014).

Chapter 5

Understanding the explosion mechanism of Type Iax supernovae

A separate class of SNe exist at the lower luminous and faster-declining side of the Phillips relation, which are called SNe Iax. SN 2002cx was the first of this class studied in details in [Li et al. \(2003\)](#). The most important distinguishing feature of Iax is their low expansion velocity of 2000 (SN 2008ha, [Foley et al. 2009](#)) - 8000 km s⁻¹ (SN 2012Z, [Stritzinger et al. 2014](#)) as compared to “normal” Ia ($v \sim 11\,000$ km s⁻¹, [Wang et al. 2009b](#)). Their pre-maximum spectra are similar to the bright 1991T-like objects (but with much lower velocities). The spectra are dominated by ions of C II, C III, O I, IMEs like Mg II, Si II, Si III, S II, Ca II, Sc II, Ti II and also IGEs like Fe II, Co II, Fe III, Co III. The later spectra are dominated with permitted Fe lines with low expansion velocities ([Jha et al. 2006](#)). There are studies which have shown that inner ejecta in Type Iax are denser than normal Ia, possibly due to a bound remnant ([Maeda & Kawabata 2022](#)).

The peak magnitude of SNe Iax spans a wide range. 2005hk ($M_B = -18.02 \pm 0.32$ mag, Phillips et al. 2007), 2012Z ($M_B = -17.61$ mag, Yamanaka et al. 2015), 2020rea ($M_B = -18.30 \pm 0.12$ mag, Singh et al. 2022) lies on the brighter end, while 2008ha ($M_B = -18.02 \pm 0.32$ mag, Foley et al. 2009), 2010ae ($M_B = -13.44 \pm 0.54$ mag, Stritzinger et al. 2014), 2019gsc ($M_g = -13.8 \pm 0.2$ mag, Srivastav et al. 2020), 2021fcg ($M_r = -12.7 \pm 0.2$ mag, Karambelkar et al. 2021) lies on the fainter end. There are some objects which have luminosities intermediate between the bright and faint ones, like 2019muj ($M_B = -16.36 \pm 0.06$ mag, Barna et al. 2021). The I light curve does not show the secondary peak, typical of normal Ia caused either due to higher ionization of the absorption lines of Fe and Co (Kasen 2006) or strong mixing in the ejecta, which reduces the Fe-peak elements in the central region (Blinnikov et al. 2006). The optical colours (eg. $B - V$) show significant scatter, which can be related to host galaxy reddening or intrinsic to the SN itself (Foley et al. 2013).

The lower line velocities observed in SNe Iax suggest that the explosion energies must be lower. The explosion produces lesser amount of ejecta as compared to SNe Ia and leaves behind a bound remnant (Kawabata et al. 2021). The abundance distribution in the ejecta is mixed (Phillips et al. 2007). These features can be explained by pure deflagration of M_{ch} CO WD of varying strengths (Fink et al. 2014)[F14]. These models can produce a range of ^{56}Ni mass and hence the luminosity observed in bright and intermediate luminosity Iax. For the fainter Iax, like SN 2008ha, pure deflagration in M_{ch} carbon-oxygen-neon (CONE) WDs has been proposed (Kromer et al. 2015). SNe Iax show signatures of unburned carbon/oxygen in their spectra. These are essential in understanding the explosion models. Three-dimensional deflagration will produce unburned material in the inner parts of the ejecta near the center. A detonation will burn the materials in the inner regions and leave unburned material at lower density outer regions (Gamezo et al. 2003). The velocity of the unburned layers can constrain the models. The presence of CO indicates the nature of the progenitor - carbon-oxygen (CO) WDs

(Phillips et al. 2007) or carbon-oxygen-neon WDs (Kromer et al. 2015) for the lower luminous subclass of SNe Iax.

There have been a few studies to understand the progenitors of Iax. A blue progenitor was detected for SN 2012Z in deep pre-explosion Hubble Space Telescope (HST) images. The colours and luminosity indicated the progenitor to be a WD accreting matter from a helium star (McCully et al. 2014, 2021). In the case of SN 2004cs and SN 2007J, He I emission feature was detected in their post-maximum spectrum (Foley et al. 2009, 2013), which was explained as being due to a CO WD accreting matter from a He-donor, or due to interaction with circumstellar material (Foley et al. 2009). However, in case of 2007J, the large helium content ($\sim 0.01 M_{\odot}$) challenges the helium shell accretion scenario on a M_{ch} WD (Magee et al. 2019). A source consistent with the position of 2008ha was detected in the post-explosion HST image, which could be the progenitor WD remnant, or the companion star. This source is redder than the progenitor of 2012Z (Foley et al. 2014). The faint SN 2008ha has been proposed to be of core-collapse origin (Valenti et al. 2009). But based on the presence of S II in the near maximum spectrum Foley et al. (2010a) argued for thermonuclear origin. S is the product of CO burning of a WD and its presence in the outer layers indicates a thermonuclear explosion. Most massive star progenitor scenarios were rejected as progenitors for SN 2008ge from the SFR of the host (Foley et al. 2010c). Using pre-explosion HST images for SN 2014dt, red giant or horizontal branch stars ($M_{\text{initial}} \geq 8 M_{\odot}$) and massive main-sequence stars ($M_{\text{initial}} \geq 16 M_{\odot}$) are ruled out as possible progenitors (Foley et al. 2015). SN 2014dt shows mid-IR flux excess consistent with emission from newly formed dust. The derived mass-loss rate is consistent with either an AGB or red-giant star (Fox et al. 2016).

The observed diversity and the possibility of a diverse class of progenitors make it important to study SNe Iax. In this chapter, we present observations of three SNe Iax - SNe 2020sck, 2022eyw, and 2022xlp. For SN 2020sck, we have performed

radiative transfer simulations with TARDIS, and compared the synthetic spectra to observations. For 2022eyw, and 2022xlp we have presented the observations and have compared these objects with respect to other Type Iax from the literature. We discuss possible explosion models that can explain SNe 2020sck, 2022eyw, 2022xlp and other Iax.

5.1 SN 2020sck: deflagration in a carbon-oxygen white dwarf

5.1.1 Introduction

SN 2020sck was discovered by [Fremling \(2020\)](#) on 2020 August 25, 10:03 UT (JD = 2459086.92) with a magnitude of 19.7 mag in ZTF-*r* filter. The last non-detection was reported on 2020 August 25 09:07 UT with a limiting magnitude of 20.63 mag in the same filter. The object was classified as SN Iax based on a spectrum obtained on 2020 August 30, 03:43 UT (JD=2459091.66) by the Liverpool Telescope ([Prentice et al. 2020](#)). The important parameters of 2020sck and its host galaxy are presented in Table 5.1.

5.1.2 Observations

Imaging of SN 2020sck in Bessell's *UBVRI* bands was carried out with HFOSC on HCT. Photometric observations with HCT started on 2020 August 31, at 5.4 days before *B*-band maximum and continued till 2020 November 13. The local stars in the SN field (FIGURE 5.1), are calibrated using Landolt standards PG 1633+099 and PG 0231+051 observed on 2020 September 01, PG 2331+055, PG 2213-006

TABLE 5.1: Parameters of 2020sck and its host.

Parameters	Value	Ref.
<i>SN2020sck:</i>		
<i>SN 2020sck/ZTF20abwrcmq:</i>		
RA (J2000)	$\alpha = 01^{\text{h}}10^{\text{m}}34^{\text{s}}84$	2
DEC (J2000)	$\delta = +02^{\circ}06'50''15$	2
Discovery Date	2020 August 25 10:03 UT (JD 2459086.92)	2
Last non-detection	2020 August 25 09:07 UT (JD 2459086.88)	2
Date of explosion	2020-08-20 21:15 UT $2459082.39^{+1.57}_{-1.37}$	1
Date of <i>B</i> -band Maxima	2020 September 06 08:09 UT (JD 2459098.84 \pm 0.30)	1
$\Delta m_{15}(B)$	2.03 \pm 0.05 mag	1
$E(B - V)_{\text{Galactic}}$	0.0256 \pm 0.0014 mag	3
$E(B - V)_{\text{Host}}$	0.00 mag	1
M_{Ni}	$0.13^{+0.02}_{-0.01} M_{\odot}$	1
M_{ej}	$0.34^{+0.07}_{-0.10} M_{\odot}$	1
E_{k}	$0.05^{+0.01}_{-0.01} \times 10^{51} \text{ erg s}^{-1}$	1
<i>Host Galaxy:</i>		
Name	2MASX J01103497+0206508	
Type	H-II galaxy	4
RA (J2000)	$\alpha = 01^{\text{h}}10^{\text{m}}34^{\text{s}}99$	4
DEC (J2000)	$\delta = +02^{\circ}06'51''48$	4
Redshift	$z = 0.016 \pm 0.00010$	4
Distance modulus	$\mu = 34.24 \pm 0.22 \text{ mag}$	5
$12 + \log(\frac{O}{H})$	8.54 \pm 0.05 dex	1
SFR	0.09 $M_{\odot} \text{ yr}^{-1}$	1

(1) This paper; (2) Fremling 2020; Prentice et al. 2020 (3) Schlafly & Finkbeiner

(2011) (4) Skrutskie et al. (2006) (5) <http://leda.univ-lyon1.fr/>

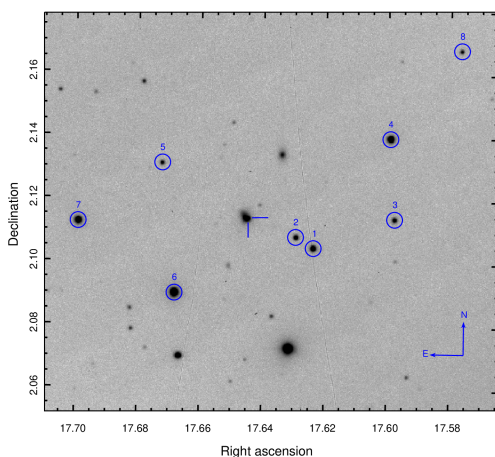


FIGURE 5.1: The field of SN 2020sck. This is a $\sim 7 \times 7$ arcmin² image in *B*-band (300 sec exposure) taken with HCT on 2020 September 11. The stars circled in blue are the secondary standards used for photometric calibration. The SN is marked with crosshair.

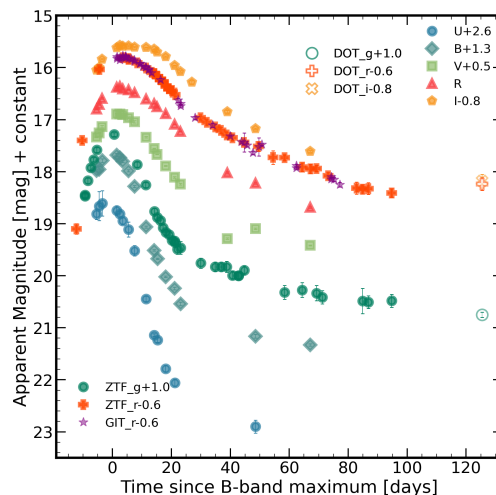


FIGURE 5.2: *UBVRI*, *ZTF-g*, *ZTF-r*, *GIT-r'* band light curves of SN 2020sck. Also plotted are the *g*, *r* and *i*-band magnitudes obtained from DOT. *UBVRI* magnitudes are in *Vega* system, and *ZTF-g*, *ZTF-r*, *GIT-r'*, *DOT-g*, *DOT-r* and *DOT-i* magnitudes are in *AB* system.

observed on 2020 September 07, PG 2331+055 observed on 2020 September 24, PG 0231+051 observed on 20 September 27 and PG 2213-006 observed on 2020 October 25. The *UBVRI* magnitudes of the local standards are listed in TABLE 5.2. To obtain the SN magnitudes, host template subtraction has been performed using deep stacked images of the SN field observed on 2021 July 16 under good seeing conditions, after the SN had faded beyond the detection limit.

SN 2020sck was followed up in SDSS-*r'* filter with the 0.7 m fully robotic GROWTH-India Telescope (GIT). The observations began on 2020 September 07 and continued till 2020 November 23. We used the targeted mode of operation and obtained 300 sec exposure images.

The SN magnitudes in Bessell *UBVRI* and SDSS-*r'* are listed in TABLE 5.4, and TABLE 5.5.

TABLE 5.2: Magnitudes of the secondary calibration stars in the field of 2020sck.

ID	U	B	V	R	I
1	16.156 ± 0.061	16.047 ± 0.010	15.374 ± 0.004	15.013 ± 0.009	14.592 ± 0.012
2	17.069 ± 0.061	17.019 ± 0.010	16.442 ± 0.004	16.139 ± 0.009	15.759 ± 0.012
3	18.229 ± 0.063	17.016 ± 0.010	15.544 ± 0.004	14.521 ± 0.009	13.345 ± 0.012
4	15.991 ± 0.061	15.199 ± 0.009	14.177 ± 0.004	13.639 ± 0.009	13.059 ± 0.012
5	18.522 ± 0.065	17.763 ± 0.011	16.809 ± 0.004	16.254 ± 0.009	15.685 ± 0.014
6	14.292 ± 0.061	14.235 ± 0.009	13.671 ± 0.004	13.382 ± 0.009	13.027 ± 0.011
7	15.054 ± 0.061	15.096 ± 0.009	14.513 ± 0.004	14.208 ± 0.010	13.816 ± 0.012
8	19.227 ± 0.069	17.865 ± 0.011	16.452 ± 0.004	15.560 ± 0.010	14.655 ± 0.012

Late phase observations of 2020sck was obtained with the ARIES-Devasthal Faint Object Spectrograph and Camera mounted on the 3.6 m DOT (Omar et al. 2019). Imaging in SDSS- g , r and i bands were performed on 2021, January 11. The data has been reduced in the standard manner as for HFOSC. To obtain the SN magnitudes, template subtraction has been performed with SDSS images in g , r and i bands. The SN magnitudes are calibrated using photometric zero points calculated using SDSS catalog (Ahumada et al. 2020). Table 5.6 lists the magnitudes obtained with DOT.

SN 2020sck was also observed with ZTF (Bellm et al. 2019) in g , and r bands. The photometric data were collected from the public archive*.

Spectroscopic monitoring of SN 2020sck with HCT started on 2020 August 31 (JD=2459093.31) and continued till 2020 October 03 (JD=2459126.34). Low-medium resolution spectra were obtained with HFOSC using Gr7 and Gr8. The spectroscopic observations log is provided in TABLE 5.3. Telluric features are removed from the spectra. The spectra are corrected for a redshift of $z=0.016$.

*<https://alerce.online/>

TABLE 5.3: Spectroscopic observations log of 2020sck from HCT.

JD (2459000+)	Date	Phase* (d)	Range (Å)
93.31	2020-08-31	-5.53	3500-7800; 5200-9100
94.27	2020-09-01	-4.57	3500-7800; 5200-9100
95.34	2020-09-02	-3.50	3500-7800; 5200-9100
100.24	2020-09-07	1.40	3500-7800; 5200-9100
101.45	2020-09-08	2.61	3500-7800
104.35	2020-09-11	5.51	3500-7800; 5200-9100
106.39	2020-09-13	7.55	3500-7800; 5200-9100
109.28	2020-09-16	10.44	3500-7800; 5200-9100
113.18	2020-09-20	14.34	3500-7800
117.31	2020-09-24	18.47	3500-7800; 5200-9100
120.40	2020-09-27	21.56	3500-7800
122.39	2020-09-29	23.55	3500-7800; 5200-9100
126.34	2020-10-03	27.50	3500-7800; 5200-9100

*Time since *B*-maximum (JD 2459098.84).TABLE 5.4: *UBVRI* magnitudes of 2020sck from HCT.

JD	Phase*	<i>U</i> (error)	<i>B</i>	<i>V</i>	<i>R</i>	<i>I</i>
2459093.4	-5.5	16.21 0.10	16.68 0.01	16.84 0.01	16.80 0.01	16.85 0.01
2459094.2	-4.6	16.06 0.28	16.66 0.06	16.76 0.01	16.71 0.01	16.80 0.01
2459095.3	-3.5	16.01 0.24	16.49 0.04	16.63 0.02	16.59 0.01	16.64 0.01
2459100.3	1.5	16.14 0.09	16.38 0.03	16.39 0.02	16.38 0.01	16.42 0.02
2459101.4	2.6	16.21 0.05	16.43 0.02	16.40 0.01	16.36 0.01	16.38 0.01
2459102.4	3.6	16.35 0.07	16.50 0.02	16.40 0.02	16.41 0.01	16.39 0.02
2459104.4	5.6	16.51 0.14	16.68 0.02	16.46 0.02	16.43 0.01	16.38 0.02
2459106.4	7.6	--	--	--	--	16.40 0.01
2459106.5	7.6	16.92 0.10	16.98 0.02	16.54 0.02	16.49 0.01	--
2459110.4	11.6	17.84 0.05	17.76 0.02	16.84 0.01	16.60 0.01	16.41 0.01
2459113.2	14.4	18.54 0.03	18.21 0.01	17.06 0.01	16.69 0.01	16.45 0.01
2459114.2	15.4	--	--	17.17 0.00	16.76 0.01	16.50 0.01
2459114.4	15.6	18.64 0.04	18.37 0.01	--	--	--
2459117.2	18.4	19.19 0.06	18.72 0.01	17.39 0.01	16.88 0.01	16.59 0.01

SN 2020sck *UBVRI* - Continued on next page

Table 5.4 – continued from previous page

JD	Phase*	U (error)	B	V	R	I
2459120.3	21.5	19.46 0.07	18.94 0.02	17.61 0.01	17.09 0.01	16.76 0.01
2459122.3	23.5	--	19.24 0.03	17.74 0.02	17.23 0.01	16.87 0.01
2459126.3	27.4	--	--	--	--	17.08 0.03
2459138.4	39.6	--	--	18.79 0.02	18.02 0.02	17.65 0.02
2459148.2	49.4	20.30 0.12	19.86 0.03	18.60 0.01	18.23 0.01	17.97 0.01
2459167.1	68.2	--	--	--	18.69 0.01	18.41 0.02

*Time since B -max (JD 2459098.84).

TABLE 5.5: Photometry of 2020sck in r' -band with GIT.

JD	Phase*	r' (err)
2459100.4	1.6	16.39 0.04
2459101.4	2.5	16.41 0.01
2459102.4	3.5	16.37 0.02
2459103.4	4.5	16.39 0.02
2459104.4	5.4	16.43 0.02
2459105.4	6.4	16.44 0.02
2459106.4	7.4	16.48 0.02
2459108.4	9.4	16.52 0.01
2459109.4	10.4	16.58 0.03
2459110.4	11.3	16.59 0.03
2459111.4	12.3	16.65 0.02
2459112.4	13.3	16.70 0.02
2459115.4	16.3	16.83 0.02
2459121.4	22.2	17.23 0.04
2459122.4	23.2	17.30 0.02
2459127.4	28.1	17.57 0.02
2459133.4	34.0	17.71 0.04
2459139.4	39.9	17.92 0.01

Table 5.5

JD	Phase*	r' (err)
2459143.4	43.8	18.03 0.02
2459144.4	44.8	18.04 0.18
2459145.3	45.7	18.09 0.03
2459147.3	47.7	18.24 0.03
2459149.4	49.7	18.12 0.17
2459150.4	50.7	18.08 0.01
2459162.4	62.5	18.53 0.02
2459174.3	74.2	18.74 0.04
2459175.3	75.2	18.75 0.04
2459177.3	77.2	18.85 0.04

*Time since B -max (JD 2459098.84).

TABLE 5.6: gri magnitudes of 2020sck from DOT.

JD	Phase*	g (err)	r (err)	i (err)
2459226.4	127.6	19.75 0.05	18.84 0.12	18.98 0.13

*Time since B -max (2459098.84).

5.1.3 Extinction and distance modulus

The $(B-V)$ colour of the SN during +30 – 90 days can be used to get the reddening due to the host galaxy (Phillips et al. 1999). However, this relation may not strictly hold for Iax, due to the scatter in the evolution. NaID line is not detected in our low resolution spectra. Therefore, assuming zero host extinction, we correct the data only for the Galactic $E(B-V)=0.0256$ by using an extinction law of $R_V = 3.1$ (Fitzpatrick 1999). From the prominent hydrogen emission lines in the spectra of 2020sck, we estimate a redshift of $z=0.016$ for the host. Using $\mu=34.24 \pm 0.22$

mag[†] derived from the Virgo infall assuming $H_0 = 70 \text{ km s}^{-1} \text{ Mpc}^{-1}$ (Makarov et al. 2014), we find the absolute magnitude M_B to be $-17.81 \pm 0.22 \text{ mag}$.

5.1.4 Light curve

5.1.4.1 Light Curve Analysis

The light curves of 2020sck in *UBgVrRI* bands are shown in FIGURE 5.2. 2020sck was followed from -5.38 d to $+67.11 \text{ d}$ since *B*-band maximum in *UBVRI* and -13.36 d to $+95.42 \text{ d}$ since *r*-band maximum in *ZTF-g*, and *r* bands. We fit the *UBVRI*, *ZTF-g*, and *r* bands using the `gaussian_process` package in `scikit-learn` to find the maximum JD, maximum magnitude, and the associated errors in each band. TABLE 5.7 lists the important photometric parameters of SN 2020sck. 2020sck reached its peak *B*-band magnitude of $16.53 \pm 0.02 \text{ mag}$ at JD 2459098.84. The maximum in *U*-band occurred at -2.0 d and that in *VRI*-bands at $+2 \text{ days}$, $+2.8$ and $+4.7 \text{ days}$, respectively since *B*-band maximum. This indicates that the ejecta is cooling with time and follows a simple thermal model. The delay in *V*-band with respect to *B*-max is similar to that seen in 2002cx and 2005hk. The *R* and *I*-bands show no secondary maximum as are seen for SNe Ia. In FIGURE 5.3, the light curves of 2020sck in *UBVRI* have been compared with other SNe Iax. SN 2020sck has a decline rate of $\Delta m_{15}(B)=2.03 \pm 0.05 \text{ mag}$ which is faster than bright SNe Iax like 2002cx and 2005hk and slower than some of the low luminosity objects like 2008ha, 2010ae, 2019muj. SN 2020sck shows a decline rate in *V*-band ($\Delta m_{15}(V)=0.80 \text{ mag}$) similar to 2002cx and 2012Z. The redder bands show slower decline ($\Delta m_{15}(R)=0.42 \text{ mag}$, $\Delta m_{15}(I)=0.27 \text{ mag}$).

[†]<http://leda.univ-lyon1.fr/>

TABLE 5.7: Photometric parameters of 2020sck.

Filter	$\lambda_{\text{eff}}(\text{\AA})$	JD (Max)	m_{λ}^{max}	$\Delta m_{15}(\lambda)$	M_{λ}^{max}	Colors (B -max)
U	3663.6	2459096.84 ± 0.57	16.03 ± 0.06	2.17 ± 0.06	-18.33 ± 0.23	–
B	4363.2	2459098.84 ± 0.30	16.53 ± 0.02	2.03 ± 0.05	-17.81 ± 0.22	$(U - B)_0 = -0.35 \pm 0.02$
V	5445.8	2459100.84 ± 0.26	16.41 ± 0.02	0.80 ± 0.03	-17.91 ± 0.22	$(B - V)_0 = -0.08 \pm 0.03$
R	6414.2	2459101.57 ± 0.48	16.39 ± 0.01	0.42 ± 0.02	-17.93 ± 0.22	$(V - R)_0 = -0.01 \pm 0.01$
I	7978.8	2459103.58 ± 1.40	16.37 ± 0.02	0.27 ± 0.02	-17.91 ± 0.22	$(R - I)_0 = -0.02 \pm 0.01$
$ZTF - g$	4722.7	2459099.14 ± 0.34	16.27 ± 0.03	1.54 ± 0.04	-18.07 ± 0.22	–
$ZTF - r$	6339.6	2459100.28 ± 0.76	16.34 ± 0.03	0.49 ± 0.03	-17.96 ± 0.22	–

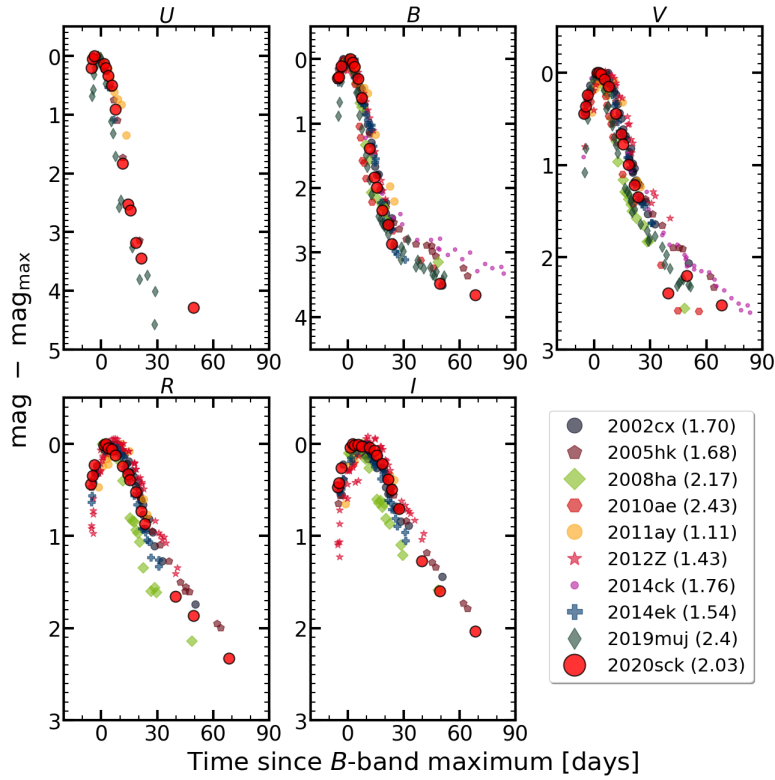


FIGURE 5.3: $UBVRI$ LCs of 2020sck plotted with other Iax. The phase is measured with respect to B -max. The light curves are shifted to their peak magnitudes. The $\Delta m_{15}(B)$ of each SN are quoted in parentheses.

TABLE 5.8: Properties of the comparison sample.

SN (Name)	M_B (mag)	M_V	$\Delta m_{15}(B)$	$\Delta m_{15}(V)$	$\Delta m_{15}(g)$	$\Delta m_{15}(r)$	$12 + \log(\frac{Q}{H})$ (dex)	Reference
SN 2002cx	-17.53 ± 0.26	-17.49 ± 0.22	1.70 ± 0.1	0.73	–	–	–	1, 2
SN 2005hk	-18.02 ± 0.32	-18.08 ± 0.29	1.68 ± 0.05	0.92	1.36 ± 0.01	0.70	–	2, 3
SN 2008ha	-13.74 ± 0.15	-14.21 ± 0.15	2.17 ± 0.02	1.29	1.80 ± 0.03	1.11	8.16 ± 0.15	4
SN 2009ku	–	–	-18.4	–	0.59	–	–	5
SN 2010ae	-13.44 ± 0.54	-13.80	2.43 ± 0.11	1.15	1.51 ± 0.05	1.01	8.40 ± 0.18	6
SN 2011ay	-18.15 ± 0.17	-18.39 ± 0.18	1.11 ± 0.16	0.95	–	–	–	7
SN 2012Z	-17.61	-18.04	1.57 ± 0.07	0.89	1.30 ± 0.01	0.66	8.51 ± 0.31	8
PS1-12bwh	–	–	–	–	1.35 ± 0.09	0.60	8.87 ± 0.19	9
SN 2013en	–	–	–	–	–	–	–	10
SN 2014ck	-17.37 ± 0.15	-17.29 ± 0.15	1.76 ± 0.15	0.88	1.59 ± 0.1	0.58	–	11
SN 2014dt	-18.13 ± 0.04	-18.33 ± 0.02	1.35 ± 0.06	–	–	–	–	12
SN 2014ek	-17.32 ± 0.23	-17.66 ± 0.20	1.54 ± 0.17	0.90	–	–	–	13
SN 2015H	–	–	–	–	–	0.69	–	14
SN 2019gsc	–	–	–	–	–	0.91	8.10 ± 0.06	15
SN 2019muj	-16.36 ± 0.06	-16.42 ± 0.0	2.4	1.2	2.0	1.0	–	16

References: (1) Li et al. (2003); (2) Phillips et al. (2007) (3) Sahu et al. (2008); (4) Foley et al. (2009); (5) Narayan et al. (2011); (6) Stritzinger et al. (2014); (7) Szalai et al. (2015); (8) Yamanaka et al. (2015); (9) Magee et al. (2017); (10) Liu et al. (2015); (11) Tomasella et al. (2016); (12) Singh et al. (2018); (13) Li et al. (2018); (14) Magee et al. (2016); (15) Srivastav et al. (2020); (16) Barna et al. (2021)

FIGURE 5.4 shows the comparison of ZTF- g , and r bands of 2020sck with other SNe Iax in similar filters. The decline rate in g -band ($\Delta m_{15}(g)=1.54$ mag) is similar to 2010ae and 2014ck. SN 2020sck has the slowest decline in r -band with a $m_{15}(r)=0.49 \pm 0.03$ mag. The decline rate for SN 2005hk and SN 2012Z in r -band are 0.70, and 0.66 mag respectively. For the fainter SNe Iax, the r -band decline rate is faster. TABLE 5.8 provides the observed properties of the comparison Iax.

The light curve decline rate of 2020sck is similar to some lower luminosity Iax in bluer bands, while it is similar to the brighter objects in the redder bands. The optical colours of 2020sck are shown in FIGURE 5.5, and FIGURE 5.6 and compared with other Iax. The trend of the colour of 2020sck matches with other well studied SNe Iax. The $(U - B)$ colour is similar to 2005hk and 2011ay. The $(B - V)$ colour is bluer near maximum in B -band (-0.08 ± 0.03 mag) and follows the same trend

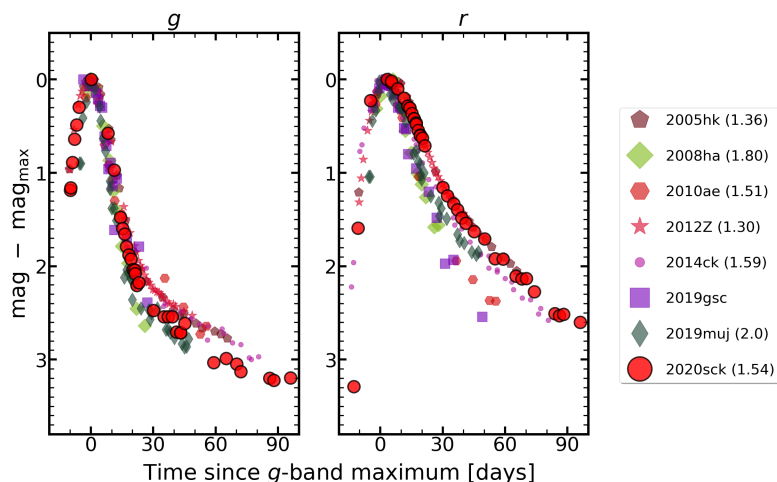


FIGURE 5.4: ZTF- g and ZTF- r light curves of 2020sck plotted with other Iax in similar filters. The phase is measured with respect to g -maximum. The light curves are normalised with respect to their respective peak magnitudes. The $\Delta m_{15}(g)$ of each SN are quoted in parentheses. The light curve data for SN 2020sck has been obtained from <https://alerce.online/object/ZTF20abwrcmq>.

as other Iax in the later phase. In comparison, the $(B - V)$ colour at B -max is 0.04 mag for 2002cx and -0.03 mag for 2005hk. The $(V - R)$ colour is also bluer than the comparison SNe. The $(R - I)$ and $(g - r)$ colour evolution is similar to SN 2005hk.

5.1.4.2 Estimation of time of first light

During the early times of the explosion, the luminosity is proportional to the surface area of an expanding fireball and hence increases with explosion time as t^2 . This assumes that the photospheric velocity and temperature do not change significantly during this phase (Riess et al. 1999). SN 2020sck was monitored with ZTF soon after its discovery (\sim JD 2459086) in g and r -bands. This allows us to place a constraint on the time of first light. We fit the early g -band LC of ZTF with a power law-

$$F(t) = A(t - t_0)^n \quad (5.1)$$

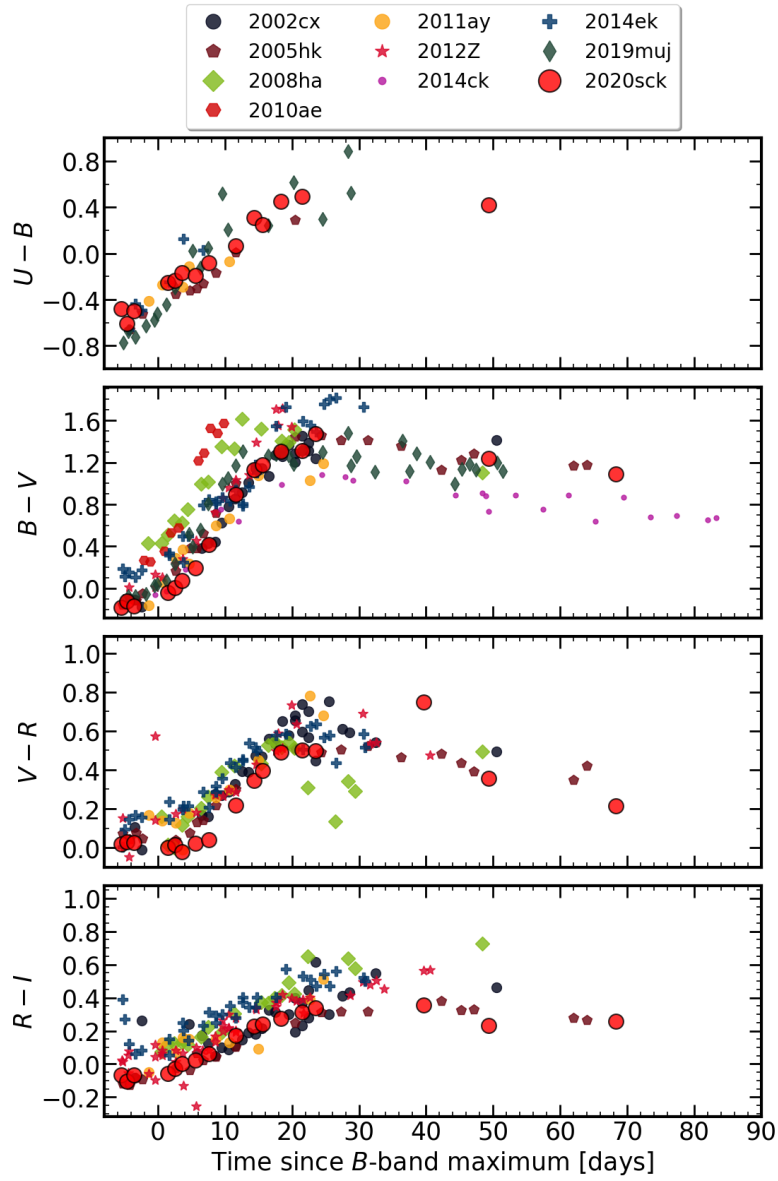


FIGURE 5.5: Colour evolution of 2020sck plotted with other Iax.

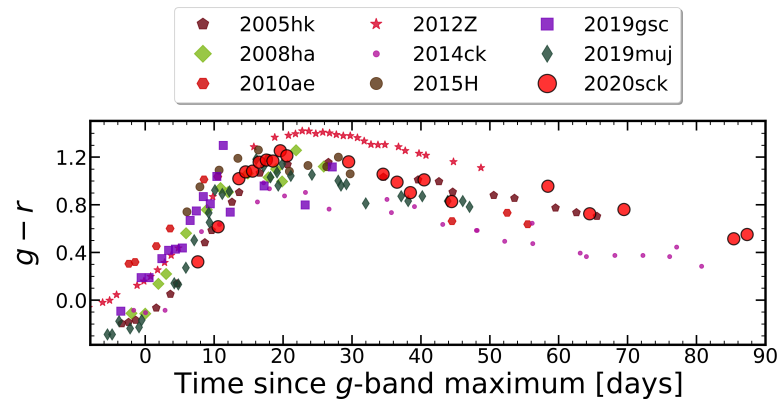


FIGURE 5.6: $(g-r)$ colour evolution of 2020sck plotted along with other Iax.

where A is a normalization constant, t_0 is the time of first light and n is the power-law index. For the “fireball model” the value of n is 2. The variation from this value hint towards the distribution of ^{56}Ni in the ejecta. A lower index value, point towards higher degrees of mixing (Firth et al. 2015). The value of n varies from ~ 1.5 to ~ 3.5 . In the fit, we kept n as a free parameter. We aimed to fit the g -band flux with a starting value of $t_0 = 2459086$ from the non-detection. However, from the fit, we get an unrealistic value of $n = 0.39$. Next, we kept the starting value of t_0 between 2459080 and 2459087 and from the fit we obtain an explosion date of 2020 August 20 21:15 UT (JD = $2459082.39_{-1.37}^{+1.57}$) and an exponent(n) of $1.79_{-0.33}^{+0.29}$. We use JD 2459082.4 as the explosion date throughout the work. The power-law fit is shown in FIGURE 5.7. From the fit, we estimate the rise time to g -max as 16.75 days and in r -band as 17.89 days. The rise time for 2020sck is similar to 2002cx-like Iax’s, for which the rise time is ~ 15.0 days. The rise times for SNe 2005hk and 2015H (Magee et al. 2016) are 15.0 days, and 15.9 days (r -band) respectively. While SNe 2008ha, 2012Z, 2019muj have lower rise times of 10, 12.0, and 9.6 days respectively. The rise time for SN 2009ku (Narayan et al. 2011) is 18.2 days, close to that for SNe Ia (~ 19.0 days).

5.1.4.3 Estimation of nickel mass

The bolometric light curve is calculated using $UBVRI$ magnitudes. The apparent magnitudes are corrected for $E(B - V)_{\text{MW}}=0.0256$, and $R_V=3.1$. The reddening corrected magnitudes are transformed into flux units using zero points from TABLE 2.1. A third-order spline curve is fit to the SED and the area under the curve is calculated using the trapezoidal rule integrating from 3000 Å to 9500 Å. For SNe Iax, a well-defined correction factor in UV and IR does not exist as there is scatter in the light curves. However, some SNe have been possible to observe in UV to IR wavelength range. For SN 2005hk, Phillips et al. (2007) have ignored the NIR flux contribution to the UVOIR bolometry during the early phase and

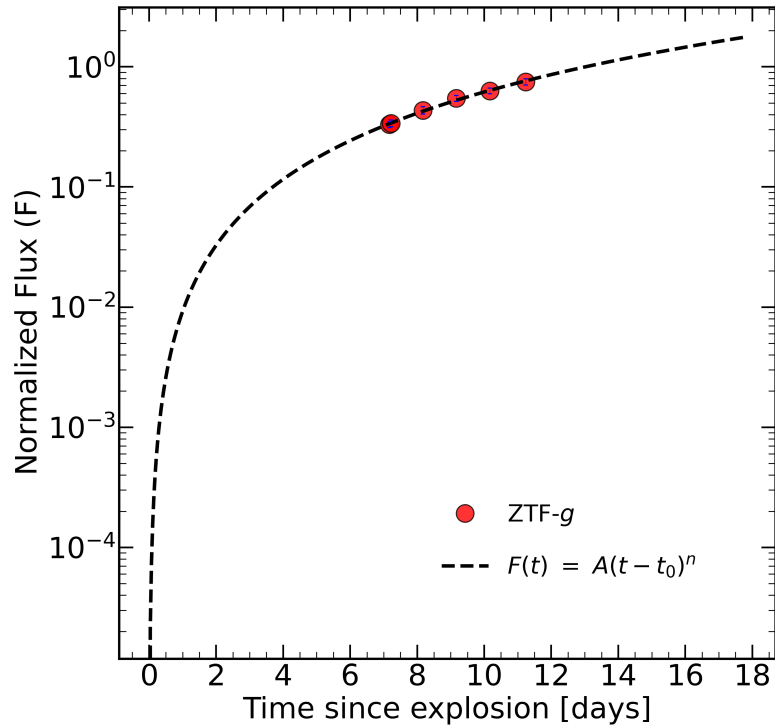


FIGURE 5.7: $F \sim t^n$ fit to the pre-max ZTF- g light curve. Flux errors are shown in blue.

have used about $\sim 20\%$ contribution to the flux in UV before maximum. For SN 2012Z, [Yamanaka et al. \(2015\)](#) have shown that the ratio of the flux in IR to the combined flux in optical and IR increases from 0.15 to 0.3 from around 8 to 25 days since the explosion. However, the evolution is significantly different from that found in SNe Ia. For SN 2014ck, [Tomasella et al. \(2016\)](#) have assumed a 10% contribution to the UV flux at maximum. SN 2014dt showed a significant increase in NIR and mid-IR flux from about 100 days post-maximum in B -band ([Fox et al. 2016](#)). For 2019gsc, [Tomasella et al. \(2020\)](#) found that the peak gri bolometric luminosity is 53 % of the peak optical-IR luminosity. To find the missing flux in UV and IR, a blackbody fit to the SED has been performed and added to the optical flux. This approach does not take into account the line-blanketing effects in the UV range and assumes that there is a contribution of UV and IR flux throughout the evolution of the bolometric luminosity. The total flux thus obtained has been converted to luminosity assuming $\mu=34.24$ mag. The quasi-bolometric light curve is shown in FIGURE 5.8. We model the quasi-bolometric

light curve with `gaussian_process` package in `scikit-learn` to estimate the peak luminosity $L_{\text{peak}}^{\text{quasi-bol}} = (3.41 \pm 0.25) \times 10^{42} \text{ erg s}^{-1}$. The peak luminosity for the blackbody bolometric LC is $L_{\text{peak}}^{\text{BB}} = (5.51 \pm 0.54) \times 10^{42} \text{ erg s}^{-1}$. The peak quasi-bolometric luminosity is 62 % of the peak blackbody luminosity ($L_{\text{opt}}/L_{\text{BB}}$). For 2019gsc, $L_{\text{opt}}/L_{\text{BB}}$ is 69 % using a similar approach (Srivastav et al. 2020).

To estimate the amount of nickel synthesized in the explosion, we fit the bolometric light curves with a modified radiation diffusion model (Chatzopoulos et al. 2012). We have used MCMC modelling technique as described in SECTION 3.1.2 to fit the model to the observations. We used flat or uniform prior for the model parameters $-0 < M_{\text{Ni}} < 1.4 M_{\odot}$, $t_{\text{lc}} > 0 \text{ d}$, $t_{\gamma} > 0 \text{ d}$ and $2459082 < t_{\text{exp}} < 2459090$. FIGURE 5.9 shows the one and two dimensional projections of the posterior distribution of the fit parameters.

The fit to the quasi-bolometric LC gives $t_{\text{exp}} = 2459084.96_{-1.74}^{+1.58}$, $M_{\text{Ni}} = 0.13_{-0.01}^{+0.02} M_{\odot}$, $t_{\text{lc}} = 10.75_{-1.96}^{+2.47}$ days and $t_{\gamma} = 35.02_{-3.00}^{+2.47}$ days. Using a constant optical opacity $\kappa_{\text{opt}} = 0.1 \text{ cm}^2 \text{ g}^{-1}$ for a Fe dominated ejecta (Pinto & Eastman 2000) and an expansion velocity $v_{\text{exp}} = 5000 \text{ km s}^{-1}$ derived from the `syn++` fitting of the near maximum spectrum, we get $M_{\text{ej}} = 0.34_{-0.10}^{+0.07} M_{\odot}$ and $E_{\text{k}} = 0.05_{-0.01}^{+0.01} \times 10^{51} \text{ erg}$. If we assume explosion of a M_{ch} WD, the bound remnant mass is $1.06 M_{\odot}$. The fit to the blackbody bolometric LC gives $M_{\text{Ni}} = 0.17_{-0.01}^{+0.01} M_{\odot}$.

The angle-averaged bolometric light curves from 3D pure deflagrations of M_{ch} CO WDs have been compared to the quasi-bolometric LC of 2020sck. In these models, no delayed detonations occur to unbind the WD completely and thus a bound remnant is left behind (Fink et al. 2014). The explosion is parametrized by multiple ignition kernels that burn at the same time. This allows for exploring varied explosion strengths. The models N1, N3, N5, N10 and N20 correspond to 1, 3, 5, 10 and 20 ignition spots placed randomly around the centre of the WD. The energy released in the explosion and the luminosity increase with an increasing

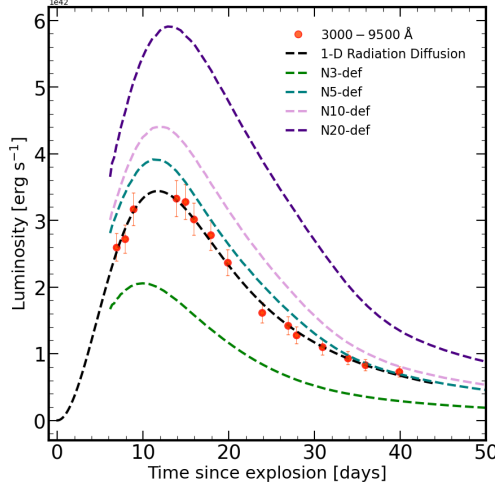


FIGURE 5.8: The quasi-bolometric LC of 2020sck fitted with 1D radiation diffusion model. Also plotted are the angle-averaged bolometric LC from the three dimensional pure deflagration models of M_{ch} WD from F14. The models have been obtained from the HESMA database.

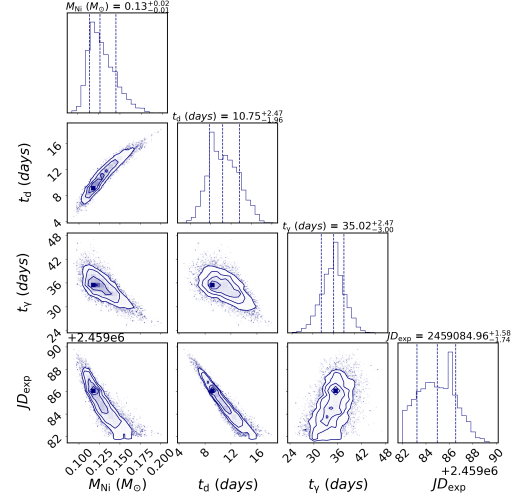


FIGURE 5.9: One and two dimensional projections of the posterior probability distribution of the fit parameters to the quasi-bolometric LC of 2020sck. The vertical dashed lines show the 16th, 50th and 84th percentiles of the samples in the distribution. See FIGURE. 5.8 for the fit.

number of spots. As the number of ignition spots increases, more matter is burnt, leading to a higher expansion velocity of the ejecta. The model N5-def with $\Delta m_{15}(B)=1.69$ mag and $M_B^{\text{max}} = -17.85$ mag matches closely with SN 2020sck, which has a $\Delta m_{15}(B)=2.03$ mag and $M_B^{\text{max}} = -17.81$ mag. In the N5-def model, the ^{56}Ni mass is $0.16 M_{\odot}$, M_{ej} is $0.37 M_{\odot}$, the mass of the bound remnant is $1.03 M_{\odot}$. These values match closely with that estimated for SN 2020sck from the quasi-bolometric LC fit with the radiation diffusion model. The kinetic energy estimated by the N5-def model is 0.135×10^{51} erg, the radiation diffusion model gives an estimate of 0.05×10^{51} erg. The models with a lesser number of ignition points (1, 3, 5) evolve asymmetrically compared to models with a larger number of ignition kernels (150, 300 etc.). So, moderate viewing angle dependence is possible in these deflagration models. The lower kinetic energy estimated by the radiation diffusion model can be explained if we assume that the explosion is similar to N5-def but with a lower line-of-sight velocity.

5.1.5 Spectral Analysis

5.1.5.1 Spectral evolution

The spectroscopic evolution of 2020sck is shown in FIGURE 5.10. The lines are identified by comparing with SNe 2002cx, 2005hk around similar phases, and also using `syn++`. The spectra in the pre-max phase show a blue continuum and presence of absorption features due to Fe III λ 4420, 5075, 5156, Fe II λ 4924, Si III λ 4568, weak absorption feature of Co II λ 4161 around \sim 4000 Å, S II λ 5449, 5623 and an asymmetric weak absorption feature at \sim 6200 Å due to Si II λ 6355. We compare the spectra of 2020sck in the pre-max phase with other SNe Iax in panel (a) of FIGURE 5.11. All the SNe except SN 2014ck show a blue continuum. The lines due to Fe III (\sim 4420 Å) and Fe III (\sim 5156 Å) are prominent in all the SNe with varying optical depth. The -5.4 d spectrum of 2020sck is similar to 2005hk, and 2019muj. The weak IME features seen in SN 2020sck is possibly due to lower density and lesser optical depth in the outer regions, which allows us to probe the hotter inner ejecta. The presence of higher ionization states of IMEs (Si III) and IGEs (Fe III) indicates a hot photosphere. SN 2014ck shows deeper Si II λ 6355 and S II features. This is because of the lower luminosity and lower photospheric temperature. Prominent C II λ 6580 absorption feature is present in the spectrum of 2014ck and 2019muj in the pre-maximum phase. But for SN 2020sck, C II feature is not seen to be developed. This hints towards the fact that the outer layers has lesser C or it is in a higher ionization state in SN 2020sck.

Around maximum the absorption features of Si II λ 6355, S II λ 5449, 5623 become prominent. Ca II H & K λ λ 3934, 3968 and Ca II NIR triplet (λ 8498) are seen to be developing. O I λ 7774 is prominently visible. C II λ 6580 and C III λ 4647 absorption features can be seen in the spectrum taken at +1.4 day. C II λ 6580 feature begins to appear around maximum with a pseudo-equivalent width (pEW)

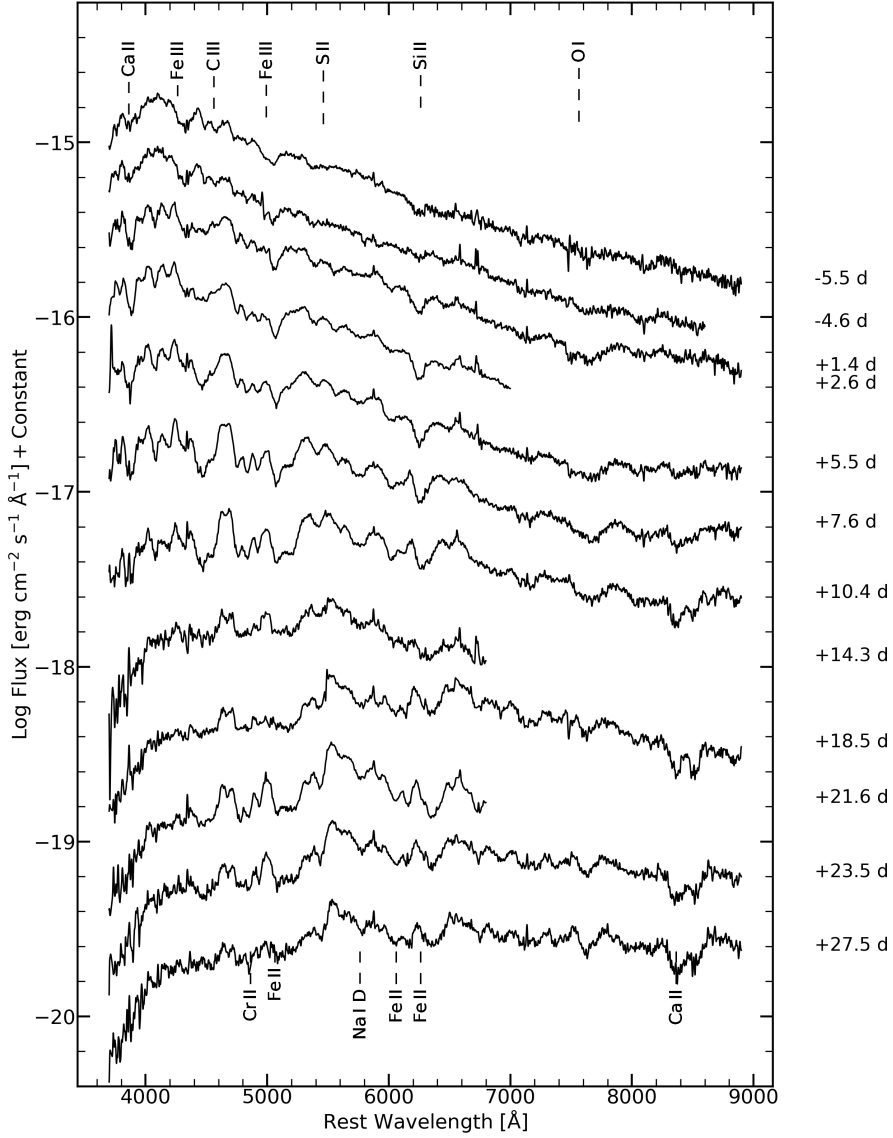


FIGURE 5.10: Spectral evolution of 2020sck from -5.5 to $+27.5$ day since the B -max. The spectra are dereddened and redshift corrected. The telluric features are removed. The spectra are smoothed for visual clarity.

of $5.25 \pm 1.05 \text{ \AA}$ at $+1.4$ d. This feature is present in our spectrum till $+10.4$ d. Appearance of carbon in the near-maximum phase implies that the carbon layer is mixed in the ejecta. Comparing with other Iax, it is seen that 2014ck and 2019muj also show prominent C II $\lambda 6580$ feature with pEW of 4 \AA and 12 \AA respectively. In the near-maximum phase, the spectrum is similar to 2019muj. The line profiles indicate lower velocities in 2020sck compared to 2005hk and 2012Z. The comparison of SN 2020sck with other SNe Iax around maximum is shown in

panel (b) of FIGURE 5.11.

Post-maximum, the Si II $\lambda 6355$ gets weakened and Fe lines dominate (panel (c) of FIGURE 5.11). The opacity of the Fe III lines decreases, or Fe III evolves to Fe II due to a decrease in temperature. Na I D absorption line can be seen to have developed. Around two weeks, Ca II NIR triplet absorption feature strengthens. At around +23 day post-maximum, lines due to Cr II (~ 4600 Å), Fe II (~ 5200 Å), Co II ($\sim 5900, 6500$ Å), Fe II ($\sim 6100, 7000$ Å) can be clearly identified. In the post-maximum phase ($\sim +10.5$ d) the spectrum of 2020sck has more similarity with SN 2005hk. While SN 2019muj shows Fe II and Co II features beyond 6500 Å, those are absent in SN 2020sck. This indicates that SN 2020sck has higher temperature than SN 2019muj in this phase.

The velocity evolution provides clues to the distribution of the elements in the ejecta and hence the explosion physics. The velocities are measured by Gaussian fit to the absorption features. In the pre-maximum phase we fit Gaussian functions to Fe III ($\lambda 4420$), Fe III ($\lambda 5156$) and Si II ($\lambda 6355$). We find the velocity of Si II to be 5712 ± 200 km s⁻¹ and that of Fe III ($\lambda 4420$) and Fe III ($\lambda 5156$) to be 6610 ± 180 km s⁻¹ and 6649 ± 200 km s⁻¹ respectively. The Fe lines have velocities ~ 800 km s⁻¹ higher than those of Si II. For SN 2007qd (McCllelland et al. 2010), SN 2014ck (Tomasella et al. 2016) the Fe lines are 800 and 1,000 km s⁻¹ higher than Si II respectively. This trend has been also seen for other SNe Iax - like SNe 2005hk, and 2010ae. This observation implies that fully burned materials are present in all the layers in the ejecta and that it supports an explosion mechanism that produces extensive mixing (Phillips et al. 2007). Around maximum, the velocity of Si II, C II $\lambda 6580$, and Ca II $\lambda 3945$ are 5185, 5211, and 5308 km s⁻¹ respectively. However, the velocity of Fe III ($\lambda 5156$) is 5558 ± 170 km s⁻¹. The velocity of Fe III ($\lambda 4420$) cannot be measured as it gets blended with other lines around the maximum. To understand the density profile and distribution of elements in the ejecta we compare the observed spectrum of 2020sck with synthetic spectrum generated

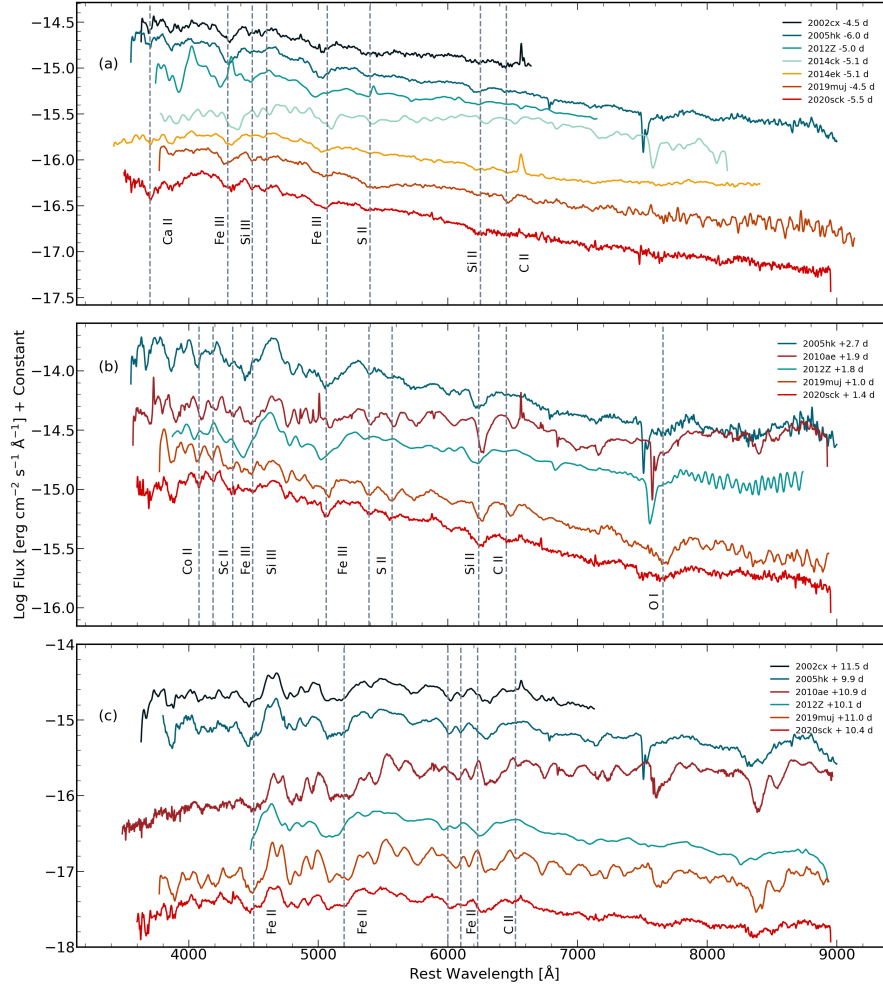


FIGURE 5.11: Comparison of the spectra of 2020sck with other Iax around similar phase. The dashed vertical lines show the position of the absorption minima of the ions for 2020sck. All spectra have been smoothed for visual clarity.

using `syn++` and TARDIS.

5.1.6 Spectral Modelling

The line velocities for SNe Iax are low and hence the spectral features post-maximum are easily identifiable than those for SNe Ia. The spectral features are identified using `syn++`. The spectrum at +1.4 d has been compared with the synthetic spectrum to identify the lines and estimate the velocities.

TABLE 5.9: **syn++** fit to the near maximum spectrum of 2020sck.

	Phase*: + 1.4 d v_{phot} : 5000 km s ⁻¹ T_{BB} : 10 500 K												
Parameters	C II	C III	O I _{PV}	O I _{DF}	Na I	Si II	Si III	S II	Ca II	Sc II	Fe II	Fe III	Co II
log (tau)	-1.5	-1.4	-1.0	-1.2	-1.8	-1.1	-1.1	-1.2	-0.1	-1.5	-0.9	-0.9	-0.9
v_{min} ($\times 10^3$ km s ⁻¹)	5.0	5.0	5.0	11.0	5.0	5.0	5.0	5.0	5.0	5.0	5.0	5.0	5.0
v_{max} ($\times 10^3$ km s ⁻¹)	7.0	8.0	15.0	15.0	10.0	12.0	7.0	7.0	8.0	7.0	7.0	8.0	7.0
aux ($\times 10^3$ km s ⁻¹)	9.0	3.0	4.5	3.0	5.0	2.5	5.0	5.0	4.0	2.5	5.0	4.0	5.0
T_{exc} ($\times 10^3$ K)	15	15	10	10	10	7	13	5	5	15	10	10	10

*Time since *B*-band maximum (JD 2459098.84).

v_{phot} : The photospheric velocity (km s⁻¹).

T_{BB} : The blackbody temperature (K).

The spectrum at +1.4 d was fit with v_{phot} of 5000 km s⁻¹ and T_{BB} of 10 500 K. The spectrum has been fit with C II, C III, O I, IMEs like Na I, Si II, Si III, S II, Ca II and IGEs like Sc II, Fe II, Fe III, Co II. To fit the broad O I absorption feature around $\sim 7600 \text{ \AA}$, we used a photospheric, and a detached component at 11 000 km s⁻¹. The line forming regions of C II, Si III, S II, Sc II, Fe II, Co II have velocities between 5000 km s⁻¹ (v_{min}) - 7000 km s⁻¹ (v_{max}). The velocity of C III and Fe III is between 5000 - 8000 km s⁻¹. Si II has been fit within velocity range of 5000 - 12 000 km s⁻¹. This velocity range of IMEs and IGEs show that the ejecta is mixed. To fit the C II and C III line profiles, an excitation temperature of 15 000 K has been used. Table 5.9 gives the details of the fit. The detection of unburned carbon is extremely important as it can constrain the explosion mechanism and the progenitor system. The presence of C II, C III, O I features hint towards thermonuclear explosion in a CO WD (Foley et al. 2010a) in contrast to ONeMg WD (Nomoto et al. 2013). The feature due to C III $\lambda 4647$ was also reported in SN 2014ck (Tomasella et al. 2016). Sc II feature was also identified in SNe 2007qd (McClelland et al. 2010), 2008ha, 2010ae, 2014ck. All the major features are reproduced well in the synthetic spectrum. FIGURE 5.12 shows the **syn++** fit to the +1.4 d spectrum of 2020sck.

To put constraint on the explosion mechanism, perform line identification, estimate the abundance of the various elements ejected and to get a knowledge of the

TABLE 5.10: Fit parameters of TARDIS model and comparison of ejecta composition with N5-def model (Fink et al. 2014).

X(C)	X(O)	X(Si)	X(S)	X(Ca)	X(Ti)	X(Cr)	X(Co)	X(Fe)	X(Ni)
Phase*: - 5.5 d v_{inner} : 6800 km s ⁻¹ v_{outer} : 12000 km s ⁻¹ L_{SN} : 8.95 log L_{\odot} t_{inner} : 11287 K									
0.003	0.355	0.15	0.005	0.018	0.000	0.000	0.010	0.020	0.410
Phase*: + 1.4 v_{inner} : 6200 v_{outer} : 12000 L_{SN} : 9.05 t_{inner} : 10033									
0.003	0.355	0.15	0.005	0.018	0.000	0.000	0.010	0.020	0.410
Phase*: + 10.4 v_{inner} : 5800 v_{outer} : 12000 L_{SN} : 8.85 t_{inner} : 7780									
0.003	0.200	0.080	0.005	0.018	0.020	0.020	0.010	0.180	0.410
N5-def model mean abundances									
0.114	0.157	0.065	0.023	0.003	0.00	0.00	0.009	0.01	0.427

*Time since B -band maximum (JD 2459098.84); v_{inner} : Inner velocity of the ejecta (km s⁻¹).

v_{outer} : Outer velocity of the ejecta (km s⁻¹); L_{SN} : Luminosity of the SN (log L_{\odot}).

t_{inner} : Temperature of the photosphere (K).

ionisation state, we compare the observed spectra of 2020sck at -5.5 , $+1.4$, and $+10.4$ days with synthetic spectrum generated using TARDIS.

For generating the synthetic spectra, we considered the angle-averaged density profile of the 3D pure deflagration explosion simulation (N5-def, F14). In the N5-def explosion, Fe and ^{56}Ni are also distributed to the outer parts of the ejecta. C and O are distributed in the entire ejecta and not limited to the outer regions. This indicates a mixed composition. We considered a uniform mass fraction of elements throughout the entire ejecta.

For comparing the observed spectrum at -5.5 d, we generate the synthetic spectrum with $t_{\text{exp}}=12.0$ d, $L_{\text{SN}}=8.95$ log L_{\odot} and a velocity interval of 8000 (v_{inner})-12000 (v_{outer}) km s⁻¹ (see panel (a) of FIGURE 5.15). However, we find that the absorption features are very strong. Also, the continuum seems to be bluer. This could be due to higher ejecta density. Decreasing the v_{inner} increases the optical depth further and increases the line strengths. We then fit the spectra by considering a modified version of the N5-def density profile and a velocity interval of 6800 - 12000 km s⁻¹. In this case, the density profile in the outer ejecta ($v >$

7200 km s⁻¹) has been reduced (N5-def $\rho \times 0.1$). This steep change in the density profile has been supported by other studies (Sahu et al. 2008; Magee et al. 2017; Barna et al. 2018). The ejecta’s innermost regions are denser than the outermost region. In FIGURE 5.14 we compare the density profile used for SN 2020sck with the N5-def density profile (F14) and W7 profile (Nomoto et al. 1984). We also show the density profiles used for the study of 2005hk (Sahu et al. 2008; Barna et al. 2018), PS1-12bwh (Magee et al. 2017). In the case of 2005hk, Sahu et al. (2008) homologously scaled the density profile to increase the density in the inner regions, while Barna et al. (2018) used an exponential density profile with a cut-off velocity v_{cut} chosen to match the deflagration density profiles. In PS1-12bwh, Magee et al. (2017) used N5-def density profile for velocity lower than 5800 km s⁻¹ and N5-def $\rho \times 0.2$ for velocities above 5800 km s⁻¹.

A uniform composition of elements throughout the entire ejecta ($v \geq v_{\text{inner}}$) is supported by the mixed abundance structure in pure deflagration models. The **syn++** synthetic spectrum also indicates the elements are distributed throughout the entire ejecta. In this case, we find the photospheric temperature to be $t_{\text{inner}} = 11\,287$ K, similar to that found by a blackbody fit to the photometric SED (11 037 K). The synthetic spectrum reproduces the features due to Ca II (H & K), Fe III $\lambda 4420$, Fe III $\lambda 5156$, S II, and Si II $\lambda 6355$. C II $\lambda 6578$ feature is reproduced with a mass fraction $X(\text{C}) = 0.003$, while it is 0.114 in the N5-def model of F14.

To further investigate the effect of the abundance structure, and density profile, we compare the spectrum at +1.4 d with a synthetic spectrum generated with $t_{\text{exp}}=18.0$ d, $L_{\text{SN}}=9.05 \log L_{\odot}$ and a velocity interval of 6200 (v_{inner}) - 12 000 (v_{outer}) km s⁻¹. We used the same mass fraction for the elements. The photospheric temperature (t_{inner}) is 10 033 K. This matches well with that found from the synthetic spectrum generated by **syn++**, $T_{\text{phot}}= 10\,500$ K. Here, the absorption features due to C, Si, S, Ca and Fe are reproduced well. However, the absorption feature around ~ 4200 Å due to Co are not reproduced (panel (b) in FIGURE 5.15).

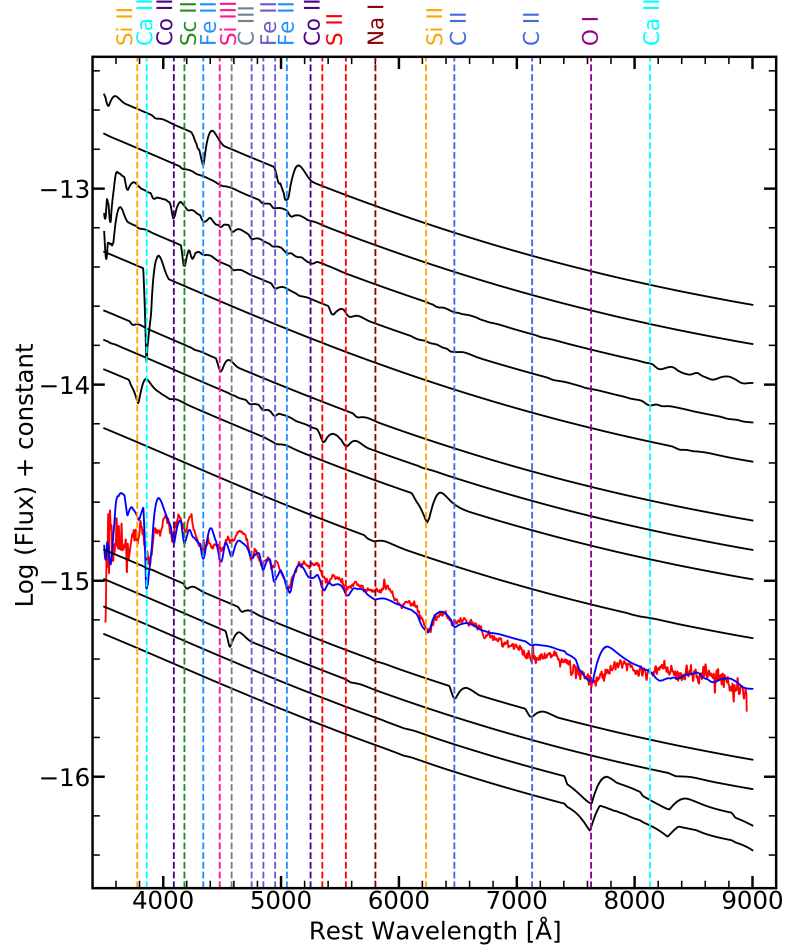


FIGURE 5.12: Dereddened and redshift corrected spectra of SN 2020sck at +1.4 d since B -max (shown in red). Overplotted in blue is the synthetic spectra calculated using `syn++`. The contributions from each ion are shown by dashed vertical lines. The observed spectrum has been smoothed for visual clarity.

The synthetic spectrum at +10.4 d has been generated with $t_{\text{exp}}=26.0$ d, $L_{\text{SN}}=8.85$ $\log L_{\odot}$ and a velocity interval of 5800 (v_{inner}) - 12 000 (v_{outer}) km s^{-1} . The photospheric temperature is 7780 K. In this model, we consider two cases - (i) With Ti and Cr in the ejecta and (ii) Without Ti and Cr (panel (c) in FIGURE 5.15). Introducing Ti and Cr reduces the flux in the bluer region around ~ 4300 Å. In this phase we increase the Fe mass fraction from $X(\text{Fe}) = 0.02$ to $X(\text{Fe}) = 0.18$. Similarly, we decrease $X(\text{Si})$ from 0.15 to 0.08. This means that the ejecta is entering into an Fe-dominated phase. The absorption features due to Fe II ($\lambda 4549$), Fe II ($\lambda 5018$), Fe II ($\lambda 6149$), Fe II ($\lambda 6247$), Fe II ($\lambda 6456$), C II ($\lambda 6578$), Ca II-IR triplet, an O I ($\lambda 7774$) are reproduced in the synthetic spectrum also.

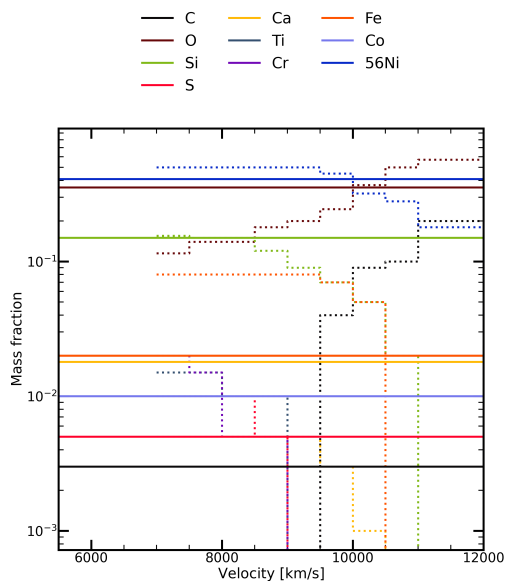


FIGURE 5.13: Comparison of the uniform abundance of elements used for SN 2020sck with the stratified abundance for SN 2005hk (Barna et al. 2018). The solid lines show the mass fractions of the elements in the ejecta of SN 2020sck while the dotted lines in the same colour shows the mass fraction in the ejecta of SN 2005hk.

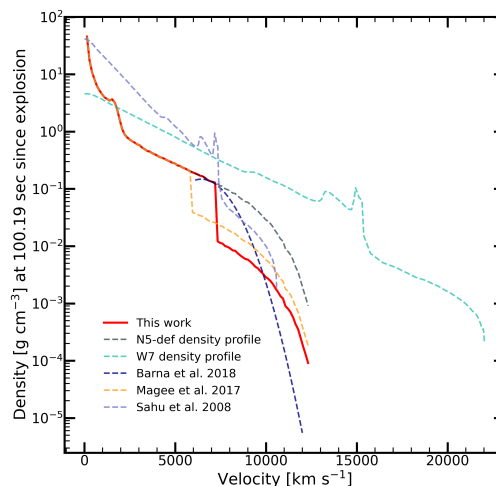


FIGURE 5.14: Density against velocity plot (in red) used in TARDIS for generating the synthetic spectrum. The density is similar to N5-def density profile below 7200 km s^{-1} and N5-def $\rho \times 0.1$ for velocity above 7200 km s^{-1} . Also plotted for comparison - N5-def profile (F14), W7 profile (Nomoto et al. 1984), density profile for 2005hk from Sahu et al. (2008) and Barna et al. (2018), density profile used for the study of PS1-12bwh (Magee et al. 2017).

While the 3D deflagration models predict a mixed abundance structure, Barna et al. (2018) made a template-based approach with stratified abundance structure to explore the ejecta of several bright SNe Iax. In the template model, the mass fraction of the IGEs and IMEs decreases with velocity and C is tolerated only in the outermost regions. However, in this work, we model the spectra using the same mass fraction over the velocity interval for the elements in the ejecta. This is in close resemblance to the 3D hydrodynamic simulations. TABLE 5.10 lists the mass fractions of the elements used in the synthetic spectrum and comparison with the N5-def model mean abundances taken from F14. In FIGURE 5.13 we compare the uniform abundance of the elements in the ejecta of SN 2020sck with the stratified abundance structure for SN 2005hk (Barna et al. 2018).

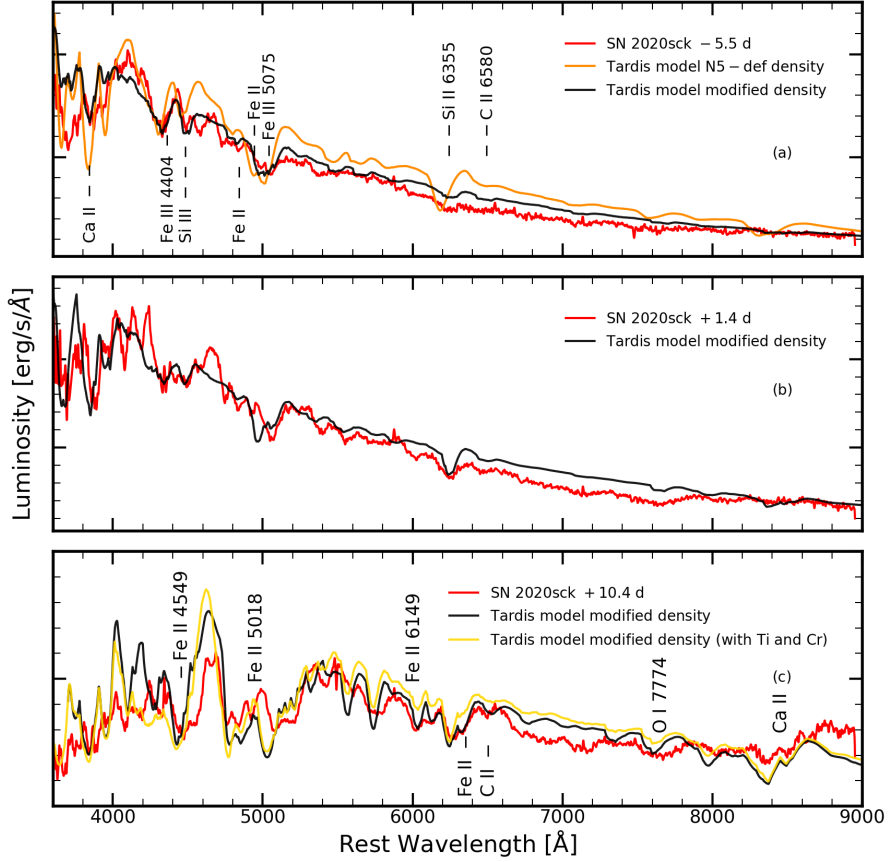


FIGURE 5.15: Panel (a) Spectrum of SN 2020sck at -5.5 d plotted along with synthetic spectrum generated using TARDIS with N5-def density profile (dark-orange) and a modified N5-def density profile (black). Panel (b) The $+1.4$ d spectrum of 2020sck plotted with TARDIS spectrum generated using the modified N5-def density profile. Panel (c) Post-maximum $+10.4$ d spectrum of 2020sck compared with TARDIS spectrum generated using the N5-def modified density profile without (black) and, with Ti and Cr (gold). The angle-averaged density profile has been obtained from HESMA database. The observed spectra of 2020sck have been smoothed.

From the TARDIS models, we find that the inner density is higher and steeply decreases towards the outer regions. From the `syn++` synthetic spectrum we find that C, O and Fe group elements are located in the ejecta between $5000 - 8000$ km s^{-1} . Using a uniform composition of the elements between $5800 - 12000$ km s^{-1} in the ejecta we confirm that most of the prominent features of C, O, Fe, Si and Ca can be reproduced in the TARDIS synthetic spectrum as well. However, some features due to C III (~ 4600 Å), Co II (~ 4100 Å), Fe II (~ 4800 Å) are reproduced well in the `syn++` model but not in the TARDIS model. The analyses presented here

indicate the elements in the ejecta of SN 2020sck are mostly mixed and support an explosion that is probably due to the pure deflagration of a CO WD.

5.1.7 Host Galaxy

The metallicity of the host galaxy 2MASX J01103497+0206508 can be determined from the narrow emission features in the SN spectrum. We fit Gaussian profiles to the narrow H α λ 6563 and [N II] λ 6583. Using the empirical relation derived by Pettini & Pagel (2004) with the N2 index ($\log \frac{[\text{N II}] \lambda 6583}{\text{H}\alpha \lambda 6563}$), we find the oxygen abundance to be $12 + \log(\text{O}/\text{H}) = 8.54 \pm 0.05$ dex. Metallicity values of few SNe Iax have been obtained using the same relation of Pettini & Pagel (2004) - SNe 2008ha, 2010ae, 2012Z, PS1-12bwh, 2019gsc. These metallicities for the comparison SNe are given in TABLE 5.8. SN 2008ha ($L_{\text{peak}} = 9.5 \times 10^{40}$ erg s $^{-1}$) and SN 2019gsc ($L_{\text{peak}} = 7.4 \times 10^{40}$ erg s $^{-1}$) have metal poor environments and low peak luminosities. There could be a relation between metallicity of the host galaxy and peak supernova magnitude, with low luminosity SNe Iax having lower metallicity and vice-versa (FIGURE 5.16). However, there exist no clear correlation which demonstrates that SNe Iax tend to form in sub/super-solar metallicity environments (Magee et al. 2017).

Using the spectrum at +23 d obtained with a 1.92'' slit, we find the star formation rate (SFR) of the H II region near the SN. We derive an SFR of $0.09 M_{\odot} \text{ yr}^{-1}$ from the luminosity of the H α λ 6563 line (Kennicutt 1998). Young massive stars ($\geq 10 M_{\odot}$) mostly contribute to the integrated line flux. From the forbidden [O II] λ 3727 line luminosity, we obtain an SFR of $0.02 M_{\odot} \text{ yr}^{-1}$. The SFR derived from [O II] is less precise and suffers from systematic errors due to extinction (Kennicutt 1998). In comparison, the SFR of the host of SN 2008ha is $0.07 M_{\odot} \text{ yr}^{-1}$ (Foley et al. 2009). This was derived using far-infrared luminosity.

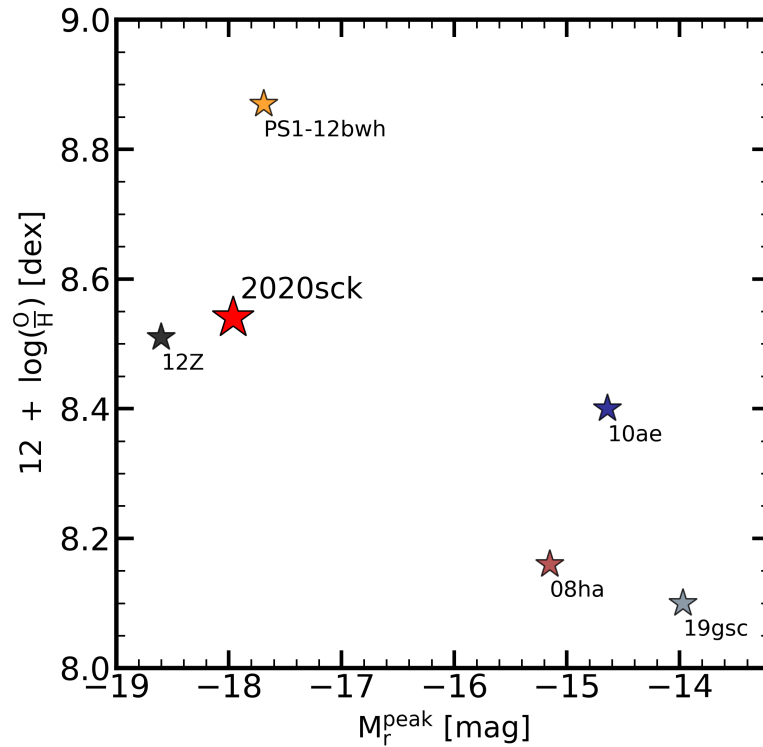


FIGURE 5.16: $12 + \log(\text{O}/\text{H})$ plotted against r -band peak magnitude for a sample SNe Iax. The luminous objects have higher metallicity.

5.2 Diversity in the Iax class: 2022eyw and 2022xlp

5.2.1 Introduction

SN 2022eyw was discovered on March 22, 2022, 11:04:36.19 (JD 2459660.96) by [Chambers et al. \(2022\)](#) at 19.66 mag (AB) in i -band. The object was classified as Type Ia with a spectrum observed on March 24, 2022, 16:30:43 (JD 2459663.19) by [Tagchi et al. \(2022\)](#). It was further classified as a Iax by [Balcon 2022](#); [Fulton et al. 2022](#). The SN was followed up photometrically with the GIT from March 25, 2022 (JD 2459664.27) in $u'g'r'i'z'$, and spectra were obtained with the HCT starting from March 25, 2022 (JD 2459664.41).

SN 2022xlp was discovered on October 13, 2022, 19:23:22.00 (JD 2459866.31) by

Itagaki (2022) at 17.00 mag (Vega). The object was classified as Type Ia with a spectrum observed on October 15, 2022, 19:52:53 (JD 2459868.33) by Taguchi et al. (2022). The SN was followed up photometrically with GIT from October 16, 2022 23:02:24.00 (JD = 2459869.46) in $u'g'r'i'z'$, and spectra were observed with HCT starting from October 16, 2022, 23:39:51.43 (JD 2459869.49).

5.2.2 Light Curve Analysis

2022eyw was followed up with the GIT from -9.9 day to $+120.0$ day since g' maximum. The photometric log is provided in TABLE 5.11. The SN reached its peak in g' -band on April 04, 2022 (JD 2459674.28) with a peak magnitude (m_g) of 15.49 ± 0.01 mag and a $\Delta m_{15}(g) = 1.39 \pm 0.03$ mag. The u' -band peak occurred at JD 2459671.51, -2.77 days before g' -max, while the peak in r' , i' , z' -band occurred at JD 24595677.97 ($+3.69$ days), 2459679.62 ($+5.34$ days), and 2459681.02 ($+6.74$ days) respectively.

The decline rate of 2005hk in g -band is 1.36 ± 0.01 mag, that of SN 2012Z is 1.30 ± 0.01 mag. The decline rate (Δm_{15}) of 2022eyw in r' , i' , and z' -bands are 0.70 ± 0.03 , 0.50 ± 0.03 , and 0.43 ± 0.04 mag respectively. The decline rate in r -band of 2005hk, and 2012Z are 0.70 and 0.66 mag respectively. The decline rates of SN 2005hk, and SN 2012Z in i -band are 0.60 and 0.54 mag respectively. The optical light curves of 2022eyw are shown in FIGURE 5.17.

The Galactic $E(B - V)$ in the direction of 2022eyw is 0.012 ± 0.001 mag. In the near maximum spectra taken at -1.8 day since g' -max, we detect NaID with a pEW of 0.35 ± 0.03 Å at the redshift of the host. Using the empirical relation, $E(B - V) = 0.16 \times \text{pEW}(\text{NaID})$, we get $E(B - V)_{\text{host}} = 0.06 \pm 0.01$ mag. Using a redshift $z = 0.0087 \pm 0.0003$ (Ann et al. 2015), and assuming $H_0 = 73.0$ km s $^{-1}$ Mpc $^{-1}$, $\Omega_\lambda = 0.73$, $\Omega_M = 0.27$, we get $\mu = 32.85 \pm 0.06$ mag. Using

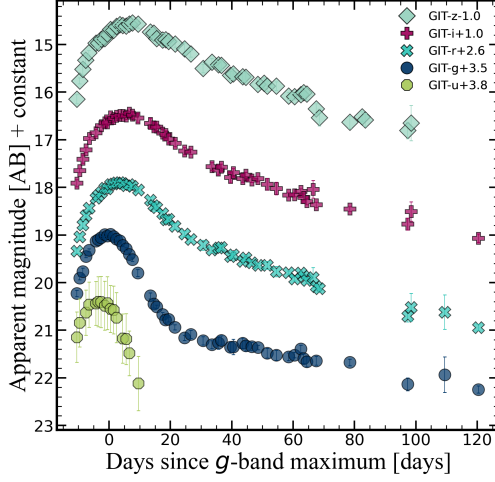


FIGURE 5.17: $u'g'r'i'z'$ light curves of 2022eyw.

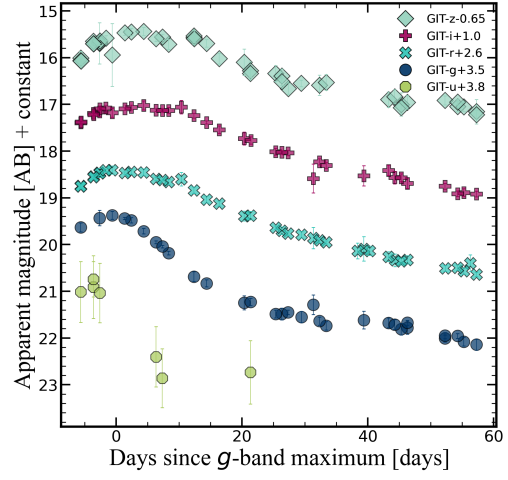


FIGURE 5.18: $u'g'r'i'z'$ light curves of 2022xlp.

$E(B - V)_{total} = 0.072$ mag, and $R_V = 3.1$, we get a peak magnitude $M_g = -17.63 \pm 0.06$ mag. In comparison, the peak magnitudes of SNe 2005hk and 2012Z are -18.08 ± 0.25 mag, and -18.40 ± 0.09 mag respectively. The peak magnitude of 2002cx is -17.53 ± 0.26 mag in B -band. 2022eyw thus falls in the brighter end of the Type Ia class (TABLE 5.8).

2022xlp was followed up with the GIT from -5.0 day to $+57.6$ day since g' -band maximum. The photometric log is presented in TABLE 5.12. The SN reached its peak magnitude in g' -band on October 22, 2022, 01:40:48.00 (JD 2459874.57) with a peak magnitude (m_g) of 15.89 ± 0.05 mag and a $\Delta m_{15}(g) = 1.43 \pm 0.09$ mag. The r' , i' , z' peaks occurred at JD 2459875.77 ($+1.2$ days), 2459876.86 ($+2.3$ days), and 2459877.59 ($+3.02$ days) respectively.

The decline rate (Δm_{15}) of 2022xlp in r' , i' , and z' -bands are 0.56 ± 0.07 , 0.43 ± 0.04 , and 0.51 ± 0.06 mag respectively. The Galactic $E(B - V)$ in the direction of 2022xlp is 0.0183 ± 0.0003 mag. Na ID is not detected in the spectra at the host redshift and therefore we assume negligible host extinction. Using a redshift of $z = 0.003 \pm 0.00002$, for the host NGC 3938, and assuming $H_0 = 73.0$ km s $^{-1}$ Mpc $^{-1}$, $\Omega_\lambda = 0.73$, $\Omega_M = 0.27$, we find $\mu = 30.72 \pm 0.02$ mag. Using $E(B - V)_{total} =$

TABLE 5.11: $u'g'r'i'z'$ magnitudes of 2022eyw from GIT.

JD	Phase*	u' (err)	g' (err)	r' (err)	i' (err)	z' (err)
2459664.3	-9.9	17.35 0.53	16.73 0.06	16.74 0.05	16.91 0.08	17.15 0.10
2459665.2	-9.0	17.05 0.51	16.40 0.04	16.44 0.05	16.65 0.04	16.76 0.06
2459666.2	-8.0	--	16.27 0.07	16.19 0.08	16.40 0.09	16.52 0.12
2459667.2	-7.0	16.83 0.48	15.95 0.02	15.99 0.03	16.21 0.05	16.33 0.09
2459668.2	-6.0	16.66 0.48	15.82 0.03	15.84 0.03	--	16.17 0.04
2459668.3	-5.9	--	--	--	15.97 0.03	--
2459670.5	-3.7	16.64 0.46	15.63 0.06	15.63 0.05	15.85 0.07	15.97 0.10
2459671.3	-3.0	16.60 0.52	15.60 0.03	15.57 0.05	--	15.97 0.05
2459672.2	-2.1	16.61 0.54	15.55 0.03	15.51 0.04	15.70 0.03	15.88 0.08
2459673.3	-1.0	16.69 0.51	15.49 0.04	15.42 0.04	--	--
2459673.4	-0.9	--	--	--	15.64 0.04	15.87 0.07
2459674.2	-0.1	16.63 0.56	15.52 0.04	15.43 0.07	15.64 0.06	15.78 0.07
2459675.3	1.0	16.75 0.49	15.49 0.03	15.34 0.04	15.52 0.04	15.68 0.05
2459676.2	1.9	16.77 0.50	15.53 0.04	15.33 0.05	15.55 0.07	15.70 0.10
2459677.2	2.9	16.93 0.53	15.59 0.04	15.30 0.04	15.50 0.02	15.62 0.07
2459678.3	4.0	--	15.62 0.03	15.30 0.03	15.48 0.04	15.58 0.07
2459679.3	5.0	17.37 0.52	15.72 0.03	15.32 0.03	15.49 0.04	15.60 0.08
2459680.3	6.0	--	--	15.36 0.06	15.50 0.07	15.61 0.08
2459680.4	6.1	17.39 0.53	15.79 0.03	--	--	--
2459681.3	7.0	17.68 0.47	--	--	--	--
2459681.4	7.1	--	15.91 0.03	15.34 0.04	15.44 0.05	15.57 0.07
2459682.4	8.0	--	16.02 0.04	15.38 0.04	15.48 0.06	15.54 0.06
2459684.2	9.8	--	16.30 0.07	--	15.54 0.09	15.57 0.08
2459684.3	9.9	18.32 0.57	--	15.46 0.04	--	--
2459688.2	13.8	--	16.78 0.06	15.67 0.06	15.66 0.11	15.74 0.08
2459689.3	14.9	--	--	--	--	15.76 0.08
2459689.4	15.0	--	16.95 0.08	15.78 0.05	15.73 0.08	--
2459690.2	15.8	--	--	15.83 0.08	--	--

SN 2022eyw - Continued on next page

Table 5.11 – continued from previous page

JD	Phase*	u' (err)	g' (err)	r' (err)	i' (err)	z' (err)
2459690.3	15.9	--	17.01 0.04	--	15.73 0.06	15.87 0.12
2459692.2	17.8	--	17.17 0.04	15.95 0.05	15.86 0.08	15.90 0.13
2459693.2	18.8	--	17.28 0.07	--	15.89 0.08	15.90 0.10
2459693.3	18.9	--	--	16.08 0.06	--	--
2459694.2	19.7	--	17.27 0.05	16.07 0.05	15.99 0.08	15.93 0.10
2459696.3	21.8	--	17.44 0.06	16.22 0.06	16.08 0.07	15.99 0.06
2459699.3	24.8	--	--	--	--	16.09 0.12
2459699.4	24.9	--	17.66 0.05	16.38 0.06	16.24 0.08	--
2459701.4	26.9	--	17.59 0.08	16.50 0.05	16.26 0.05	16.20 0.07
2459705.4	30.9	--	17.72 0.09	16.61 0.10	--	16.50 0.09
2459708.3	33.7	--	17.80 0.08	16.72 0.06	16.56 0.08	16.37 0.08
2459710.4	35.8	--	17.77 0.13	16.67 0.08	16.63 0.10	16.42 0.07
2459711.3	36.7	--	17.71 0.10	16.66 0.05	16.57 0.07	16.43 0.09
2459714.3	39.7	--	17.86 0.11	16.85 0.05	16.79 0.12	16.65 0.09
2459715.3	40.7	--	17.85 0.16	16.81 0.07	16.69 0.08	16.61 0.12
2459718.3	43.6	--	17.77 0.11	16.95 0.05	16.81 0.08	16.68 0.10
2459719.3	44.6	--	--	--	--	16.69 0.10
2459719.4	44.7	--	17.83 0.10	16.88 0.06	16.74 0.06	--
2459721.3	46.6	--	17.84 0.09	16.98 0.04	16.84 0.06	--
2459723.3	48.6	--	17.86 0.05	17.03 0.04	16.82 0.05	16.83 0.09
2459725.3	50.6	--	--	--	--	16.81 0.11
2459726.3	51.6	--	17.98 0.10	17.03 0.08	16.93 0.12	16.87 0.11
2459729.3	54.5	--	18.03 0.10	17.17 0.11	17.02 0.13	16.87 0.09
2459733.3	58.5	--	18.06 0.08	17.19 0.03	17.16 0.04	17.08 0.08
2459735.3	60.5	--	18.02 0.06	17.32 0.04	17.16 0.04	17.09 0.06
2459737.3	62.5	--	17.89 0.07	17.20 0.04	17.08 0.06	17.05 0.10
2459738.2	63.4	--	--	17.27 0.05	17.21 0.06	17.01 0.10
2459738.3	63.5	--	18.10 0.10	--	--	--
2459739.2	64.4	--	18.16 0.11	17.35 0.06	17.30 0.07	17.04 0.13

SN 2022eyw - Continued on next page

Table 5.11 – continued from previous page

JD	Phase*	u' (err)	g' (err)	r' (err)	i' (err)	z' (err)
2459741.3	66.4	--	--	17.29 0.21	17.04 0.19	--
2459742.3	67.4	--	18.14 0.09	17.48 0.05	17.36 0.06	17.35 0.10
2459743.3	68.4	--	--	17.53 0.07	--	17.53 0.18
2459753.3	78.3	--	18.18 0.07	--	17.45 0.05	17.63 0.13
2459757.3	82.3	--	--	--	--	17.51 0.10
2459758.3	83.3	--	--	--	--	17.58 0.14
2459772.1	97.0	--	18.64 0.14	18.10 0.12	17.77 0.13	17.80 0.18
2459773.2	98.1	--	--	17.92 0.29	17.51 0.20	17.65 0.37
2459784.2	109.0	--	18.43 0.37	18.02 0.36	--	--
2459795.2	119.9	--	18.74 0.08	18.34 0.07	18.07 0.09	--

*Time since g' -max (JD 2459674.28).

0.0183 mag, and $R_V = 3.1$, we get a peak magnitude $M_g = -14.90 \pm 0.02$ mag. In comparison, some of the fainter Iax like 2008ha, and 2010ae have peak absolute magnitudes of -14.01 ± 0.14 mag, and $-13.54 \geq M_g \geq -15.33 \pm 0.54$ mag. The decline rate in g' -band for SN 2008ha is 1.80 ± 0.03 mag, and SN 2010ae is 1.51 ± 0.05 mag. 2022xlp falls in the low luminous category of Iax. The optical light curves of 2022xlp are shown in FIGURE 5.18.

5.2.3 Spectral Analysis

The early phase spectral evolution of 2022eyw, and 2022xlp is presented here. 2022eyw has been followed up from -10.8 day to $+2.2$ day since g' -band maximum. The log of spectroscopic observations is presented in TABLE 5.13. The spectra in the very early phase (-10.8 day) show no strong features from IMEs like Si II, S II, and show only weak features of Ca II. Absorption features due to Fe III at 4400 \AA and 5000 \AA are prominent. The features due to Si II, S II appear near maximum (-2.8 day). There is also the presence of C II $\lambda 6580$ feature. We measured the

TABLE 5.12: $u'g'r'i'z'$ magnitudes of 2022xlp from GIT.

JD	Phase*	u' (err)	g' (err)	r' (err)	i' (err)	z' (err)
2459869.5	-5.0	17.21 0.65	16.13 0.10	16.15 0.06	16.39 0.03	16.70 0.09
2459871.5	-3.0	17.02 0.52	--	15.95 0.04	16.20 0.04	16.33 0.06
2459872.4	-2.1	--	15.93 0.17	15.86 0.10	16.16 0.10	--
2459872.5	-2.0	17.24 0.64	--	15.88 0.05	16.09 0.04	16.32 0.19
2459873.4	-1.1	--	--	15.81 0.03	16.07 0.05	16.23 0.05
2459874.4	-0.1	--	15.87 0.08	15.81 0.08	--	--
2459874.5	0.0	--	--	--	16.18 0.10	16.59 0.67
2459876.4	1.9	--	15.94 0.02	15.87 0.02	16.10 0.03	16.12 0.06
2459877.5	3.0	--	15.98 0.06	15.84 0.05	16.07 0.05	16.10 0.08
2459879.4	4.9	--	16.21 0.06	--	--	--
2459879.5	5.0	--	--	15.85 0.08	16.02 0.10	16.09 0.08
2459881.4	6.9	18.60 0.64	16.45 0.03	16.00 0.04	16.12 0.03	16.24 0.06
2459882.4	7.9	19.06 0.63	16.54 0.03	16.02 0.02	16.13 0.03	16.21 0.06
2459883.4	8.9	--	16.68 0.04	16.06 0.06	16.13 0.06	16.37 0.11
2459885.4	10.9	--	--	16.00 0.14	16.06 0.14	--
2459887.4	12.9	--	17.19 0.10	--	--	16.19 0.11
2459887.5	13.0	--	--	16.24 0.07	16.24 0.05	16.23 0.12
2459889.4	14.9	--	17.33 0.08	16.44 0.08	16.39 0.03	16.34 0.08
2459891.4	16.8	--	--	16.52 0.06	16.54 0.08	16.67 0.11
2459895.4	20.8	--	17.75 0.15	16.79 0.10	16.73 0.14	16.75 0.28
2459896.4	21.8	18.93 0.68	17.73 0.08	16.78 0.09	--	16.96 0.14
2459896.5	21.9	--	--	--	16.77 0.08	--
2459900.4	25.8	--	17.99 0.08	17.04 0.04	17.01 0.07	16.99 0.17
2459901.4	26.8	--	17.98 0.13	17.10 0.08	17.03 0.04	17.10 0.12
2459902.4	27.8	--	17.95 0.05	17.16 0.04	17.04 0.06	17.31 0.12
2459904.5	29.9	--	18.05 0.12	17.19 0.07	--	17.20 0.07
2459906.4	31.8	--	17.79 0.21	17.26 0.23	17.59 0.31	--
2459907.4	32.8	--	18.14 0.08	17.31 0.05	17.23 0.07	17.24 0.22

SN 2022xlp - Continued on next page

Table 5.12 – continued from previous page

JD	Phase*	u' (err)	g' (err)	r' (err)	i' (err)	z' (err)
2459908.4	33.8	--	18.24 0.09	17.35 0.03	17.31 0.06	17.18 0.17
2459913.4	38.8	--	--	17.54 0.17	--	--
2459914.4	39.8	--	18.11 0.19	17.49 0.26	17.53 0.22	--
2459915.4	40.8	--	--	17.53 0.10	--	--
2459918.4	43.8	--	18.18 0.10	17.66 0.10	17.41 0.11	17.55 0.16
2459919.4	44.8	--	18.21 0.10	17.74 0.14	17.57 0.13	17.49 0.15
2459920.4	45.8	--	18.31 0.12	17.76 0.08	17.57 0.08	17.68 0.18
2459921.4	46.8	--	18.23 0.10	17.73 0.08	17.69 0.11	17.61 0.14
2459927.3	52.6	--	18.48 0.08	--	--	17.57 0.10
2459927.4	52.7	--	--	17.91 0.06	17.75 0.06	--
2459929.3	54.6	--	18.46 0.05	17.89 0.06	17.91 0.06	17.65 0.08
2459930.3	55.6	--	18.58 0.09	17.97 0.07	17.89 0.08	17.70 0.10
2459931.3	56.6	--	--	17.80 0.18	--	--
2459932.3	57.6	--	18.64 0.12	18.04 0.04	17.92 0.06	17.84 0.18

*Time since g' -max (JD 2459874.5).

velocity of Si II absorption feature from the spectra. The velocity declines from $6756 \pm 100 \text{ km s}^{-1}$ at -2.8 day to $6476 \pm 150 \text{ km s}^{-1}$ at -1.8 day. We did not measure the Si II velocity further as it blends with Fe II. The velocity of Si II is around 6500 km s^{-1} for 2005hk, and 7500 km s^{-1} for 2012Z (Stritzinger et al. 2014) around similar phases. The early phase spectral evolution of 2022eyw is shown in FIGURE 5.19. We compare 2022eyw at two different phases (pre-max, and post-max) with other SNe Iax of its type in FIGURE 5.21, and FIGURE 5.22.

2022xlp has been followed from -5.1 day to $+11.9$ day g' -band maximum. The log of spectroscopic observations is presented in TABLE 5.14. The early phase spectra shows Si II, S II, Ca II, Fe II, Si III, Fe III. One of the most important feature of 2022xlp is the strong C II $\lambda 6580$ feature. This feature is present in the spectra till $+6.9$ day. 2022xlp has narrow lines compared to 2022eyw due to its lower

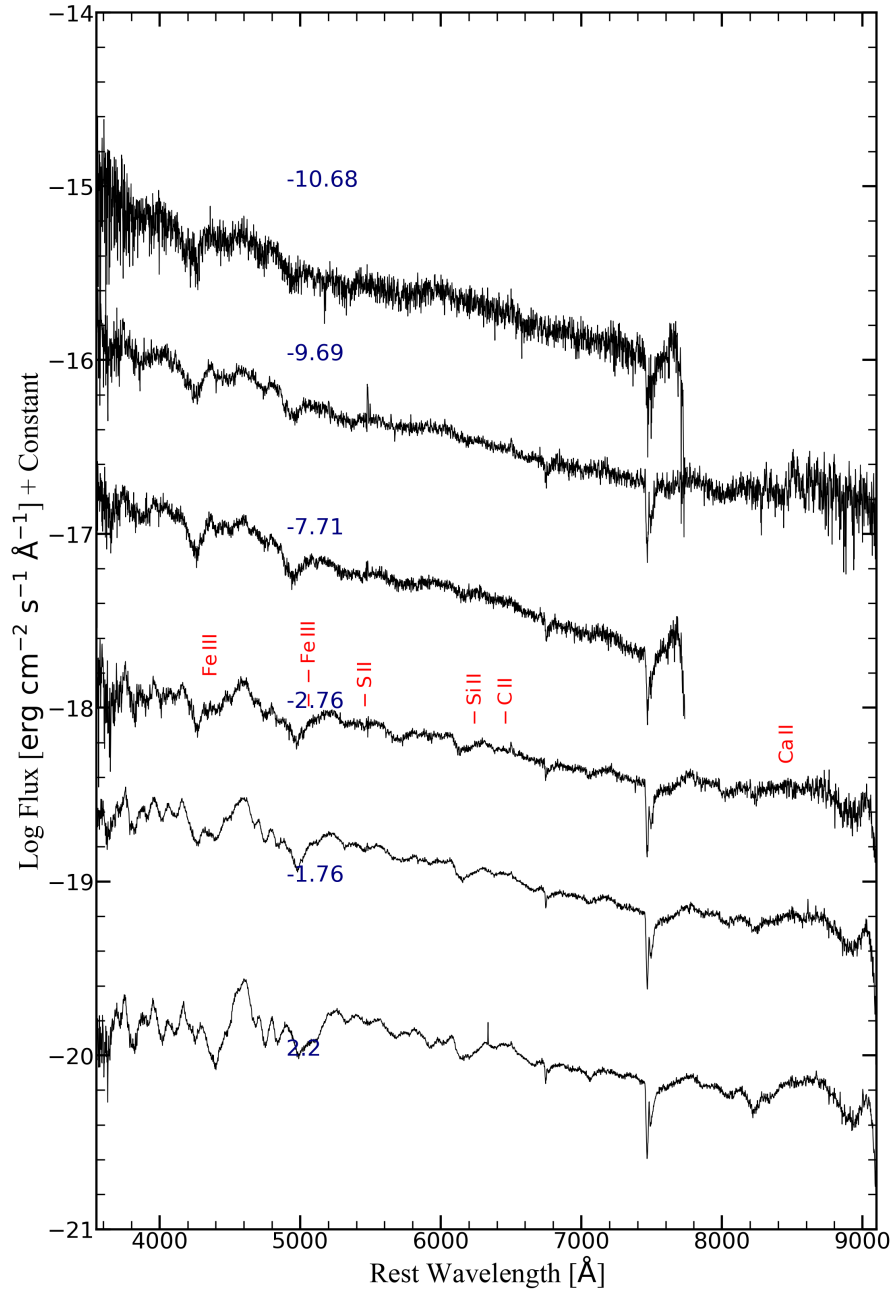


FIGURE 5.19: The early phase spectral evolution of 2022eyw. The phases are with respect to the g' -max.

TABLE 5.13: Spectroscopic observations log of 2022eyw from HCT.

Date	Phase*	Range
	(d)	(Å)
2022-03-25	-10.68	3500–7800
2022-03-26	-9.69	3500-7800; 5200-9100
2022-03-28	-7.71	3500–7800
2022-04-02	-2.76	3500-7800; 5200-9100
2022-04-03	-1.76	3500-7800; 5200-9100
2022-04-07	+2.2	3500-7800; 5200-9100

*Rest frame time since g' -maximum (JD 2459674.28).

velocities. The Si II velocity decreases from 4560 ± 300 at -5.1 day to 3021 ± 100 km s $^{-1}$ at $+1.9$ day. The velocity of C II is even lower. It evolves from 3745 ± 100 at -5.1 day to 2052 ± 80 km s $^{-1}$ at $+1.9$ day. The velocity of Si II line for some low luminous objects like 2008ha, and 2010ae are 3700, and 5000 km s $^{-1}$ respectively. The early phase spectral evolution of 2022xlp is shown in FIGURE 5.20. We also show the comparison of the spectrum at -3.1 day, and $+1.9$ day with SNe 2010ae (Stritzinger et al. 2015), 2008ha (Foley et al. 2010a), 2014ck (Tomasella et al. 2016), and 2019muj (Barna et al. 2021) around similar phases.

It is important to note that bright and faint SNe Iax show distinctly different spectral features in the early and near maximum phases shown in this study. Due to the high velocities in the more energetic and brighter explosions, the lines are broad, and blended in bright SNe Iax. While, the lines are narrow, and comparatively more lines are identified in fainter SNe Iax. Also, due to lower temperatures, in the fainter Iax, the atoms are in their lower ionization states, so features due to Fe II, Si II $\lambda 5972$, S II, appear quite early in their evolution. But, for the brighter Iax, initially the photosphere is hot and has higher opacity. So, not many lines become prominent in the early phase. To some extent, the spectroscopic features help in understanding the brightness of the explosion.

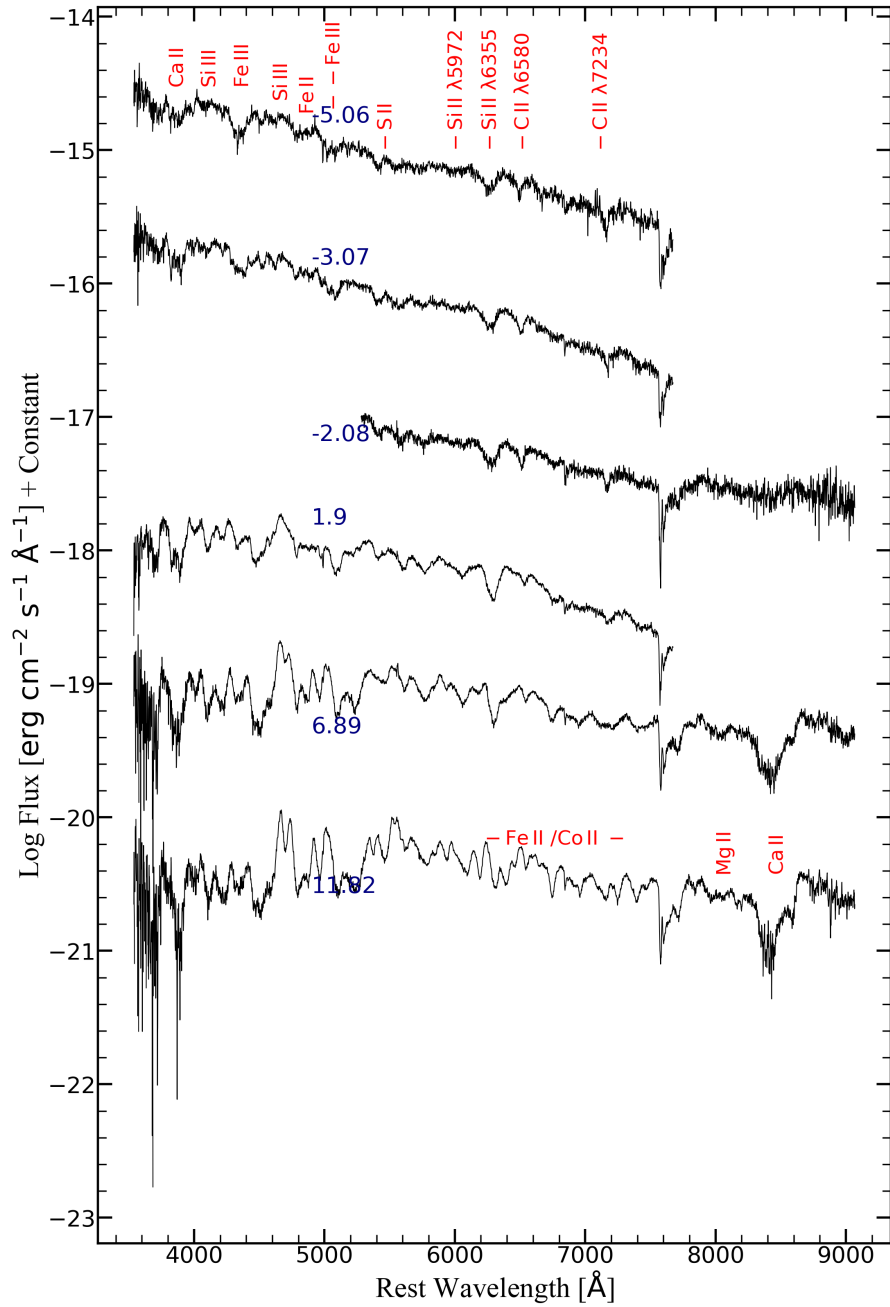


FIGURE 5.20: The early phase spectral evolution of 2022xlp. The phases are with respect to the g' -max.

TABLE 5.14: Spectroscopic observations log of 2022xlp from HCT.

Date	Phase*	Range
	(d)	(Å)
2022-10-16	-5.06	3500–7800
2022-10-18	-3.07	3500–7800
2022-10-19	-2.08	5200-9100
2022-10-23	+1.90	3500–7800
2022-10-28	+6.89	3500-7800; 5200-9100
2022-11-02	+11.82	3500-7800; 5200-9100

*Rest frame time since g' -maximum (JD 2459874.5).

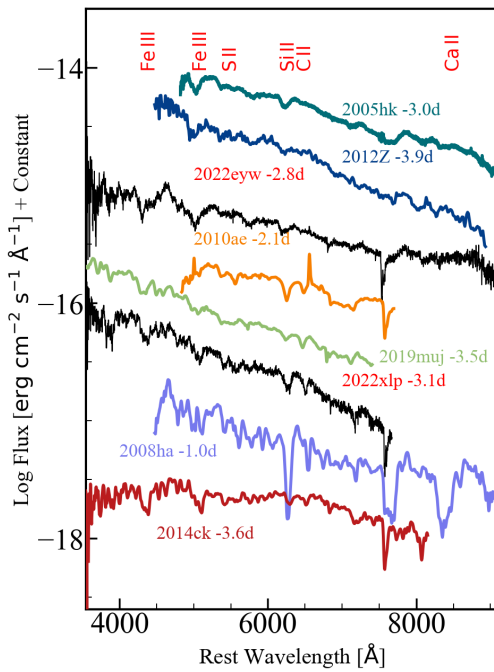


FIGURE 5.21: Comparison of SNe 2022eyw, and 2022xlp with other Type Iax SNe at pre-max phases. The comparison spectra are corrected for redshift.

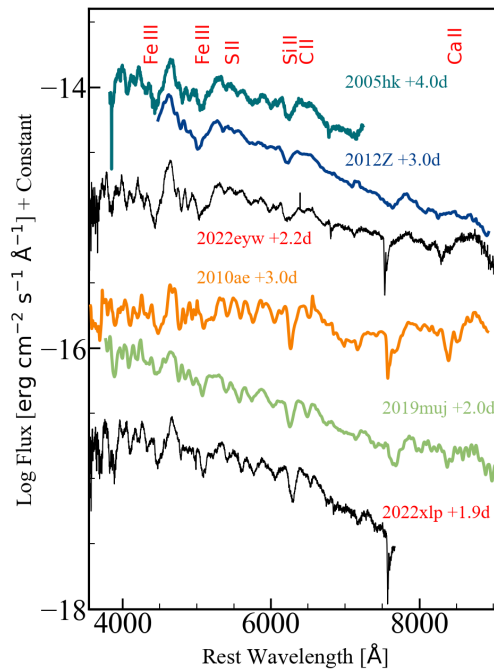


FIGURE 5.22: Comparison of SNe 2022eyw, and 2022xlp with other Type Iax SNe at post-max phases. The comparison spectra are corrected for redshift.

5.2.4 Estimation of Ni mass

We obtained the quasi-bolometric luminosity of 2022eyw, and 2022xlp using $g'r'i'z'$ band magnitudes for all epochs. For 2022eyw, the apparent magnitudes are corrected for $E(B - V)_{total}=0.072$ mag using $R_V=3.1$. The reddening corrected magnitudes are transformed to flux using zeropoints from CHAPTER 2, TABLE 2.1 for the respective filters. A spline curve has been fit to the SED and the area under the curve has been integrated using the trapezoidal rule between $3800 \text{ \AA} - 10000 \text{ \AA}$. Finally the integrated flux has been converted to luminosity using $\mu = 32.85 \pm 0.06$ mag. For 2022xlp, we have used a total reddening $E(B - V)=0.0183$ mag and $\mu = 30.72 \pm 0.02$ mag. The integration has been carried out using the same wavelength range as for 2022eyw.

We estimate the ^{56}Ni mass synthesized in the explosion by fitting EQUATION 3.5 to the quasi-bolometric LCs. For 2022eyw, we estimate $M_{\text{Ni}} = 0.09_{-0.01}^{+0.01} M_{\odot}$, $t_{\text{lc}} = 14.35_{-0.33}^{+0.41}$ days, $t_{\gamma} = 34.29_{-0.77}^{+0.66}$ days, and $t_{\text{exp}} = 2459658.92_{-0.14}^{+0.13}$. Using constant optical opacity $\kappa_{\text{opt}} = 0.1 \text{ cm}^2\text{g}^{-1}$ for an Fe-dominated ejecta, and $v_{\text{exp}} = 6500 \text{ km s}^{-1}$ from the spectrum near-maximum, we get $M_{\text{ej}} = 1.04_{-0.05}^{+0.06} M_{\odot}$, and $E_{\text{k}} = 0.26_{-0.01}^{+0.01} \times 10^{51} \text{ erg}$.

For 2022xlp, we estimate $M_{\text{Ni}} = 0.01_{-0.005}^{+0.005} M_{\odot}$, $t_{\text{lc}} = 9.94_{-0.14}^{+0.13}$ days, $t_{\gamma} = 37.30_{-0.13}^{+0.14}$ days, and $t_{\text{exp}} = 2459861.25_{-0.13}^{+0.14}$. Using constant optical opacity $\kappa_{\text{opt}} = 0.1 \text{ cm}^2\text{g}^{-1}$, and $v_{\text{exp}} = 3000 \text{ km s}^{-1}$ from the spectrum near-maximum, we get $M_{\text{ej}} = 0.23_{-0.01}^{+0.01} M_{\odot}$, and $E_{\text{k}} = 0.012_{-0.003}^{+0.003} \times 10^{51} \text{ erg}$. The quasi-bolometric luminosity of 2022eyw, and 2022xlp are shown in FIGURE 5.23.

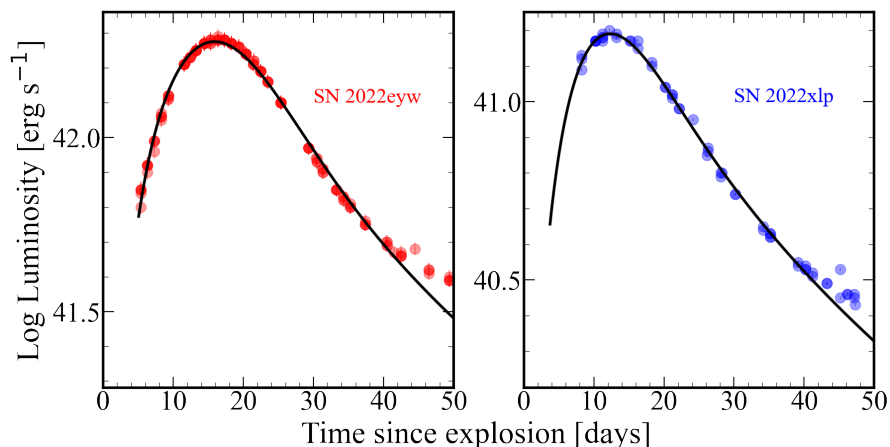


FIGURE 5.23: 1D radiation diffusion model fit to 2022eyw, and 2022xlp. Quasi-bolometric LCs are constructed by considering the flux from 3800 Å to 10000 Å. See Table 5.15 for the fit parameters.

TABLE 5.15: Fit parameters of 1D radiation diffusion model (CHAPTER 3, EQUATION 3.5) to SNe Iax.

SN	M_{Ni} (M_{\odot})	t_{lc} (days)	t_{γ} (days)	JD_{exp}	M_{ej} (M_{\odot})	v_{exp} (km s^{-1})	E_{K} ($\times 10^{51}$ erg)
SN 2002cx	$0.07^{+0.01}_{-0.01}$	$12.29^{+2.12}_{-1.78}$	$42.6^{+3.1}_{-4.2}$	$2452402.43^{+1.12}_{-1.85}$	$0.69^{+0.20}_{-0.24}$	6000	$0.15^{+0.04}_{-0.05}$
SN 2005hk	$0.14^{+0.01}_{-0.01}$	$15.00^{+1.84}_{-1.58}$	$52.8^{+4.3}_{-2.9}$	$2453669.65^{+1.02}_{-1.17}$	$1.13^{+0.27}_{-0.23}$	6500	$0.29^{+0.06}_{-0.06}$
SN 2008ha	$0.004^{+0.000}_{-0.000}$	$9.30^{+1.79}_{-0.52}$	$27.3^{+0.1}_{-0.2}$	$2454773.02^{+0.36}_{-2.03}$	$0.13^{+0.04}_{-0.01}$	2000	$0.003^{+0.0009}_{-0.0003}$
SN 2010ae	$0.006^{+0.001}_{-0.001}$	$5.43^{+1.79}_{-0.52}$	$38.5^{+2.9}_{-1.5}$	$2455246.48^{+0.5}_{-1.1}$	$0.13^{+0.08}_{-0.02}$	5500	$0.02^{+0.01}_{-0.00}$
SN 2012Z	$0.17^{+0.01}_{-0.01}$	$12.97^{+0.66}_{-0.50}$	$44.4^{+1.2}_{-1.2}$	$2455954.32^{+0.31}_{-0.37}$	$1.04^{+0.1}_{-0.09}$	8000	$0.39^{+0.08}_{-0.14}$
SN 2014ck	$0.03^{+0.01}_{-0.01}$	$8.32^{+0.58}_{-0.57}$	$39.6^{+1.9}_{-1.4}$	$2456835.55^{+0.25}_{-0.24}$	$0.16^{+0.02}_{-0.02}$	3000	$0.009^{+0.001}_{-0.001}$
SN 2014ek	$0.12^{+0.01}_{-0.01}$	$16.10^{+1.21}_{-2.41}$	$27.0^{+1.37}_{-0.37}$	$2456944.12^{+1.39}_{-0.63}$	$0.90^{+0.14}_{-0.27}$	4500	$0.11^{+0.02}_{-0.03}$
SN 2019gsc	$0.0019^{+0.000}_{-0.000}$	$9.85^{+0.25}_{-0.26}$	$42.9^{+0.37}_{-0.43}$	$2458627.24^{+0.3}_{-0.3}$	$0.26^{+0.098}_{-0.084}$	3500	$0.019^{+0.007}_{-0.006}$
SN 2019muj	$0.017^{+0.001}_{-0.001}$	$6.2^{+0.63}_{-0.93}$	$28.4^{+0.65}_{-0.70}$	$2458699.52^{+0.65}_{-0.46}$	$0.14^{+0.05}_{-0.03}$	5000	$0.024^{+0.006}_{-0.005}$
SN 2020sck	$0.13^{+0.02}_{-0.01}$	$10.75^{+2.47}_{-1.96}$	$35.02^{+2.47}_{-3.00}$	$2459084.96^{+1.58}_{-1.74}$	$0.34^{+0.07}_{-0.10}$	5000	$0.05^{+0.01}_{-0.01}$
SN 2022eyw	$0.09^{+0.01}_{-0.01}$	$14.35^{+0.41}_{-0.33}$	$34.29^{+0.66}_{-0.77}$	$2459658.92^{+0.13}_{-0.14}$	$1.04^{+0.06}_{-0.05}$	6500	$0.26^{+0.01}_{-0.01}$
SN 2022xlp	$0.01^{+0.005}_{-0.005}$	$9.94^{+0.13}_{-0.14}$	$37.30^{+0.14}_{-0.13}$	$2459861.25^{+0.14}_{-0.13}$	$0.23^{+0.01}_{-0.01}$	3000	$0.012^{+0.003}_{-0.003}$

Note: All the parameters are explained in SECTION 3.1.1

5.3 Explosion Models

We discuss possible explosion models based on the propagation of the burning front and progenitor scenarios which can explain SNe 2020sck, 2022eyw, 2022xlp and similar Iax.

First, we consider the deflagration-to-detonation transition (DDT) models. Here the deflagration flame turns into detonation due to turbulent velocity fluctuations. In three dimensional simulations of M_{ch} WDs, a range of observed luminosity can be produced (Sim et al. 2013). By varying the deflagration strength and central density of the WD, a set of models have been generated to account for the observed properties of SNe Ia (Seitenzahl et al. 2013). In the set of models, the explosions have been generated by considering a distribution of ignition points. The models with greater deflagration strengths produce a lesser amount of ^{56}Ni because the WD expands more before detonation sets in. The models produce a range of ^{56}Ni mass of 0.32 - 1.1 M_{\odot} . This mass range is higher than that found for 2020sck (0.13 M_{\odot}), 2022eyw (0.09 M_{\odot}), and 2022xlp (0.01 M_{\odot}). We also considered a sample of SNe Iax and constructed the quasi-bolometric (3000 Å to 9500 Å). The quasi-bolometric LCs have been fit with EQUATION 3.5.

TABLE 5.15 shows the fit parameters of EQUATION 3.5 to the SNe Iax sample considered here, and FIGURE 5.24 shows the fit of EQUATION 3.5 to the quasi-bolometric LCs of the sample. The ^{56}Ni range (0.004 M_{\odot} - 0.17 M_{\odot}) estimated from the fitting is lower than that inferred from the DDT models. The kinetic energy produced by the DDT models ($E_k = 1.20 - 1.67 \times 10^{51}$ erg) is also higher than that observed for SNe Iax. The range of kinetic energy estimated from the fitting is 0.003×10^{51} erg (SN 2008ha) - 0.39×10^{51} erg (SN 2012Z). The peak magnitude for the DDT model with the weakest deflagration N1 (with one ignition spot) is $M_B = -19.93$. But, the model with the strongest deflagration N1600 (with 1600 deflagration spots and a central density $\rho_c = 2.9 \times 10^9$ gm cm $^{-3}$) gives a

peak magnitude $M_B = -18.26$ mag observed in the brighter Iax. However, the IME production for model N1600 is too large ($M(\text{Si}) = 0.36 M_\odot$) and the velocity higher compared to SNe Iax. The $(B - V)$ colour for the DDT models at B -max is too red ($0.15 - 0.56$ mag) compared to SN 2020sck with $(B - V) = -0.08$ mag. The DDT models do not seem to explain most of the observed properties of 2020sck and the sample Iax.

Next we discuss the pulsational delayed detonation (PDD) model. Due to slow deflagration in a WD, it expands but remains bound. As the burning stops, the infalling CO layer compresses the IGE-rich mixed layers. As a result, detonation is triggered by compression and ignition (Khokhlov 1991b; Hoefflich et al. 1995). In the one-dimensional case, several models have been generated by varying the transition density. This gives rise to a range of ^{56}Ni mass ($0.12 - 0.66 M_\odot$). The ^{56}Ni mass found for SN 2020sck matches with the model PDD5 (the deflagration is turned to detonation at a transition density of $\rho_{\text{tr}} = 0.76 \times 10^7 \text{ g cm}^{-3}$) for which the amount of ^{56}Ni produced is $0.12 M_\odot$. However, the average expansion velocity for this model is 8400 km s^{-1} . This is higher than that found in 2020sck ($\sim 5000 \text{ km s}^{-1}$). The $(B - V)$ colour in the PDD5 model is 0.44 mag which is redder than 2020sck (-0.08 mag).

In the PDD models, the kinetic energy varies from $0.34 - 1.52 \times 10^{51}$ erg. The range of velocity and hence, kinetic energy is also observed in SNe Iax. The extreme case PDD535 ($\rho_{\text{tr}} = 0.45 \times 10^7 \text{ gm cm}^{-3}$) (Hoefflich et al. 1995) has low ^{56}Ni mass ($0.16 M_\odot$) and low average expansion velocities $\sim 4500 \text{ km s}^{-1}$. Due to the pulsation, the material which is falling back interacts with the outgoing detonation wavefront. As a result, a dense shell of mass is formed surrounded by fast-moving layers. These fast-moving layers take away some kinetic energy and decelerate the inner parts of the expanding ejecta. This results in lower expansion velocities. However, in the case of PDD535, the Fe and Ni layers are located below 4000 km s^{-1} . By comparing the synthetic spectra with the observations of

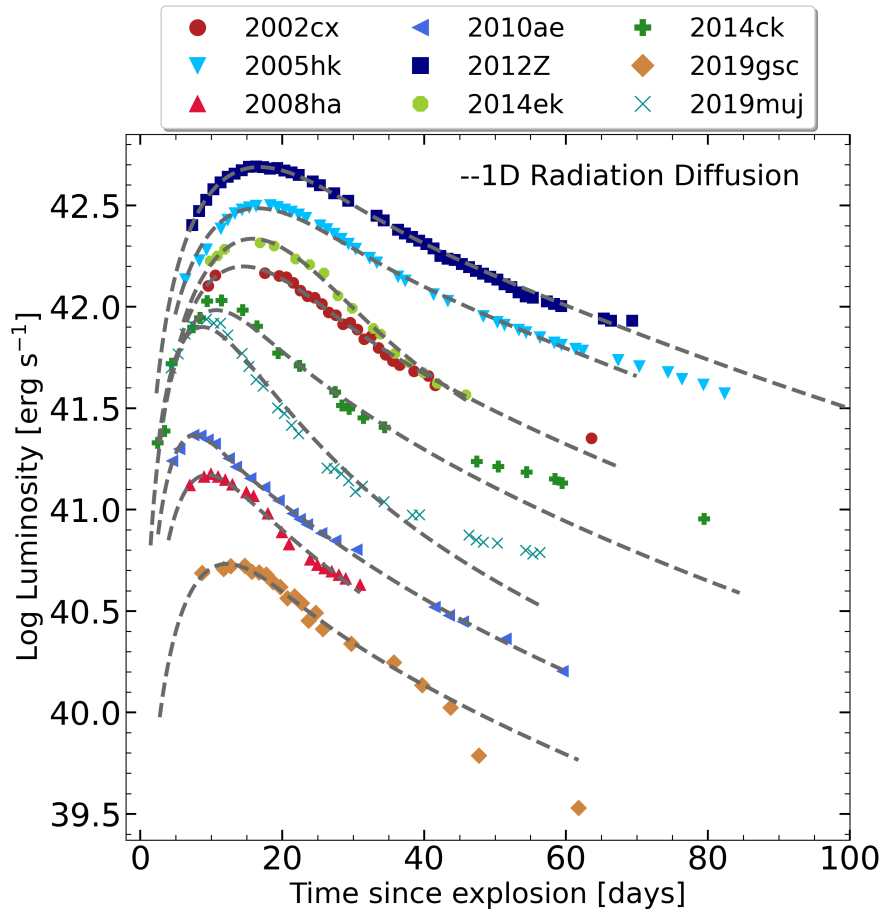


FIGURE 5.24: 1D radiation diffusion model fit to a sample of SNe Iax. A quasi-bolometric LC has been constructed by considering the flux from 3000 \AA to 9500 \AA for all objects. See Table 5.15 for the fit parameters.

SN 2020sck, we find that the Fe and Ni line forming layers are present in the outer parts of the ejecta ($\geq 7000 \text{ km s}^{-1}$). The $(B - V)$ colour is 0.60 mag which is redder than that for SN 2020sck. Hence, the PDD models also do not reproduce some of the observed properties of SN 2020sck.

Previous study by Fink et al. (2014)[F14] have shown that most of the observed properties of SNe Iax class (brighter and intermediate luminosity) can be successfully described by pure deflagrations of M_{ch} CO white dwarf. F14 have generated a set of models by varying the deflagration strength (varying the number of ignition spots). These models produce a range of ^{56}Ni mass ($0.03 - 0.34 M_{\odot}$), with the peak B -band magnitude varying from -16.55 (N1) to -18.11 (N1600). The models

also produce mixed abundance distribution in which Fe and Ni can be present in the outer layers. The models with a lesser number of spots has more viewing angle dependence compared to models with more ignition spots. Models with weak and intermediate deflagration strengths (N1 - N100) produce lesser ejecta and a bound remnant. Comparing with the various models, we find that the explosion properties of the N5-def model with five ignition points (with the central density of the WD being $\rho_c = 2.9 \times 10^9 \text{ gm cm}^{-3}$) matches well with that found by fitting the quasi-bolometric LC of 2020sck with radiation diffusion model. Also, the N5-def density profile with a steep decrease in the outer layers can successfully reproduce the observed spectral features. The rise times to B -maximum for pure deflagration models are less (7.6 d - 14.4 d) compared to 2020sck, but fit the range observed in the sample Iax.

In a recent study by [Lach et al. \(2022\)](#)[L22], 3D hydrodynamic simulations of pure deflagration in M_{ch} WD are generated using a single spot ignition approach. In this work, the metallicity, central density (ρ_c), and the ignition spot location from the center is varied to generate a suite of models. The models have peak magnitude within the range of -15.04 (for a model with the ignition spot at 114 km from the center, ρ_c of $6.0 \times 10^9 \text{ g cm}^{-3}$, and solar metallicity) to -17.43 mag (with the ignition spot at 10 km from the center, ρ_c of $4.0 \times 10^9 \text{ g cm}^{-3}$, and solar metallicity). The models in L22 do not reach the peak magnitudes for some of the brighter members of the Iax category, like 2005hk, 2012Z, 2020rea. In both the works of F14, and L22, the elements are mixed, that is - Fe-group elements, IMEs, and unburned elements are present throughout the ejecta. 2022eyw is best explained by the brightest model from L22, and we compare the spectral evolution of 2022xlp with the model with ignition spot at 114 km from the center, with a ρ_c of $6.0 \times 10^9 \text{ g cm}^{-3}$, and with solar metallicity (See FIGURE 5.25). This model being on the fainter end, produces very less ^{56}Ni ($0.0058 M_\odot$), and ejected mass ($0.014 M_\odot$). The fainter SNe Iax like SN 2008ha, SN 2019gsc, SN 2021fcg are not explained by pure deflagrations in a CO WD. This indicates diversity in the

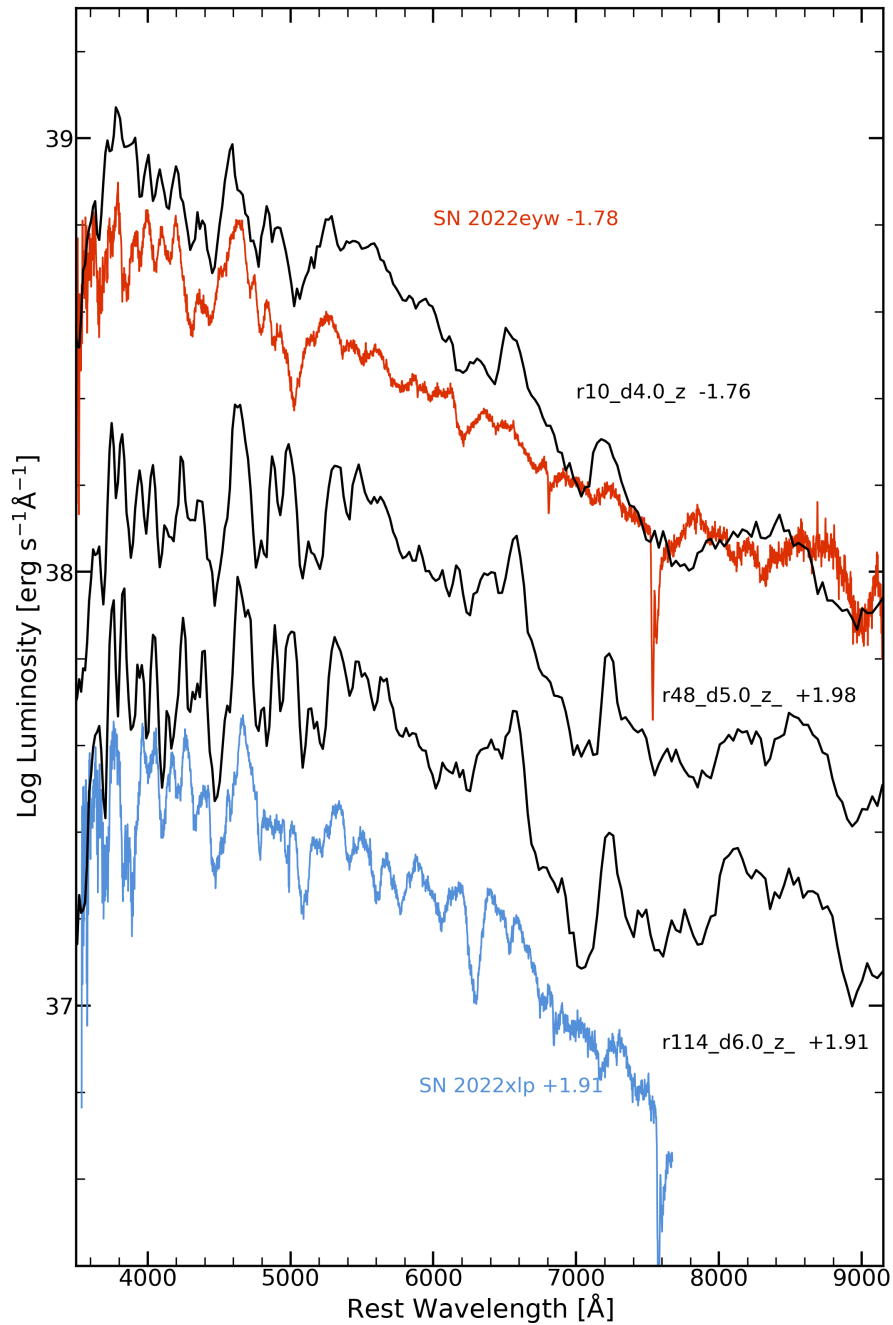


FIGURE 5.25: Comparison of 2022eyw, and 2022xlp spectra with models from Lach et al. (2022).

SNe Iax class in terms of explosion mechanism and/or progenitor properties. We discuss two more models from the literature, which are proposed to explain the fainter Iax.

To reach the lower luminosity end of the Iax class, it is important that the explosion

produces less ^{56}Ni . The ^{56}Ni production can be less, if the burning is quenched at early times. F14 has used a composition of the WD which is $X(\text{Ne}) = 0.025$, $X(\text{C}) = 0.475$, and $X(\text{O}) = 0.50$ by mass. But a change in composition of the WD undergoing explosion can give rise to SNe Iax (Kromer et al. 2015). A WD with a CO core and a ONe layer can undergo deflagration and produce a thermonuclear event. In the 3D simulations of Kromer et al. (2015), the composition is - a CO core (mass upto $0.2 M_{\odot}$) comprised of $X(\text{O}) = 0.5$, $X(\text{C}) = 0.5$, surrounded by CONe layer (mass upto $1.1 M_{\odot}$) consisting of $X(\text{Ne}) = 0.47$, $X(\text{O}) = 0.5$, $X(\text{C}) = 0.03$, and a layer of $X(\text{O}) = 0.5$, and $X(\text{C}) = 0.5$, in the outer part upto $1.4 M_{\odot}$. A carbon burning flame originating from the inside of the WD, when reaches the layer of lesser C abundance (ONe layer) is turned off. Thus the ejected mass is less ($0.014 M_{\odot}$), and a small amount of ^{56}Ni ($0.003 M_{\odot}$) is produced. The bound remnant is quite massive in this case with a mass of $1.39 M_{\odot}$. The abundance structure is mixed as is expected for deflagration models, and the observables have strong viewing angle dependence. The peak luminosity in B -band is in the range of -13.2 mag to -14.6 mag. This explains the faint Iax's like SN 2008ha, SN 2010ae. But the model light curves decline quite faster than observations, possibly because of the lower ejected mass in the models ($0.014 M_{\odot}$) than inferred from the observations ($0.13 M_{\odot}$ for SN 2008ha). The early phase spectra does not have narrow absorption features due to IMEs as seen in the spectra of 2008ha (Kromer et al. 2015). This points towards higher velocities in the models.

Another possible mechanism to produce faint SNe Iax comes from the double degenerate scenario. In the 3D simulation generated by Kashyap et al. (2018), the merger of a CO WD of $1.1 M_{\odot}$, and an ONe WD of $1.2 M_{\odot}$ is considered. After the merger, the CO WD forms a disk around the primary massive ONe WD. The temperature, and pressure required for detonation is reached in the CO disk. The detonation however, is only able to burn the disc and the ONe WD remains almost intact. The conditions for O detonation are different than C detonation. So, the detonation does not burn the ONe WD, and it remains almost intact. This

TABLE 5.16: Comparing the explosion properties of SN 2020sck with single degenerate M_{ch} white dwarf explosion models.

Explosion Model	Velocity	Peak Magnitude	Color	Rise-Time	Spectra	^{56}Ni	Ref.
Deflagration-to-Detonation	✗	✗	✗	✓	✗	✗	1
Pulsational Delayed Detonation (Except PDD5 and PDD535)	✗	✗	✗	✓	✗	✗	2
PDD5	✗	✓	✗	✗	✗	✓	2
PDD535	✗	✓	✗	✗	✗	✓	2
Pure Deflagration (N5-def)	✓	✓	✓	✗	✓	✓	3

References: (1) [Seitenzahl et al. \(2013\)](#), [Sim et al. \(2013\)](#); (2) [Hoefflich et al. \(1995\)](#); (3) [Fink et al. \(2014\)](#)

Note: If the model matches the observed property of SN 2020sck, we put a ✓ else ✗

produces a bound remnant. The ^{56}Ni mass produced is extremely small ($0.00056 M_{\odot}$), and the ejected mass is around $0.08 M_{\odot}$. The peak bolometric magnitude is ~ -11.4 mag. This is fainter than the faintest Iax SN 2021fcg ([Karambelkar et al. 2021](#)).

In Table 5.16, we compare various explosion scenarios of single degenerate M_{ch} WD and show which model can best explain the observed properties of 2020sck. Based on the observational studies by [Phillips et al. \(2007\)](#), [Li et al. \(2003\)](#), and multi-dimensional simulations by F14, L22 we conclude that the observed parameters of SNe Iax can be explained by pure deflagration of white dwarfs.

5.4 Summary

SN 2020sck is a SN Iax with a $\Delta m_B(15) = 2.03 \pm 0.05$ mag, and $M_B = -17.81 \pm 0.22$ mag. From the pre-maximum observations in the ZTF- g band, we constrained the date of explosion as 2020 August 20 (JD = 2459082.4). The light curves in R and I -bands do not exhibit any secondary maximum. The maximum $(B - V)$ colour is bluer compared to the sample of SNe Iax. By fitting the quasi-bolometric, and

blackbody corrected bolometric LC of 2020sck with 1D radiation diffusion model we find $0.13 M_{\odot}$, and $0.17 M_{\odot}$ of ^{56}Ni respectively. The mass ejected is $0.34 M_{\odot}$ with a kinetic energy of 0.05×10^{51} erg. The angle-averaged bolometric LC of 3D pure deflagration model N5-def matches with the quasi-bolometric luminosity of 2020sck.

The spectral characteristics of 2020sck are similar to 2005hk and 2019muj. The comparison of the near-maximum spectrum of 2020sck with `syn++` model spectrum shows the presence of higher ionization states of elements like C III, Si III, Fe III indicating a hot photosphere. Presence of unburned C, and O points towards a CO WD progenitor. Fe lines are found at higher velocities than IMEs indicating that the ejecta is mixed. Angle-averaged one-dimensional density profile of pure deflagration explosion of M_{ch} WD with a steep decrease in the outer layers can successfully reproduce the prominent absorption features in the spectra of 2020sck.

Next we studied two more SNe Iax - SN 2022eyw, and SN 2022xlp. 2022eyw falls at the brighter end (-17.63 mag), while 2022xlp (-14.90 mag) lies at the fainter end of the Iax class. 2022eyw is spectroscopically similar to SN 2005hk, SN 2012Z, while 2022xlp is more similar to SN 2010ae, SN 2019muj. We compare both the SNe with deflagration models from L22. However, we do not rule out the possibility of deflagration in a CO Ne WD or double degenerate scenario. In the case of merger of a CO, and ONe WD, the merger of a more massive ONe will cause higher temperature and densities in the CO disk. This may produce brighter events. Pure deflagration in a M_{ch} WD is a promising scenario for bright and intermediately bright SNe Iax. In the 3D hydrodynamical simulations, it is shown that the more powerful the deflagration is, the more luminous the event, and more mass is ejected. The bound remnant in that case is less massive. Sometimes, the bound remnant after ignition can get a kick velocity which can detach it from the binary system. L22 calculated kick velocities in the range of 7 - 370 km s^{-1} . The search for such remnant is ongoing [Vennes et al. 2017](#); [Raddi et al. 2019](#). In

the case of fainter SNe Iax, the bound remnant is more massive. The chances for finding the bound remnant is more in that case, but multiple burning can finally unbind the WD.

We plan to perform radiative transfer simulations with TARDIS to understand the elemental abundance in the ejecta of SN 2022eyw, and SN 2022xlp. We will perform modelling of the spectra at various phases to study the abundance pattern similar to [Stehle et al. \(2005\)](#), and will use that abundance to construct light curves. 3D hydrodynamical simulations considering pure deflagrations in a M_{ch} WD, has shown that the abundance structure in the ejecta is mixed. But [Barna et al. \(2018\)](#), modelled the spectral evolution of bright SNe Iax in 1D and found that the Fe-group, and IMEs decreases towards the outer regions of the ejecta, and unburned elements like C is present only in the outer regions. [Magee et al. \(2022\)](#) found that stratification of elemental abundance is not strictly required to explain the velocity of the features and ionization within the ejecta. We will look into the abundance pattern to verify whether both faint and bright SNe Iax follow uniform or stratified abundances. More studies of SNe Iax will help to understand the correlation with their host galaxy environment.

Chapter 6

Conclusions and Future Work

In this thesis, we have presented observations of various normal SNe Ia, and Iax. We have performed analytical modelling of the bolometric luminosities, and numerical radiative transfer modelling with **TARDIS**, and **SEDONA**. From the analytical modelling of the bolometric/pseudo-bolometric light curves, we got information on the various explosion parameters like - ^{56}Ni mass, M_{ej} , and E_k . From the numerical radiative transfer models we have inferred about the abundance distribution of elements, and density profiles. The abundances and density structure have been compared with angle-averaged 1D profiles from 3D hydrodynamical simulations of WD explosion models available in the literature. Since the computationally costly 3D simulations are run for specific binary/WD configurations, we aimed for a suite of radiative transfer models with **SEDONA**. We have constructed 1D density profiles by varying the kinetic energy and total mass, and observables like light curves, and spectra in optical are compared to individual SNe. We have also explored various progenitor scenarios/explosion models proposed to explain the faint, and bright SNe Iax.

SN 2017hpa is a normal Ia which showed prominent features due to unburned C in

its pre-maximum spectra. It increases the sample of C-positive SNe Ia. SN 2011aa has the slowest decline rate in B -band, and hence it can help in constraining the decline rate and absolute magnitude relation up to lower $\Delta m_{15}(B)$ (EQUATION 1.2). We also study five SNe Ia showing C in the spectra in the early phase, C II $\lambda 6580$ velocities being lower than Si II $\lambda 6355$, and NUV-blue. We have developed radiative transfer simulations with SEDONA by varying the mass, and kinetic energy which can be used for these five objects as well as other objects.

We study three SNe Iax – SN 2020sck, SN 2022eyw, and SN 2022xlp. This increases the sample of Iax. The study of these objects have revealed that deflagrations in WD is the most promising explosion scenario for bright and intermediately bright SNe Iax, while double degenerate scenario may be at play for the faintest members of this class.

6.1 Future with thermonuclear explosions

With the advent of sky surveys like ZTF, ASAS-SN, ATLAS it has become possible to study the early phase evolution of thermonuclear SNe to distinguish between the possible explosion models. It is observed that SNe Ia show different rise times to maximum. This is primarily attributed to the distribution of ^{56}Ni throughout the ejecta. This can be due to different explosion mechanisms and progenitor properties. In the double detonation explosion model, the burning of accreted He on the surface of WDs produces radioactive ^{56}Ni , ^{48}Cr on the outer regions of the ejecta. This gives rise to early flux excess in the light curves. The early flux excess could also be due to clumped Ni in the ejecta due to asymmetrical deflagration, or ^{56}Ni mixing. Survey studies reduce systematic errors due to calibration. Also, studying samples of SNe Ia will reduce uncertainties due to reddening. Though the explosion mechanisms may not vary with redshift, the progenitor evolves with

redshift. The population of SNe Ia is skewed towards brighter explosions with broader light curves at higher redshift (Howell et al. 2007). At higher redshifts, the galaxies are younger with lower metallicity. The main sequence stars, which essentially become white dwarfs having varied metallicity cause a variation in the amount of ^{56}Ni synthesized. This causes a variation in the peak luminosities. For lower metallicity more ^{56}Ni is produced, and less stable Fe-group elements (Timmes et al. 2003). Variation in the amount of ^{56}Ni introduces scatter in the luminosities, and hence the measurement of distances. Upcoming and future surveys like LSST in optical and near-IR, and ROMAN in IR will monitor SNe Ia at higher redshifts and help understand the SNe Ia explosions better and provide strict estimates of the Universe's expansion rate.

The synthetic spectra and light curves presented in this work are generated assuming LTE ionization, and excitation. As the SN expands and ages, the ejecta becomes optically thin. The density in the ejecta becomes low, thus collisions between ions and electrons become infrequent to assume LTE. The SN thus enters the nebular phase, where the spectral features are mostly emission lines. Because of the low densities, the emission lines are mostly forbidden lines. The continuum opacity from Thomson scattering decreases due to recombination.

The nebular phase light curves offers insights into the radioactive decay isotopes. The isotopic ratio $^{57}\text{Ni} / ^{56}\text{Ni}$ obtained from the late time light curves of SN 2014J has been compared with predictions of delayed detonation models to put tighter constrain on the explosion mechanism (Li et al. 2019b). The late time photometry of SN 2011fe revealed the decay of ^{55}Fe (Tucker et al. 2022). The nebular phase observations and modelling acts as a valuable probe of the central density of the WD, its composition, mixing within the ejecta, and acts as a smoking gun for the explosion mechanism. A higher central density WD will produce more Fe-group elements like (^{54}Fe , ^{58}Ni) than lower central density WD. This can differentiate between M_{ch} , and sub- M_{ch} WD scenario (Iwamoto et al. 1999). I will focus on

modelling the nebular phase spectra by extending the capabilities of TARDIS to include non-thermal energy deposition (from ^{56}Ni decay), γ -ray transport physics. The temperature in each zone can be calculated by balancing the non-thermal heating and cooling by emission lines. The sum of all line transitions gives the line emissivity which is equal to the radioactive energy deposition. We can also relax the sampling of photons from a sharp blackbody photosphere (which is currently an assumption in TARDIS) and include the gamma-ray sampling from ^{56}Ni decay. This will be a major upgrade to TARDIS.

The modelling of the nebular spectra has been used to understand the progenitor white dwarf mass and put constrain on the M_{ch} versus sub- M_{ch} mass scenario (Botyánszki & Kasen 2017). The violent merger of WDs produce copious amounts of oxygen, which are imprinted in the nebular phase as [O III] or [O I] (Mazzali et al. 2022). The double-peaked emission profile in the nebular phase can be used to understand the WD explosions arising from collision models (Dong et al. 2015). For SN 2005E-like Ca-rich transients, the nebular phase spectra showing [O I], and [Ca II] lines can be a probe to solve the debate of whether they have massive star origin (SN 2019ehk, De et al. 2021) or He detonation on the surface of a WD (SN 2018byg, De et al. 2019). The He detonation scenario can also be confirmed based on metal-rich content at the outer layers. By modeling the nebular phase spectra, the line ratios of [Ca II] and [Fe III] can be obtained and compared with theoretical predictions of M_{ch} and sub- M_{ch} scenarios (Polin et al. 2019, 2021). The JWST observations of SNe Ia at nebular phases offer unique insights into the explosion mechanism. Recently, spectroscopic observations in mid-IR, and NIR of SN 2021aefx at nebular phases show emission due to Ar, Fe, Ni. The Ar features have velocities higher than Fe group, indicating stratification in the ejecta (Kwok et al. 2023). This favours a delayed detonation kind of explosion. Another work modelled the JWST spectrum at +323 day to find that detonation happened off-center with respect to the deflagration point (DerKacy et al. 2023). The spectroscopy of fainter SNe are not usually obtained at nebular phases as they

decline faster. Future ground based telescopes like 30 m TMT, 39 m ELT will be very crucial for getting extremely late phase spectra of faint SNe Ia. More such analysis of normal as well as peculiar events will help in detailed understanding of the zoo of thermonuclear explosions.

Some of the interesting thermonuclear explosions are SNe Ia showing CSM signatures. We have observed an explosion - SN 2022erq with GIT, and HCT. The SN show features due to circumstellar interaction (CSI) like $H\alpha$, $H\beta$. It is found that for Ia-CSM, the spectrum can be understood by decomposing into a continuum due to CSM and 1991T-like features (Taddia et al. 2012). It is of great interest to see if they are coming from the same progenitor as 1991T and have similar explosion mechanism, then why some of them shows CSM features while others do not. The hydrogen features hint towards a non-degenerate companion, or a scenario where the WDs merge inside a H-rich common envelope. We compare the spectra of 2022erq with 2002ic to find that features due to Fe are slowly evolving. We plan to perform a detailed study of the photometric and spectroscopic data, and model the light curves with SEDONA, to understand the density profile, and the CSM mass.

The SNe Iax progenitor system is very interesting and less understood. Especially at the fainter end of the SNe Iax class, the deflagration models fail to reproduce the observations. For this reason hybrid CO Ne WD, and double degenerate scenarios are proposed. Super-AGB stars in a particular mass range capable of burning carbon but beneath the oxygen burning limit will form an ONe WD (Schwab et al. 2016). It is important to study how the ONe WD can bypass the gravitational collapse to a NS and produce a thermonuclear explosion (TE). Studies have shown that convective mixing can prevent the C burning to reach the center of the WD thus producing a hybrid CO Ne WD. The hybrid WD at the end of its super-AGB phase forms a C-rich core (Denissenkov et al. 2013). These hybrid WDs are potential progenitors of the fainter Iax ($M_B < -15.0$ mag, Kromer et al. 2015).

This hybrid CONe WD can produce TE if it accretes mass to M_{ch} limit. Now the question is how the CONe WD can reach the M_{ch} limit? CONe WD near the M_{ch} limit can produce subluminous SNe Ia events in the context of a SD channel. However, in the DD channel the merger of the ONe with a CO WD can produce a failed explosion where detonation sets in at the thick disk of the matter accreted from CO secondary, but the primary does not get affected by the detonation. This can give rise to faint SNe Iax with a bound remnant.

We can plan to study stellar evolutionary models with MESA producing ONe WD with unburnt C that can be possible progenitors of Iax. The mass accretion onto the CONe WD to trigger a TE can be studied. Detailed hydrodynamical simulation of the convective hybrid WD is required for this purpose. We can also study the binary evolution of double degenerate systems up to the point of merger to understand the ejection efficiency of the common envelope (CE). Also, the dependency of the retention efficiency of the accreted mass on the angular momentum of such systems can be studied. We are planning to resolve the stellar structure of binary stars that can lead to SNe Iax in terms to initial WD mass, initial donor star mass, mass transfer rate, accretion efficiency and orbital period. Using binary population synthesis models created with COSMIC (Breivik et al. 2019) we can understand the rate of mergers which can account for SNe Iax. This study will help understanding the progenitors of SNe Iax when they are observed with present and future surveys like ZTF, LSST etc. The bound remnant in SNe Iax is very promising, since detection of a bound remnant will be a breakthrough in directly interpreting the progenitor.

It is essential to study samples of thermonuclear SNe of different kinds as mentioned in SECTION 1.3. But it is equally important to study individual SNe Ia showing distinct properties in detail. We therefore, propose to address both these aspects in our future studies.

Bibliography

- Ahumada, R., Prieto, C. A., Almeida, A., et al. 2020, *Astrophys. J. Suppl.*, 249, 3, doi: [10.3847/1538-4365/ab929e](https://doi.org/10.3847/1538-4365/ab929e)
- Ambwani, K., & Sutherland, P. 1988, *Astrophys. J.*, 325, 820, doi: [10.1086/166052](https://doi.org/10.1086/166052)
- Ann, H. B., Seo, M., & Ha, D. K. 2015, *Astrophys. J. Suppl.*, 217, 27, doi: [10.1088/0067-0049/217/2/27](https://doi.org/10.1088/0067-0049/217/2/27)
- Anupama, G. C., Sahu, D. K., & Jose, J. 2005, *Astron. Astrophys.*, 429, 667, doi: [10.1051/0004-6361:20041687](https://doi.org/10.1051/0004-6361:20041687)
- Arnett, W. D. 1982, *Astrophys. J.*, 253, 785, doi: [10.1086/159681](https://doi.org/10.1086/159681)
- Ashall, C., Lu, J., Burns, C., et al. 2020, *Astrophys. J. Lett.*, 895, L3, doi: [10.3847/2041-8213/ab8e37](https://doi.org/10.3847/2041-8213/ab8e37)
- Astropy Collaboration, Robitaille, T. P., Tollerud, E. J., et al. 2013, *Astron. Astrophys.*, 558, A33, doi: [10.1051/0004-6361/201322068](https://doi.org/10.1051/0004-6361/201322068)
- Astropy Collaboration, Price-Whelan, A. M., Lim, P. L., et al. 2022, *Astrophys. J.*, 935, 167, doi: [10.3847/1538-4357/ac7c74](https://doi.org/10.3847/1538-4357/ac7c74)
- Balcon, C. 2022, Transient Name Server Classification Report, 2022-792, 1
- Barna, B., Szalai, T., Kerzendorf, W. E., et al. 2018, *Mon. Not. Roy. Astron. Soc.*, 480, 3609, doi: [10.1093/mnras/sty2065](https://doi.org/10.1093/mnras/sty2065)
- Barna, B., Szalai, T., Jha, S. W., et al. 2021, *Mon. Not. Roy. Astron. Soc.*, 501, 1078, doi: [10.1093/mnras/staa3543](https://doi.org/10.1093/mnras/staa3543)
- Baron, E., Höflich, P., Krisciunas, K., et al. 2012, *Astrophys. J.*, 753, 105, doi: [10.1088/0004-637X/753/2/105](https://doi.org/10.1088/0004-637X/753/2/105)
- Bellm, E. C., Kulkarni, S. R., Graham, M. J., et al. 2019, *Pub. Astron. Soc. Pac.*, 131, 018002, doi: [10.1088/1538-3873/aaecbe](https://doi.org/10.1088/1538-3873/aaecbe)
- Benetti, S., Cappellaro, E., Mazzali, P. A., et al. 2005, *Astrophys. J.*, 623, 1011, doi: [10.1086/428608](https://doi.org/10.1086/428608)
- Bertin, E. 2006, in *Astronomical Society of the Pacific Conference Series*, Vol. 351, *Astronomical Data Analysis Software and Systems XV*, ed. C. Gabriel, C. Arviset, D. Ponz, & S. Enrique, 112
- Bertin, E. 2011, in *Astronomical Society of the Pacific Conference Series*, Vol. 442, *Astronomical Data Analysis Software and Systems XX*, ed. I. N. Evans, A. Accomazzi, D. J. Mink, & A. H. Rots, 435

- Bertin, E., & Arnouts, S. 1996, *Astron. Astrophys. Suppl.*, 117, 393, doi: [10.1051/aas:1996164](https://doi.org/10.1051/aas:1996164)
- Bertin, E., Mellier, Y., Radovich, M., et al. 2002, in *Astronomical Society of the Pacific Conference Series*, Vol. 281, *Astronomical Data Analysis Software and Systems XI*, ed. D. A. Bohlender, D. Durand, & T. H. Handley, 228
- Betoule, M., Kessler, R., Guy, J., et al. 2014, *Astron. Astrophys.*, 568, A22, doi: [10.1051/0004-6361/201423413](https://doi.org/10.1051/0004-6361/201423413)
- Blanton, M. R., & Roweis, S. 2007, *Astron. J.*, 133, 734, doi: [10.1086/510127](https://doi.org/10.1086/510127)
- Blinnikov, S. I., Röpke, F. K., Sorokina, E. I., et al. 2006, *Astron. Astrophys.*, 453, 229, doi: [10.1051/0004-6361:20054594](https://doi.org/10.1051/0004-6361:20054594)
- Blondin, S., Matheson, T., Kirshner, R. P., et al. 2012, *Astron. J.*, 143, 126, doi: [10.1088/0004-6256/143/5/126](https://doi.org/10.1088/0004-6256/143/5/126)
- Botyánszki, J., & Kasen, D. 2017, *Astrophys. J.*, 845, 176, doi: [10.3847/1538-4357/aa81d8](https://doi.org/10.3847/1538-4357/aa81d8)
- Branch, D., Doggett, J. B., Nomoto, K., & Thielemann, F. K. 1985, *Astrophys. J.*, 294, 619, doi: [10.1086/163329](https://doi.org/10.1086/163329)
- Branch, D., & Wheeler, J. C. 2017, *Supernova Explosions*, doi: [10.1007/978-3-662-55054-0](https://doi.org/10.1007/978-3-662-55054-0)
- Branch, D., Dang, L. C., Hall, N., et al. 2006, *Pub. Astron. Soc. Pac.*, 118, 560, doi: [10.1086/502778](https://doi.org/10.1086/502778)
- Breivik, K., Coughlin, S., Zevin, M., et al. 2019, COSMIC-PopSynth/COSMIC: COSMIC, v3.2.0, Zenodo, doi: [10.5281/zenodo.3561144](https://doi.org/10.5281/zenodo.3561144)
- Brown, P. J., Holland, S. T., Immler, S., et al. 2009, *Astron. J.*, 137, 4517, doi: [10.1088/0004-6256/137/5/4517](https://doi.org/10.1088/0004-6256/137/5/4517)
- Brown, P. J., Kuin, P., Scalzo, R., et al. 2014, *Astrophys. J.*, 787, 29, doi: [10.1088/0004-637X/787/1/29](https://doi.org/10.1088/0004-637X/787/1/29)
- Bulla, M., Sim, S. A., Pakmor, R., et al. 2016, *Mon. Not. Roy. Astron. Soc.*, 455, 1060, doi: [10.1093/mnras/stv2402](https://doi.org/10.1093/mnras/stv2402)
- Burns, C. R., Ashall, C., Contreras, C., et al. 2020, *Astrophys. J.*, 895, 118, doi: [10.3847/1538-4357/ab8e3e](https://doi.org/10.3847/1538-4357/ab8e3e)
- Cao, Y., Kulkarni, S. R., Howell, D. A., et al. 2015, *Nature*, 521, 328, doi: [10.1038/nature14440](https://doi.org/10.1038/nature14440)
- Cao, Y., Johansson, J., Nugent, P. E., et al. 2016, *Astrophys. J.*, 823, 147, doi: [10.3847/0004-637X/823/2/147](https://doi.org/10.3847/0004-637X/823/2/147)
- Cardelli, J. A., Clayton, G. C., & Mathis, J. S. 1989, *Astrophys. J.*, 345, 245, doi: [10.1086/167900](https://doi.org/10.1086/167900)
- Cartier, R., Hamuy, M., Pignata, G., et al. 2014, *Astrophys. J.*, 789, 89, doi: [10.1088/0004-637X/789/1/89](https://doi.org/10.1088/0004-637X/789/1/89)
- Chakradhari, N. K., Sahu, D. K., Srivastav, S., & Anupama, G. C. 2014, *Mon. Not. Roy. Astron. Soc.*, 443, 1663, doi: [10.1093/mnras/stu1258](https://doi.org/10.1093/mnras/stu1258)

- Chambers, K. C., Boer, T. D., Bulger, J., et al. 2022, Transient Name Server Discovery Report, 2022-762, 1
- Chatzopoulos, E., Wheeler, J. C., & Vinko, J. 2012, *Astrophys. J.*, 746, 121, doi: [10.1088/0004-637X/746/2/121](https://doi.org/10.1088/0004-637X/746/2/121)
- Childress, M. J., Scalzo, R. A., Sim, S. A., et al. 2013, *Astrophys. J.*, 770, 29, doi: [10.1088/0004-637X/770/1/29](https://doi.org/10.1088/0004-637X/770/1/29)
- Clocchiatti, A., & Wheeler, J. C. 1997, *Astrophys. J.*, 491, 375, doi: [10.1086/304961](https://doi.org/10.1086/304961)
- Colgate, S. A., & McKee, C. 1969, *Astrophys. J.*, 157, 623, doi: [10.1086/150102](https://doi.org/10.1086/150102)
- Contardo, G., Leibundgut, B., & Vacca, W. D. 2000, *Astron. Astrophys.*, 359, 876. <https://arxiv.org/abs/astro-ph/0005507>
- Cowsik, R., Srinivasan, R., & Prabhu, T. 2002, in Astronomical Society of the Pacific Conference Series, Vol. 266, Astronomical Site Evaluation in the Visible and Radio Range, ed. J. Vernin, Z. Benkhaldoun, & C. Muñoz-Tuñón, 424
- De, K., Fremling, U. C., Gal-Yam, A., et al. 2021, *Astrophys. J. Lett.*, 907, L18, doi: [10.3847/2041-8213/abd627](https://doi.org/10.3847/2041-8213/abd627)
- De, K., Kasliwal, M. M., Polin, A., et al. 2019, *Astrophys. J. Lett.*, 873, L18, doi: [10.3847/2041-8213/ab0aec](https://doi.org/10.3847/2041-8213/ab0aec)
- Denissenkov, P. A., Herwig, F., Truran, J. W., & Paxton, B. 2013, *Astrophys. J.*, 772, 37, doi: [10.1088/0004-637X/772/1/37](https://doi.org/10.1088/0004-637X/772/1/37)
- DerKacy, J. M., Ashall, C., Hoefflich, P., et al. 2023, *Astrophys. J. Lett.*, 945, L2, doi: [10.3847/2041-8213/acb8a8](https://doi.org/10.3847/2041-8213/acb8a8)
- Dessart, L., Blondin, S., Hillier, D. J., & Khokhlov, A. 2014, *Mon. Not. Roy. Astron. Soc.*, 441, 532, doi: [10.1093/mnras/stu598](https://doi.org/10.1093/mnras/stu598)
- Dilday, B., Howell, D. A., Cenko, S. B., et al. 2012, *Science*, 337, 942, doi: [10.1126/science.1219164](https://doi.org/10.1126/science.1219164)
- Dong, S., Katz, B., Kushnir, D., & Prieto, J. L. 2015, *Mon. Not. Roy. Astron. Soc.*, 454, L61, doi: [10.1093/mnrasl/slv129](https://doi.org/10.1093/mnrasl/slv129)
- Drout, M. R., Soderberg, A. M., Mazzali, P. A., et al. 2013, *Astrophys. J.*, 774, 58, doi: [10.1088/0004-637X/774/1/58](https://doi.org/10.1088/0004-637X/774/1/58)
- Dutta, A., Anupama, G. C., Chakradhari, N. K., & Sahu, D. K. 2022, *Astrophys. J. Lett.*, 938, L22, doi: [10.3847/2041-8213/ac940d](https://doi.org/10.3847/2041-8213/ac940d)
- Dutta, A., Singh, A., Anupama, G. C., Sahu, D. K., & Kumar, B. 2021, *Mon. Not. Roy. Astron. Soc.*, 503, 896, doi: [10.1093/mnras/stab481](https://doi.org/10.1093/mnras/stab481)
- Filippenko, A. V., Richmond, M. W., Matheson, T., et al. 1992a, *Astrophys. J. Lett.*, 384, L15, doi: [10.1086/186252](https://doi.org/10.1086/186252)
- Filippenko, A. V., Richmond, M. W., Branch, D., et al. 1992b, *Astron. J.*, 104, 1543, doi: [10.1086/116339](https://doi.org/10.1086/116339)
- Fink, M., Kromer, M., Hillebrandt, W., et al. 2018, *Astron. Astrophys.*, 618, A124, doi: [10.1051/0004-6361/201833475](https://doi.org/10.1051/0004-6361/201833475)

- Fink, M., Kromer, M., Seitenzahl, I. R., et al. 2014, *Mon. Not. Roy. Astron. Soc.*, 438, 1762, doi: [10.1093/mnras/stt2315](https://doi.org/10.1093/mnras/stt2315)
- Firth, R. E., Sullivan, M., Gal-Yam, A., et al. 2015, *Mon. Not. Roy. Astron. Soc.*, 446, 3895, doi: [10.1093/mnras/stu2314](https://doi.org/10.1093/mnras/stu2314)
- Fitzpatrick, E. L. 1999, *Pub. Astron. Soc. Pac.*, 111, 63, doi: [10.1086/316293](https://doi.org/10.1086/316293)
- Floers, A., Taubenberger, S., Vogl, C., et al. 2017, *The Astronomer's Telegram*, 10896, 1
- Foley, R. J., Brown, P. J., Rest, A., et al. 2010a, *Astrophys. J. Lett.*, 708, L61, doi: [10.1088/2041-8205/708/1/L61](https://doi.org/10.1088/2041-8205/708/1/L61)
- Foley, R. J., McCully, C., Jha, S. W., et al. 2014, *Astrophys. J.*, 792, 29, doi: [10.1088/0004-637X/792/1/29](https://doi.org/10.1088/0004-637X/792/1/29)
- Foley, R. J., Narayan, G., Challis, P. J., et al. 2010b, *Astrophys. J.*, 708, 1748, doi: [10.1088/0004-637X/708/2/1748](https://doi.org/10.1088/0004-637X/708/2/1748)
- Foley, R. J., Sanders, N. E., & Kirshner, R. P. 2011, *Astrophys. J.*, 742, 89, doi: [10.1088/0004-637X/742/2/89](https://doi.org/10.1088/0004-637X/742/2/89)
- Foley, R. J., Van Dyk, S. D., Jha, S. W., et al. 2015, *Astrophys. J. Lett.*, 798, L37, doi: [10.1088/2041-8205/798/2/L37](https://doi.org/10.1088/2041-8205/798/2/L37)
- Foley, R. J., Chornock, R., Filippenko, A. V., et al. 2009, *Astron. J.*, 138, 376, doi: [10.1088/0004-6256/138/2/376](https://doi.org/10.1088/0004-6256/138/2/376)
- Foley, R. J., Rest, A., Stritzinger, M., et al. 2010c, *Astron. J.*, 140, 1321, doi: [10.1088/0004-6256/140/5/1321](https://doi.org/10.1088/0004-6256/140/5/1321)
- Foley, R. J., Challis, P. J., Filippenko, A. V., et al. 2012, *Astrophys. J.*, 744, 38, doi: [10.1088/0004-637X/744/1/38](https://doi.org/10.1088/0004-637X/744/1/38)
- Foley, R. J., Challis, P. J., Chornock, R., et al. 2013, *Astrophys. J.*, 767, 57, doi: [10.1088/0004-637X/767/1/57](https://doi.org/10.1088/0004-637X/767/1/57)
- Foreman-Mackey, D. 2016, *The Journal of Open Source Software*, 1, 24, doi: [10.21105/joss.00024](https://doi.org/10.21105/joss.00024)
- Foreman-Mackey, D., Hogg, D. W., Lang, D., & Goodman, J. 2013a, *Pub. Astron. Soc. Pac.*, 125, 306, doi: [10.1086/670067](https://doi.org/10.1086/670067)
- Foreman-Mackey, D., Conley, A., Meierjurgen Farr, W., et al. 2013b, emcee: The MCMC Hammer. <http://ascl.net/1303.002>
- Fox, O. D., Johansson, J., Kasliwal, M., et al. 2016, *Astrophys. J. Lett.*, 816, L13, doi: [10.3847/2041-8205/816/1/L13](https://doi.org/10.3847/2041-8205/816/1/L13)
- Fremling, C. 2020, *Transient Name Server Discovery Report*, 2020-2629, 1
- Friedman, A. S., Wood-Vasey, W. M., Marion, G. H., et al. 2015, *Astrophys. J. Suppl.*, 220, 9, doi: [10.1088/0067-0049/220/1/9](https://doi.org/10.1088/0067-0049/220/1/9)
- Fulton, M., Srivastav, S., Smartt, S. J., et al. 2022, *Transient Name Server Classification Report*, 2022-833, 1
- Gagliano, R., Post, R., Weinberg, E., Newton, J., & Puckett, T. 2017, *Transient Name Server Discovery Report*, 2017-1164, 1

- Gamezo, V. N., Khokhlov, A. M., Oran, E. S., Chtchelkanova, A. Y., & Rosenberg, R. O. 2003, *Science*, 299, 77, doi: [10.1126/science.299.5603.77](https://doi.org/10.1126/science.299.5603.77)
- Ganeshalingam, M., Li, W., Filippenko, A. V., et al. 2012, *Astrophys. J.*, 751, 142, doi: [10.1088/0004-637X/751/2/142](https://doi.org/10.1088/0004-637X/751/2/142)
- Garavini, G., Nobili, S., Taubenberger, S., et al. 2007, *Astron. Astrophys.*, 471, 527, doi: [10.1051/0004-6361:20066971](https://doi.org/10.1051/0004-6361:20066971)
- Garnavich, P. M., Bonanos, A. Z., Krisciunas, K., et al. 2004, *Astrophys. J.*, 613, 1120, doi: [10.1086/422986](https://doi.org/10.1086/422986)
- Gehrels, N., Chincarini, G., Giommi, P., et al. 2004, *Astrophys. J.*, 611, 1005, doi: [10.1086/422091](https://doi.org/10.1086/422091)
- Gerardy, C. L., Höflich, P., Fesen, R. A., et al. 2004, *Astrophys. J.*, 607, 391, doi: [10.1086/383488](https://doi.org/10.1086/383488)
- Goldstein, D. A., & Kasen, D. 2018, *Astrophys. J. Lett.*, 852, L33, doi: [10.3847/2041-8213/aaa409](https://doi.org/10.3847/2041-8213/aaa409)
- Gurugubelli, K., Sahu, D. K., Anupama, G. C., Anto, P., & Arora, S. 2011, Central Bureau Electronic Telegrams, 2653, 3
- Han, X., Zheng, W., Stahl, B. E., et al. 2020, *Astrophys. J.*, 892, 142, doi: [10.3847/1538-4357/ab7a27](https://doi.org/10.3847/1538-4357/ab7a27)
- Hicken, M., Garnavich, P. M., Prieto, J. L., et al. 2007, *Astrophys. J. Lett.*, 669, L17, doi: [10.1086/523301](https://doi.org/10.1086/523301)
- Hicken, M., Challis, P., Jha, S., et al. 2009, *Astrophys. J.*, 700, 331, doi: [10.1088/0004-637X/700/1/331](https://doi.org/10.1088/0004-637X/700/1/331)
- Hillebrandt, W., & Niemeyer, J. C. 2000, *Ann. Rev. Astron. Astrophys.*, 38, 191, doi: [10.1146/annurev.astro.38.1.191](https://doi.org/10.1146/annurev.astro.38.1.191)
- Höflich, P., Khokhlov, A. M., & Wheeler, J. C. 1995, *Astrophys. J.*, 444, 831, doi: [10.1086/175656](https://doi.org/10.1086/175656)
- Hogg, D. W. 2022, arXiv e-prints, arXiv:2206.00989, doi: [10.48550/arXiv.2206.00989](https://doi.org/10.48550/arXiv.2206.00989)
- Horne, K. 1986, *Pub. Astron. Soc. Pac.*, 98, 609, doi: [10.1086/131801](https://doi.org/10.1086/131801)
- Howell, D. A. 2001, *Astrophys. J. Lett.*, 554, L193, doi: [10.1086/321702](https://doi.org/10.1086/321702)
- Howell, D. A., Sullivan, M., Conley, A., & Carlberg, R. 2007, *Astrophys. J. Lett.*, 667, L37, doi: [10.1086/522030](https://doi.org/10.1086/522030)
- Howell, D. A., Sullivan, M., Nugent, P. E., et al. 2006, *Nature*, 443, 308, doi: [10.1038/nature05103](https://doi.org/10.1038/nature05103)
- Hunter, J. D. 2007, *Computing in Science & Engineering*, 9, 90, doi: [10.1109/MCSE.2007.55](https://doi.org/10.1109/MCSE.2007.55)
- Iben, I., J., & Tutukov, A. V. 1984, *Astrophys. J. Suppl.*, 54, 335, doi: [10.1086/190932](https://doi.org/10.1086/190932)
- Itagaki, K. 2022, Transient Name Server Discovery Report, 2022-2971, 1

- Iwamoto, K., Brachwitz, F., Nomoto, K., et al. 1999, *Astrophys. J. Suppl.*, 125, 439, doi: [10.1086/313278](https://doi.org/10.1086/313278)
- Jeffery, D. J., & Branch, D. 1990, in *Supernovae, Jerusalem Winter School for Theoretical Physics*, ed. J. C. Wheeler, T. Piran, & S. Weinberg, Vol. 6, 149
- Jha, S., Branch, D., Chornock, R., et al. 2006, *Astron. J.*, 132, 189, doi: [10.1086/504599](https://doi.org/10.1086/504599)
- Jha, S., Riess, A. G., & Kirshner, R. P. 2007, *Astrophys. J.*, 659, 122, doi: [10.1086/512054](https://doi.org/10.1086/512054)
- Jha, S. W., Maguire, K., & Sullivan, M. 2019, *Nature Astronomy*, 3, 706, doi: [10.1038/s41550-019-0858-0](https://doi.org/10.1038/s41550-019-0858-0)
- Karambelkar, V. R., Kasliwal, M. M., Maguire, K., et al. 2021, *Astrophys. J. Lett.*, 921, L6, doi: [10.3847/2041-8213/ac2e90](https://doi.org/10.3847/2041-8213/ac2e90)
- Kasen, D. 2006, *Astrophys. J.*, 649, 939, doi: [10.1086/506588](https://doi.org/10.1086/506588)
- Kasen, D., Röpke, F. K., & Woosley, S. E. 2009, *Nature*, 460, 869, doi: [10.1038/nature08256](https://doi.org/10.1038/nature08256)
- Kasen, D., Thomas, R. C., & Nugent, P. 2006, *Astrophys. J.*, 651, 366, doi: [10.1086/506190](https://doi.org/10.1086/506190)
- Kashyap, R., Haque, T., Lorén-Aguilar, P., García-Berro, E., & Fisher, R. 2018, *Astrophys. J.*, 869, 140, doi: [10.3847/1538-4357/aaedb7](https://doi.org/10.3847/1538-4357/aaedb7)
- Kasliwal, M. M., Kulkarni, S. R., Gal-Yam, A., et al. 2010, *Astrophys. J. Lett.*, 723, L98, doi: [10.1088/2041-8205/723/1/L98](https://doi.org/10.1088/2041-8205/723/1/L98)
- . 2012, *Astrophys. J.*, 755, 161, doi: [10.1088/0004-637X/755/2/161](https://doi.org/10.1088/0004-637X/755/2/161)
- Kawabata, M., Maeda, K., Yamanaka, M., et al. 2020, *Astrophys. J.*, 893, 143, doi: [10.3847/1538-4357/ab8236](https://doi.org/10.3847/1538-4357/ab8236)
- . 2021, *Pub. Astron. Soc. Japan*, doi: [10.1093/pasj/psab075](https://doi.org/10.1093/pasj/psab075)
- Kennicutt, Robert C., J. 1998, *Ann. Rev. Astron. Astrophys.*, 36, 189, doi: [10.1146/annurev.astro.36.1.189](https://doi.org/10.1146/annurev.astro.36.1.189)
- Kerzendorf, W., Nöbauer, U., Sim, S., et al. 2019, *tardis-sn/tardis: TARDIS v3.0 alpha2, v3.0-alpha.2*, Zenodo, doi: [10.5281/zenodo.2590539](https://doi.org/10.5281/zenodo.2590539)
- Kerzendorf, W., Sim, S., Vogl, C., et al. 2023, *tardis-sn/tardis: TARDIS v2023.04.23, release-2023.04.23*, Zenodo, doi: [10.5281/zenodo.7855824](https://doi.org/10.5281/zenodo.7855824)
- Kerzendorf, W. E., & Sim, S. A. 2014, *Mon. Not. Roy. Astron. Soc.*, 440, 387, doi: [10.1093/mnras/stu055](https://doi.org/10.1093/mnras/stu055)
- Khatami, D. K., & Kasen, D. N. 2019, *Astrophys. J.*, 878, 56, doi: [10.3847/1538-4357/ab1f09](https://doi.org/10.3847/1538-4357/ab1f09)
- Khokhlov, A., Mueller, E., & Hoefflich, P. 1993, *Astron. Astrophys.*, 270, 223
- Khokhlov, A. M. 1991a, *Astron. Astrophys.*, 245, 114
- . 1991b, *Astron. Astrophys.*, 245, L25

- Könyves-Tóth, R., Vinkó, J., Ordasi, A., et al. 2020, *Astrophys. J.*, 892, 121, doi: [10.3847/1538-4357/ab76bb](https://doi.org/10.3847/1538-4357/ab76bb)
- Krisciunas, K., Li, W., Matheson, T., et al. 2011, *Astron. J.*, 142, 74, doi: [10.1088/0004-6256/142/3/74](https://doi.org/10.1088/0004-6256/142/3/74)
- Kromer, M., Ohlmann, S., & Röpke, F. K. 2017, *Memorie della Societa Astronomica Italiana*, 88, 312, doi: [10.48550/arXiv.1706.09879](https://doi.org/10.48550/arXiv.1706.09879)
- Kromer, M., Ohlmann, S. T., Pakmor, R., et al. 2015, *Mon. Not. Roy. Astron. Soc.*, 450, 3045, doi: [10.1093/mnras/stv886](https://doi.org/10.1093/mnras/stv886)
- Kromer, M., Fremling, C., Pakmor, R., et al. 2016, *Mon. Not. Roy. Astron. Soc.*, 459, 4428, doi: [10.1093/mnras/stw962](https://doi.org/10.1093/mnras/stw962)
- Kumar, H., Bhalerao, V., Anupama, G. C., et al. 2022, *Astron. J.*, 164, 90, doi: [10.3847/1538-3881/ac7bea](https://doi.org/10.3847/1538-3881/ac7bea)
- Kurucz, R. L., & Bell, B. 1995, Atomic line list
- Kushnir, D., & Katz, B. 2019, Research Notes of the American Astronomical Society, 3, 162, doi: [10.3847/2515-5172/ab5064](https://doi.org/10.3847/2515-5172/ab5064)
- Kushnir, D., Katz, B., Dong, S., Livne, E., & Fernández, R. 2013, *Astrophys. J. Lett.*, 778, L37, doi: [10.1088/2041-8205/778/2/L37](https://doi.org/10.1088/2041-8205/778/2/L37)
- Kwok, L. A., Jha, S. W., Temim, T., et al. 2023, *Astrophys. J. Lett.*, 944, L3, doi: [10.3847/2041-8213/acb4ec](https://doi.org/10.3847/2041-8213/acb4ec)
- Lach, F., Callan, F. P., Bubeck, D., et al. 2022, *Astron. Astrophys.*, 658, A179, doi: [10.1051/0004-6361/202141453](https://doi.org/10.1051/0004-6361/202141453)
- Landau, L. D., & Lifshitz, E. M. 1987, Fluid Mechanics
- Landolt, A. U. 1992, *Astron. J.*, 104, 340, doi: [10.1086/116242](https://doi.org/10.1086/116242)
- Lang, D., Hogg, D. W., Mierle, K., Blanton, M., & Roweis, S. 2010, *Astron. J.*, 139, 1782, doi: [10.1088/0004-6256/139/5/1782](https://doi.org/10.1088/0004-6256/139/5/1782)
- Langer, N., Deutschmann, A., Wellstein, S., & Höflich, P. 2000, *Astron. Astrophys.*, 362, 1046. <https://arxiv.org/abs/astro-ph/0008444>
- Li, L., Wang, X., Zhang, J., et al. 2018, *Mon. Not. Roy. Astron. Soc.*, 478, 4575, doi: [10.1093/mnras/sty1303](https://doi.org/10.1093/mnras/sty1303)
- Li, W., Filippenko, A. V., Chornock, R., et al. 2003, *Pub. Astron. Soc. Pac.*, 115, 453, doi: [10.1086/374200](https://doi.org/10.1086/374200)
- Li, W., Leaman, J., Chornock, R., et al. 2011a, *Mon. Not. Roy. Astron. Soc.*, 412, 1441, doi: [10.1111/j.1365-2966.2011.18160.x](https://doi.org/10.1111/j.1365-2966.2011.18160.x)
- Li, W., Bloom, J. S., Podsiadlowski, P., et al. 2011b, *Nature*, 480, 348, doi: [10.1038/nature10646](https://doi.org/10.1038/nature10646)
- Li, W., Wang, X., Vinkó, J., et al. 2019a, *Astrophys. J.*, 870, 12, doi: [10.3847/1538-4357/aaec74](https://doi.org/10.3847/1538-4357/aaec74)
- Li, W., Wang, X., Hu, M., et al. 2019b, *Astrophys. J.*, 882, 30, doi: [10.3847/1538-4357/ab2b49](https://doi.org/10.3847/1538-4357/ab2b49)

- Lira, P., Suntzeff, N. B., Phillips, M. M., et al. 1998, *Astron. J.*, 115, 234, doi: [10.1086/300175](https://doi.org/10.1086/300175)
- Liu, Z.-W., Zhang, J. J., Ciabattari, F., et al. 2015, *Mon. Not. Roy. Astron. Soc.*, 452, 838, doi: [10.1093/mnras/stv1303](https://doi.org/10.1093/mnras/stv1303)
- Livio, M., & Riess, A. G. 2003, *Astrophys. J. Lett.*, 594, L93, doi: [10.1086/378765](https://doi.org/10.1086/378765)
- Lu, J., Ashall, C., Hsiao, E. Y., et al. 2021, *Astrophys. J.*, 920, 107, doi: [10.3847/1538-4357/ac1606](https://doi.org/10.3847/1538-4357/ac1606)
- Maeda, K., & Kawabata, M. 2022, *Astrophys. J.*, 941, 15, doi: [10.3847/1538-4357/ac9df2](https://doi.org/10.3847/1538-4357/ac9df2)
- Maeda, K., & Terada, Y. 2016, *International Journal of Modern Physics D*, 25, 1630024, doi: [10.1142/S021827181630024X](https://doi.org/10.1142/S021827181630024X)
- Maeda, K., Benetti, S., Stritzinger, M., et al. 2010, *Nature*, 466, 82, doi: [10.1038/nature09122](https://doi.org/10.1038/nature09122)
- Magee, M. R., Gillanders, J. H., Maguire, K., Sim, S. A., & Callan, F. P. 2022, *Mon. Not. Roy. Astron. Soc.*, 509, 3580, doi: [10.1093/mnras/stab3123](https://doi.org/10.1093/mnras/stab3123)
- Magee, M. R., & Maguire, K. 2020, *Astron. Astrophys.*, 642, A189, doi: [10.1051/0004-6361/202037870](https://doi.org/10.1051/0004-6361/202037870)
- Magee, M. R., Sim, S. A., Kotak, R., Maguire, K., & Boyle, A. 2019, *Astron. Astrophys.*, 622, A102, doi: [10.1051/0004-6361/201834420](https://doi.org/10.1051/0004-6361/201834420)
- Magee, M. R., Kotak, R., Sim, S. A., et al. 2016, *Astron. Astrophys.*, 589, A89, doi: [10.1051/0004-6361/201528036](https://doi.org/10.1051/0004-6361/201528036)
- . 2017, *Astron. Astrophys.*, 601, A62, doi: [10.1051/0004-6361/201629643](https://doi.org/10.1051/0004-6361/201629643)
- Maguire, K., Sullivan, M., Thomas, R. C., et al. 2011, *Mon. Not. Roy. Astron. Soc.*, 418, 747, doi: [10.1111/j.1365-2966.2011.19526.x](https://doi.org/10.1111/j.1365-2966.2011.19526.x)
- Maguire, K., Sullivan, M., Pan, Y. C., et al. 2014, *Mon. Not. Roy. Astron. Soc.*, 444, 3258, doi: [10.1093/mnras/stu1607](https://doi.org/10.1093/mnras/stu1607)
- Makarov, D., Prugniel, P., Terekhova, N., Courtois, H., & Vauglin, I. 2014, *Astron. Astrophys.*, 570, A13, doi: [10.1051/0004-6361/201423496](https://doi.org/10.1051/0004-6361/201423496)
- Marion, G. H., Vinko, J., Wheeler, J. C., et al. 2013, *Astrophys. J.*, 777, 40, doi: [10.1088/0004-637X/777/1/40](https://doi.org/10.1088/0004-637X/777/1/40)
- Mazzali, P. A. 2001, *Mon. Not. Roy. Astron. Soc.*, 321, 341, doi: [10.1046/j.1365-8711.2001.04018.x](https://doi.org/10.1046/j.1365-8711.2001.04018.x)
- Mazzali, P. A., Benetti, S., Stritzinger, M., & Ashall, C. 2022, *Mon. Not. Roy. Astron. Soc.*, 511, 5560, doi: [10.1093/mnras/stac409](https://doi.org/10.1093/mnras/stac409)
- Mazzali, P. A., Cappellaro, E., Danziger, I. J., Turatto, M., & Benetti, S. 1998, *Astrophys. J. Lett.*, 499, L49, doi: [10.1086/311345](https://doi.org/10.1086/311345)
- Mazzali, P. A., & Hachinger, S. 2012, *Mon. Not. Roy. Astron. Soc.*, 424, 2926, doi: [10.1111/j.1365-2966.2012.21433.x](https://doi.org/10.1111/j.1365-2966.2012.21433.x)
- Mazzali, P. A., & Lucy, L. B. 1993, *Astron. Astrophys.*, 279, 447

- Mazzali, P. A., Röpke, F. K., Benetti, S., & Hillebrandt, W. 2007, *Science*, 315, 825, doi: [10.1126/science.1136259](https://doi.org/10.1126/science.1136259)
- Mazzali, P. A., Sauer, D. N., Pastorello, A., Benetti, S., & Hillebrandt, W. 2008, *Mon. Not. Roy. Astron. Soc.*, 386, 1897, doi: [10.1111/j.1365-2966.2008.13199.x](https://doi.org/10.1111/j.1365-2966.2008.13199.x)
- Mazzali, P. A., Benetti, S., Altavilla, G., et al. 2005, *Astrophys. J. Lett.*, 623, L37, doi: [10.1086/429874](https://doi.org/10.1086/429874)
- McClelland, C. M., Garnavich, P. M., Galbany, L., et al. 2010, *Astrophys. J.*, 720, 704, doi: [10.1088/0004-637X/720/1/704](https://doi.org/10.1088/0004-637X/720/1/704)
- McCully, C., Jha, S. W., Foley, R. J., et al. 2014, *Nature*, 512, 54, doi: [10.1038/nature13615](https://doi.org/10.1038/nature13615)
- McCully, C., Crawford, S., Kovacs, G., et al. 2018, *astrophy/astrocrappy: v1.0.5* Zenodo Release, v1.0.5, Zenodo, doi: [10.5281/zenodo.1482019](https://doi.org/10.5281/zenodo.1482019)
- McCully, C., Jha, S. W., Scalzo, R. A., et al. 2021, arXiv e-prints, arXiv:2106.04602. <https://arxiv.org/abs/2106.04602>
- Milne, P. A., Brown, P. J., Roming, P. W. A., Bufano, F., & Gehrels, N. 2013, *Astrophys. J.*, 779, 23, doi: [10.1088/0004-637X/779/1/23](https://doi.org/10.1088/0004-637X/779/1/23)
- Mulligan, B. W., & Wheeler, J. C. 2017, *Mon. Not. Roy. Astron. Soc.*, 467, 778, doi: [10.1093/mnras/stw3383](https://doi.org/10.1093/mnras/stw3383)
- Narayan, G., Foley, R. J., Berger, E., et al. 2011, *Astrophys. J. Lett.*, 731, L11, doi: [10.1088/2041-8205/731/1/L11](https://doi.org/10.1088/2041-8205/731/1/L11)
- Nomoto, K. 1982a, *Astrophys. J.*, 253, 798, doi: [10.1086/159682](https://doi.org/10.1086/159682)
- . 1982b, *Astrophys. J.*, 257, 780, doi: [10.1086/160031](https://doi.org/10.1086/160031)
- Nomoto, K., Kamiya, Y., & Nakasato, N. 2013, in *Binary Paths to Type Ia Supernovae Explosions*, ed. R. Di Stefano, M. Orio, & M. Moe, Vol. 281, 253–260, doi: [10.1017/S1743921312015165](https://doi.org/10.1017/S1743921312015165)
- Nomoto, K., Thielemann, F. K., & Yokoi, K. 1984, *Astrophys. J.*, 286, 644, doi: [10.1086/162639](https://doi.org/10.1086/162639)
- Nugent, P., Phillips, M., Baron, E., Branch, D., & Hauschildt, P. 1995, *Astrophys. J. Lett.*, 455, L147, doi: [10.1086/309846](https://doi.org/10.1086/309846)
- Nugent, P. E., Sullivan, M., Cenko, S. B., et al. 2011, *Nature*, 480, 344, doi: [10.1038/nature10644](https://doi.org/10.1038/nature10644)
- Omar, A., Reddy, B. K., Kumar, T., & Pant, J. 2019, *Bulletin de la Societe Royale des Sciences de Liege*, 88, 31. <https://arxiv.org/abs/1908.02531>
- Paczynski, B. 1976, in *Structure and Evolution of Close Binary Systems*, ed. P. Eggleton, S. Mitton, & J. Whelan, Vol. 73, 75
- Pakmor, R., Kromer, M., Röpke, F. K., et al. 2010, *Nature*, 463, 61, doi: [10.1038/nature08642](https://doi.org/10.1038/nature08642)
- Pakmor, R., Kromer, M., Taubenberger, S., et al. 2012, *Astrophys. J. Lett.*, 747, L10, doi: [10.1088/2041-8205/747/1/L10](https://doi.org/10.1088/2041-8205/747/1/L10)

- pandas development team, T. 2020, pandas-dev/pandas: Pandas, latest, Zenodo, doi: [10.5281/zenodo.3509134](https://doi.org/10.5281/zenodo.3509134)
- Pankey, Titus, J. 1962, PhD thesis, Howard University, Washington DC
- Parrent, J. T., Thomas, R. C., Fesen, R. A., et al. 2011, *Astrophys. J.*, 732, 30, doi: [10.1088/0004-637X/732/1/30](https://doi.org/10.1088/0004-637X/732/1/30)
- Pellegrino, C., Howell, D. A., Sarbadhicary, S. K., et al. 2020, *Astrophys. J.*, 897, 159, doi: [10.3847/1538-4357/ab8e3f](https://doi.org/10.3847/1538-4357/ab8e3f)
- Pettini, M., & Pagel, B. E. J. 2004, *Mon. Not. Roy. Astron. Soc.*, 348, L59, doi: [10.1111/j.1365-2966.2004.07591.x](https://doi.org/10.1111/j.1365-2966.2004.07591.x)
- Phillips, M. M. 1993, *Astrophys. J. Lett.*, 413, L105, doi: [10.1086/186970](https://doi.org/10.1086/186970)
- Phillips, M. M., Lira, P., Suntzeff, N. B., et al. 1999, *Astron. J.*, 118, 1766, doi: [10.1086/301032](https://doi.org/10.1086/301032)
- Phillips, M. M., Wells, L. A., Suntzeff, N. B., et al. 1992, *Astron. J.*, 103, 1632, doi: [10.1086/116177](https://doi.org/10.1086/116177)
- Phillips, M. M., Li, W., Frieman, J. A., et al. 2007, *Pub. Astron. Soc. Pac.*, 119, 360, doi: [10.1086/518372](https://doi.org/10.1086/518372)
- Pinto, P. A., & Eastman, R. G. 2000, *Astrophys. J.*, 530, 757, doi: [10.1086/308380](https://doi.org/10.1086/308380)
- Polin, A., Nugent, P., & Kasen, D. 2019, *Astrophys. J.*, 873, 84, doi: [10.3847/1538-4357/aafb6a](https://doi.org/10.3847/1538-4357/aafb6a)
- . 2021, *Astrophys. J.*, 906, 65, doi: [10.3847/1538-4357/abcccc](https://doi.org/10.3847/1538-4357/abcccc)
- Poole, T. S., Breeveld, A. A., Page, M. J., et al. 2008, *Mon. Not. Roy. Astron. Soc.*, 383, 627, doi: [10.1111/j.1365-2966.2007.12563.x](https://doi.org/10.1111/j.1365-2966.2007.12563.x)
- Poznanski, D., Chornock, R., Nugent, P. E., et al. 2010, *Science*, 327, 58, doi: [10.1126/science.1181709](https://doi.org/10.1126/science.1181709)
- Prabhu, T. P., & Anupama, G. C. 2010, in *Astronomical Society of India Conference Series*, Vol. 1, *Astronomical Society of India Conference Series*, 193–201
- Prentice, S., Maguire, K., Magee, M. R., & Deckers, M. 2020, *Transient Name Server Classification Report*, 2020-2685, 1
- Puckett, T., Newton, J., Balam, D. D., et al. 2011, *Central Bureau Electronic Telegrams*, 2653, 1
- Raddi, R., Hollands, M. A., Koester, D., et al. 2019, *Mon. Not. Roy. Astron. Soc.*, 489, 1489, doi: [10.1093/mnras/stz1618](https://doi.org/10.1093/mnras/stz1618)
- Raskin, C., & Kasen, D. 2013, *Astrophys. J.*, 772, 1, doi: [10.1088/0004-637X/772/1/1](https://doi.org/10.1088/0004-637X/772/1/1)
- Raskin, C., Timmes, F. X., Scannapieco, E., Diehl, S., & Fryer, C. 2009, *Mon. Not. Roy. Astron. Soc.*, 399, L156, doi: [10.1111/j.1745-3933.2009.00743.x](https://doi.org/10.1111/j.1745-3933.2009.00743.x)
- Rasmussen, C., & Williams, C. 2006, *Gaussian Processes for Machine Learning, Adaptive Computation and Machine Learning* (Cambridge, MA, USA: MIT Press), 248

- Riess, A. G., Nugent, P., Filippenko, A. V., Kirshner, R. P., & Perlmutter, S. 1998a, *Astrophys. J.*, 504, 935, doi: [10.1086/306106](https://doi.org/10.1086/306106)
- Riess, A. G., Press, W. H., & Kirshner, R. P. 1995, *Astrophys. J. Lett.*, 438, L17, doi: [10.1086/187704](https://doi.org/10.1086/187704)
- . 1996, *Astrophys. J.*, 473, 88, doi: [10.1086/178129](https://doi.org/10.1086/178129)
- Riess, A. G., Filippenko, A. V., Challis, P., et al. 1998b, *Astron. J.*, 116, 1009, doi: [10.1086/300499](https://doi.org/10.1086/300499)
- Riess, A. G., Filippenko, A. V., Li, W., et al. 1999, *Astron. J.*, 118, 2675, doi: [10.1086/301143](https://doi.org/10.1086/301143)
- Rodrigo, C., & Solano, E. 2020, in XIV.0 Scientific Meeting (virtual) of the Spanish Astronomical Society, 182
- Rodrigo, C., Solano, E., & Bayo, A. 2012, SVO Filter Profile Service Version 1.0, IVOA Working Draft 15 October 2012, doi: [10.5479/ADS/bib/2012ivoa.rept.1015R](https://doi.org/10.5479/ADS/bib/2012ivoa.rept.1015R)
- Roming, P. W. A., Kennedy, T. E., Mason, K. O., et al. 2005, *Space Sci. Rev.*, 120, 95, doi: [10.1007/s11214-005-5095-4](https://doi.org/10.1007/s11214-005-5095-4)
- Rosswog, S., Kasen, D., Guillochon, J., & Ramirez-Ruiz, E. 2009, *Astrophys. J. Lett.*, 705, L128, doi: [10.1088/0004-637X/705/2/L128](https://doi.org/10.1088/0004-637X/705/2/L128)
- Sahu, D. K., Tanaka, M., Anupama, G. C., et al. 2008, *Astrophys. J.*, 680, 580, doi: [10.1086/587772](https://doi.org/10.1086/587772)
- Schlafly, E. F., & Finkbeiner, D. P. 2011, *Astrophys. J.*, 737, 103, doi: [10.1088/0004-637X/737/2/103](https://doi.org/10.1088/0004-637X/737/2/103)
- Schwab, J., Quataert, E., & Kasen, D. 2016, *Mon. Not. Roy. Astron. Soc.*, 463, 3461, doi: [10.1093/mnras/stw2249](https://doi.org/10.1093/mnras/stw2249)
- Science Software Branch at STScI. 2012, PyRAF: Python alternative for IRAF. <http://ascl.net/1207.011>
- Seitzzahl, I. R., Ciaraldi-Schoolmann, F., Röpke, F. K., et al. 2013, *Mon. Not. Roy. Astron. Soc.*, 429, 1156, doi: [10.1093/mnras/sts402](https://doi.org/10.1093/mnras/sts402)
- Seitzzahl, I. R., Kromer, M., Ohlmann, S. T., et al. 2016, *Astron. Astrophys.*, 592, A57, doi: [10.1051/0004-6361/201527251](https://doi.org/10.1051/0004-6361/201527251)
- Sharma, Y., Sollerman, J., Fremling, C., et al. 2023, arXiv e-prints, arXiv:2301.04637, doi: [10.48550/arXiv.2301.04637](https://doi.org/10.48550/arXiv.2301.04637)
- Shen, K. J., Blondin, S., Kasen, D., et al. 2021, *Astrophys. J. Lett.*, 909, L18, doi: [10.3847/2041-8213/abe69b](https://doi.org/10.3847/2041-8213/abe69b)
- Silverman, J. M., Nugent, P. E., Gal-Yam, A., et al. 2013, *Astrophys. J. Suppl.*, 207, 3, doi: [10.1088/0067-0049/207/1/3](https://doi.org/10.1088/0067-0049/207/1/3)
- Sim, S. A., Röpke, F. K., Hillebrandt, W., et al. 2010, *Astrophys. J. Lett.*, 714, L52, doi: [10.1088/2041-8205/714/1/L52](https://doi.org/10.1088/2041-8205/714/1/L52)
- Sim, S. A., Seitzzahl, I. R., Kromer, M., et al. 2013, *Mon. Not. Roy. Astron. Soc.*, 436, 333, doi: [10.1093/mnras/stt1574](https://doi.org/10.1093/mnras/stt1574)

- Singh, M., Misra, K., Sahu, D. K., et al. 2018, *Mon. Not. Roy. Astron. Soc.*, 474, 2551, doi: [10.1093/mnras/stx2916](https://doi.org/10.1093/mnras/stx2916)
- . 2022, *Mon. Not. Roy. Astron. Soc.*, 517, 5617, doi: [10.1093/mnras/stac3059](https://doi.org/10.1093/mnras/stac3059)
- Skrutskie, M. F., Cutri, R. M., Stiening, R., et al. 2006, *Astron. J.*, 131, 1163, doi: [10.1086/498708](https://doi.org/10.1086/498708)
- Smartt, S. J. 2009, *Ann. Rev. Astron. Astrophys.*, 47, 63, doi: [10.1146/annurev-astro-082708-101737](https://doi.org/10.1146/annurev-astro-082708-101737)
- Sparks, W. M., & Stecher, T. P. 1974, *Astrophys. J.*, 188, 149, doi: [10.1086/152697](https://doi.org/10.1086/152697)
- Srivastav, S., Ninan, J. P., Kumar, B., et al. 2016, *Mon. Not. Roy. Astron. Soc.*, 457, 1000, doi: [10.1093/mnras/stw039](https://doi.org/10.1093/mnras/stw039)
- Srivastav, S., Smartt, S. J., Leloudas, G., et al. 2020, *Astrophys. J. Lett.*, 892, L24, doi: [10.3847/2041-8213/ab76d5](https://doi.org/10.3847/2041-8213/ab76d5)
- Stalin, C. S., Hegde, M., Sahu, D. K., et al. 2008, Bulletin of the Astronomical Society of India, 36, 111. <https://arxiv.org/abs/0809.1745>
- Stanishev, V., Goobar, A., Benetti, S., et al. 2007, *Astron. Astrophys.*, 469, 645, doi: [10.1051/0004-6361:20066020](https://doi.org/10.1051/0004-6361:20066020)
- Starrfield, S., Truran, J. W., Sparks, W. M., & Kutter, G. S. 1972, *Astrophys. J.*, 176, 169, doi: [10.1086/151619](https://doi.org/10.1086/151619)
- Stehle, M., Mazzali, P. A., Benetti, S., & Hillebrandt, W. 2005, *Mon. Not. Roy. Astron. Soc.*, 360, 1231, doi: [10.1111/j.1365-2966.2005.09116.x](https://doi.org/10.1111/j.1365-2966.2005.09116.x)
- Stritzinger, M., Mazzali, P. A., Sollerman, J., & Benetti, S. 2006, *Astron. Astrophys.*, 460, 793, doi: [10.1051/0004-6361:20065514](https://doi.org/10.1051/0004-6361:20065514)
- Stritzinger, M. D., Hsiao, E., Valenti, S., et al. 2014, *Astron. Astrophys.*, 561, A146, doi: [10.1051/0004-6361/201322889](https://doi.org/10.1051/0004-6361/201322889)
- Stritzinger, M. D., Valenti, S., Hoefflich, P., et al. 2015, *Astron. Astrophys.*, 573, A2, doi: [10.1051/0004-6361/201424168](https://doi.org/10.1051/0004-6361/201424168)
- Stritzinger, M. D., Shappee, B. J., Piro, A. L., et al. 2018, *Astrophys. J. Lett.*, 864, L35, doi: [10.3847/2041-8213/aadd46](https://doi.org/10.3847/2041-8213/aadd46)
- Szalai, T., Vinkó, J., Sárneczky, K., et al. 2015, *Mon. Not. Roy. Astron. Soc.*, 453, 2103, doi: [10.1093/mnras/stv1776](https://doi.org/10.1093/mnras/stv1776)
- Taddia, F., Stritzinger, M. D., Phillips, M. M., et al. 2012, *Astron. Astrophys.*, 545, L7, doi: [10.1051/0004-6361/201220105](https://doi.org/10.1051/0004-6361/201220105)
- Tagchi, K., Namekata, K., Kawabata, M., Nakaoka, T., & Yamanaka, M. 2022, Transient Name Server Classification Report, 2022-783, 1
- Taguchi, K., Maeda, K., & Kawabata, M. 2022, Transient Name Server Classification Report, 2022-2999, 1
- Taubenberger, S. 2017, The Extremes of Thermonuclear Supernovae, ed. A. W. Alsabti & P. Murdin, 317, doi: [10.1007/978-3-319-21846-5_37](https://doi.org/10.1007/978-3-319-21846-5_37)

- Taubenberger, S., Kromer, M., Pakmor, R., et al. 2013a, *Astrophys. J. Lett.*, 775, L43, doi: [10.1088/2041-8205/775/2/L43](https://doi.org/10.1088/2041-8205/775/2/L43)
- Taubenberger, S., Benetti, S., Childress, M., et al. 2011, *Mon. Not. Roy. Astron. Soc.*, 412, 2735, doi: [10.1111/j.1365-2966.2010.18107.x](https://doi.org/10.1111/j.1365-2966.2010.18107.x)
- Taubenberger, S., Kromer, M., Hachinger, S., et al. 2013b, *Mon. Not. Roy. Astron. Soc.*, 432, 3117, doi: [10.1093/mnras/stt668](https://doi.org/10.1093/mnras/stt668)
- Taubenberger, S., Floers, A., Vogl, C., et al. 2019, *Mon. Not. Roy. Astron. Soc.*, 488, 5473, doi: [10.1093/mnras/stz1977](https://doi.org/10.1093/mnras/stz1977)
- Thomas, R. C., Nugent, P. E., & Meza, J. C. 2011, *Pub. Astron. Soc. Pac.*, 123, 237, doi: [10.1086/658673](https://doi.org/10.1086/658673)
- Thompson, T. A. 2011, *Astrophys. J.*, 741, 82, doi: [10.1088/0004-637X/741/2/82](https://doi.org/10.1088/0004-637X/741/2/82)
- Timmes, F. X., Brown, E. F., & Truran, J. W. 2003, *Astrophys. J. Lett.*, 590, L83, doi: [10.1086/376721](https://doi.org/10.1086/376721)
- Tody, D. 1993, in *Astronomical Society of the Pacific Conference Series*, Vol. 52, *Astronomical Data Analysis Software and Systems II*, ed. R. J. Hanisch, R. J. V. Brissenden, & J. Barnes, 173
- Tomasella, L., Cappellaro, E., Benetti, S., et al. 2016, *Mon. Not. Roy. Astron. Soc.*, 459, 1018, doi: [10.1093/mnras/stw696](https://doi.org/10.1093/mnras/stw696)
- Tomasella, L., Stritzinger, M., Benetti, S., et al. 2020, *Mon. Not. Roy. Astron. Soc.*, 496, 1132, doi: [10.1093/mnras/staa1611](https://doi.org/10.1093/mnras/staa1611)
- Tucker, M. A., Shappee, B. J., Kochanek, C. S., et al. 2022, *Mon. Not. Roy. Astron. Soc.*, 517, 4119, doi: [10.1093/mnras/stac2873](https://doi.org/10.1093/mnras/stac2873)
- Turatto, M., Benetti, S., & Cappellaro, E. 2003, in *From Twilight to Highlight: The Physics of Supernovae*, ed. W. Hillebrandt & B. Leibundgut, 200, doi: [10.1007/10828549_26](https://doi.org/10.1007/10828549_26)
- Valenti, S., Pastorello, A., Cappellaro, E., et al. 2009, *Nature*, 459, 674, doi: [10.1038/nature08023](https://doi.org/10.1038/nature08023)
- Van Der Walt, S., Colbert, S. C., & Varoquaux, G. 2011, *Computing in Science & Engineering*, 13, 22
- van Dokkum, P. G. 2001, *Pub. Astron. Soc. Pac.*, 113, 1420, doi: [10.1086/323894](https://doi.org/10.1086/323894)
- Vennes, S., Nemeth, P., Kawka, A., et al. 2017, *Science*, 357, 680, doi: [10.1126/science.aam8378](https://doi.org/10.1126/science.aam8378)
- Vinkó, J., Sárneczky, K., Takáts, K., et al. 2012, *Astron. Astrophys.*, 546, A12, doi: [10.1051/0004-6361/201220043](https://doi.org/10.1051/0004-6361/201220043)
- Virtanen, P., Gommers, R., Oliphant, T. E., et al. 2020, *Nature Methods*, 17, 261, doi: <https://doi.org/10.1038/s41592-019-0686-2>
- Vogl, C., Sim, S. A., Noebauer, U. M., Kerzendorf, W. E., & Hillebrandt, W. 2019, *Astron. Astrophys.*, 621, A29, doi: [10.1051/0004-6361/201833701](https://doi.org/10.1051/0004-6361/201833701)
- Wang, B., & Han, Z. 2012, *New Astronomy Reviews*, 56, 122, doi: [10.1016/j.newar.2012.04.001](https://doi.org/10.1016/j.newar.2012.04.001)

- Wang, X., Li, W., Filippenko, A. V., et al. 2009a, *Astrophys. J.*, 697, 380, doi: [10.1088/0004-637X/697/1/380](https://doi.org/10.1088/0004-637X/697/1/380)
- Wang, X., Filippenko, A. V., Ganeshalingam, M., et al. 2009b, *Astrophys. J. Lett.*, 699, L139, doi: [10.1088/0004-637X/699/2/L139](https://doi.org/10.1088/0004-637X/699/2/L139)
- Webbink, R. F. 1984, *Astrophys. J.*, 277, 355, doi: [10.1086/161701](https://doi.org/10.1086/161701)
- Wee, J., Chakraborty, N., Wang, J., & Penprase, B. E. 2018, *Astrophys. J.*, 863, 90, doi: [10.3847/1538-4357/aacd4e](https://doi.org/10.3847/1538-4357/aacd4e)
- Wheeler, J. C., Johnson, V., & Clocchiatti, A. 2015, *Mon. Not. Roy. Astron. Soc.*, 450, 1295, doi: [10.1093/mnras/stv650](https://doi.org/10.1093/mnras/stv650)
- Woosley, S. E., & Weaver, T. A. 1986, *Ann. Rev. Astron. Astrophys.*, 24, 205, doi: [10.1146/annurev.aa.24.090186.001225](https://doi.org/10.1146/annurev.aa.24.090186.001225)
- . 1994, *Astrophys. J.*, 423, 371, doi: [10.1086/173813](https://doi.org/10.1086/173813)
- Yamanaka, M., Maeda, K., Kawabata, K. S., et al. 2015, *Astrophys. J.*, 806, 191, doi: [10.1088/0004-637X/806/2/191](https://doi.org/10.1088/0004-637X/806/2/191)
- Yaron, O., & Gal-Yam, A. 2012, *Pub. Astron. Soc. Pac.*, 124, 668, doi: [10.1086/666656](https://doi.org/10.1086/666656)
- Yoon, S. C., & Langer, N. 2005, *Astron. Astrophys.*, 435, 967, doi: [10.1051/0004-6361:20042542](https://doi.org/10.1051/0004-6361:20042542)
- Zhang, J.-J., Wang, X.-F., Bai, J.-M., et al. 2014, *Astron. J.*, 148, 1, doi: [10.1088/0004-6256/148/1/1](https://doi.org/10.1088/0004-6256/148/1/1)
- Zhang, K., Wang, X., Zhang, J., et al. 2016, *Astrophys. J.*, 820, 67, doi: [10.3847/0004-637X/820/1/67](https://doi.org/10.3847/0004-637X/820/1/67)